UNIVERSITA' DEGLI
STUDI DI MODENA E REGGIO EMILIA

UNIVERSITÉ LILLE 1
N° d'ordre : 40542

THÈSE en Co-Tutelle

présentée par

Emanuele PAGANELLI

pour obtenir le grade de:

DOCTEUR EN SCIENCES DE LA TERRE DE L'UNIVERSITE DE LILLE 1
Spécialité: Géosciences, Ecologie, Paléontologie et Océanographie

MELT PERCOLATION AND STAGNATION IN A COLD SUBOCEANIC MANTLE (ANDREW BAIN TRANSFORM FAULT, SOUTHWEST INDIAN RIDGE)

Percolation et stagnation des liquides magmatiques dans le manteau supérieur d'une dorsale océanique froide (Zone transformante Andrew Bain, dorsale sud-ouest indienne)

Directeurs de thèse: Daniele BRUNELLI et Monique SEYLER

Soutenue à l'Université de Modène, le 02 septembre 2011

Après avis des rapporteurs :

Jean-Yves COTTIN	Professeur, Université de Saint-Etienne
Michel GREGOIRE	Directeur de Recherches, CNRS-Université Toulouse 3

Devant la commission d'examen formée de :

Enrico BONATTI	Université de Modène et Université de Columbia (U.S.A.)	Président
Daniele BRUNELLI	Université de Modène	Directeur de thèse
Jannik INGRIN	Université Lille 1	Examinateur
Monique SEYLER	Université Lille 1	Directrice de thèse
Paola TARTAROTTI	Université de Milan	Rapporteur

Université Lillle 1 SCIENCES ET TECHNOLOGIES

UNIVERSITÀ DEGLI STUDI
DI MODENA E REGGIO EMILIA

Dottorato di ricerca in Earth System Sciences: Environment, Resources and Cultural Heritage

nell'ambito della scuola di dottorato in Earth System Sciences: Environment, Resources and Cultural Heritage

Ciclo XXIII

Melt percolation and stagnation in a cold suboceanic mantle

In co-tutela con l'Université Lille 1

Candidato: **Emanuele Paganelli**

Relatore Italiano (Tutor): **Dott. Daniele Brunelli**
Relatore Francese (tutor): **Prof. Monique Seyler**

Coordinatore del Dottorato: Prof. Maria Giovanna Vezzalini
Direttore della Scuola di dottorato: Prof. Maria Giovanna Vezzalini

PERCOLATION ET STAGNATION DES LIQUIDES MAGMATIQUES DANS LE MANTEAU SUPERIEUR D'UNE DORSALE OCEANIQUE FROIDE (ZONE TRANSFORMANTE ANDREW BAIN, DORSALE SUD-OUEST INDIENNE)

Mots-clés: 1) péridotite; 2) dorsale océanique; 3) faille transformante; 4) océan indien; 5) fusion partielle; 6) réaction solide-liquide; 7) refertilisation; 8) éléments en traces

Le manteau asthénosphérique est le siège de processus pétrologiques qui se produisent à forte profondeur, dont les effets sont masqués, voire effacés, au cours de la décompression et de la fusion partielle qui accompagnent l'ouverture d'une dorsale océanique. Pour avoir accès à ces processus, il est nécessaire d'étudier des échantillons de manteau qui ont subi un très faible degré de fusion partielle. Les régions de dorsales océaniques, qui sont caractérisées par des vitesses d'expansion très lentes et/ou par des anomalies thermiques froides, sont donc des régions privilégiées pour l'étude de ces processus profonds. La zone de fracture Andrew Bain, une des failles transformantes les plus importantes du système mondial de dorsales médio-océaniques et située dans l'océan sud-ouest indien, en est un exemple remarquable. Elle forme, avec les zones de fracture Du Toit, Prince Edward et Marion, une partie de la marge entre les plaques africaine et antarctique. Elle est caractérisée par une structure lenticulaire. Son rejet long de ~750 km met en contact la zone axiale de la dorsale sud-ouest indienne avec une lithosphère océanique ancienne et refroidi, ce qui a pour effet d'accentuer le refroidissement de cette parte de dorsale (« cold-ridge effect ») ; or, la dorsale sud-ouest indienne est une dorsale ultra-lente, et donc déjà caractérisée par une structure thermique plus froide que la normale. Il en résulte une très faible production magmatique, qui se traduit par une croûte océanique quasi-absente et un manteau lithosphérique très épais qui affleure directement sur le fond océanique.

La campagne océanographique S23-AB06 menée conjointement par la l'Italie et la Russie a permis d'échantillonner le massif d'intersection sud entre la dorsale sud-ouest indienne et la faille Andrew Bain. Les échantillons prélevés sont presqu'exclusivement des roches ultramafiques représentées par des péridotites montrant des imprégnations par des assemblages pyroxénitiques équilibrés dans le champ de stabilité du spinelle (associations minérales à sp +cpx ± opx ± ol), ou par des assemblages minéralogiques à plagioclase (pl + cpx ± ol). Les assemblages à plagioclase forment aussi des schlieren qui définissent une linéation magmatique. Les roches prélevées à l'axe de la dorsale montrent en plus des agrégats gabbroiques tardifs et des veines diversement enrichies en clinopyroxènes.

Les éléments majeurs et en traces des assemblages minéralogiques ont été analysés par EMPA et LA-ICP-MS sur les minéraux non altérés. Les pyroxènes dans les péridotites à spinelle et les péridotites à plagioclases ont des compositions résiduelles variables, indiquant un processus de fusion partielle associé à un rééquilibrage progressif à des conditions P-T de plus en plus basses. La

variabilité des compositions à l'échelle de la lame mince correspond à la variabilité des compositions à l'échelle de l'échantillonnage. Le processus de rééquilibrage s'est probablement effectué par des réactions entre péridotites et liquides percolant et par de la diffusion à l'état solide.

La modélisation des compositions chimiques montre que ces liquides sont des liquides de fusion générés dans un grand intervalle de pression. Cette modélisation montre en outre que certains de ces liquides sont probablement générés par la fusion de lithologies enrichies en éléments incompatibles et de lithologies qui sont typiques des domaines de transition océan-continent. La modélisation suggère aussi que la fusion a commencé dans le champ de stabilité du grenat mais s'est arrêtée à relativement haute pression à cause du refroidissement lithosphérique. Ceci a permis la refertilsation de larges portions de manteau sous la zone de fracture d'Andrew Bain.

MELT PERCOLATION AND STAGNATION IN A COLD SUBOCEANIC MANTLE (ANDREW BAIN TRANSFORM FAULT, SOUTHWEST INDIAN RIDGE)

Key-words: 1) peridotite; 2) mid-ocean ridge; 3) transform fault; 4) Indian ocean;
5) partial melting; 6) solid-liquid reaction; 7) referilization; 8) trace elements

The roots of the melting region beneath a Mid Oceanic Ridge host a number of processes usually hidden to the petrological studies because strongly overprinted by the following intense partial melting and strong melt/rock interaction. Samples of mantle that underwent very low degrees of partial melting are required to unravel such an early story. These can only be recovered in cold stretches of the Mid Oceanic Ridges such as those characterized by very slow spreading rates or cold thermal anomalies. A remarkable example is the Andrew Bain Fracture Zone (ABFZ), one of the largest transform faults in the Earth's Mid Ocean Ridge system. The ABFZ is located on the South West Indian Ridge and constitutes with Du Toit FZ, Prince Edward FZ and Marion FZ a part of the plate margin between Africa and Antarctica. It reaches 750 km in length and is characterized by a lens-shape structure. A strong age contrast results in an enhanced cold-edge effect, thicker than normal lithosphere and large residual ultramafic outcrops at the seafloor.

During the Italian-Russian expedition S23-AB06, the Southern Ridge Transform Intersection (RTI) has been sampled allowing the recovery of almost exclusively ultramafic material in the major part of the dredging sites. The samples are spinel- and plagioclase-bearing peridotites showing hybrid textures characterized either by impregnation of mineral assemblages equilibrated in the deeper part of the spinel stability field (sp + cpx ± opx ±ol) or plagioclase-field equilibrated patches. Mineral trails (pl + cpx ± ol) define lineation; they are associated with the formation of plagioclase coronas around pristine spinel. The samples collected from the ridge axis also show late-stage gabbroic pockets and veins variably enriched in clinopyroxene.

Major and trace element compositions of fresh mineral relics have been determined by EMPA and LA-ICP-MS techniques. Concerning the major element analysis, pyroxenes and spinels of both spinel-bearing peridotites and plagioclase-bearing peridotites follow a main melting trend accompanied by a progressive re-equilibration to lower P/T facies at all scales. Thin section-scale variability matches inter-site compositional variability. Progressive re-equilibration to lower P/T conditions can be accounted for by the presence of percolating melts and solid diffusion.

Major and trace element modeling shows that percolating melts are generated over a wide pressure range starting in the garnet stability field. They also show that some melts are possibly generated by incompatible element enriched lithologies and by lithologies that can be typical of ocean-continent transition. Moreover, modeling suggests melting started in garnet stability field but stopped early due to the lithospheric cooling, allowing percolating melt to refertilize large mantle portions beneath ABFZ.

Abstract

Index

Chapter 1

Geological Setting

1.1 South West Indian Ridge

The South West Indian Ridge (SWIR) represents the present-day plate boundary between Antarctica and Africa Plates. It runs from the Bouvet Triple Junction (55°S, 0°E) to the Rodriguez Triple Junction (25°S, 70°E), reaching about 7700 km of length (FISHER & GOODWILLIE, 1997).

The SWIR is one of the slowest ridges of the world wide mid-oceanic ridge system, its full spreading rate ranging from 13 to 16 mm/yr (PATRIAT ET AL., 2008). Like the major part of ridges the morphology and tectonic features of this ridge vary all across its entire length (GEORGEN ET AL., 2001). In fact, it is easy to identify two different sectors comparable in length, one shifted northward and the other southward, linked together by four large fracture zones that, in less than 400 km, offset the SWIR for more than 1200 km. Moving eastward they are: Du Toit Fracture Zone (DTFZ), Andrew Bain Fracture Zone (ABFZ), Marion

Fracture Zone (MFZ) and Prince Edward Fracture Zone (PEFZ), that altogether constitute the transform Andrew Bain system (SCLATER ET AL., 2005). The two parts of SWIR, west and east of the Andrew Bain system, are structurally complex and heterogeneous.

Near Bouvet Triple Junction, the SWIR is characterized by short segments separated by transform faults that display offsets greater than 100 km, with volcanic activity influenced by the proximity of Bouvet hot-spot (LIGI ET AL., 1999). Moving eastward (5° E - 15° E), the SWIR axis is characterized by the magmatic starved oblique spreading supersegment described by DICK ET AL. (2003) as representative of the ultraslow spreading class of mid-ocean ridges. Between 15° E and 25° E, two linear segments are present, scarcely magmatic and displaying no large transform faults: this "orthogonal" supersegment is oriented approximately perpendicularly to the spreading direction and is morphologically and geophysically similar to first-order ridge segments described along the slow-spreading Mid-Atlantic Ridge (GRINDLEY ET AL., 1998, DICK ET AL., 2003).

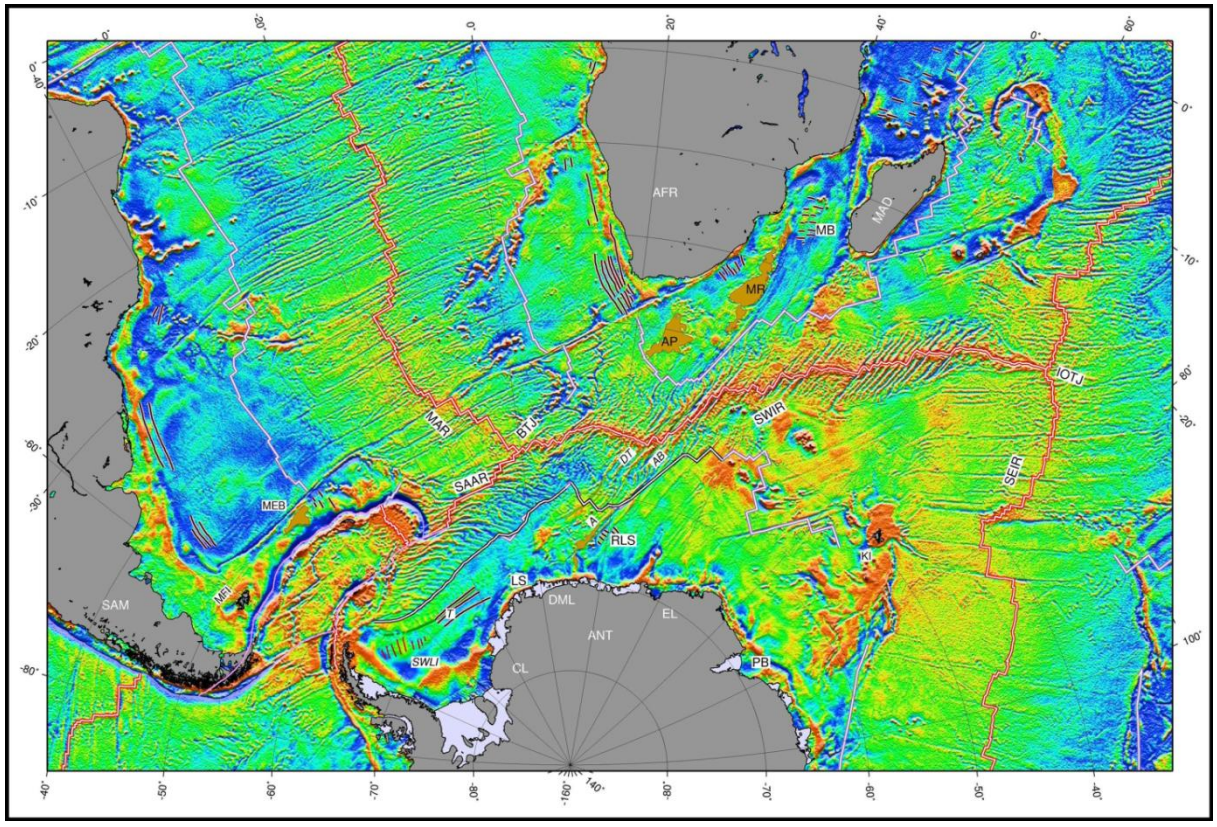

Figure 1.1.1 – *Principal features of the ridge system in South America, Africa and Antarctica. Image has been realized using free air gravimetric anomalies collected from satellite-derived gravimetry data: SANDWELL & SMITH (1997) concerning the region above 60° S, and LAXON AND MCADOO (1998) concerning the region below 60° S. White lines represent 83.5 Ma isochrone. Current expansion center are represented by red lines. A: Astrid FZ. ANT: Antarctica. AFR: Africa. BTJ: Bouvet Triple Junction. CL: Coats Land. DML: Dronning Maud Land. EL: Enderby Land. FMI: Falkland/Malvinas Islands. IOTJ: Indian Ocean Triple Junction. KI: Kerguelen Island. LS: Lazarew Sea. MAD: Madagascar. MAR: Mid Atlantic Ridge. MEB: Maurice Ewing Bank. MB: Mozambique Basin. PB: Pridtz Bay. RLS: Riisen-Larsen Sea. SAAR: South American - Antarctic Ridge. SAM: South America. SEIR: Southeast Indian Ridge. SWIR: Southwest Indian Ridge. (from http://gqt.conae.gov.ar/iaa/ipyg/Introduccion/Framework.jpg)*

East of the Andrew Bain system, the ridge presents a large swell due to the presence of the Marion hot-spot. In this part of the SWIR, the segmentation is irregular, depths are shallower and magmatism is enhanced in response to the interaction with the hot-spot itself (GEORGEN ET AL., 2001). The influence of the hot-spot stops against the Gallieni Fracture Zone, to the east the SWIR displays again a strong segmentation, associated to a weak magmatism and large exposures of mantle rocks leading to a peculiar ridge morphology defined as “smooth seafloor” (CANNAT ET AL., 2006) It is worth noting that in this region the SWIR is younger than the western regions, this is because it started to form about 45 Ma, due to the eastward migration of the Rodriguez Triple Junction.

1.2 Tectonic evolution of the South West Indian Ridge

The South West Indian Ocean originated from the rifting of Gondwana, and the following splitting of Antarctica and India from Africa and South America (LIVERMORE & HUNTER, 1996). Magnetic anomalies data suggest that the oceanization started in late Jurassic (SIMPSON ET AL., 1979; LABREQUE & D.E.HAYES, 1979), and expansion history of the SWIR appears to be

characterized by a general trend of decreasing spreading rate, varying from fast to slow and ultra-slow spreading rates. Based on satellite-derived bathymetric data, several phases have been recognized in the spreading history of the SWIR (ROYER ET AL., 1988; BERNARD ET AL., 2005).

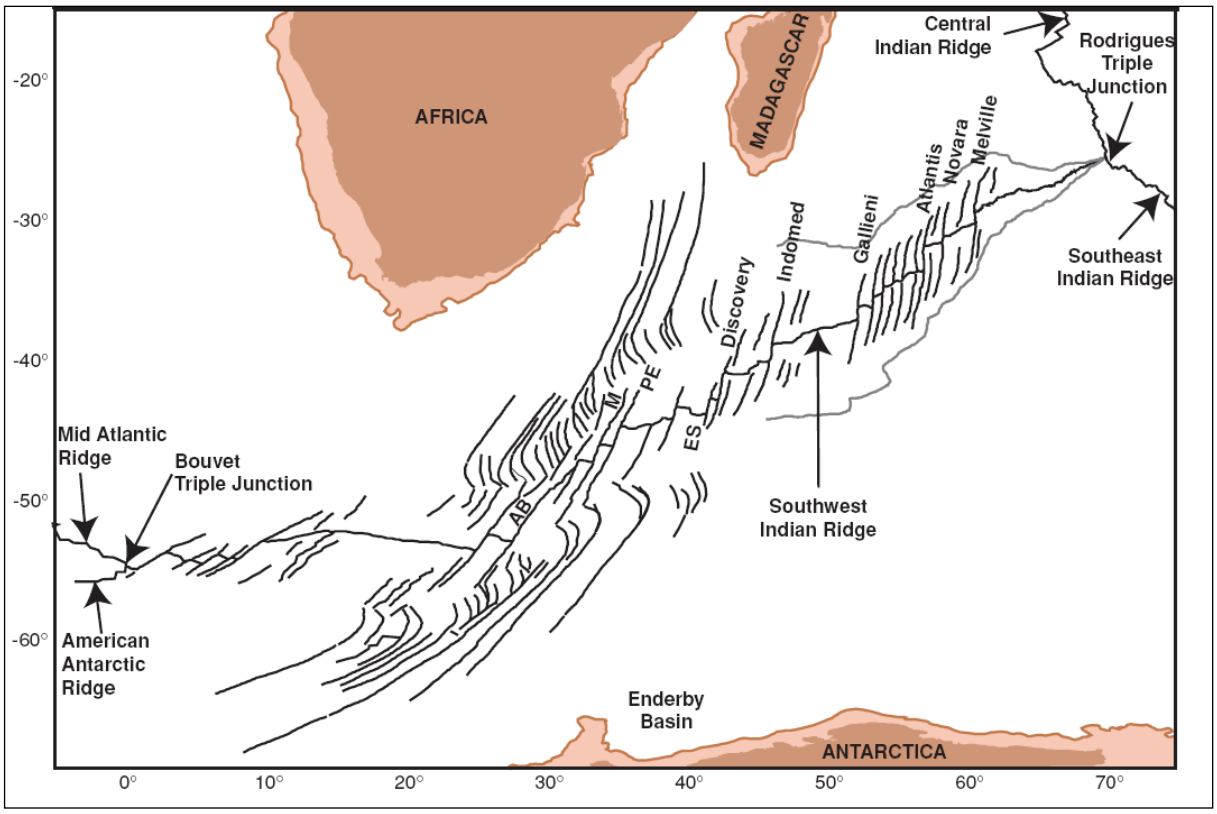

Figure 1.2.1 *– (from BERNARD ET AL., 2005): present-day tectonic setting of South West Indian Ridge. Sea-floor bathymetry allows detecting the most important variations in time of the rotation poles of Africa Plate and Antarctica Plate. Ridge is included between Bouvet Triple Junction, in west, and Rodriguez Triple Junction, in east.*

First phase is between the opening of the Indian ocean till 64 Ma. Opening occurred on a NE-SW direction, with a fast spreading rate (60 mm/yr, full spreading). Later the spreading direction changed from NE-SW to NW-SE, while expansion rate dropped to values of 10 mm/yr (ROYER ET AL., 1988).

In the period between 64 and 59 Ma the African Plate changed the direction of movement, moving northwestward with respect to the Antarctica Plate. This change lasted for a short time till the Miocene when the plates returned to their original directions, while spreading rate increased again up to 29mm/yr (ROYER ET AL., 1988). Then, at about 24 Ma, the spreading rate dropped down very quickly to 14 mm/yr (full spreading), while eulerian pole remained in the same position (PATRIAT ET AL., 2008). During early Miocene, the SWIR was affected by another great tectonic event: from 30 Ma, African Plate broke in two new different plates, the Nubian Plate to the West, and Somalian Plate to the East (EBINGER ET AL., 2000). Such a period seems to be contemporaneous with the relative acceleration of Indian Plate with respect to Antarctica plate, resulting in the eastward movement of the Rodriguez Triple Junction. The increment of spreading rate between India and Africa started about 71 Ma, until when, at about 51 Ma, collision between India and Asia took place. The collision reduced its strength about 43 Ma, however the rotation and movement parameters that control the SWIR topography appear to have changed as a consequence of this collision (BERNARD ET AL., 2006).

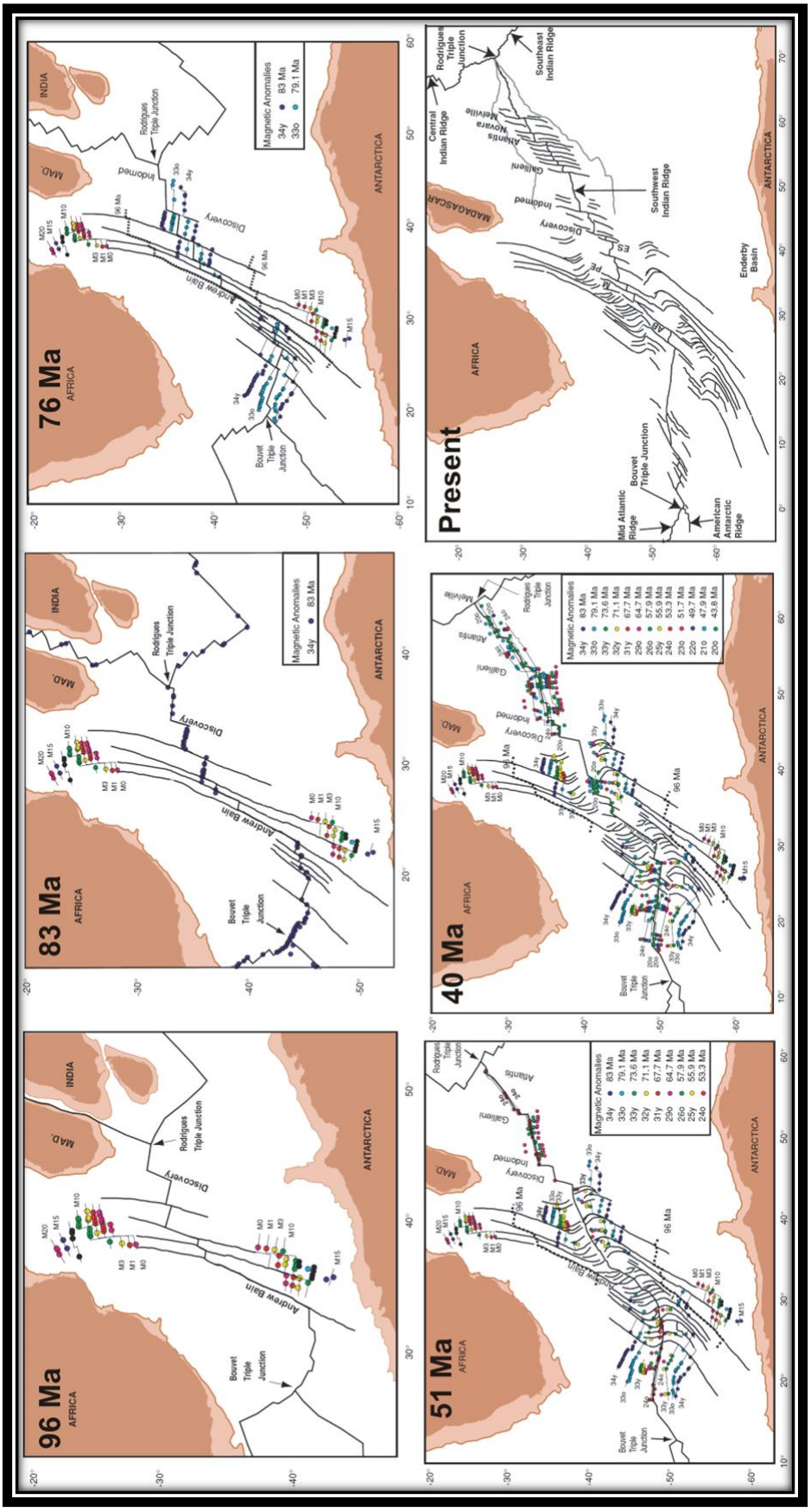

Figure 1.2.2 – *Evolution history of SWIR tectonic (from BERNARD ET AL., 2005). The evolution of the ridge has undergone an important changing 50-40 Ma (anticlockwise rotation of eulerian poles), to return then in a similar spreading direction existing before this rotation.*

Proposed eulerian poles for Nubia-Somalia are mainly located to the south with respect to Africa continent, but north with respect to the SWIR (CHU & GORDON, 1999; LEMAUX ET AL., 2002; HORNER-JOHNSON ET AL., 2005). Such a position for the eulerian pole would cause the compressional regime of the southern portion of this plate boundary and the extensional regime in the northern part.

These eulerian poles have been calculated assuming that all the deformation due to the relative movement of Nubia with respect to Somalia is focused on a "standard" plate boundary, i.e. very narrow. This plate boundary should then intersects the SWIR in the ABFZ region. The assumption of a narrow plate boundary, where all the deformation in concentrated, is generally accepted, and it results correct in most cases. However, in some geodynamic settings, wider deformation domains have been proposed, better explaining tectonic features. Nubia-Somalia plate boundary could be one of these cases: the absence of a clear topographic feature that marks this plate boundary, the absence of a narrow seismic active region, the localization of great magnitude earthquakes on the ocean floor shifted northward with respect of the SWIR are all features that can lead to this particular condition. Some actual cinematic models try to consider this situation. HORNER-JOHNSON ET AL. (2005) show a result in agreement with a plate boundary that can reaches 700 km in width, situated between 26.3° E and 32.2° E, thus including the ABFZ domain. However, authors point out that this region shouldn't be wide enough to enclose all observed earthquakes, and that the SWIR angular velocities are not in agreement with the ones observed in Red Sea and Gulf of Aden. Somalia plate seems not to be completely brittle, but to be characterized by wide deformation zones (HORNER-JOHNSON ET AL., 2005). Recently, TAKEUCHI ET AL. (2010) discard the possibility that ABFZ can represent by itself this plate boundary, as proposed before by LEMAUX ET AL. (2002), because the magnetic anomalies of the west and east regions of the

sea-floor with respect to the ABFZ seem to be in agreement with a unique eulerian pole. This hypothesis can be anyway in agreement with HORNER-JOHNSON ET AL. (2005), by the way the plate boundary should be so wide that can deny a clear observation in the differences in magnetic anomalies.

From this, it is clear that the cinematic setting of this crustal portion is complex and not yet clear. Despite of that, it is difficult to think Somalia plate to be brittle and, thus, to find a well defined Antarctica-Nubia-Somalia triple junction.

1.3 The Andrew Bain Fracture Zone

The Andrew Bain Fracture Zone (ABFZ) is a major transform domain in the SWIR (Fig. 1.3.1). Its southern end lies at 53° S and 28° E, and its northern end at 47° S and 32°30' E. As mentioned before the ABFZ is a complex system composed by several fracture zones that offset the SWIR (Fig. 1.3.1). The most important ones have been investigated by FISHER & GOODWILLIE, (1997). The major fracture zones nearby the Andrew Bain domain are: Du Toit FZ, Andrew Bain FZ and the double fracture zone of Prince Edward, of which the most western part has been then renamed Marion Fracture Zone by SCLATER ET AL. (1997).

In the whole, these fracture zones displace about 400 km of ocean ridge and split the SWIR in two parts that show roughly the same length. Bathymetric features on the sea-floor show the relative movement of the Somalia Plate with respect to Antarctica Plate from late Jurassic, when the two continents start to separate (BERNARD ET AL., 2005).

ABFZ has been partially investigated and scarcely sampled during few oceanic expeditions in last years (GRINDLAY ET AL., 1996, FISHER & GOODWILLIE, 1997, SCLATER ET AL., 2005). Despite the fact that the present seismicity appears to be localized on a unique linear structure, topography and satellite-derived free-air gravity anomalies (SANDWELL & SMITH, 1997) show a wide and complex deformation domain (Fig. 1.3.2) characterized by a series of sub-parallel humps and valleys that range in a 800 km long and 100 km wide region of the sea-floor and reaches 6500 m in depth. The central part of the transform domain is characterized by

oblique structures showing *en-echelon* arrangement. BERNARD ET AL. (2005) and SCLATER ET AL. (2005) give a synthesis of the complexity of this region, explaining it through a series of transtensive events, resulting from changes in the ridge-transform-ridge geometric relationships. These changes seem to be induced by the movements of the Africa-Antarctica eulerian pole. The ridge axis arrangement has occurred trough strong rotations, as it can be seen in the sea-floor topography defining a large sigmoidal shaped region (Fig. 1.3.2).

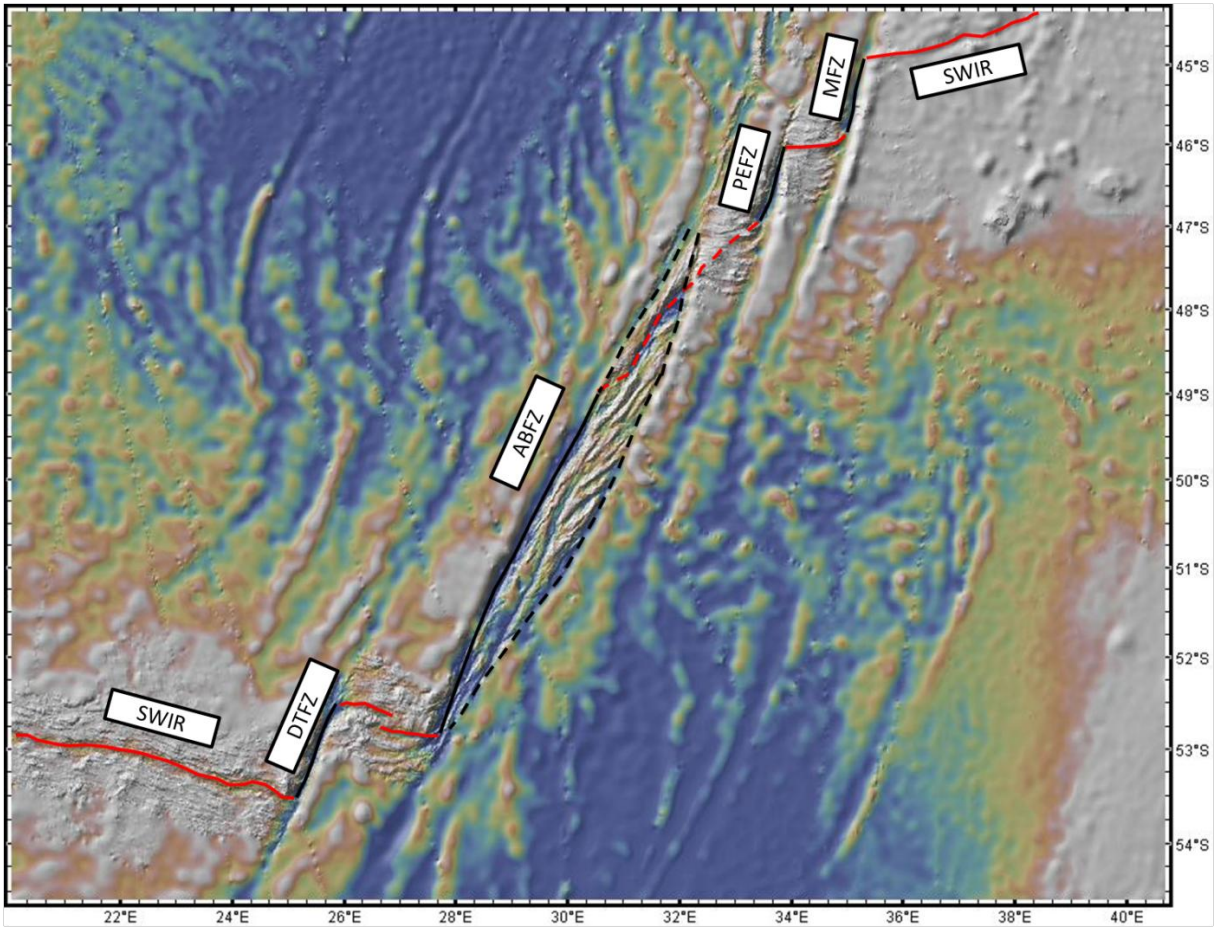

Figure 1.3.1: *tectonic setting of the fracture zone system of the SWIR nearby the Andrew Bain Mega-transform. Bathymetry and topography from GeoMapApp©.*

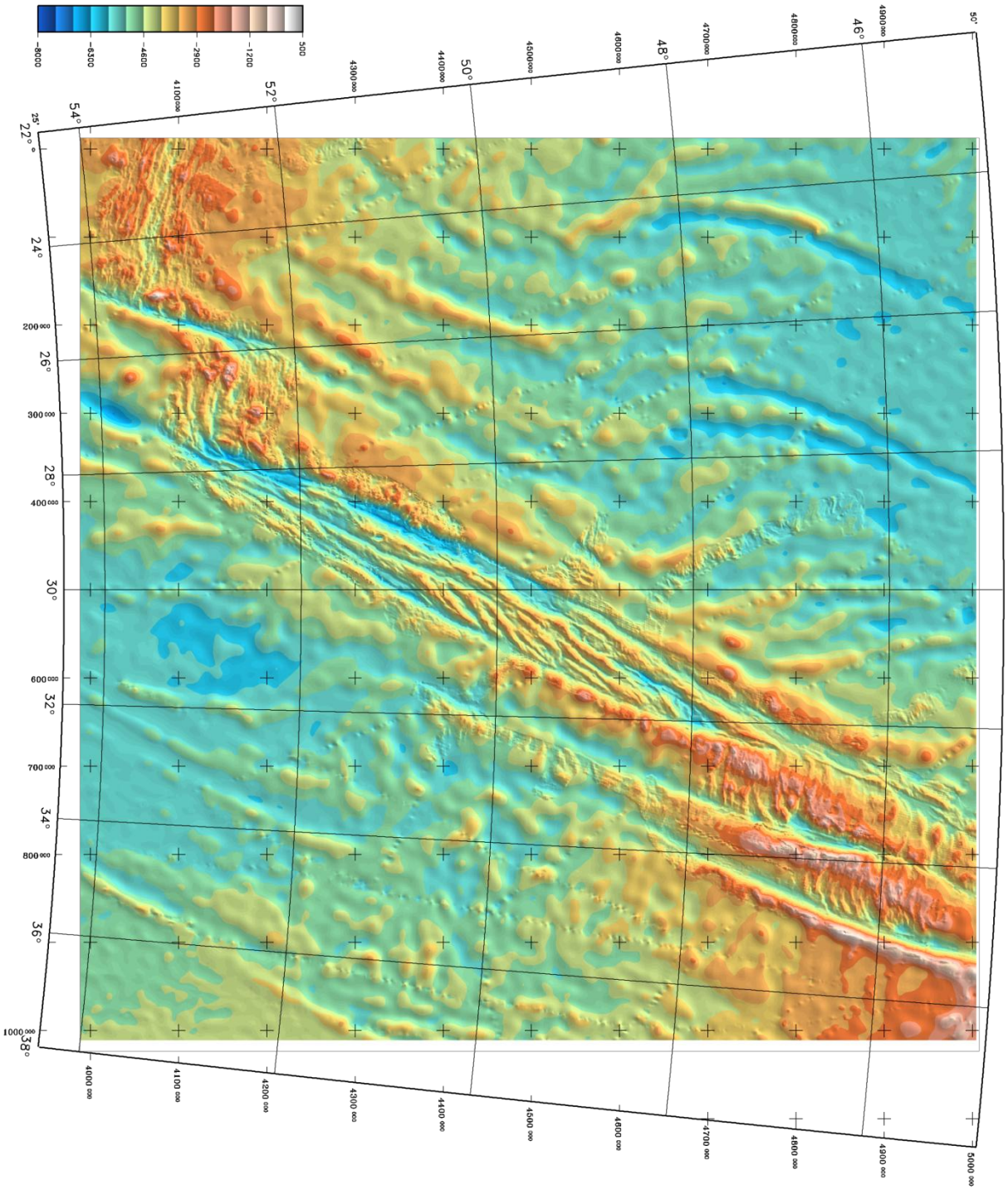

Figure 1.3.2 – *(from PASINI, 2009) Integrated bathymetric/gravimetric map of the SWIR portion that encloses the transform domain of ABFZ.*

ABFZ ranges from the southern end of the Mozambican continental margin trough Astrid Ridge to almost the continental margin of the Antarctica Plate (SCLATER ET AL., 2005). The transform domain represents the western edge of the Marion Swell, a wide region where the sea-floor shows a high topography that lies between the Madagascar Plateau and the Del Cano Rise, departing from 35° E to 50.5° E (FISHER AND GOODWILLIE, 1997). As described above, ABFZ offsets the SWIR of about 750 km and represents part of the Africa-Antarctica plate boundary. Considering the very slow spreading rate of the plates separated by the transform (around 16 mm/yr) the age contrast reaches 55 My (LIGI ET AL., 2006).

Based on multibeam data (*SCLATER ET AL.*, 2005), ABFZ, between the southern ridge-transform intersection and the northern ridge-transform intersection, appears to be characterized by a 80 to 120 km wide region that shows a rugged topography, representing the transform domain. This region is characterized, to the southwest, by a 450 km long and 20 km wide valley oriented north-northeast. In its eastern part, several wrinkles run towards the centre of the transform domain, ending in a series of deep overlapping basins that are linked, through a 100 km long and 10 km wide north-northeast warding valley, to the northern ridge transform intersection.

ABFZ is in fact constituted by a long and deep south-west warding valley linked by en-echelon basins to a shorter, shallower and thinner northeast trending valley. To the south with respect to these basins, a series of inactive ridges show an *en-echelon* arrangement, while a series of valleys appears to be disposed with an angle of 10°-20° with respect to the direction of crustal growth.

This region, characterized by this complex topography, has been explained by SCLATER ET AL. (2005) as two different *pull-apart* structures linked together by a *strike-slip* basin, resulting in a deformation structure similar to the ones that is possible to observe in continental transform domain. Moreover, SCLATER and coworkers (2005) are not in agreement with the numerical model proposed by LIGI ET AL. (2002) to explain the geometry shown by the oceanic

mega-transform domains. According to LIGI ET AL. (2002), as the case of Romanche Fracture Zone in the Equatorial Atlantic Ocean, the transform domain of ABFZ shows an lensoidal region characterized by an irregular topography, a unique, long and continuous transform fault, able to define the active plate boundary. Instead, SCLATER ET AL. (2005) deny that the transform fault of ABFZ has been a unique and long *strike-slip* fault, but a group of *strike-slip* faults separated each other by one or more regions of crustal growth. Moreover, the contrast age shouldn't have been high enough to allow the formations of anomalous lithospheric lenses (very thick and very cold) in the middle of the transform domain. In second instance, the transform fault of the ABFZ shows only transtensive features, while the transform fault of the Romanche Fracture Zone shows alternations of transtensive and transpressive phases. Another factor is represented by the influence of the Marion Plume on the northern sector of the ABFZ: the high temperature and the enhanced melt supply due to the presence of the plume can have a huge influence on the lithospheric rheology. Marion Plume can lead to a less cold mantle beneath the northern part of the ABFZ with respect to the southern part, causing an increase in spreading rate of the northern part of the transform (up to medium-slow spreading ridge). Finally, in the period between 20 and 3.2 Ma, the crustal growth region has moved northward, creating the valley and *en-echelon* ridge series, stretching the transform towards southwest, and reducing it in the northeast (SCLATER ET AL., 2005).

1.4. The Southern Ridge-Transform Intersection

During the oceanic expedition R/V Strakhof 2006, bathymetric data was collected and it was possible to obtain a bathymetric map of the southern ridge-transform intersection (Fig. 1.4.1). According to these data, it was possible to elaborate a tridimensional reconstruction of the studied area (Fig. 1.4.2).

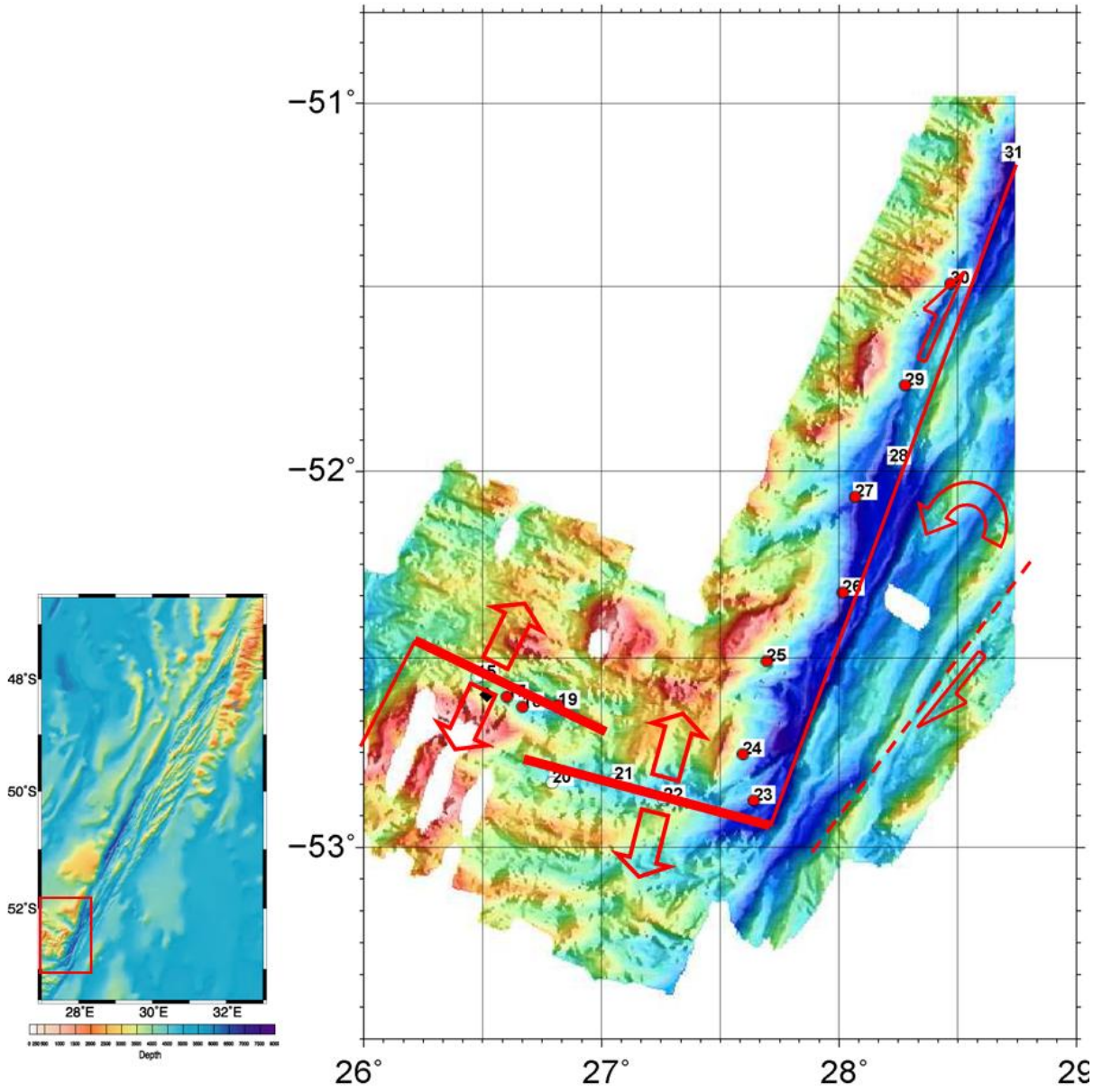

Figure 1.4.1 – *Zooming on the southern ridge-transform intersection of the ABFZ. Bathymetry has been collected during the oceanic expedition S23. The dredging sites are also reported in figure as red dots. The structural interpretation of the relative movements and of the plate boundaries is based on the magnetic anomalies from* LIGI ET AL.*, 2006.*

Mapping has been carried out using a multibeam oceanic system RESON SeaBat-8150, 12 kHz, 234 beams, 150° of coverage.

Collected data fit very well with data from GRINDLAY ET AL. (1996) and allow identifying the transform valley and the major shifting domain position.

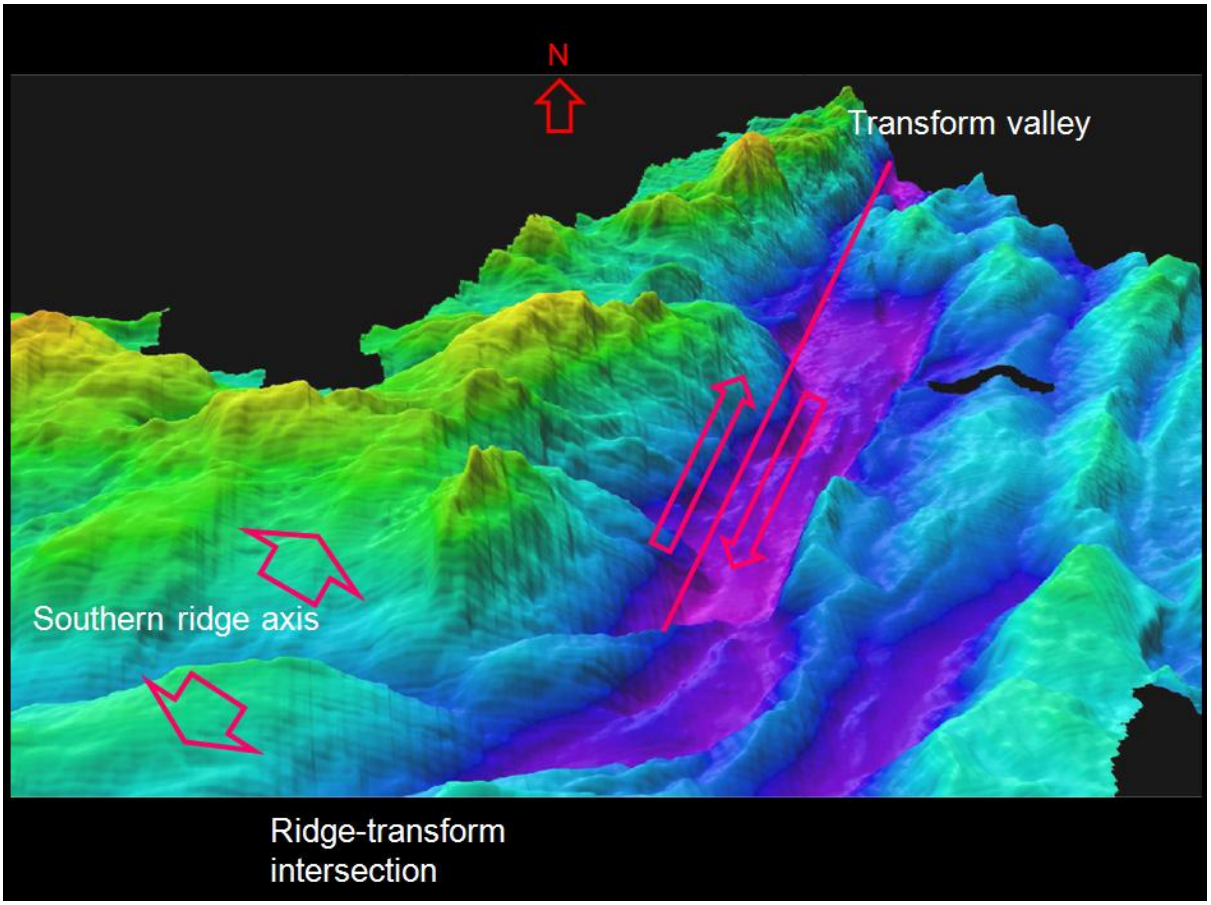

Figure 1.4.2 – *Tridimensional reconstruction of the southern Ridge-Transform Intersection between ABFZ and SWIR. The depth of the transform valley basins reaches 6500 m.*

The southern ridge axis, linking Du Toit and AB fracture zones, is 100 km long; it is located at 25°30' E – 28° E and 53° S, and it is composed by two different overlapping ridges that show distinct axial valleys, characterized by a different morphology (Fig. 1.4.1 and Fig. 1.4.2). The two valleys form an overlapping spreading center in the middle region of the segment. The western valley appears 3500-5000 m deep and 2-5 km wide, with an orientation of 108° N,

perpendicular to the spreading direction (18° N). In this sector it is difficult to distinguish an axial neo-volcanic ridge, but a coarse topographic high is present in the central part of the axial valley. The position of the southern spreading center is marked by an asymmetric valley that shows an east-west direction. The spreading center is located in the middle of this valley. The western ridge segment is characterized by shallow depth and negative Bouguer anomaly (LIGI ET AL., 2006) suggesting a magmatic active region beneath. The eastern ridge segment links the expansion center to the transform valley. It consists of a deep rift valley where it is not possible to recognize a volcanic axial zone at the performed resolution. In this sector neither magnetic nor Bouguer anomalies are recognizable suggesting a reduced magmatic building of the crust and a likely large exposure of ultramafic material at the seafloor.

A series of linear transform faults in the southern part of the ABFZ can give information about the movement of this part of transform domain. This situation appears to be very different with respect to its northern part, where transtensive pull-apart relay basins are present.

In the middle of the transform, during the oceanic expedition S23, a seismic line has been performed. The sediment thickness reaches 1000 m in the inner part of the transform valley. It has been possible, also, to detect reflectors in this central part of the transform valley. Such reflectors should point out that the high oblique reliefs are due to faults and block rotations, and do not have intrusive origin (LIGI ET AL., 2006).

ABFZ shows a very high age contrast (55My), the highest in the world's ridge system, given that the Romanche Fracture Zone attains 50My. This leads to an enhanced cold ridge edge effect, affecting the rheology of the lithosphere and significantly lowering the melt production. For this reason, ultramafic material composed sea-floor should be expected.

1.5 Sampling

During oceanic expedition AB06S23, on board of R/V "Akademik Nikolaj Strakhov", the southern RTI has been sampled.

In the following table, all the dredge positions are reported. Also dredging depths and times are reported. Letter “T” in the time columns indicates the *Greenwich Mean Time*.

Dredge code	Start	LON-S dd:mm	LAT-S dd:mm	Depth m	End	LON-E dd:mm	LAT-E dd:mm	Depth m
S2315	2006-02-17 T08:06	26:28.60	-52:33.08	4364	2006-02-17 T11:39	26:28.44	-52:34.96	3612
S2317	2006-02-17 T14:59	26:36.17	-52:36.17	2480	2006-02-17 T17:53	26:25.07	-52:36.32	2300
S2318	2006-02-17 T21:56	26:40.02	-52:37.75	4569	2006-02-17 T22:57	26:38.75	-52:38.75	3950
S2319	2006-02-18 T01:54	26:49.08	-52:37.50	4769	2006-02-18 T04:27	26:51.96	-52:35.61	3865
S2320	2006-02-18 T06:56	26:47.52	-52:49.77	4720	2006-02-18 T10:18	26:47.52	-52:52.21	3669
S2321	2006-02-18 T14:01	27:03.27	-52:49.21	4625	2006-02-18 T16:23	27:10.91	-52:46.53	3551
S2322	2006-02-18 T21:38	27:15.80	-52:52.49	4805	2006-02-19 T00:31	27:21.77	-52:54.88	4034
S2323	2006-02-19 T04:30	27:38.51	-52:52.59	6023	2006-02-19 T08:19	27:31.90	-52:50.60	4750
S2324	2006-02-19 T11:30	27:35.69	-52:45.28	4654	2006-02-19 T13:34	27:33.53	-52:44.54	3300
S2325	2006-02-22 T17:15	27:41.78	-52:30.48	4112	2006-02-23 T00:27	27:39.66	-52:30.12	4007
S2326	2006-02-23 T05:08	28:00.97	-52:19.50	5968	2006-02-23 T09:33	27:56.70	-52:19.45	4720
S2327	2006-02-23 T14:10	28:04.12	-52:04.15	5800	2006-02-23 T19:38	28:04.94	-52:03.02	5400
S2328	2006-02-23 T23:06	28:12.70	-51:58.42	5767	2006-02-24 T04:32	28:03.75	-51:55.12	4749
S2329	2006-02-24 T09:18	28:16.75	-51:46.11	5490	2006-02-24 T15:45	28:15.46	-51:45.77	5120
S2330	2006-02-24 T20:08	28:28.20	-51:29.61	5416	2006-02-24 T23:55	28:20.34	-51:30.79	3010
S2331	2006-02-24 T06:09	28:41.79	-51:09.03	6386	2006-02-24 T11:15	28:34.91	-51:03.82	3850

Figure 1.5.1 – *List and positions of the sampling during AB06S23.*

In Fig. 1.5.2 position of each dredge has been reported on the RTI bathymetric map. Each dot represents a different dredging site and the number the final part of the dredge code.

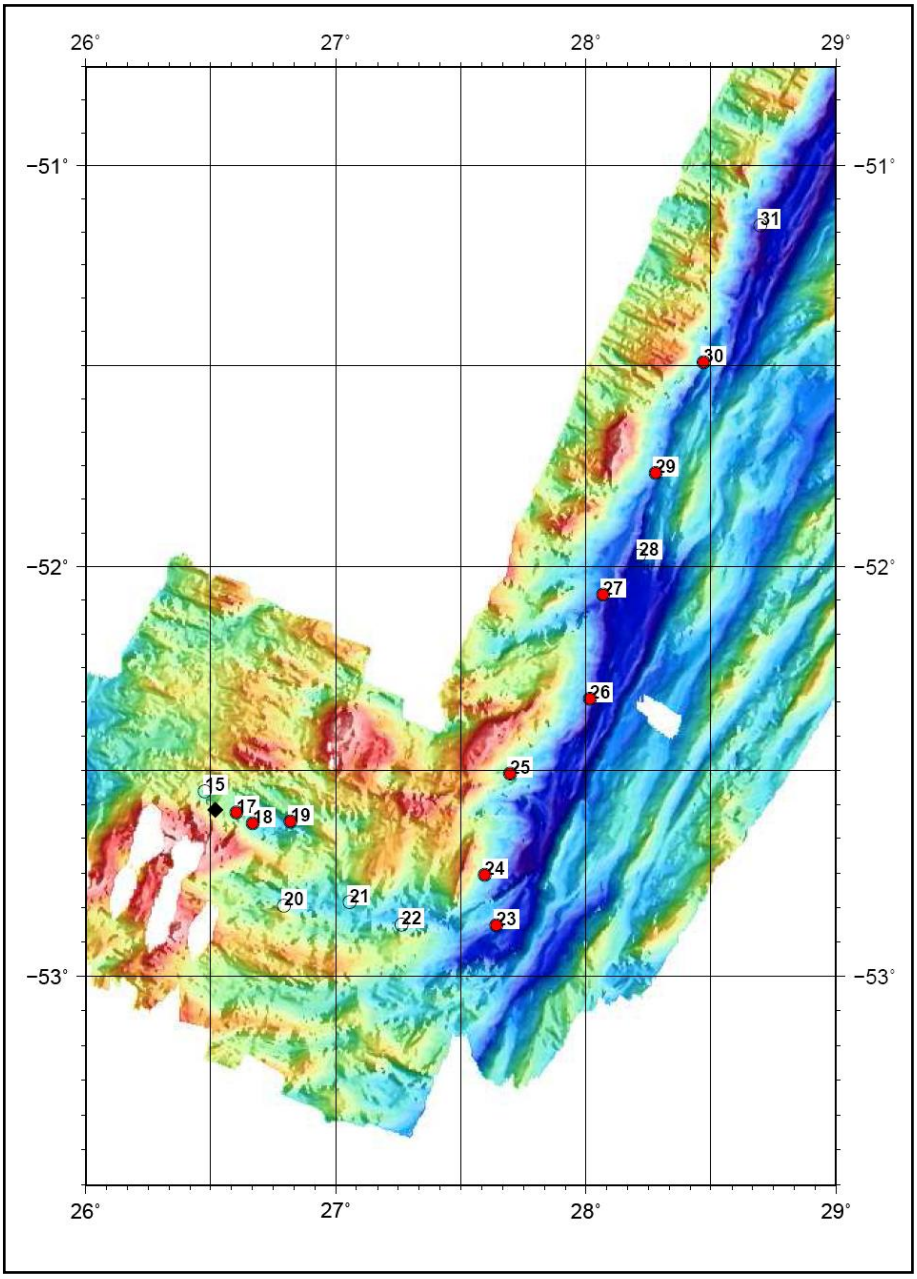

Figure 1.5.2 – *Dredging site position in the southern ridge transform intersection obteined by Global Positioning System for each dredging site. Red dots represent dredges carrying some material, while empty dots represent dredging sites that did not provide any material.*

Finally, the black diamond represents a lost dredge. Coordinates have been obtained by the Global Positioning System that is present on board of the R/V Strakhov.

Three of the ten dredges come from the ridge segment that links ABFZ to Du Toit Fracture Zone. The other dredges come from the western wall of the transform valley, moving northward from the RTI, where seven dredge transects have been done, separated each other 30 km apart, that corresponds to about 4 My in age.

The following table gives dredge location, description and weight of sampled material.

Dredge ID	Location	Location description	Weight
S2315	Ridge Axis	Near to fracture zone	lost
S2317	Ridge Axis	Western segment, small axial basin	100 kg
S2318	Ridge Axis	Western segment, central deep basin	30 kg
S2319	Ridge Axis	Western segment; north steep fault	10 kg
S2320	Ridge Axis	Eastern segment	empty
S2321	Ridge Axis	Eastern segment	empty
S2322	Ridge Axis	Eastern segment	empty
S2323	RTI	Nodal basin; west RTI	5 kg
S2324	RTI	Inside corner high; west RTI	5 kg
S2325	Fracture Zone	Western wall	100 kg
S2326	Fracture Zone	Western wall	100 kg
S2327	Fracture Zone	Western wall	5 kg
S2328	Fracture Zone	Western wall	empty
S2329	Fracture Zone	Western wall	2 kg
S2330	Fracture Zone	Western wall	15 kg
S2331	Fracture Zone	Western wall	empty

Lithology abundances are also reported in figure 1.5.3.

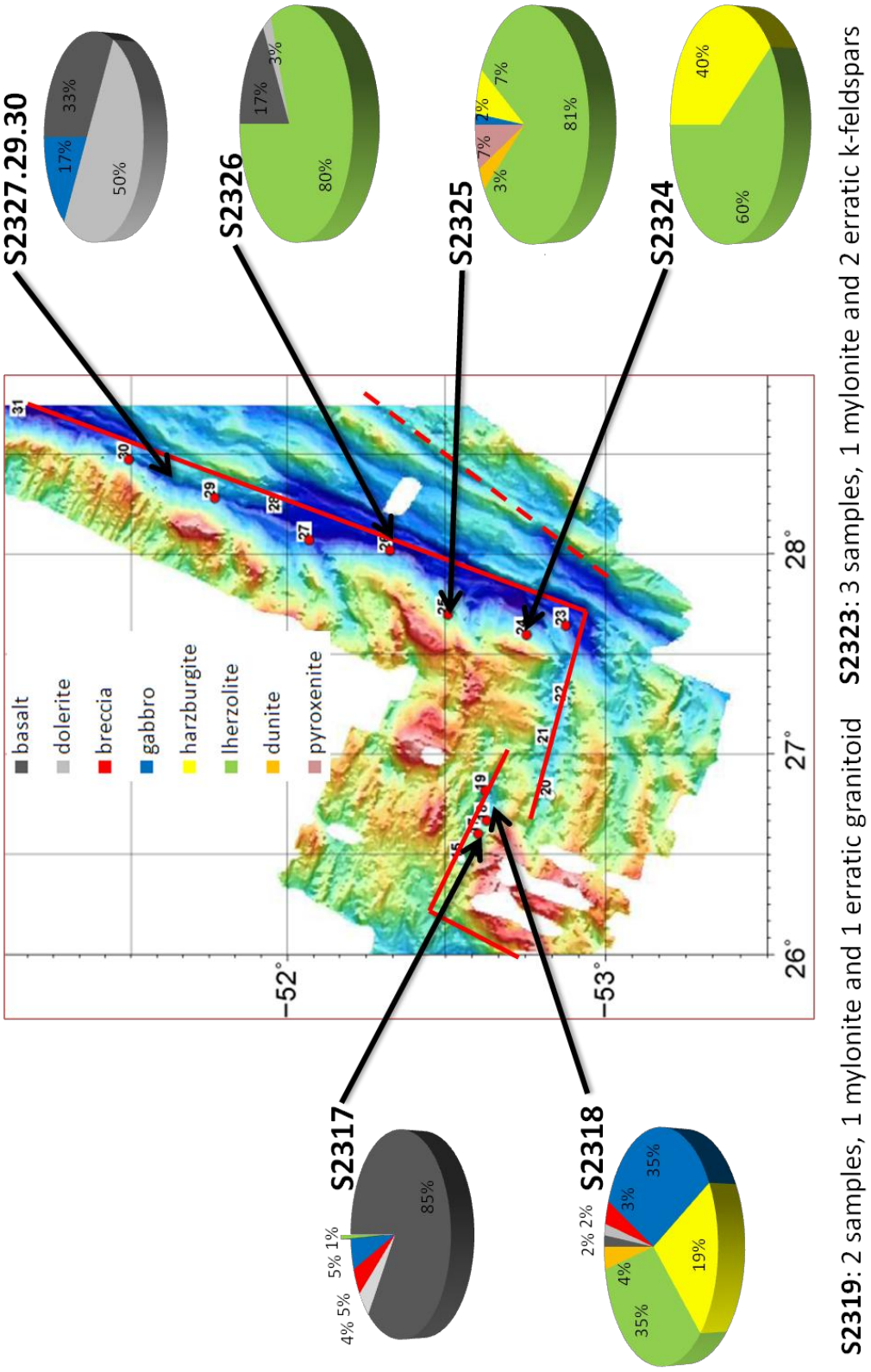

Figure 1.5.3 *– Summary of sampled material from RTI in the southern section of the ABFZ.*

1.5.1 Southern ridge axis sampling

Two dredging have been performed in the westernmost ridge segment. Dredge S2319 was performed in a narrow axial basin located in the western part of the ridge segment, while S2318 was located in the larger axial basin in its central region. S2317 dredge was collected on the bank of a conic feature that suggests recent magmatic activity. Major part of the collected material consists of basalts with minor gabbros and only one sample of peridotite. Basalts seem to belong to two different events, because some of them show a fresh glass crust, while others show stronger alteration, high vesicularity and Fe-Mn oxide crust. Both groups are aphyric with rare plagioclase phenocrysts. Small-sized gabbro samples show a variable grain-size, but appear to be highly altered. The peridotite sample, although extremely altered, is characterized by a granular texture. A breccia has been sampled, covered by Fe-Mn mineralizations.

In S2318 dredge, the majority of collected rocks are represented by ultramafic lithologies and gabbros. Gabbros show variable grain-size, varying from micro-gabbro to pegmatitic; troctolites, ol-gabbros, and leuco-gabbros are also present. Peridotites compositionally ranging from harzburgites to lherzolites show different textures varying from granular to porphyroclastic and mylonitic. They show a peculiar strong variation in modal olivine/pyroxene ratios. Clinopyroxenes define a lineation and are associated with spinel and plagioclase.

Sampling of the eastern ridge segment leads only erratic material: this segment seems to be buried by a thick layer of sediment and there is no evidence of a recent magmatic activity.

1.5.2 Western wall of the transform valley sampling

The seven dredging sites performed in the transform valley are located about 30 km from each other, corresponding to about 4 My in time at the present-day spreading rate of 16 mm/y. Only S2324, S2325 and S2326 dredges collected good material. Three of the other

dredgers collected only erratic material probably carried by icebergs from the Antarctic region, while the other dredges were empty.

The major part of the material collected in good dredges is represented by ultramafic rocks. Peridotites show granular to porphyroclastic textures (mylonitic in minor amount), varying from lherzolites to harzburgites. As the peridotites collected along the ridge axis, these peridotites also show highly variable olivine/orthopyroxene ratio, while plagioclase is here less abundant.

1.6 Summary dredging table

The complete list of samples collected during oceanic expedition AB06S23 is reported in the appendix A. The proposed classification in the column “Description” is the on board compilation done during the expedition: it can show, thus, not precise observation and mistakes.

Chapter 2

Petrography of mantle-derived peridotites

2.1 Sample description

Samples collected in the southern region of the ABFZ appear as rounded few centimeter sized up to ten centimeter sized pebbles, blackish or dark greenish, sometimes to reddish brown, in general showing a Fe-Mn thin crust. Once cut pyroxenes are easily recognizable: orthopyroxene appears as coarse grains, silvery crystals while clinopyroxene occurs as dark green grains. Spinel appears black, frequently showing, together with clinopyroxene mineral lineations.

In general, samples show a weak foliation and a well marked lineation. The primary lineation is due to the orthopyroxene porphyroclast orientation, while a secondary lineation, more enhanced, occurs at a low angle with respect to the first one, and it is due to the preferential orientation of spinels and clinopyroxenes, usually associated. Sometimes plagioclase forms dispersed white grains.

At a thin section scale olivine appears rarely fresh; it is usually substituted by serpentine and magnetite, forming the typical mesh and texture of serpentinization. In general, due to the serpentinization process, it is difficult to notice intergranular relationships and dimensions of the primary olivine. However, when observable, olivine grains show a wide dimensional spread (from submillimetric up to centimetric). Several generations of serpentine secondary veins cut the olivine matrix and the pyroxene aggregates.

Pyroxenes are partially altered, although at a lesser extent than the olivine matrix. The alteration consists of a pseudomorphic substitution of bastite (i.e. a finely grained, Fe-rich lizardite aggregate), easily distinguishable from olivine serpentine thanks to the lack of magnetite exsolution and the brownish color. However, there are numerous pyroxene still not fully hydrated.

Orthopyroxene occurs as porphyroclasts, up to 2 centimeters in size, and as aggregates of finer grain size. In general, it shows a thin parallel set of clinopyroxene lamellae exsolution. Clinopyroxene also appears as scattered millimetric blebs within opx, either sub-parallel to the lamellae or discordant with them. Some orthopyroxenes show deformation at various grades. In order of increasing degree of deformation, they are characterized by wavy extinction, bending of crystallographic planes and development of brittle deformation (kink bands). In general, orthopyroxenes are cut by randomly oriented fractures (sometimes sub-radial), usually filled by serpentine minerals.

Clinopyroxene appears as porphyroclasts isolated in olivine matrix and as aggregates where it shows variable grain size and where it is associated with orthopyroxene and/or spinel. Sometimes, it is included in orthopyroxenes porphyroclasts as described above. Clinopyroxene shows orthopyroxene exsolution lamellae, usually wider that the exolution lamellae within orthopyroxene and frequently organized in a double exsolution system.

Spinel shows holly-leaf grain boundaries or are interstitial. It shows high variability in grain size, ranging from centimetric (up to 1.5 cm) to submillimetric, although it rarely reaches more than 1 centimeter. It is often rimmed by plagioclase, when present, or reactional product (hydrogarnet, chlorite) due to low temperature alteration of the spinel itself or the rimming plagioclase. Often spinel shows ferric alteration that appears as an opaque rim

along borders and fractures that can spread to the total grain. Plagioclase appears as white grains scattered in some samples, often organized in chains and lineations, marking a further lineation with respect to the main lineation given by pyroxenes.

2.2 Modal composition

The mineralogy of the sampled abyssal peridotites consists of olivine ± orthopyroxene ± clinopyroxene ± spinel. Thin section observations show a different sensitivity of the primary phases to alteration. Resistance typically increases from olivine through orthopyroxene to clinopyroxene. Olivine is replaced by serpentine in mesh textures, while ortho- and clinopyroxenes are replaced by bastite. In the mesh texture, olivine is replaced by concentric layers of serpentine aggregates associated with microgranular magnetite grains. A fresh olivine kernel might be preserved at the center. Alternatively, the centre may consist of brucite or carbonate. Bastite is made up of serpentine microfibers which isomorphically replaces orthopyroxene. Because clinopyroxene is more resistant to alteration, clinopyroxene exsolution lamellae are often preserved in bastite replacing orthopyroxene. The observed substitutions are indicative of a static hydration. Under these conditions it is generally possible to reconstruct the primary mode and textural relationships because the secondary minerals perfectly pseudomorph the original phases, even if cross-cutting veins are normally abundant (MEVEL, 2003).

ABFZ peridotites showing a wide spectrum of serpentinization degree and deformation have been sorted in order to indentify the best samples representative of the deep mantle conditions. We thus selected samples showing the lower degree of serpentinization and sea-floor weathering and carrying the maximum number of mineral phases, to obtain a significant dataset. Finally, samples have to be as much representative as possible among collected rocks. Following these criteria, 19 mantle rocks have been chosen, 11 spinel peridotites and 8 plagioclase peridotites.

Section	Ol vol%	Opx vol%	Cpx vol%	Sp vol%	Plg vol%
S2324-04	63	27	8	2	0
S2325-01a	75	18	3	4	0
S2325-01b	74	14	7	5	0

S2325-03	79	14	5	2	0
S2325-05a	72	16	9	3	0
S2325-05b	74	21	3	2	0
S2325-08	79	14	6	1	0
S2325-55	69	21	8	2	0
S2326-15a	75	15	9	1	0
S2326-15b	84	16	0	0	0
S2326-16	64	25	10	1	0
S2326-18	72	21	6	1	0
S2326-21	63	22	13	2	0
S2326-24	61	25	13	1	0
S2317-135	68	26	0	3	3
S2318-28	80	10	7	0	3
S2318-31	69	15	9	1	6
S2318-35	69	19	8	1	3
S2318-49	83	10	6	0	1
S2325-51	73	14	6	1	6
S2326-01	69	22	6	1	2
S2326-02	69	14	8	2	7
S2326-09	59	29	7	2	3

Table 2.2.1 *– Modal composition of ABFZ peridotites, sampled during S23-AB06 oceanic expedition.*

Once having chosen samples, modal analysis has been performed using point-counting on standard size thin sections (2,5 x 3,5 cm). Mode was obtained by counting a minimum of 1250 points per thin section and calculated according with the following assumption:

serpentine in mesh texture and associated magnetite were calculated as olivine; bastite replacing orthopyroxene was calculated as orthopyroxene; magnetite at the rims of spinel was calculated as spinel; late tensional vein filled with serpentine fibres, carbonate or secondary minerals were not counted; correction for volume expansion were not considered; residual and secondary pyroxenes and spinels were not distinguished.
In table below, modal composition are reported.

Measures are affected by a wide and not assessable error due to heterogeneous phase distribution in thin section scale and to granulometric heterogeneity, and, of course, to strong alteration. Measured values, then, have a quasi-qualitative meaning. They suggest that the sampled rocks present a modal composition that varies from clinopyroxene-poor harzburgite to clinopyroxene-rich lherzolite. Looking at the ternary ol-opx-cpx diagram, spinel peridotites plot in the compositional filed of SWIR peridotites, showing the same enrichment in cpx content. Plagioclase peridotites display an extreme variability in opx content, while cpx content is more homogeneous.

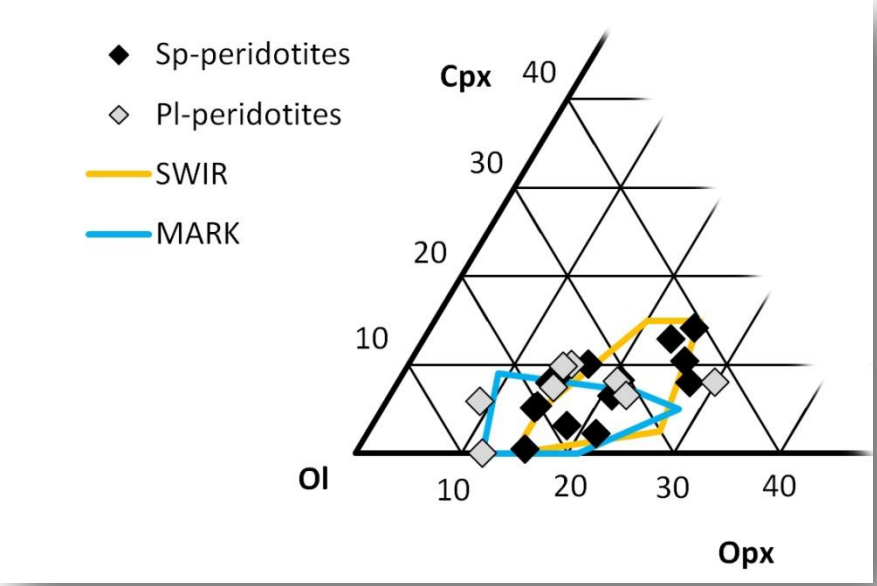

Figure 2.2.2 *– Ternary plot of modal composition of the abyssal peridotites of this study. Black dots are compositions of spinel-peridotites, grey dots are composition of plagioclase peridotites. Modal field from SWIR (yellow line) (JOHNSON ET AL., 1990; SEYLER ET AL., 2011) and from MAR (blue line) (MICHAEL & BONATTI, 1985) are also reported.*

2.3 Petrography

The sampled rocks can be divided in two macro-groups, based on plagioclase occurrence. Plagioclase-bearing peridotites occur mainly in the dredging sites located in the ridge segment west of the RTI. In fact all the S2318 peridotites are characterized by the occurrence of plagioclase. S2326 peridotites also show plagioclase occurrence, although in a lower percentage (25-30% of the sample set) with respect to S2318. In S2325 less than 15% of samples show plagioclase occurrence, while all S2324 peridotites are plagioclase-free. Hereafter I describe separately the two petrographic groups.

2.3.1 Plagioclase-free/spinel-equilibrated peridotites

Spinel peridotites from ABFZ show textures varying from proto-granular to proto-mylonitic, the majority showing a porphyroclastic texture. Olivine, ortho- and clinopyroxene appear in two different crystal habits: large, elongated, slightly deformed porphyroclasts and fine-grained (up to 0.5 mm) neoblasts, forming at least 50% of the sample. Porphyroclasts in general appear strongly kink-banded. In proto-granular samples, orthopyroxene and olivine show coarse grain size (up to several centimeters), slightly kink-banded, sometimes recrystallized in finer grain size patches. In general, porphyroclasts show rounded edges, while neoblast patches show rectilinear borders. Clinopyroxene and spinels usually appear as fine-sized crystals; sometimes clinopyroxene appear as rounded or polygonal blebs at the rims of the large opx porphyroclasts locally associated with vermicular spinel.

Orthopyroxene porphyroclasts are sub-rounded to elongated, rarely rounded, they usually mark a weak lineation in the rock. Coarse orthopyroxene porphyroclasts show clinopyroxene exsolution lamellae (Fig. 2.3.1.1), they frequently display inclusions, consisting of clinopyroxene blebs with minor olivine and rarely spinel. When clinopyroxene is included it sometimes appears as isolated sub-idiomorphic grains, sometimes it is organized in bleb

patterns that can be discordant or sub-parallel with respect to the exsolution lamellae system.

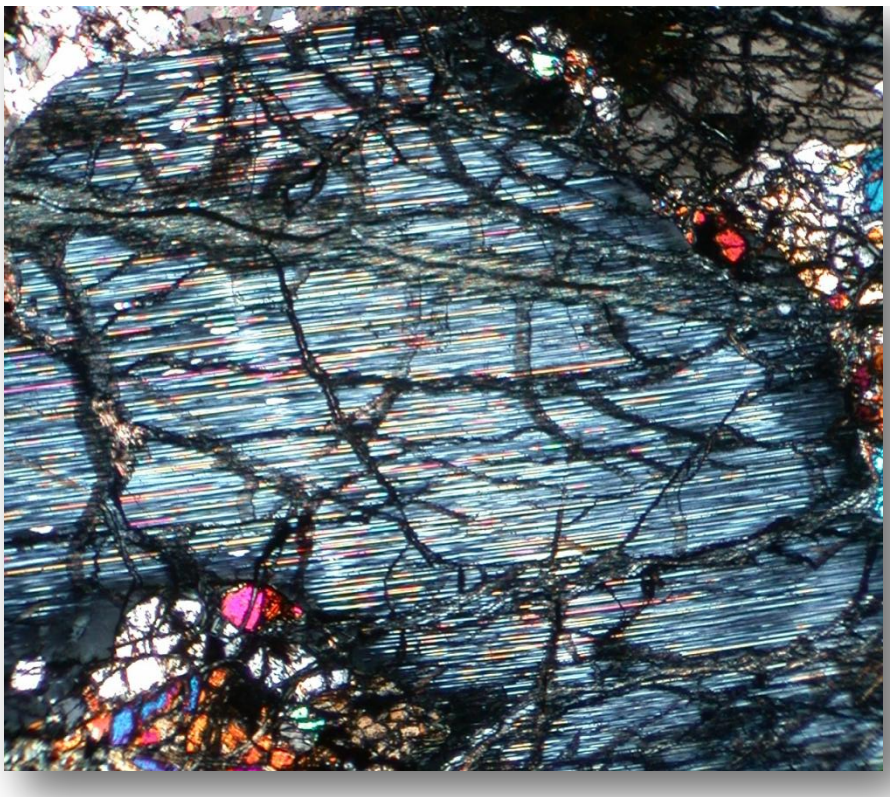

Figure 2.3.1.1 *– Orthopyroxene porphyroclast where the thick cpx exolution lamellae pattern are inside the opx porphyroclast. The crystal is affected by a set of randomly oriented fractures, some of them filled by serpentine (brown stuff).*

Clinopyroxene porphyroclasts vary much in size, but often show coarse size (up to 1 cm). They are usually characterized by curved grain boundaries, as well as a generation of exolution lamellae. These lamellae are usually wider than the ones occurring in orthopyroxene, reaching about 10-20 µm in size (Fig. 2.3.1.2). Usually they show spongy rims that enclose fine-grained crystals of olivine and orthopyroxenes, generally rounded.

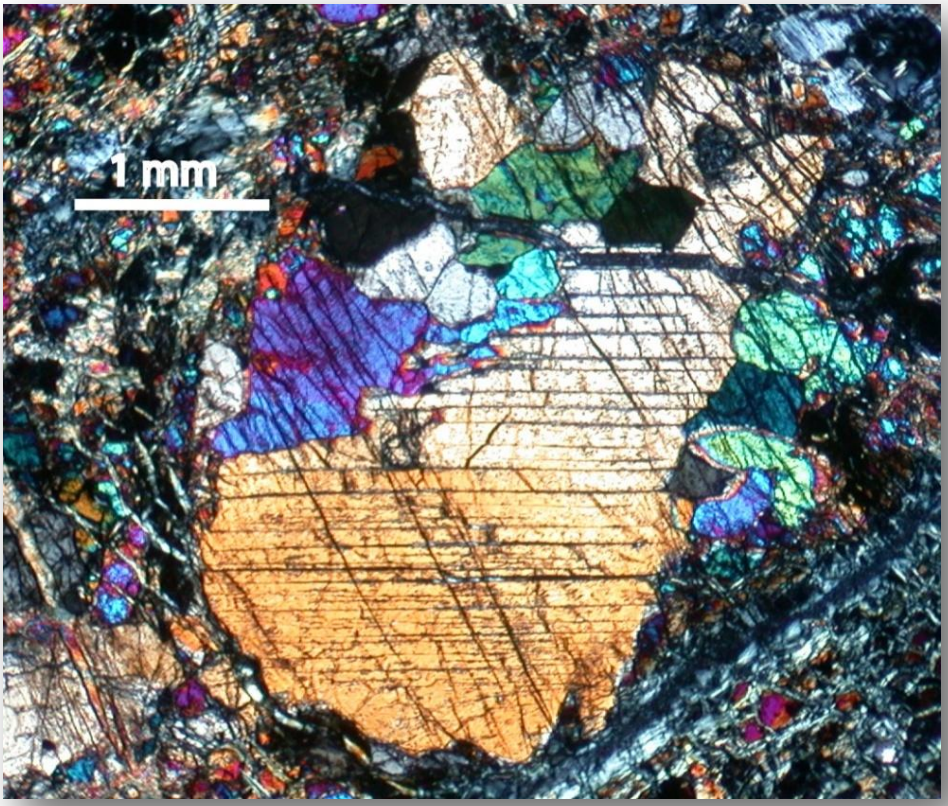

Figure 2.3.1.2 *– Clinopyroxene porphyroclast, showing irregular borders, associated with orthopyroxene and exolution lamellae.*

In other cases, clinopyroxene occurs as aggregates of several smaller grain-sized crystals (Fig. 2.3.1.3), in the olivine matrix or associated with coarse orthopyroxene porphyroclasts. In this case, it shows rectilinear rims. Clinopyroxene also forms polycrystalline aggregates, associated with spinel usually displaying vermicular or holly-leaf texture, and with minor orthopyroxene. Usually the boundary of the porphyroclastic clinopyroxenes are curved. Sometimes, single coarse clinopyroxene porphyroclast is completely isolated in the olivine matrix, and other times it is rounded by fine neoblasts, usually orthopyroxene and olivine, but sometimes also recrystallized new clinopyroxene. Clinopyroxene also occurs in interstitial position associated with olivine or pyroxene (Fig. 2.3.1.3 and Fig. 2.3.1.4). In some

cases, it is possible to observe very fine cpx grain at olivine triple junctions, or at the borders of orthopyroxene.

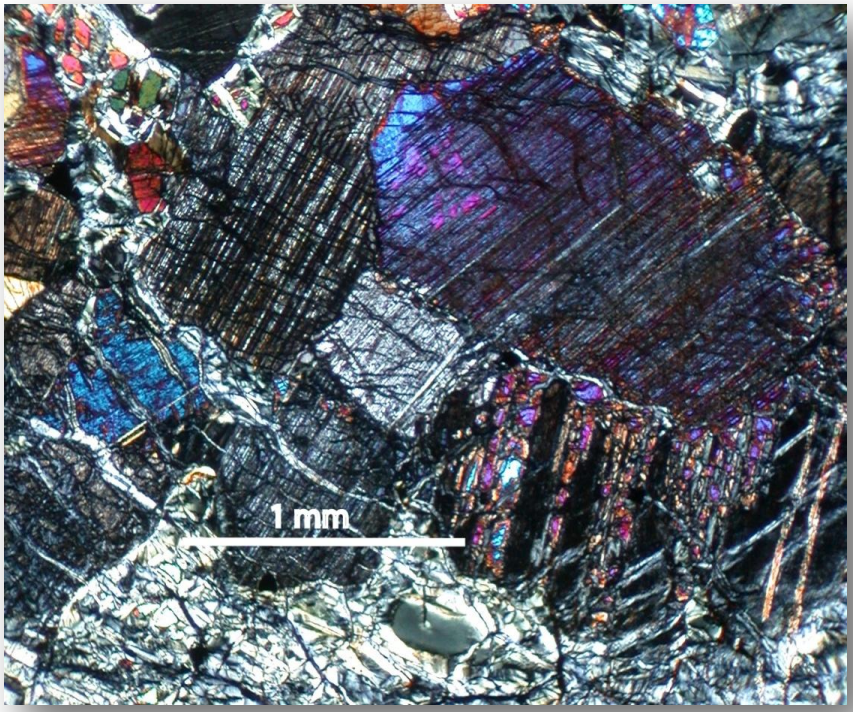

Figure 2.3.1.3 *– Clinopyroxene aggregates. Clinopyroxenes show exolution lamellae and rectilinear borders, forming 120° triple junctions.*

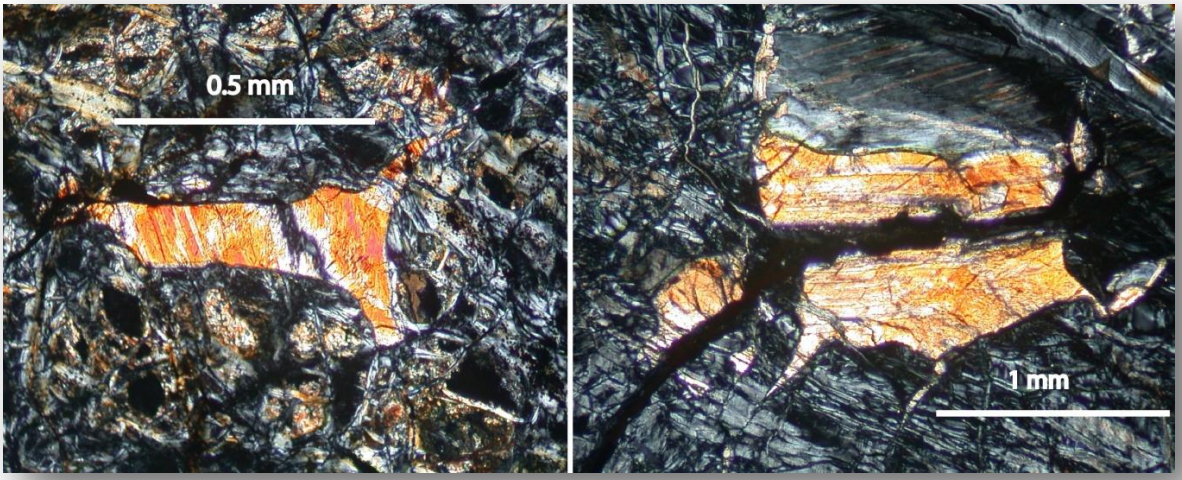

Figure 2.3.1.4 *– Interstitial clinopyroxene. Left: interstitial cpx grown in a triple junction formed by three olivine (now serpentine) crystals. Right: interstitial cpx associated with opx.*

Spinel is the only alluminous phase. It shows a lineation subconcordant with respect to the main orthopyroxene lineation. Spinel grains can reach centimeter size, but in general they do not appear larger than a few millimeters. Usually they are associated with pyroxenes (both clinopyroxene and orthopyroxene), but can also be found in the olivine matrix, where they form interstitial, submillimeter, irregular shaped grains (Fig. 2.3.1.5).

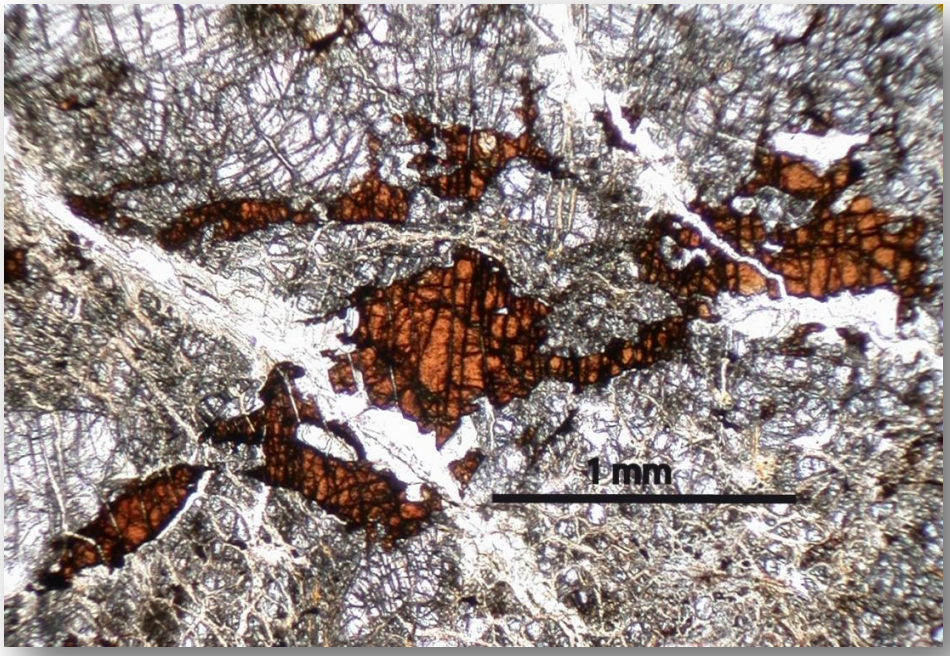

Figure 2.3.1.5 *– Spinel crystal in olivine matrix. The larger grains enclose orthopyroxene and olivine anhedral to subhedral crystals.*

In general, spinels have irregular shape boundaries that often enclose anhedral to subhedral pyroxene or olivine crystals. They also occur as holly-leaf texture, and in case of coarse spinels, they show well developed interstitial terminations (Fig. 2.3.1.5 and Fig. 2.3.1.6), that can create a link with other coarse grain spinels. The tendency to enclose part of the olivine groundmass starting by interstitial tiny termination allows us to propose the definition of pseudo-poikilitic texture for those spinels. Under these terms the large grains are viewed as oikocrysts and the enclosed olivine and/or pyroxenes as chadacrysts irrespective to the mechanism that formed such textural relationships (Fig. 2.3.1.6)

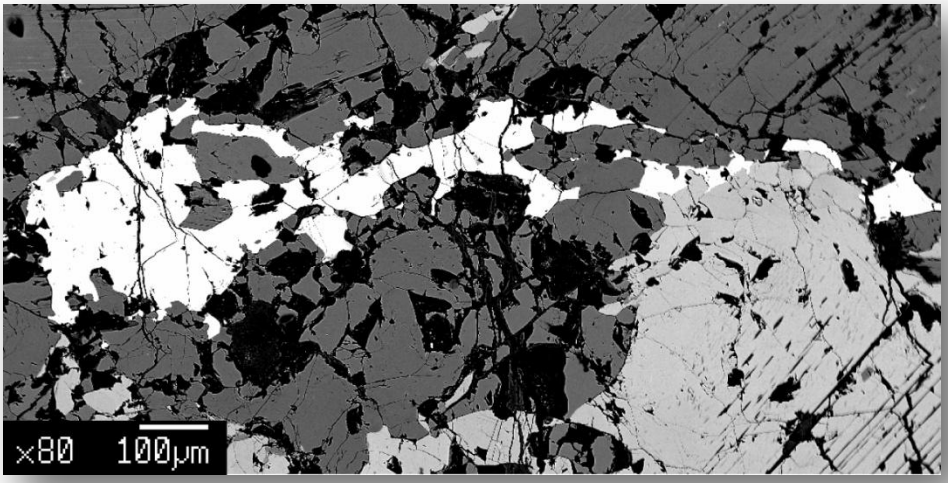

Figure 2.3.1.6 *– Large pseudo-poikilitic texture of spinel crystals associated with cpx porphyroclast (SEM image). The spinel oikocryst grain locally has interstitial habit and tiny terminations that develop surrounding portions of the olivine groundmass isolating small anhedral deeply irregular chadacrysts grains.*

2.3.2 Lower-Temperature features

Almost all ABFZ peridotites are affected by deformation events attesting for low T ductile/brittle environment.

Olivine always shows wavy extinction and kink-banding of the large grains (Fig. 2.3.2.1).

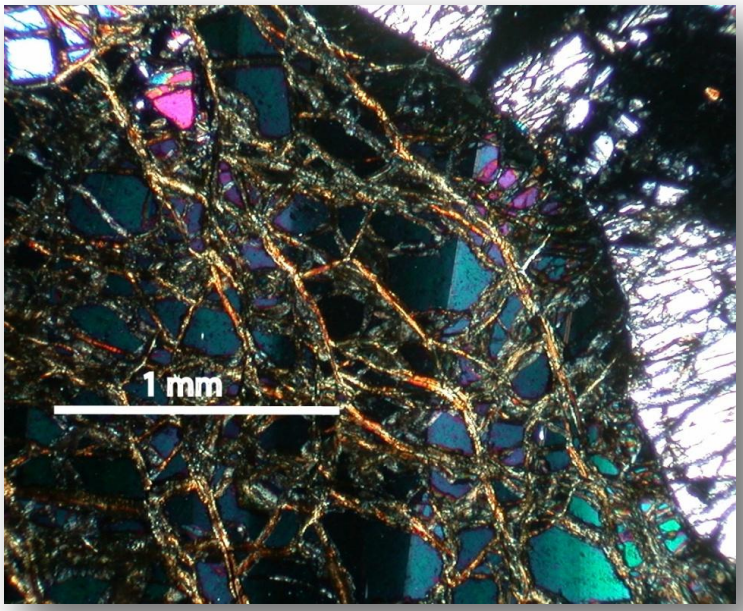

Figure 2.3.2.1 *– Kink band in partially serpentinized olivine under polarized light. White stuff in upper right corner is an orthopyroxene porphyroclast, showing curved boundary with the olivine porphyroclast.*

Orthopyroxene porphyroclasts also show wavy extinction, while kink-banding is rare. All of them present a complex, randomly oriented, fracture system (Fig. 2.3.2.2 and 2.3.2.3), sometimes showing a radial propagation typical of a decompressive fracturation accompanied by volume increase of the serpentinizing olivine. Fractures are sometimes filled

by late mineral association (serpentine to clay). Also clinopyroxene shows wavy extinction and, rarely, kink-banding (Fig. 2.3.2.6).

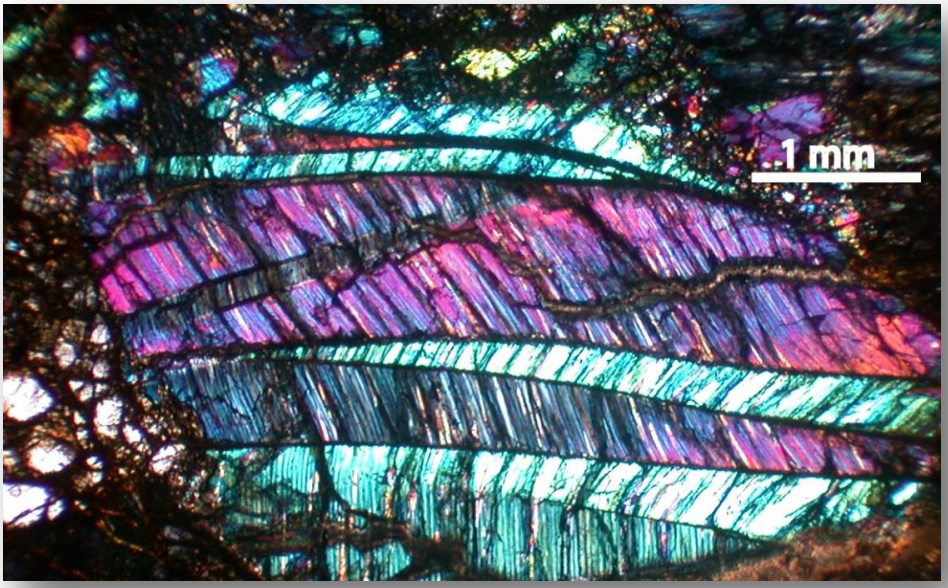

Figure 2.3.2.2 *– Wavy kink bands in orthopyroxene porphyroclast. In the upper right part tiny opx neoblasts are present, while the pale pink stuff in the left lower corner is fresh olivine. The porphyroclast show high-T exolution lamellae and it is crossed by a fracture filled by clay mineral.*

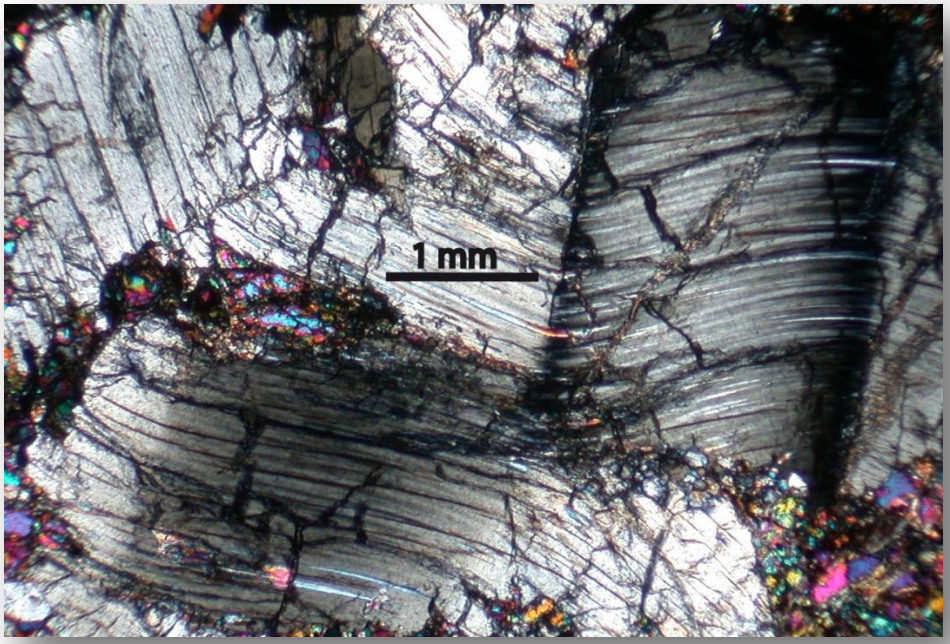

Figure 2.3.2.3 *– Kink bands and wavy extinction in orthopyroxene porphyroclasts. Opx and olivine neoblast bands mark the contact between large grains.*

Ortho- and clinopyroxene are often surrounded by selvages of small neoblasts (± olivine) up to 0.5 mm in size. Locally these aggregates are made of irregularly shaped small grains (Fig. 2.3.2.4). In other places the grain size and textural relationships (120° triple junctions) of these aggregates may suggest annealing has occurred after a first phase of grain size reduction (Fig. 2.3.2.5).

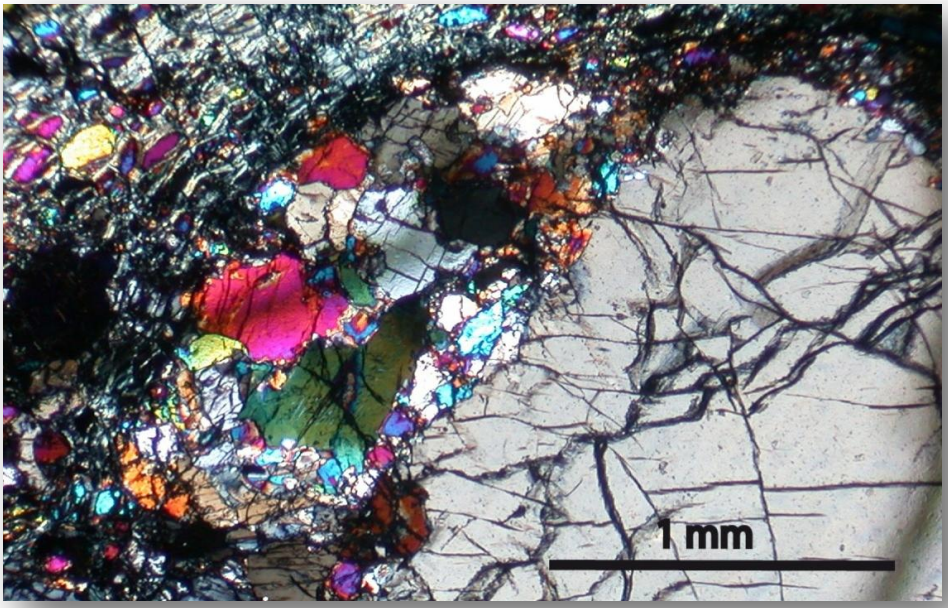

Figure 2.3.2.4 *– Orthopyroxene neoblasts associated with orthopyroxene porphyroclasts. Opx porphyroclast show a weak wavy extinction. The neoblasts do not show an exsolution lamellae pattern. The aggregates are made of irregularly shaped small grains.*

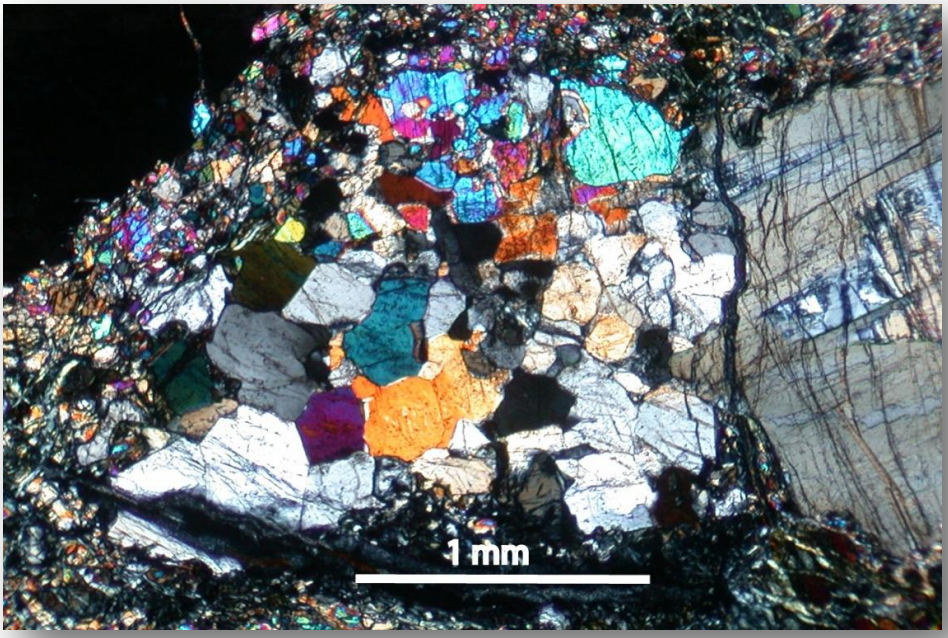

Figure 2.3.2.5 *– Orthopyroxene neoblasts associated with orthopyroxene porphyroclasts. Opx porphyroclast show a weak wavy extinction. The neoblasts do not show an exsolution lamellae pattern. The grain size and textural relationships (120° triple junctions) of these aggregates suggest annealing has occurred after a first phase of grain size reduction*

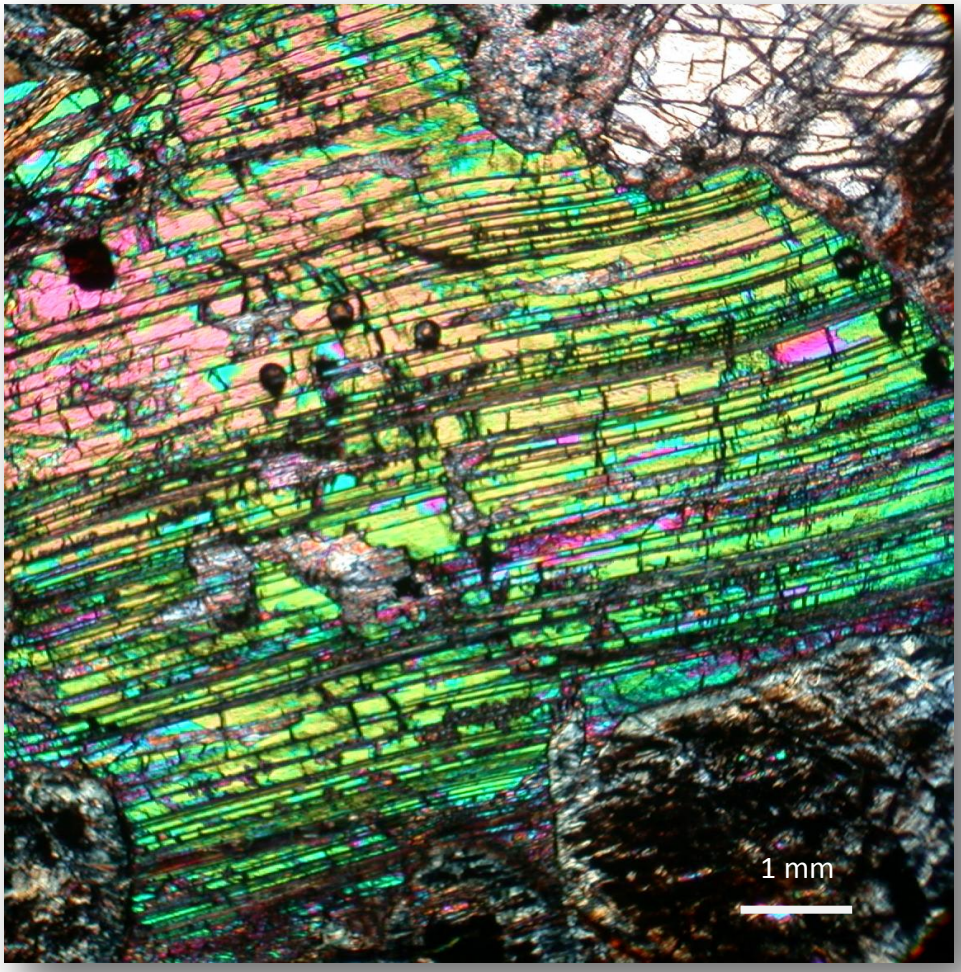

Figure 2.3.2.6 *– Clinopyroxene porphyroclast showing wavy extinction and a pattern of thick opx exsolution lamellae and irregular borders. Black spots are sites of laser ablation analysis.*

2.3.3 Plagioclase-bearing peridotites

Plagioclase-bearing peridotites are very similar to the plagioclase-free peridotites concerning the primary textural relationships. They differ for the occurrence of plagioclase as alluminous phase and for well developed melt percolation patterns. Unfortunately, plagioclase is always altered in hydrated minerals (as hydrogarnet) and in clays (Fig. 2.3.3.1).

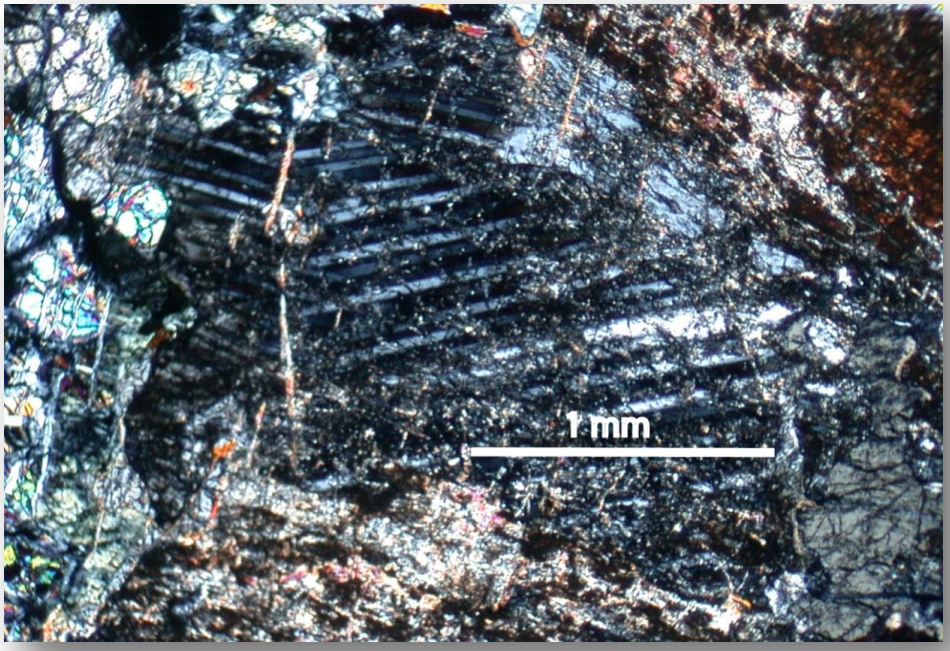

Figure 2.3.3.1 *– Partially altered plagioclase crystal. This example is only plagioclase showing partial alteration, in other cases, it is always completely altered.*

Plagioclase appears as fine-grained interstitial grains scattered in the olivine matrix and as gabbroic mineral aggregates (pl ± cpx ± ol ± opx) that can be dispersed in olivine matrix or associated to the large orthopyroxene porphyroclasts. These gabbroic aggregates usually do not show a marked lineation inside the rock.

When plagioclase is dispersed in olivine matrix, it is often associated with spinel; in that case spinels are partially surrounded by plagioclase (Fig. 2.3.3.2). In the same thin section, however, spinel can occur both rimmed by plagioclase or plagioclase-free suggesting melt percolation leading to plagioclase precipitation, resulting to heterogeneous textures at a

very short scale (mm). Sometimes plagioclase can be arranged in interconnected network with interstitial habit (Fig. 2.3.3.3). Plagioclase appears in coarse, centimetric gabbroic aggregates (Fig. 2.3.3.4) mainly in samples collected at ridge axis (especially concerning dredge S2318). Sometimes plagioclase is arranged in veins that crosscut the sample, showing linear boundaries with the host rock (Fig. 2.3.3.5).

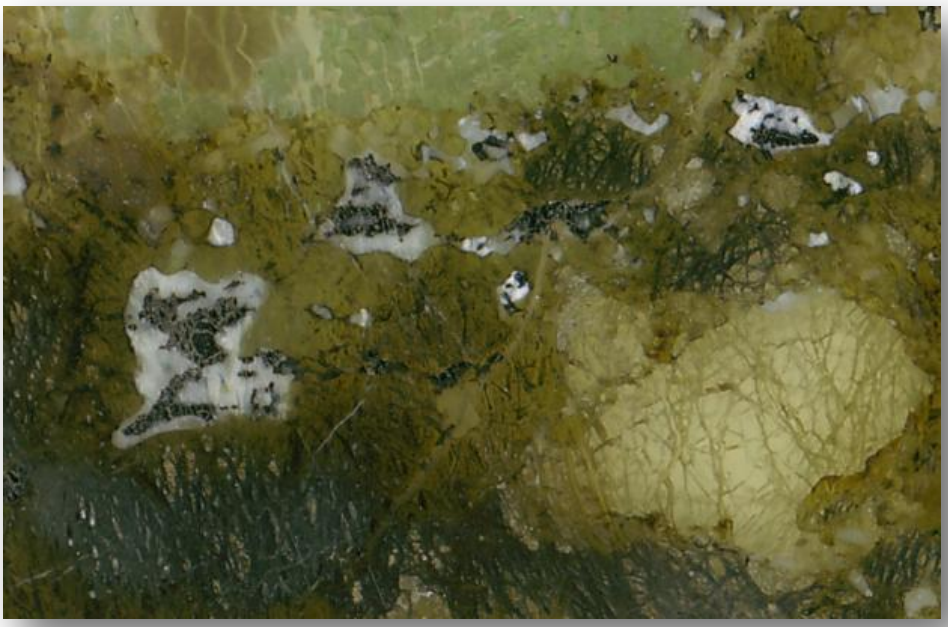

Figure 2.3.3.2 *– Plagioclase-bearing porphyroclastic peridotite. Thin section of sample S2318-35 under polarized light. The base of the picture is 25mm. Plagioclase heterogeneously rims spinel crystals, and forms isolated interstitial micro-patches. Textural relationships between spinel and plagioclase vary in the thin section. Spinel is not regularly rounded by plagioclase, suggesting it is not related to metamorphic reaction.*

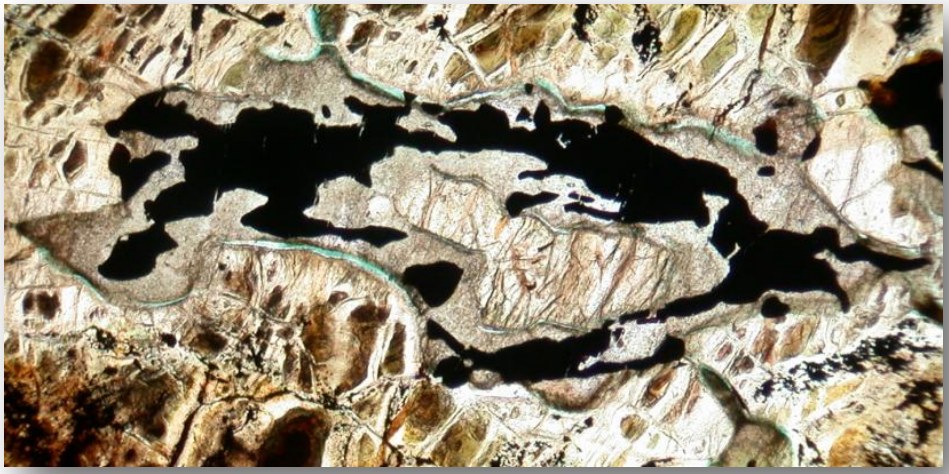

Figure 2.3.3.3 *– Plagioclase-bearing porphyroclastic peridotite. Transmitted light thin section of sample S2318-35. The base of the picture is 10mm. Plagioclase, completely altered in hydrogarnet rounds interstitial spinel crystal. In the middle and at the borders of the thin section it is possible to see the mesh-texture of serpentinized olivine. Plagioclase surrounds only partially the spinel: in some places, spinel is in contact with Fe-Mn silicate minerals, without plagioclase in between.*

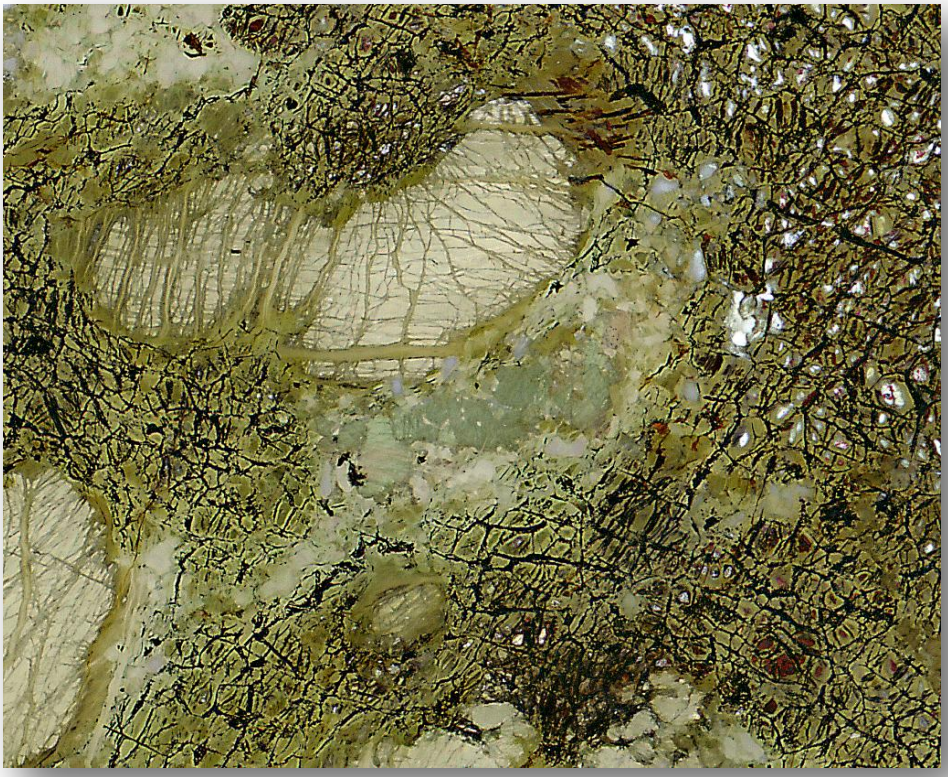

Figure 2.3.3.4 *– Sample S2318-49: gabbroic patch bearing peridotite under polarized light. The base of the figure is 35 mm. In the middle of the image, it is possible to see a gabbroic aggregate, formed by cpx + pl, close to a coarse opx porphyroclast. In the upper right corner, plagioclase appears scattered in serpentinized olivine matrix.*

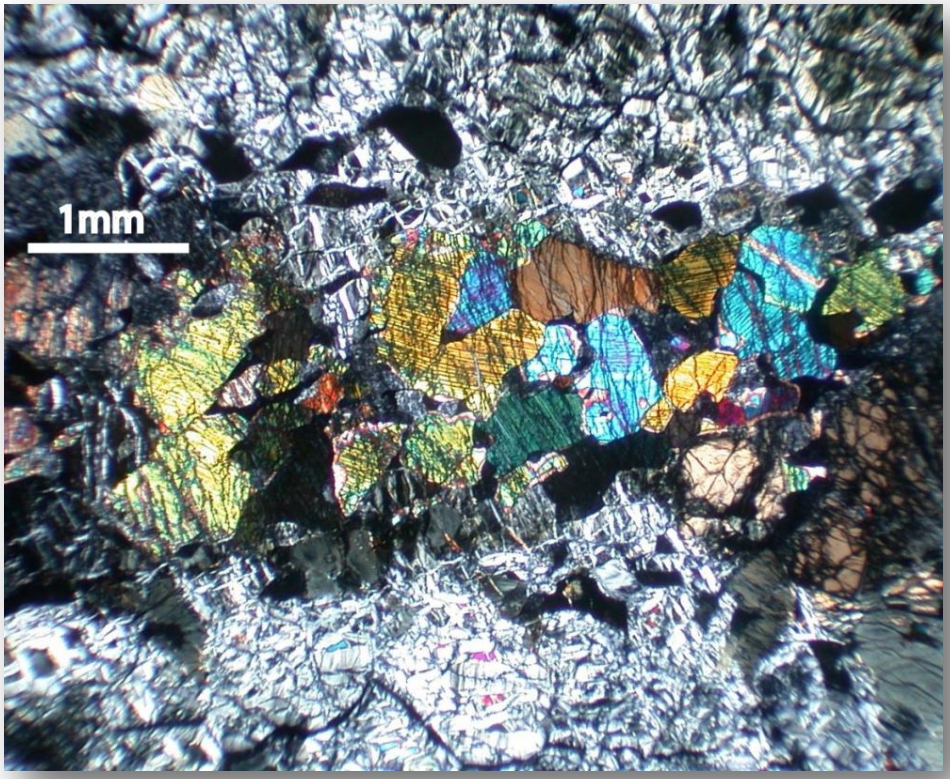

Figure 2.3.3.5 – *Gabbroic patch cross-cutting an olivine groundmass. Black and white stuff on the borders of the vein is the serpentinized olivine under X nicols. Colored crystals are cpx (±opx) and the black mineral shadows are a fine intergrowth of hydrous phases pseudomophically replacing plagioclase.*

2.3.4 Mylonites

During ABFZ sampling, some mylonites have also been sampled. The fine grain association suggests the protolith to be an ultramafic rock, formed by ol + opx + cpx + sp (Fig. 2.3.4.1). Olivine appears usually highly recrystallized in very small submillimetric neoblasts, while large opx porphyroclasts appear highly elongated with curvilinear boundaries, surrounded by fine grained neoblasts. Clinopyroxene appears mainly as fine-grained crystals associated to opx rounded porphyroclasts, they can also be found as relics of porphyroclasts fractured and elongated. Deformation has deleted all intra- and inter-grain original relationships and, for this reason, mylonites will be treated and discussed as a separated group given the impossibility to discern the original mineral paragenesis and the presence of late percolating phases such as plagioclase.

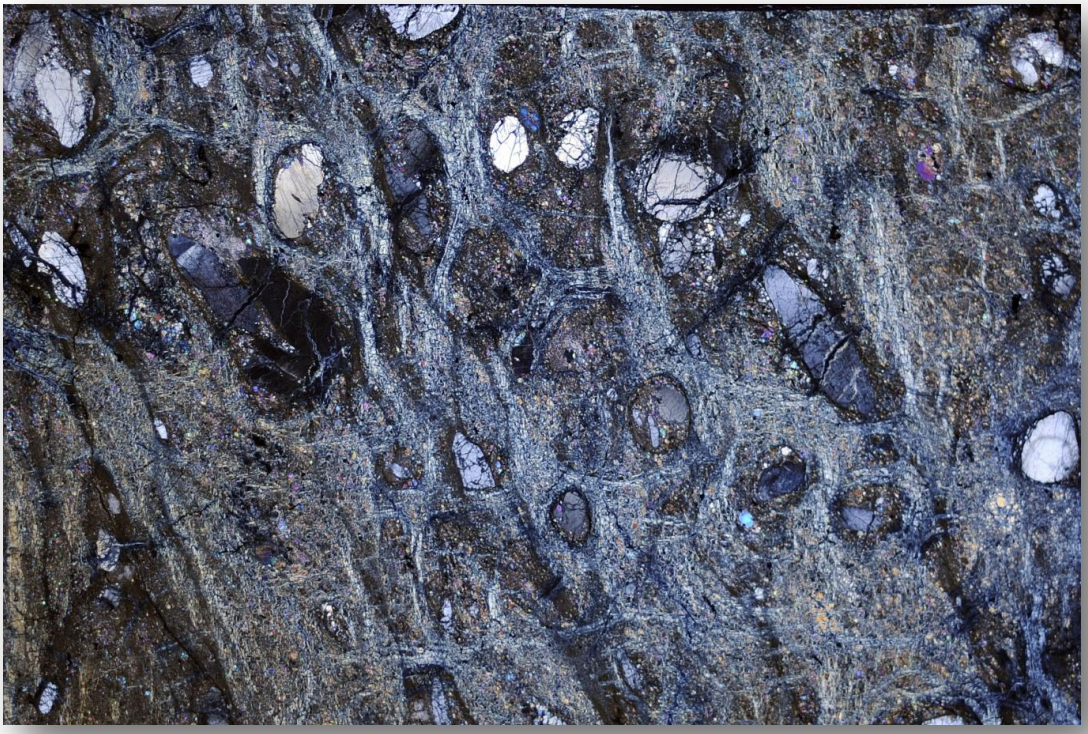

Figure 2.3.4.1 – *One of the mylonite sampled in ABFZ during oceanic expedition S23-AB06. The base of the picture is 35mm.*

Chapter 3

Major elements

3.1 – Methods

The great part of major element composition of relict primary phases has been determined by in situ quantitative analysis using the electron microprobe Jeol JXA8200 at the University of Milan, Italy. Mineral phases were measured using an acceleration potential of 15 kV, a beam current of 10 nA and a spot size of 1-2 µm. Acquisition time is 30 seconds per each element, except for Na that has been analyzed for 20 seconds. A set of international standards have been used for internal linearization (table 3.1).

A subset of analyses has been measured at Lamont-Doherty Earth Observatory of Columbia University – New York, USA, by Anna Cipriani, using a Cameca SX-100 electron microprobe at American Museum of Natural History (NY, USA), under the same analytical conditions. All the analysis have been corrected according to Bence & Albee (1968). To reduce the interlaboratory analytical bias a set of samples has been chosen and measured per each

analytical session. The results, summarized in figure 3.1.1, show that for all elements the interlaboratory deviation is within the variability observed for grain scale oxide oscillation expressed as 1σ standard deviation for each element (oxide wt%).

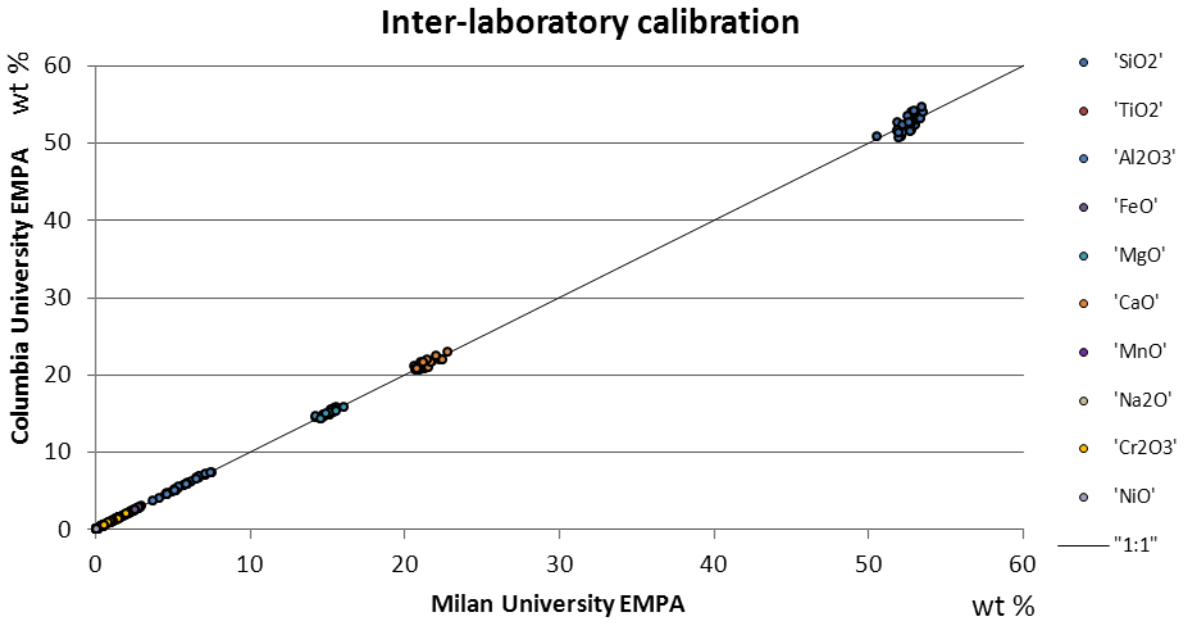

Figure 3.1.1 *– Inter-laboratory calibration analysis. Analysis have been performed at Milano University on known clinopyroxene samples already analyzed in Columbia University. Results fit the 1:1 ratio curve (solid black line).*

All analytical data are reported in table 3.1.

Element	Standard	Crystal
Si	Wollastonite	TAP
Ca	Anortite	PETH
Al	Anhortite	TAP

Fe	Fayalite	LIFH
Mg	Olivine	TAP
Na	Omphacite	TAP
Mn	Rodonite	LIFH
Ni	Niccolite	LIFH
Ti	Ilmenite	PETJ
Cr	Pure	PETJ

Table 3.1.2 – *Standards used during analysis in microprobe Jeol JXA8200 at Milano University.*

3.2 – Mineral major element compositions in spinel-equilibrated peridotites from ABFZ

Eleven samples of spinel peridotites were selected for EMP analysis representing the three peridotite-bearing dredges based on the following criteria: the possible lowest degree of serpentinization and sea-floor weathering, the maximum number of relic fresh phases and the minimal textural heterogeneity at the sample scale. Plagioclase-bearing samples are presented in a separate chapter.

3.2.1 Olivine

Due to the high degree of serpentinization it was not possible to analyze fresh olivine in every sample. When present, three spots per mineral have been performed. Mg# [defined as 100*Mg/(Mg + Fe) all Fe as Fe^{2+}] varies from 90.01 (sample S2325-55) to 91.86 (sample S2325-05) and NiO contents range from 0.37 (sample S2325-03) to 0.40 wt% (sample S2325-55), with no significant correlation with Mg# (Fig. 3.2.1.1).

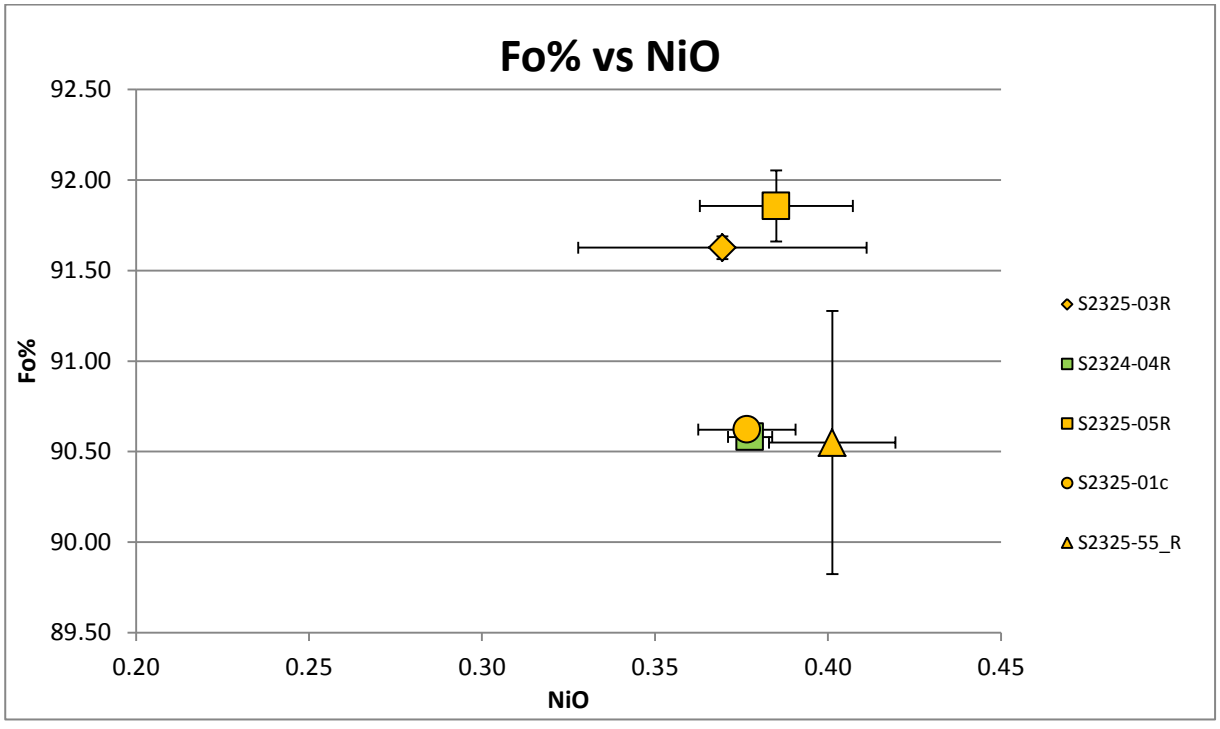

Figure 3.2.1.1 *– Fosterite content vs. NiO in olivine. Error bars represent 1σ variability at sample scale.*

3.2.2 Orthopyroxene

Opx porphyroclasts show large compositional variations. Usually the cores of the coarse porphyroclasts are enriched in Al, Na, Cr and Ca with respect to their rims, while rim silica content is higher.

In figures below, several oxide contents are reported. Each point in the plots represents the sample composition calculated as mean of 3-5 orthopyroxene grains per sample and the associated σ variability. The three different dredges are color-coded: S2324 green, S2325 yellow and S2326 red. Large symbols represent the core of the large porphyroclasts, while small symbols are representative of rims and neoblasts, both compositions are not distinguishable on the compositional base.

Orthopyroxene porphyroclasts show a strong zonation in major oxide contents moving from core to rim. In Cr_2O_3 vs. Al_2O_3 diagram (Fig. 3.2.2.1), for example, all core compositions, except sample S2324-04, show higher content in Cr and Al with respect to the rims. The three dredges form distinct compositional fields only partly overlapping. Samples from dredge S2326 show the lowest Cr content and the highest Al content. The observed values are then compared with the field of compositional variability of the Mid-Atlantic Ridge peridotites (MICHAEL & BONATTI, 1985; BRUNELLI ET AL., 2006; CANNAT ET AL., 1992; CANNAT & SEYLER, 1995; SEYLER ET AL., 1997; GHOSE ET AL., 1996; KOMOR ET AL., 1990; JUTEAU ET AL., 1990) and with the compositional field of the SWIR peridotites (JOHNSON ET AL., 1990; JOHNSON & DICK, 1992; DICK, 1989; SEYLER ET AT., 2003; WARREN ET AL., 2009, 2010; SALTERS AND DICK, 2002).

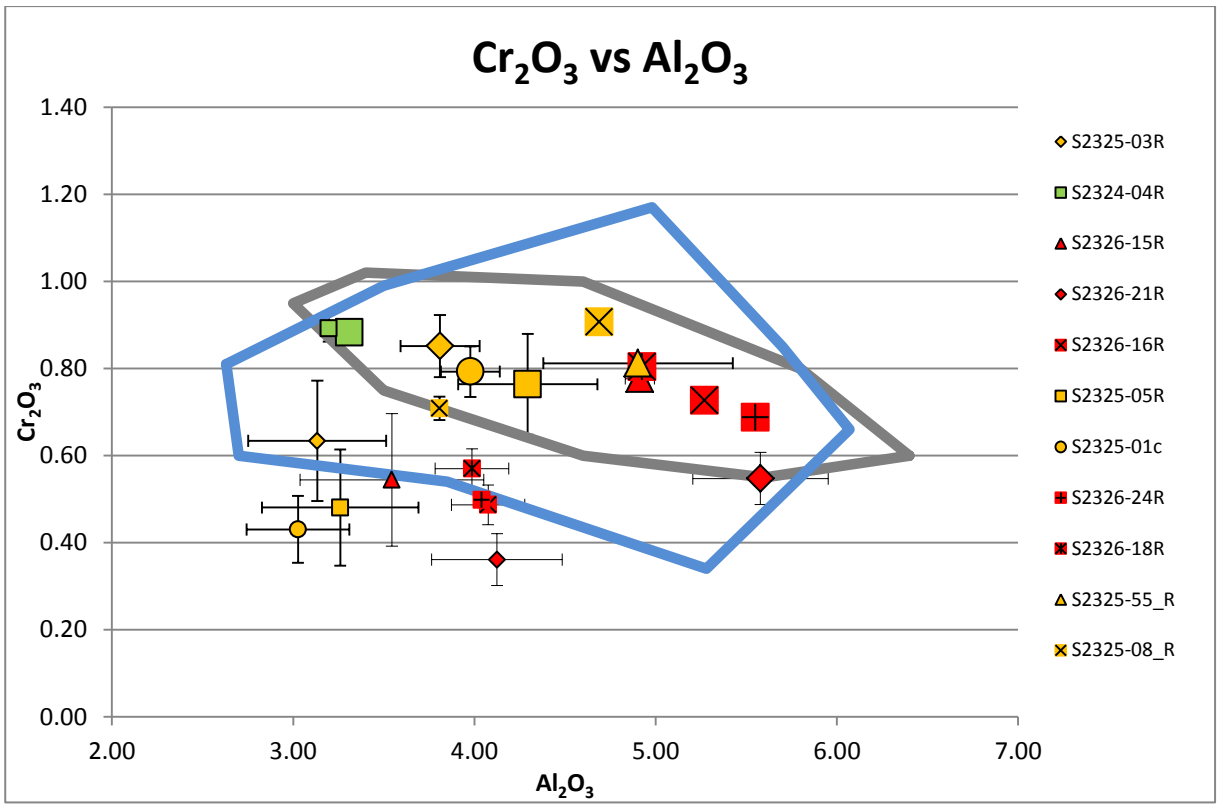

Figure 3.2.2.1 – Cr_2O_3 vs. Al_2O_3 *in orthopyroxene. Small symbols represent crystal rims, coarse symbols represent crystal cores. Error bars represent 1σ variability at sample scale. Grey line represents compositional field of MAR peridotites, blue line represents compositional field of SWIR peridotites.*

Ca (Fig. 3.2.2.2) content in orthopyroxene reflects its wollastonite ($CaSiO_3$) content. The integration of several (3-5) randomly oriented spots per grain ensures the measured values to integrate the thin exsolution pattern and be representative of higher-T equilibrated pyroxene prior low-T exsolution. Inter-sample variability is much enhanced with respect to the Al-Cr systematic. In a general way the samples richer in Al (poorer in Cr) are also those having the higher Ca-Na content. Wollastonite content is positively correlated with Al and weakly with Cr, and is negatively correlated with Mg and Fe, and shows a decrease moving

from core to rim. The observed Al-Cr depletion toward the rim corresponds to a coupled Ca-Na depletion in all samples but two (S2326-16; S2326-24).

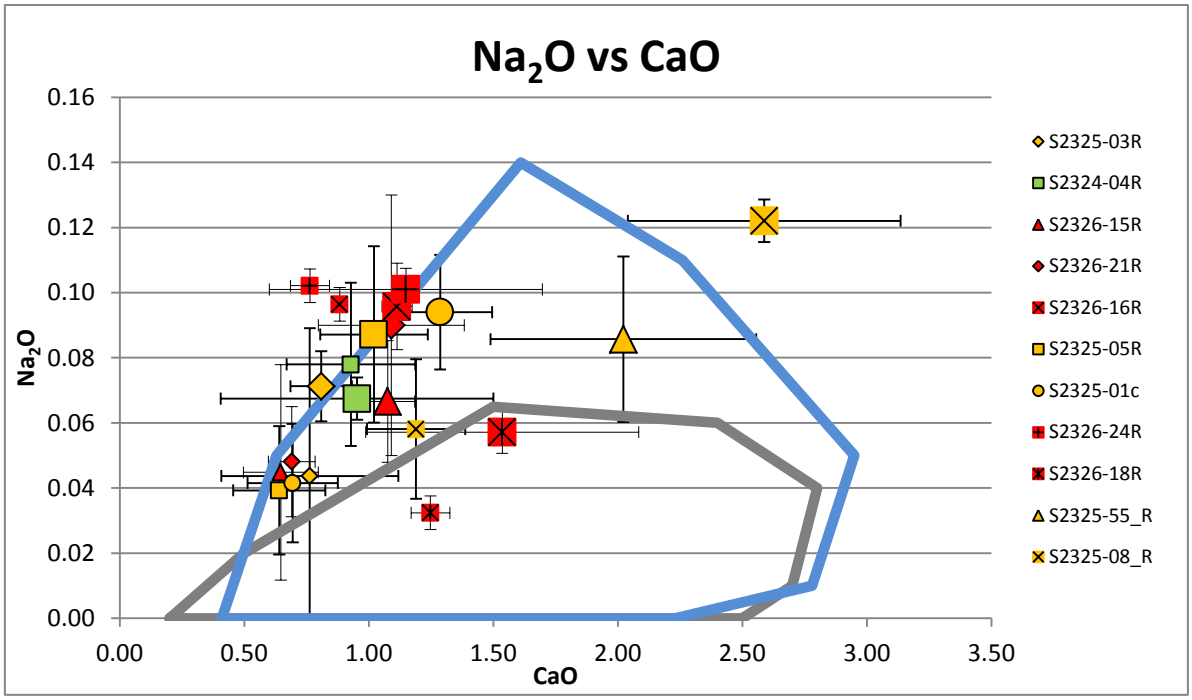

Figure 3.2.2.2 – Na_2O vs. CaO *in orthopyroxene. Smaller symbols represent crystal rims, coarse symbols represent crystal cores. Error bars represent 1σ variability at sample scale. Grey line represents compositional field of abyssal peridotites, blue line represents compositional field of SWIR peridotites.*

Compared with the compositional field of MAR peridotites (grey line), opx from ABFZ peridotites appear enriched in Na plotting close to, and partly encompassing the upper compositional end of the SWIR peridotites field.

The general behavior of Ti is less systematic (Fig. 3.2.2.3). Overall samples that appear to be more “fertile” (richer in Al, Ca, Na) also have the highest Ti contents but the variability is

higher than that observed for the other oxides. The core-rim variability shows that a large decrease in Al corresponds to a weak decreases in Ti (with the exception of sample S2325-03, where Ti increases moving to the rim). Ti content in opx from ABFZ appears to be higher than the Ti content of the abyssal peridotites (grey line), and similar to the Ti content shown by opx from SWIR (blue line) still plotting in the upper part of the compositional field.

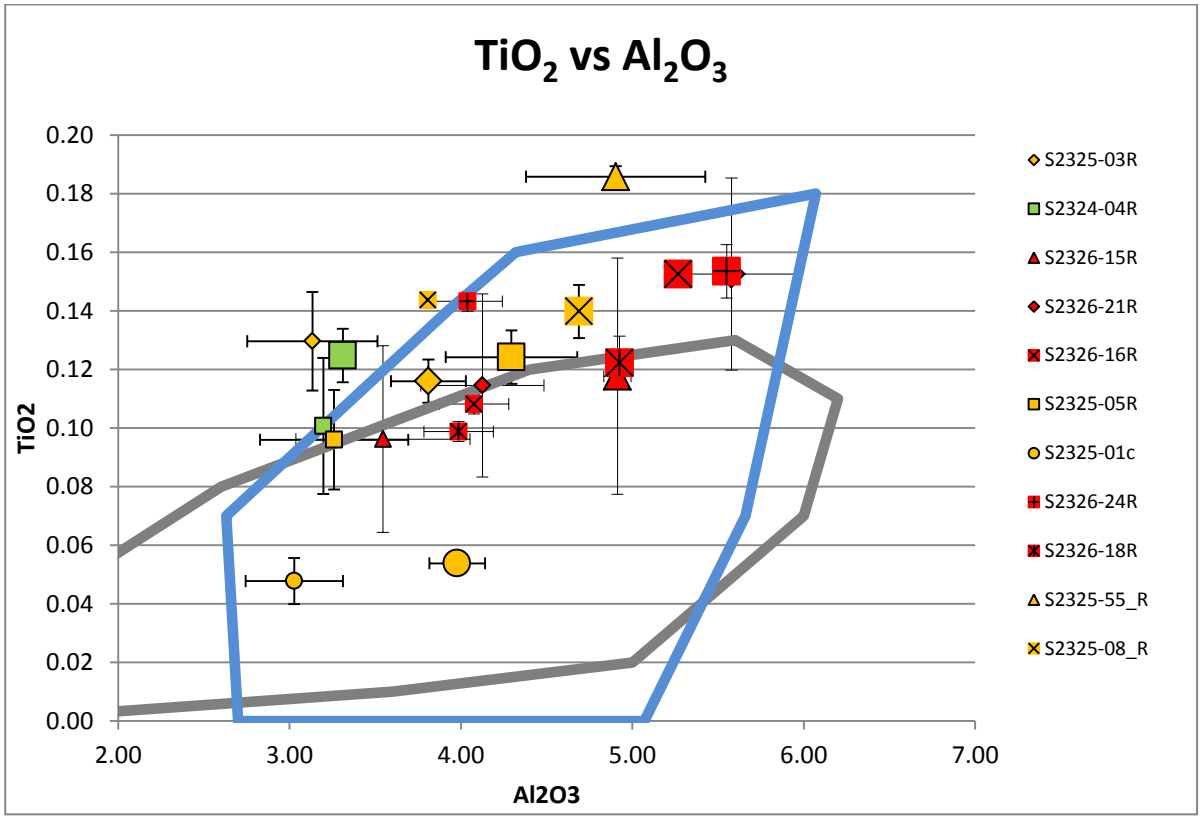

Figure 3.2.2.3 – TiO_2 vs. Al_2O_3 *in orthopyroxene. Smaller symbols represent crystal rims, coarse symbols represent crystal cores. Error bars represent 1σ variability at sample scale. Grey line represents compositional field of MAR peridotites, blue line represents compositional field of SWIR peridotites.*

Mg# [defined as 100*Mg/(Mg + Fe)] varies from 89.47 (sample S2326-21) to 92.05 (sample S2326-08). Cr# [defined as 100*Cr/(Cr + Al)] varies from 5.84 (sample S2326-21) to 15.57 (sample S2324-04). They are positively correlated (Fig. 3.2.2.4) and dredges are well separated, particularly for Mg# (except sample S2325-55). In dredge S2326, variations between core and rim are weak, while in dredge S2325 they are more enhanced, especially in Cr#. Sample S2324-04 appears richer in Cr with respect to the main trend from the most fertile rocks (S2326-21) to the less fertile (S2324-04 itself). High Mg# values appear more similar to the compositional field of the SWIR opx than to the MAR peridotites compositional field.

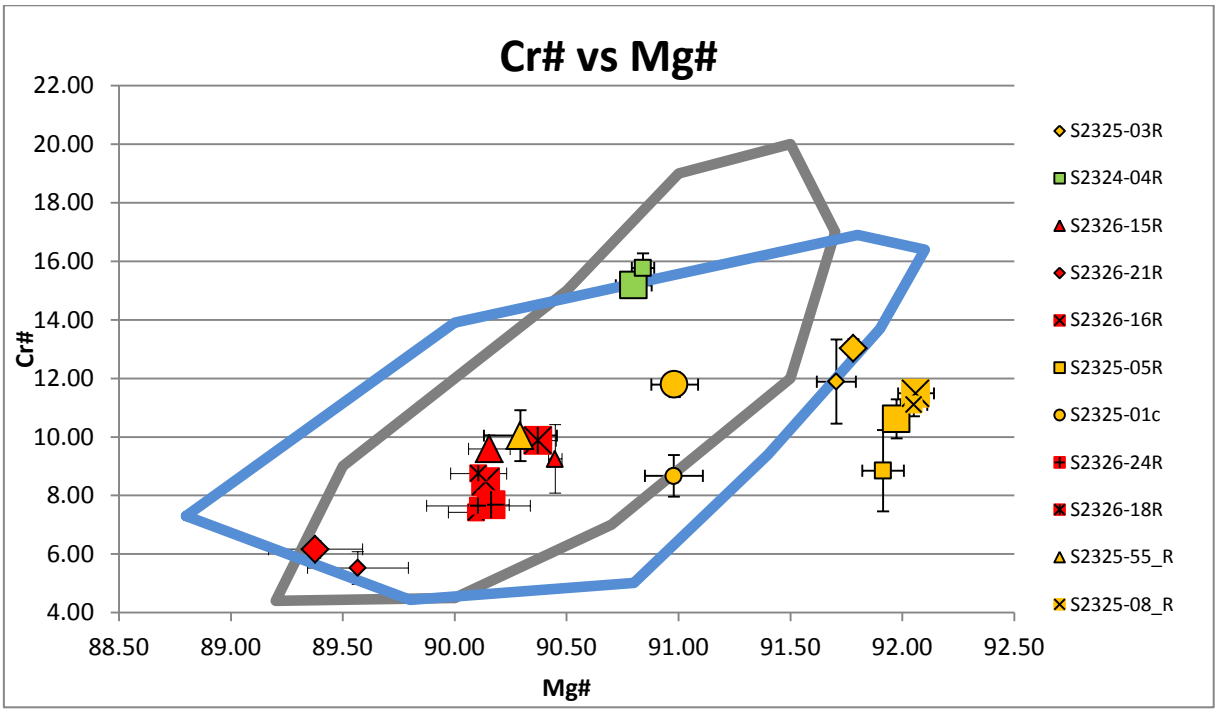

Figure 3.2.2.4 – Cr# vs. Mg# *in orthopyroxene. Small symbols represent crystal rims, coarse symbols represent crystal cores. Error bars represent 1σ variability at sample scale. Grey line represents compositional field of MAR peridotites, blue line represents compositional field of SWIR peridotites.*

3.2.3 Clinopyroxene

Cpx porphyroclasts show large compositional variations. Cores of the coarse porphyroclasts are enriched in Al, Na, Cr and Ca with respect to their rims, while rim silica and Ti contents are higher.

In the following figures, several oxide contents are reported. Each point in the plots represents the mean composition of the clinopyroxenes of each sample and the errors bars indicate the 1σ variability.

Mg# varies from 90.32 (sample S2326-24) to 93.06 (sample S2325-08). Cr# varies from 7.44 (sample S2326-21) to 21.18 (sample S2324-04). They are positively correlated (Fig. 3.2.3.1) and dredge compositional fields are well separated (a part sample S2325-55). Again the position of the sample S2324-04 suggests a possible lower Mg# with respect to the main trend.

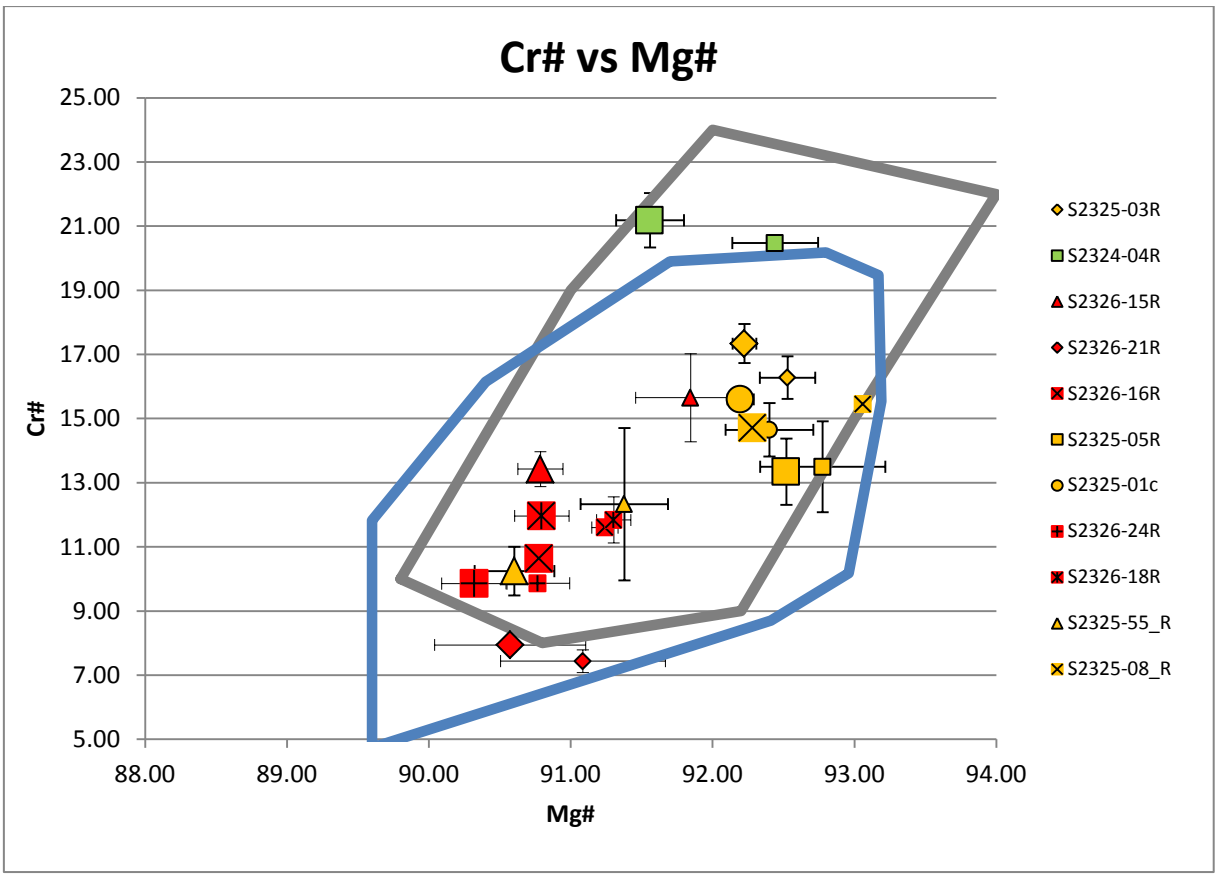

Figure 3.2.3.1 – Cr# vs. Mg# *in clinopyroxene. Small symbols represent crystal rims, coarse symbols represent crystal cores. Error bars represent 1σ variability at sample scale. Grey line represents compositional field of MAR peridotites, blue line represents compositional field of SWIR peridotites.*

Clinopyroxenes porphyroclasts are extremely zoned for Al_2O_3 and Cr_2O_3 showing the same relationships observed for opx (Fig. 3.2.3.2). Porphyroclastic cores seems to cluster on a double trend of increasing Cr and decreasing Al: samples S2326-21, S2326-18, S2325-05 and sample S2325-01 are aligned on a line that shows a lower Cr_2O_3 content with respect to the line defined by the other cpx sample cores. Except sample S2325-55, where Cr increases

toward rim (mylonite), both oxides decrease from core to rim and between the cores of large and smaller grains, in a similar way than observed for opx.

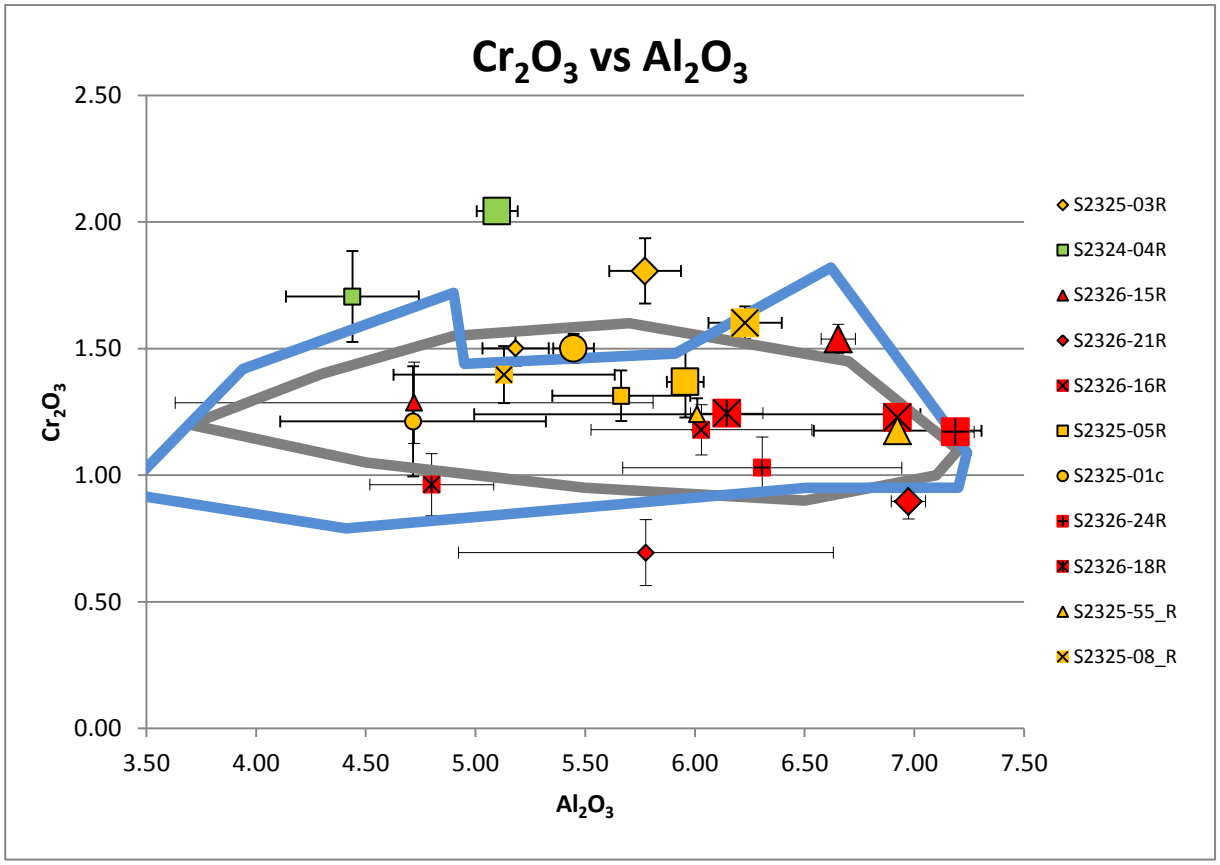

Figure 3.2.3.2 – Cr_2O_3 vs. Al_2O_3 *in clinopyroxene. Small symbols represent crystal rims, coarse symbols represent crystal cores. Error bars represent 1σ variability at sample scale. Grey line represents compositional field of MAR peridotites, blue line represents compositional field of SWIR peridotites.*

Cpx from the ABFZ samples are sodium-rich (0.55% to 1.57 wt%), as shown by figures below, where general MAR peridotite (grey line) and SWIR peridotite (blue line) compositional fields are reported. Na generally decreases moving from core to rim, while Ti increases, except sample S2326-21R that is characterized by a large dispersion of the measured values. Also Ti

contents encompass the compositional field of the MAR and SWIR peridotites. However a strict correlation between Na and Ti is absent nor is possible to find a common behavior with other oxides.

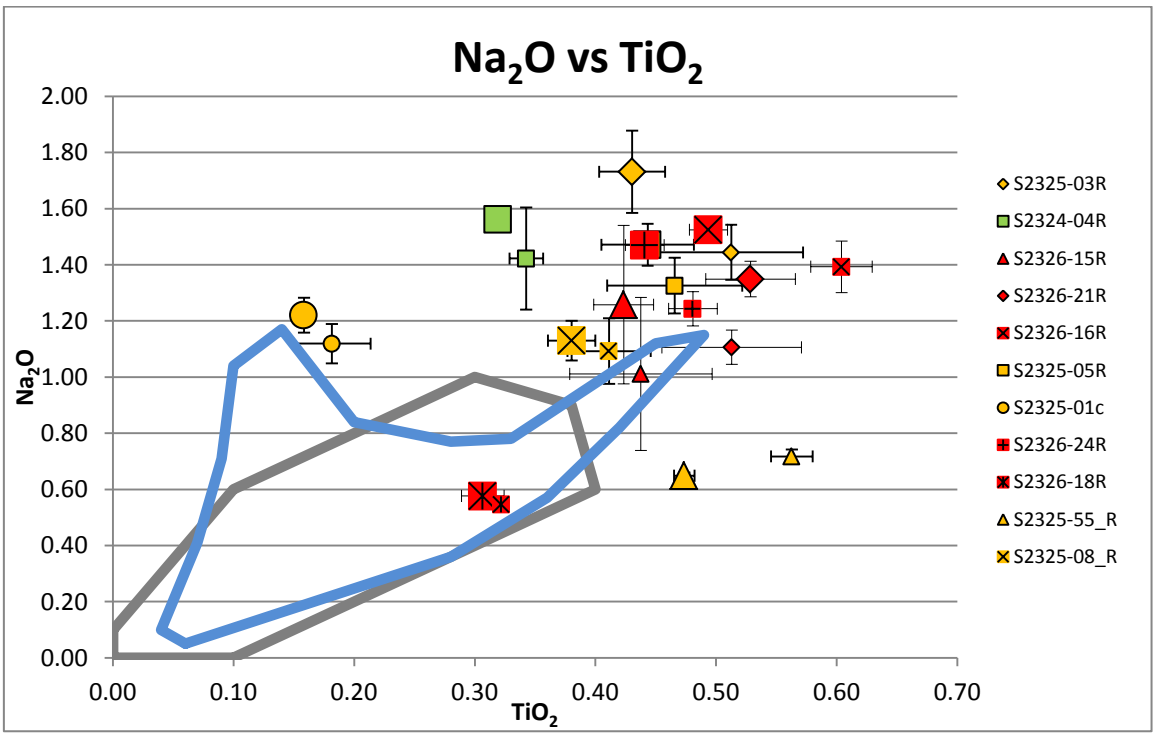

Figure 3.2.3.3 – Na_2O vs. TiO_2 *in clinopyroxene. Small symbols represent crystal rims, coarse symbols represent crystal cores. Error bars represent 1σ variability at sample scale. Grey line represents compositional field of MAR peridotites, blue line represents compositional field of SWIR peridotites.*

Na appears to behave independently from Al and Cr. Forcing the reading of the plots a possible weak positive correlation between Na and Al for the porphyroclastic cores and positive for Na and Cr can be hypothesized (Figs. 3.2.3.4 and 3.2.3.5). Some of the samples show a Cr content plotting on the higher values respect to abyssal peridotites.

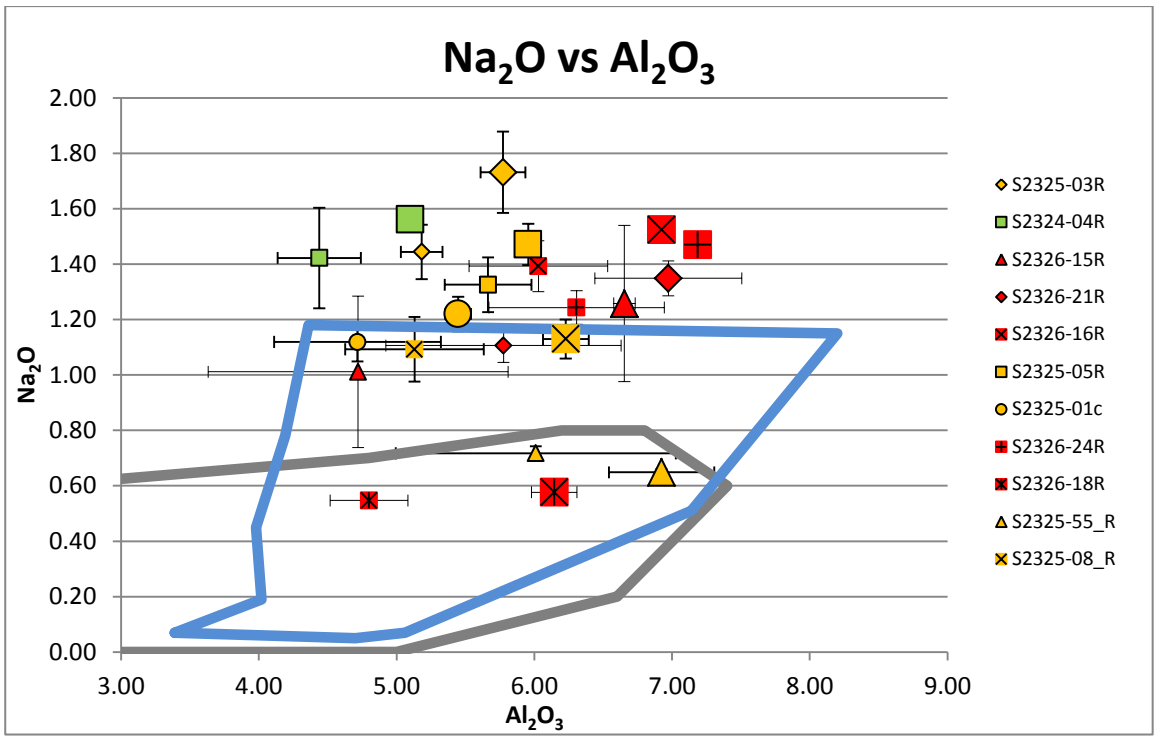

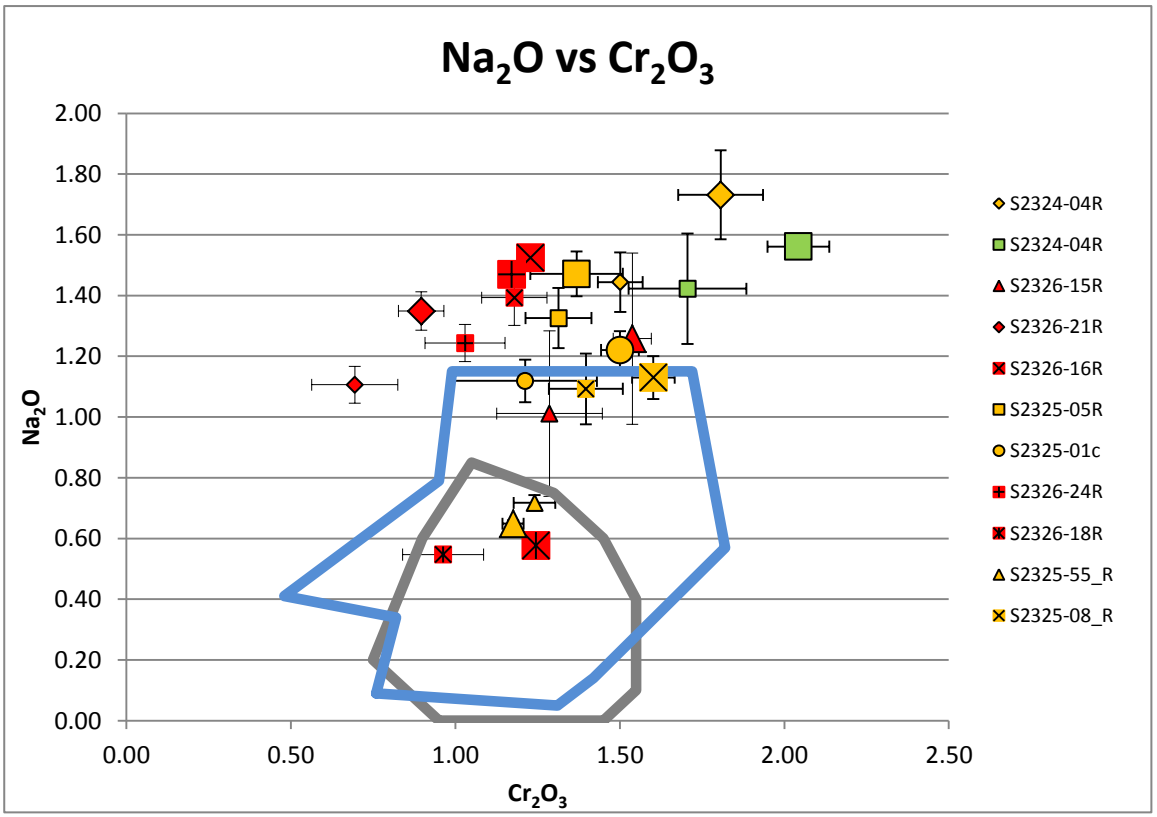

Figure 3.2.3.4 and 3.2.3.5 – Na_2O vs. Al_2O_3 and Cr_2O_3 *in clinopyroxene. Small symbols represent crystal rims, coarse symbols represent crystal cores. Error bars represent 1σ variability at sample scale. Grey line represents compositional field of MAR peridotites, blue line represents compositional field of SWIR peridotites.*

Na negatively correlates with Ca (Fig. 3.2.3.5). Core-rim variation appear as a coupled Na-decrease / Ca-increase from core to rim plotting in the main trend.

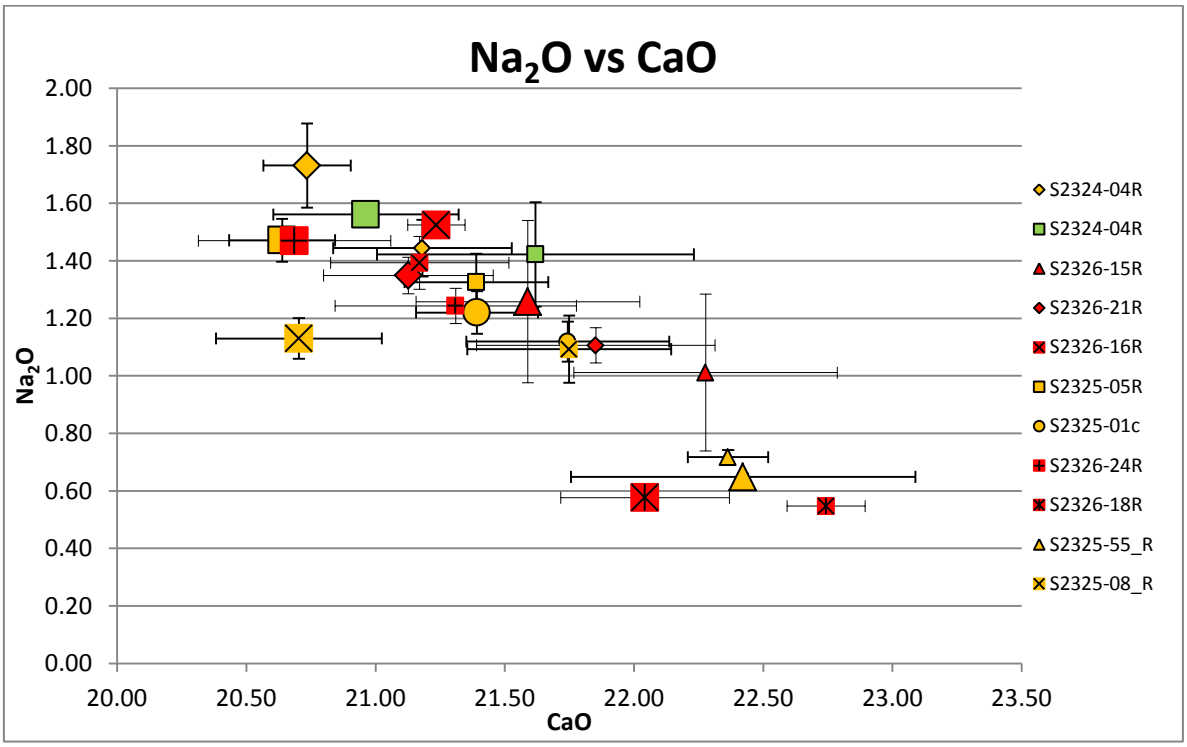

Figure 3.2.3.5 – Na_2O vs. CaO *in clinopyroxene. Small symbols represent crystal rims, coarse symbols represent crystal cores. Error bars represent 1σ variability at sample scale.*

Al^{IV} does not correlate with TiO_2 content that spreads over a large range. Only for dredge S2326 a weak negative correlation can be suggested for Ti slightly decreasing while Al^{IV} largely increases (Fig. 3.2.3.8).

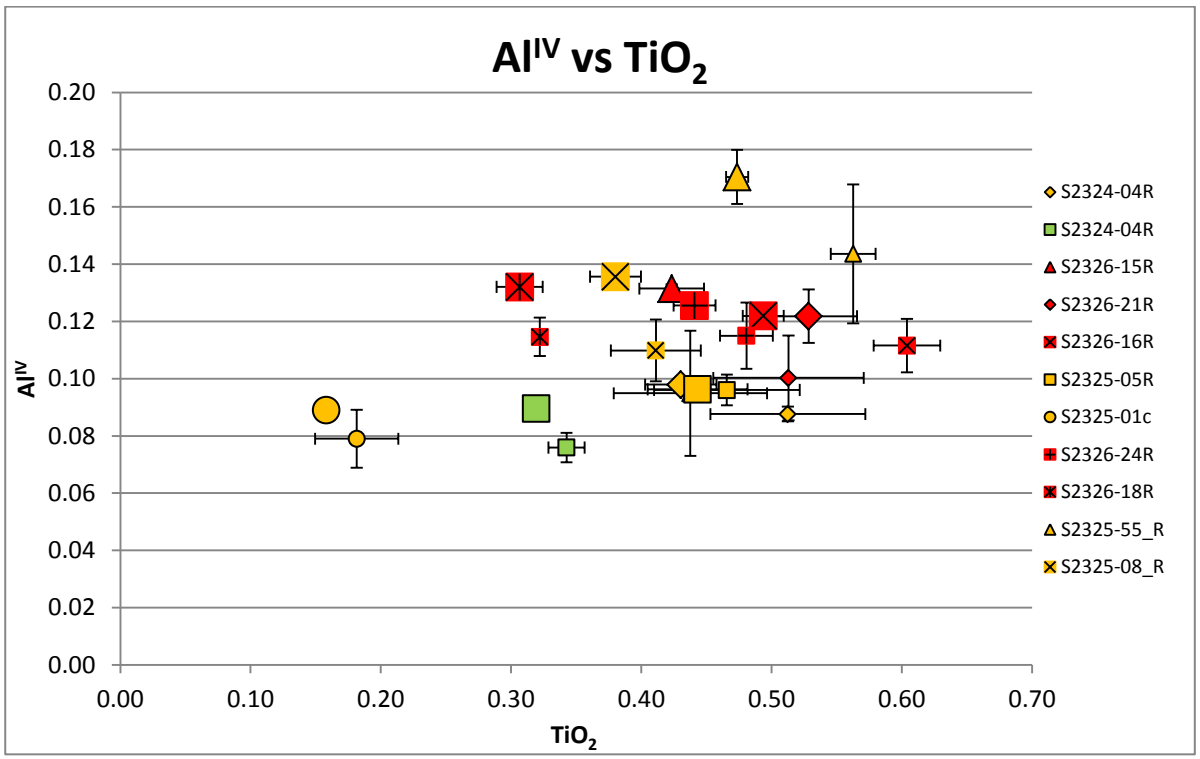

Figure 3.2.3.8 – Al^{IV} vs. TiO_2 *in clinopyroxene. Small symbols represent crystal rims, coarse symbols represent crystal cores. Error bars represent 1σ variability at sample scale.*

Ca and Mg# are positively to weakly correlated being Ca variation larger than Mg# at the dredge scale (Fig. 3.2.3.9).

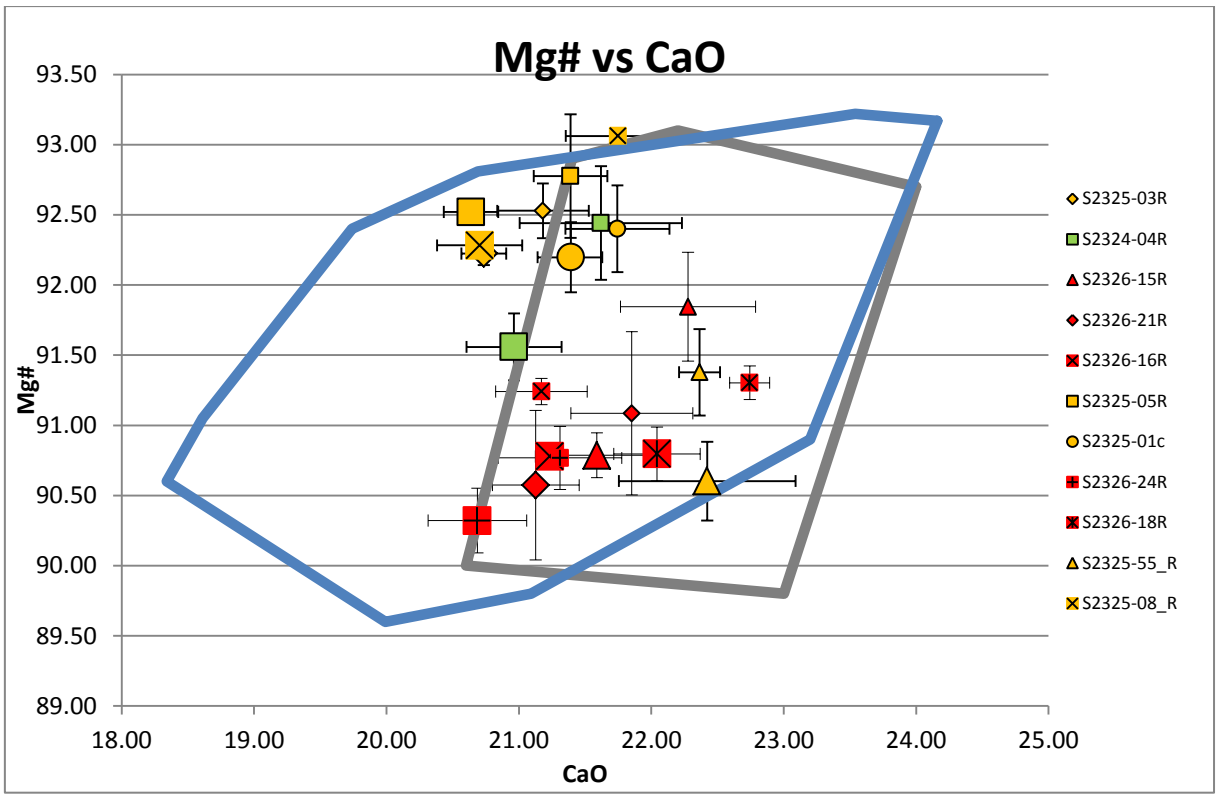

Figure 3.2.3.9 – Mg# vs. CaO *in clinopyroxene. Small symbols represent crystal rims, coarse symbols represent crystal cores. Error bars represent 1σ variability at sample scale. Grey line represents compositional field of MAR peridotites, blue line represents compositional field of SWIR peridotites.*

3.2.4 Spinel

Spinel chemical compositions from ABFZ are generally homogeneous, except sample S2326-15R, that shows wide variability. Cr# varies from 11.31 (sample S2326-21) to 35.88 (sample S2324-04), while Mg# varies from 75.12 (sample S2326-16) to 63.10 (sample S2325-55). Them fit well the abyssal peridotite compositional field. In general Mg# tends to decrease moving from core to rim, while Cr# seems not to change (Fig. 3.2.4.1).

Overall the spinel composition follows the order of fertility identified based on the orthopyroxene and partly the clinopyroxene composition. S2324-04 is the most depleted and S2326-21 the fertile-most.

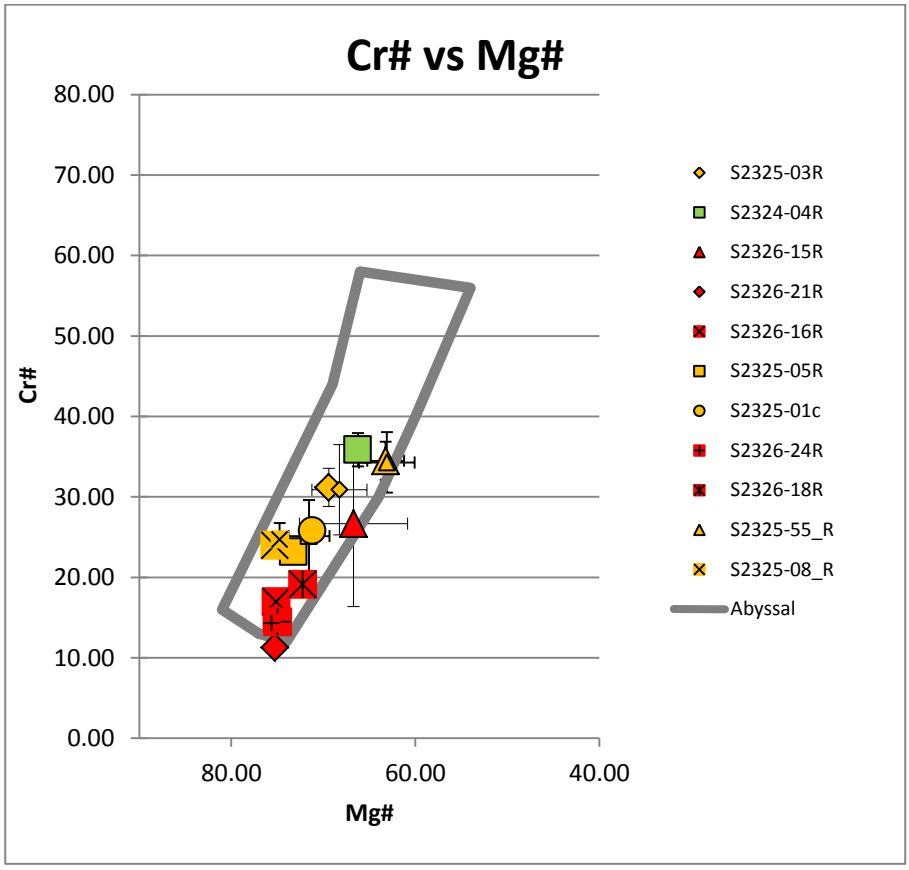

Figure 3.2.4.1 – Cr# vs. Mg# *in spinel. Small symbols represent crystal rims, coarse symbols represent crystal cores. Error bars represent 1σ variability at sample scale. Grey line represents compositional field of abyssal peridotites.*

Those abyssal spinel-peridotites considered to be pure residues have low spinel Ti content < 0.20 wt% (DICK ET AL, 2010; HELLEBRAND ET AL, 2001; HELLEBRAND ET AL , 2002; BRUNELLI ET AL, 2006; SEYLER & BONATTI, 1997); the ABFZ spinels partly fall in the abyssal peridotite field, the Ti enrichment positively correlates with the Cr# (Fig. 3.2.4.2), a feature commonly observed in spinel-peridotites associated with plagioclase-peridotites (SEYLER & BONATTI, 1997; BRUNELLI &

SEYLER, 2010). The mylonitic sample S2325-55 (that reaches values of 0.4 wt%) plots out of the field. To be noted is the wide variability of sample S2326-15 both for Ti and Cr# contents. In general Ti concentration in Spinel from ABFZ appears to be higher than the Ti concentration of normal abyssal peridotites, because they are associated with plagioclase-peridotites.

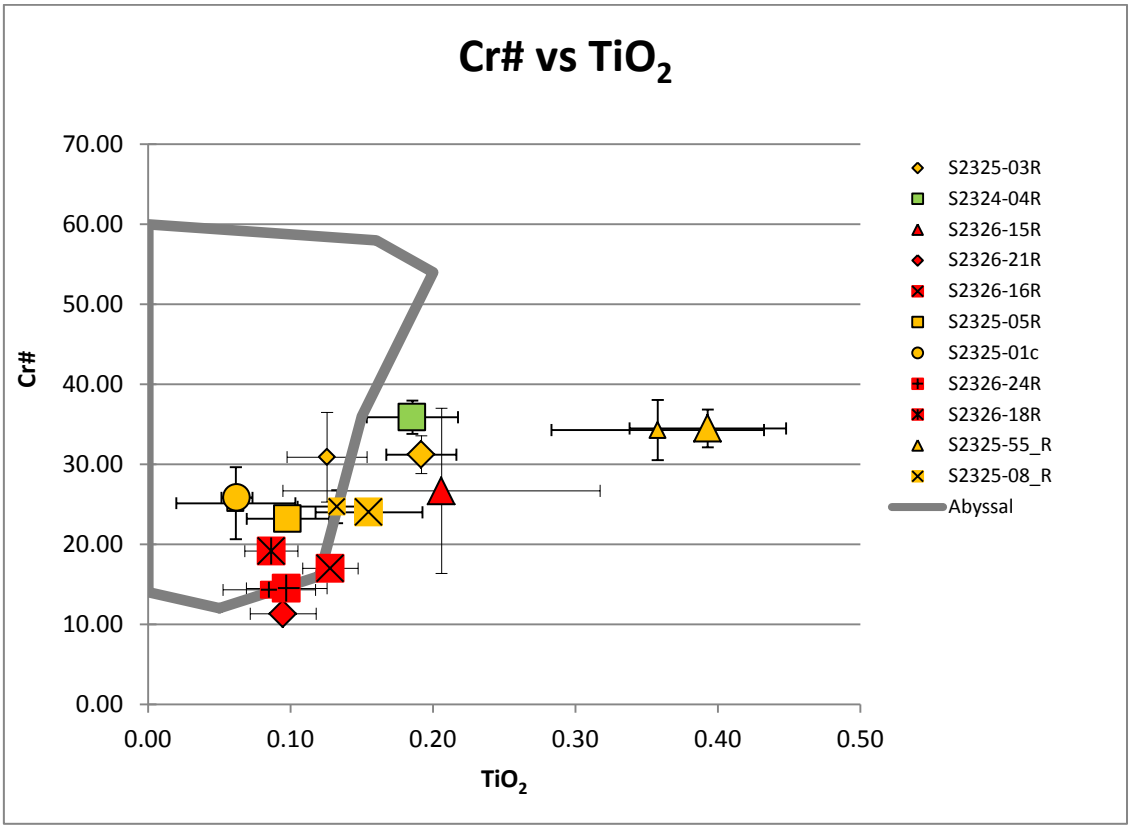

Figure 3.2.4.2 – Cr# vs. TiO_2 *in spinel. Small symbols represent crystal rims, coarse symbols represent crystal cores. Error bars represent 1σ variability at sample scale. Grey line represents compositional field of abyssal spinel-field peridotites.*

Ni content in spinels positively correlates with Mg# (Fig. 3.2.4.3). Excluding sample S2326-15, dredge S2326 spinels have NiO content between 0.3 wt% and 0.35 wt%, while other samples

show a wider variability in Ni content. The overall Ni-Cr# variability well plot in the abyssal peridotite compositional field. It also shows a weak depletion in Ni content moving from core to rim of the coarser spinels.

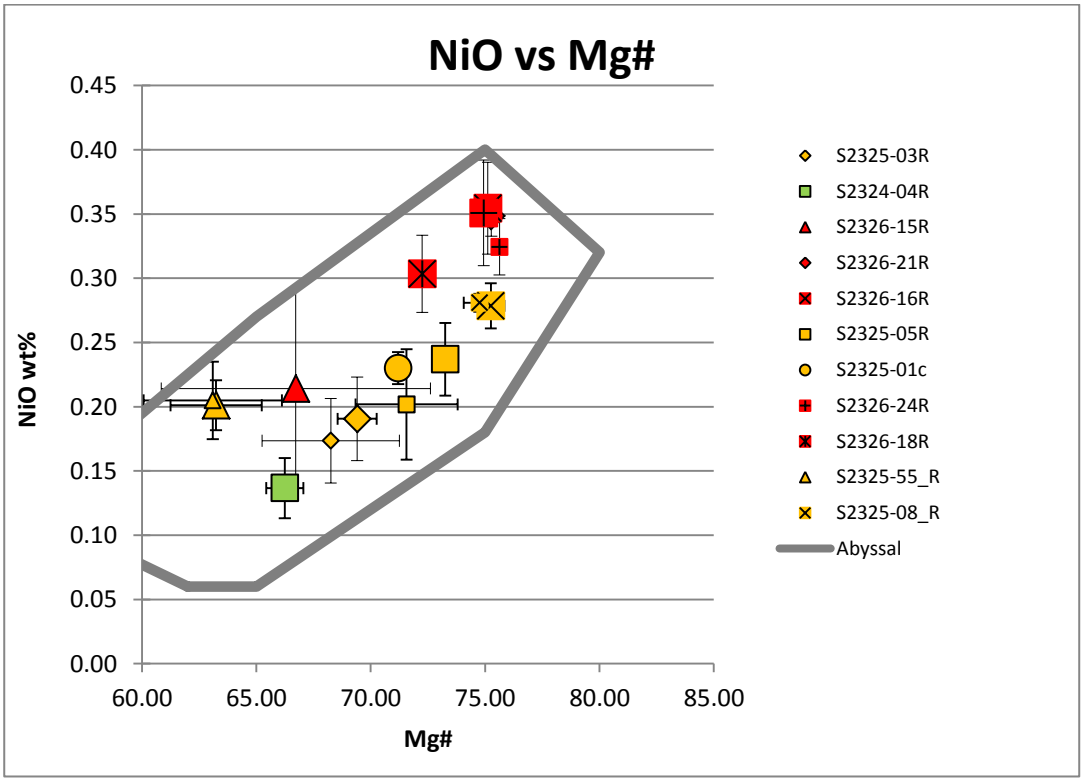

Figure 3.2.4.3 – NiO vs. Mg# *in spinel. Smaller symbols represent crystal rims, coarse symbols represent crystal cores. Error bars represent 1σ variability at sample scale. Grey line represents compositional field of abyssal peridotites.*

3.2.5 Concluding remarks

1. Some minor elements, as Na and Ti in pyroxenes, are systematically higher than average abyssal peridotite values and even higher than the reported values for the SWIR.
2. Other elements, as Ni and Cr, and the major element systematic plot well inside the abyssal peridotite field and related trends.
3. Cr# and Mg# in clinopyroxene and in spinel suggest that the more fertile (e.g. with lower Cr# and Mg#) samples are the dredge S2326 samples. The only sample from dredge S2324 appears to be the more depleted while samples from dredge S2325 appear to be in the middle. This observation can be inferred also looking at some compatible elements in spinel as Ni. However, other minor element as Na and Ti in pyroxene and in spinels seems to be not in agreement with such observation.
4. Variability that is possible to observe moving from core to rim of pyroxene crystals, seems to be in agreement with data published by SEYLER ET AL. (2003), where such trends are explained as sub-solidus re-equilibration at lower P/T conditions, feature common in abyssal peridotites.
5. Some observable trends existing moving from core to rim, as Ti in clinopyroxene, suggest possible melt/rock interaction. Moreover, the lack of correlation between some minor and incompatible elements, such as Na and Ti in clinopyroxene, can lead to the same remark.

3.3 – Mineral major element compositions in plagioclase-peridotites from ABFZ

Eight samples among plagioclase-peridotites for EMPA analysis were selected. In general, plagioclase-peridotites appear more altered than spinel-peridotites. Unfortunately neither fresh plagioclase nor olivine have been detected in the studied samples. Plagioclase is replaced by hydrated minerals (as hydrogarnet, chlorite) and clays. The range of chemical variability varies strongly form sample to sample: in a few cases, samples appear extremely homogeneous, while in other cases chemical variability is very wide, higher if compared to the spinel-peridotites. To describe mineral chemical contents in plagioclase-bearing peridotites from ABFZ, data from plagioclase-bearing peridotites (TARTAROTTI ET AL. 2002; SEYLER & BONATTI, 1997; BRUNELLI & SEYLER, 2010; DICK, 1989) have been plotted as reference (orange line) along with the compositional fields from ABFZ spinel peridotites (green line).

3.3.1 Orthopyroxene

In figures below, several oxide contents are reported. Each point represents the sample composition calculated as mean of 3-5 grains per sample and the associated 1σ variability. Color coding and symbol significance are the same as previously used except dredges S2317 (violet) and S2318 (blue) that contain only plagioclase-bearing rocks. The only sample S2317-135 recovered in its dredge is a plagioclase-bearing, cpx-free harzburgite.

In general, orthopyroxene shows depletion in Na (Fig. 3.3.1.1) and Al (Fig. 3.3.1.2) with respect to opx from the ABFZ spinel field equilibrated peridotites. This possibly reflects the occurrence of plagioclase and suggests equilibration or partial equilibration with this mineral.

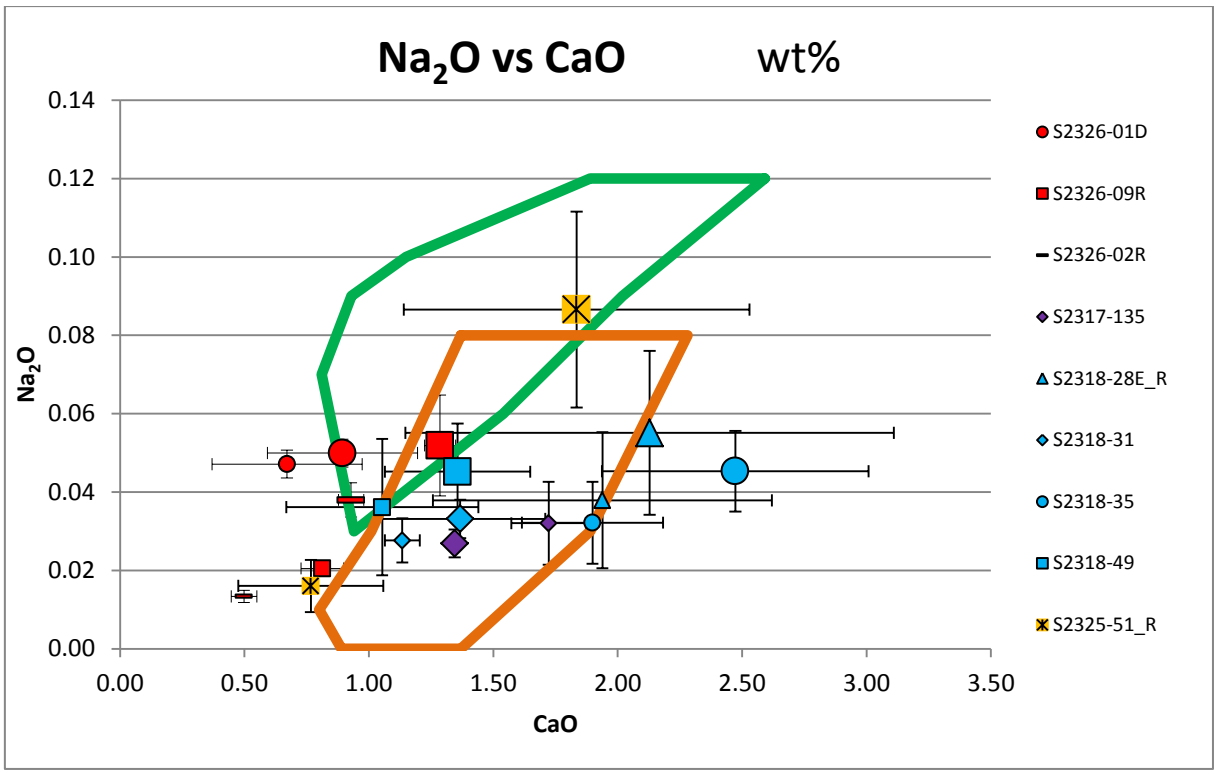

Figure 3.3.1.1 – Na_2O vs. CaO wt% *in orthopyroxene. Small symbols represent crystal rims, coarse symbols represent crystal cores. Error bars represent 1σ variability at sample scale. Grey line represents compositional field of abyssal peridotites, green line represents compositional field of ABFZ peridotites and orange line represents compositional field of plagioclase-bearing peridotite.*

However, the scatter and variability at the sample and dredge scale suggests equilibration with plagioclase to occur at different degrees. For instance samples from dredge S2326 collected along the transform wall (red color) plot in a separate group clearly visible in the Cr-Al space (Fig. 3.3.1.2). The markedly lower Cr and higher Al contents agree with the general more fertile character of the rocks collected at this site well represented by the lowest Cr# and Mg# contents of all their minerals in the spinel-field equilibrated rocks

(previous paragraph). A low degree of equilibration can be inferred because cores of the large grains still keep the high Al contents being only rims depleted by equilibration itself.

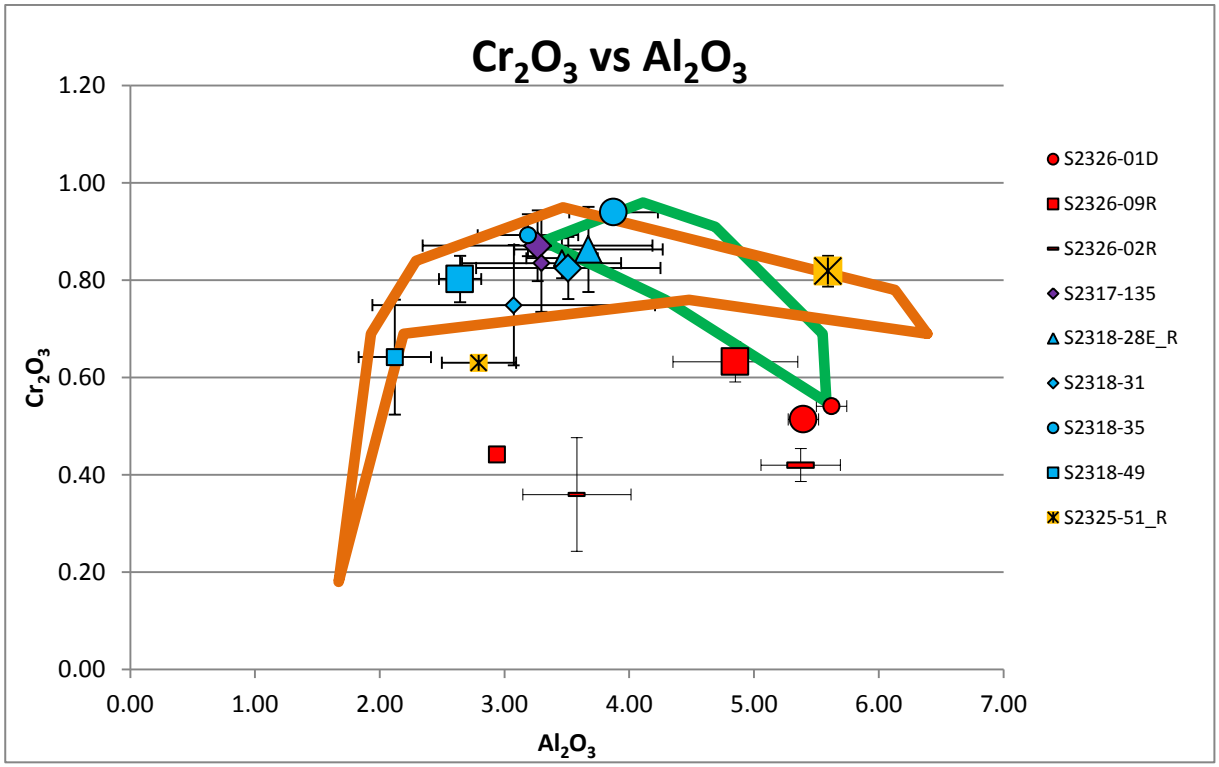

Figure 3.3.1.2 – Cr_2O_3 vs. Al_2O_3 *in orthopyroxene. Small symbols represent crystal rims, coarse symbols represent crystal cores. Error bars represent 1σ variability at sample scale. Grey line represents compositional field of abyssal peridotites, green line represents compositional field of ABFZ peridotites and orange line represents compositional field of plagioclase-bearing peridotite.*

Mg# appears to be lower if compared to spinel-peridotites from ABFZ (green line in following graph) plotting well inside the field of plagioclase-bearing peridotites (Fig. 3.3.1.3). With the exception of S2326 samples the others define a slightly negative trend of increasing Cr#

while decreasing Mg#. Still the lower Cr# of S2326 samples agrees with a lesser equilibration to plagioclase.

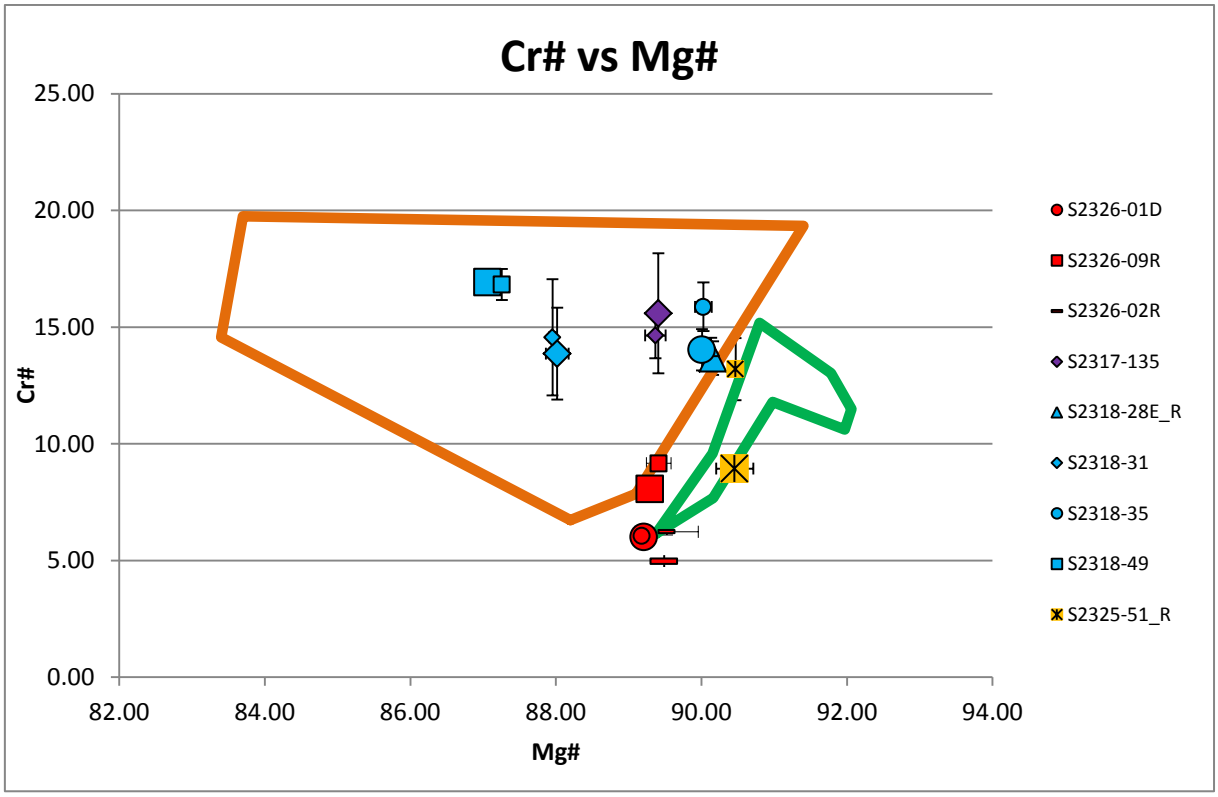

Figure 3.3.1.3 *Cr# vs. Mg# in orthopyroxene. Small symbols represent crystal rims, coarse symbols represent crystal cores. Error bars represent 1σ variability at sample scale. Grey line represents compositional field of abyssal peridotites, green line represents compositional field of ABFZ peridotites and orange line represents compositional field of plagioclase-bearing peridotite.*

With respect to the plagioclase-bearing peridotite compositional field, CaO spans over a wider range (0.5 wt% up over 2.5 wt%), Ti is systematically lower (Fig. 3.3.1.4) while Na has the same distribution.

In all plots the plagio-bearing mylonite S2325-51 shows a different behavior for the major trend. The composition of the mylonite reported in the previous paragraph (S2325-55) has also been plotted for reference even though apparently equilibrated in the spinel field. Overall they plot very close in all compositional spaces suggesting that similar lithologies or heterogeneities have been homogenized during mylonitization, and that spinel mylonite indeed can bear plagioclase.

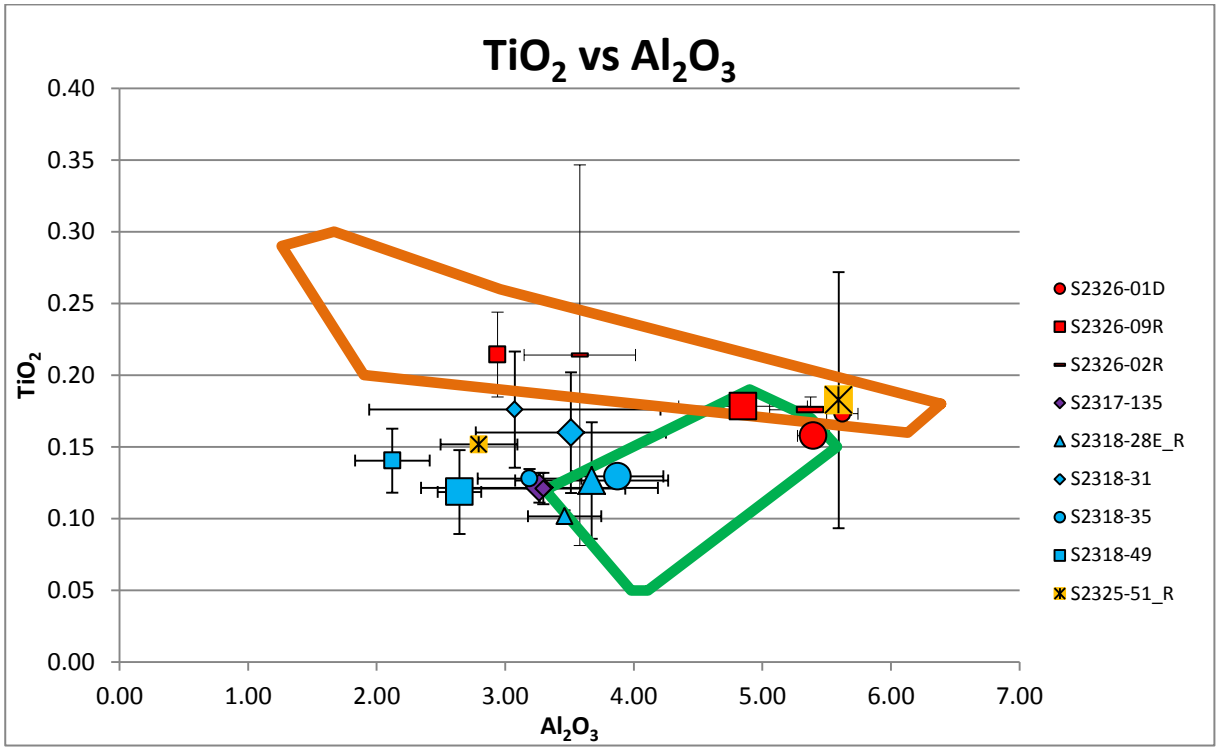

Figure 3.3.1.4 *TiO_2 vs. Al_2O_3 in orthopyroxene. Small symbols represent crystal rims, coarse symbols represent crystal cores. Error bars represent 1σ variability at sample scale. Grey line represents compositional field of abyssal peridotites, green line represents compositional field of ABFZ peridotites and orange line represents compositional field of plagioclase-bearing peridotite.*

3.3.2 Clinopyroxene

As discussed for orthopyroxenes, also clinopyroxenes from ABFZ plagioclase-bearing peridotites present a depletion in all the major element that are compatible with partial equilibration with plagioclase, e.g. Al, while showing an enrichment in Ca and Ti. Mg# show lower values if compared to the spinel-peridotites one.

As previously observed Ti and Al are highly variable in the sample suite from dredge S2326.

In figures below, several oxide contents are reported. The three different dredges are color-coded: S2318 blue, S2325 yellow and S2326 red.

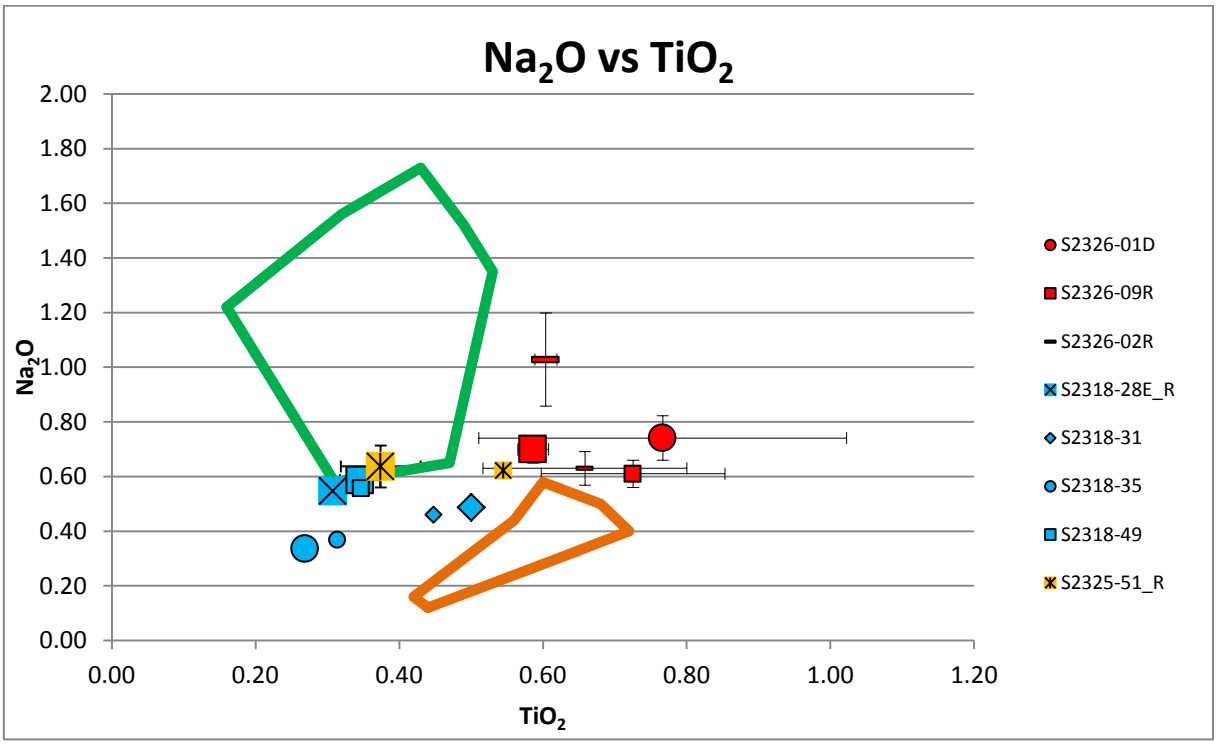

Figure 3.3.2.1 *Na_2O vs. TiO_2 in clinopyroxene. Smaller symbols represent crystal rims, coarse symbols represent crystal cores. Error bars represent 1σ variability at sample scale. Grey line represents compositional field of abyssal peridotites, green line represents compositional field of ABFZ peridotites and orange line represents compositional field of plagioclase-bearing peridotite.*

Because of the strong alteration that these samples have experienced, it was not always possible to analyze chemical content in all the rims of the analyzed crystals thus systematic core-rim compositional variations cannot be confidently inferred. Concerning Cr and Al, the general trend is a weak depletion moving from core to rim, whereas Ca and Mg# show a general enrichment moving from core to rim.

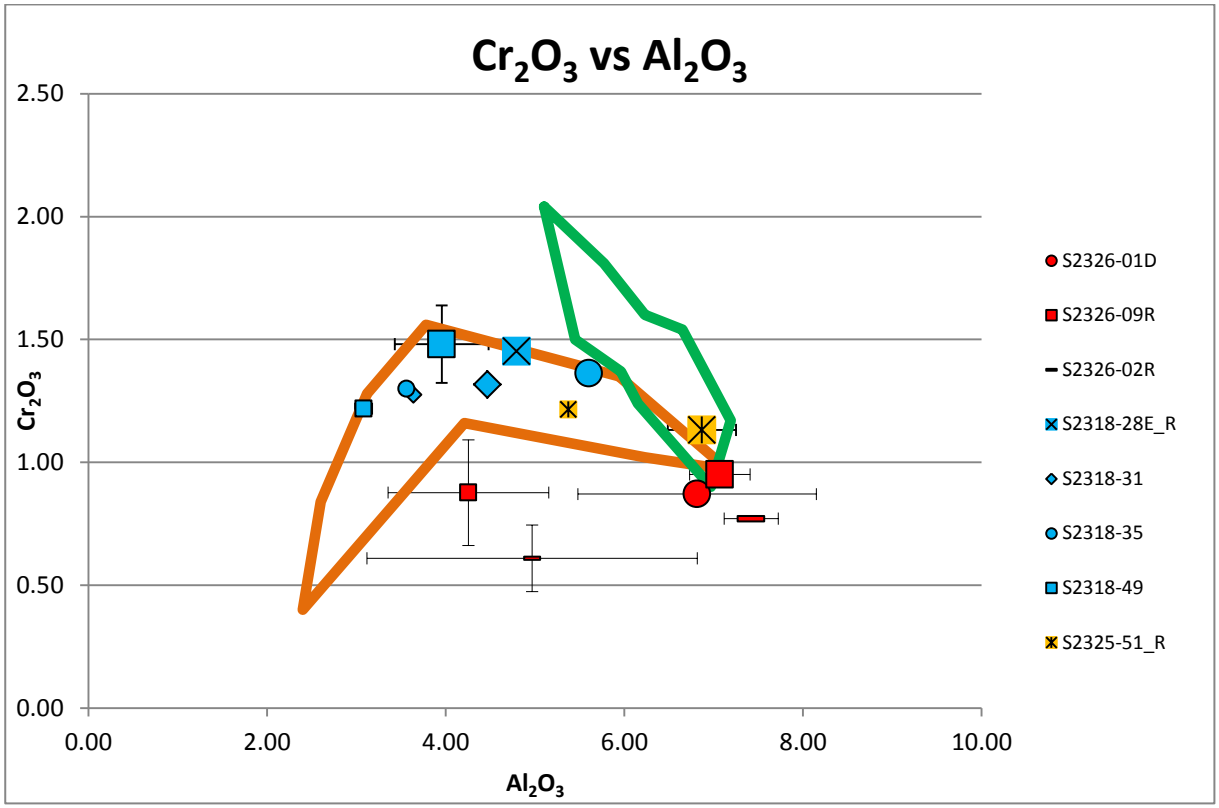

Figure 3.3.2.2 *Cr_2O_3 vs. Al_2O_3 in clinopyroxene. Small symbols represent crystal rims, coarse symbols represent crystal cores. Error bars represent 1σ variability at sample scale. Grey line represents compositional field of abyssal peridotites, green line represents compositional field of ABFZ peridotites and orange line represents compositional field of plagioclase-bearing peridotite.*

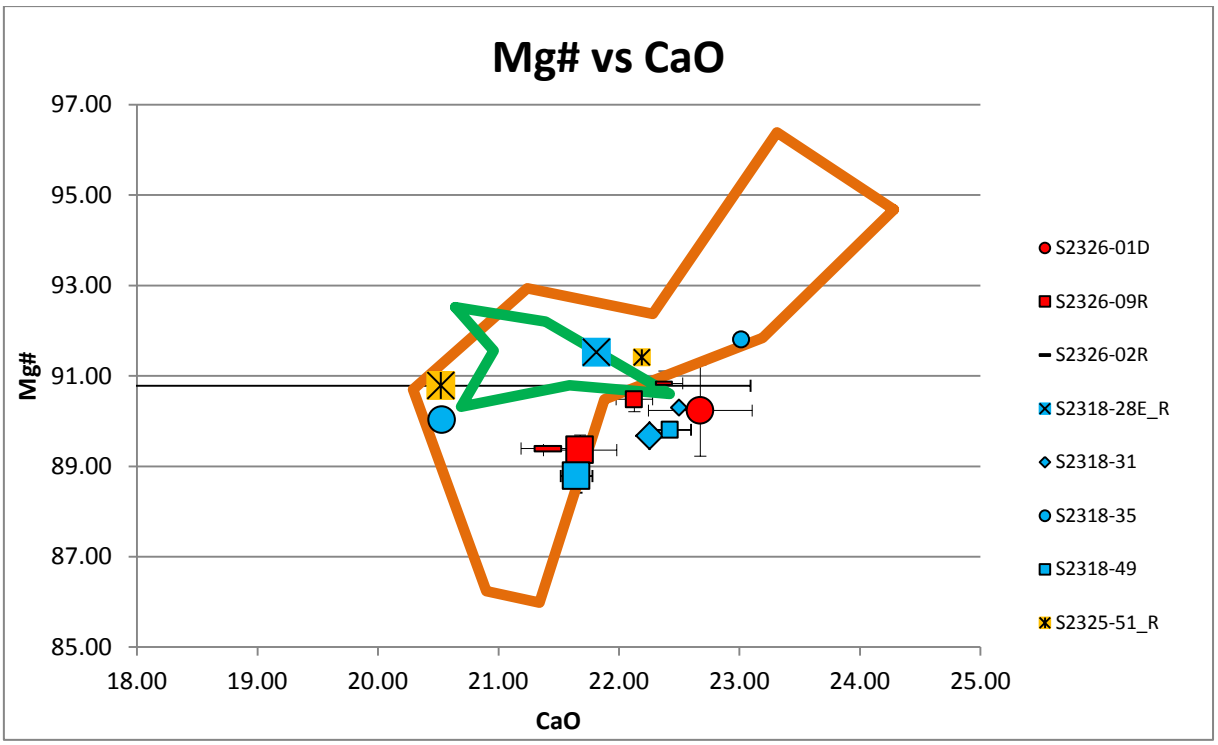

Figure 3.3.2.3 *Mg# vs. CaO in clinopyroxene. Small symbols represent crystal rims, coarse symbols represent crystal cores. Error bars represent 1σ variability at sample scale. Grey line represents compositional field of abyssal peridotites, green line represents compositional field of ABFZ peridotites and orange line represents compositional field of plagioclase-bearing peridotite.*

3.3.3 Spinel

In figures below, several oxide contents are reported.

Spinels from plagioclase-bearing peridotites collected at ABFZ are generally homogeneous, except for Ti content in some samples, especially in Sample S2326-01D. Cr# varies from 9.80 (sample S2326-02) to 45.35 (sample S2318-31), while Mg# varies from 74.34 (sample S2326-01D) to 50.53 (sample S2318-31).

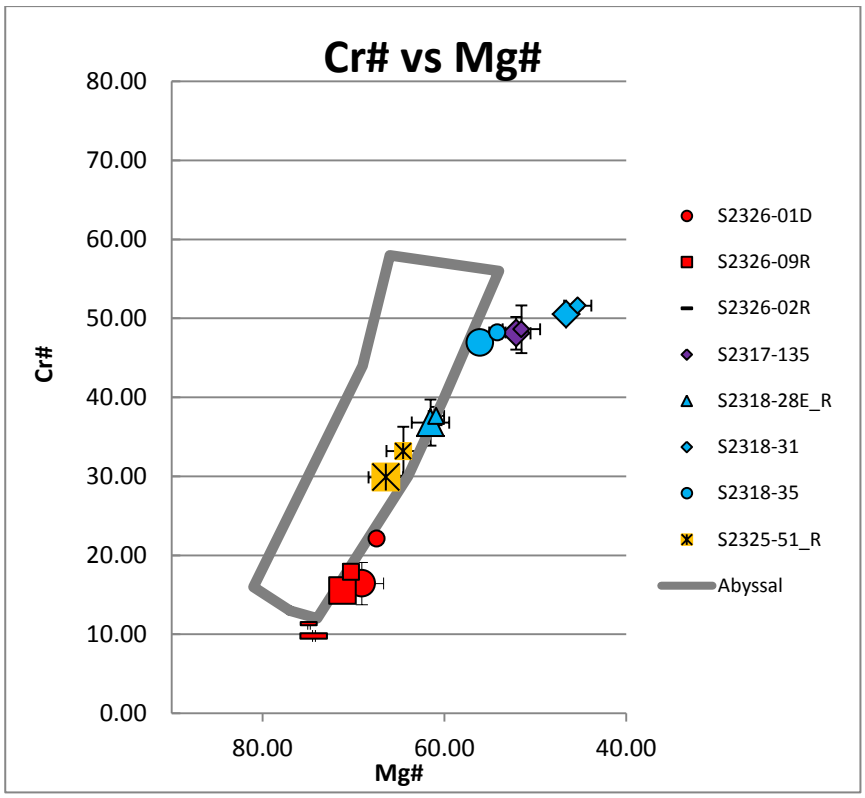

Figure 3.3.3.1 *Cr# vs. Mg# in spinel. Small symbols represent crystal rims, coarse symbols represent crystal cores. Error bars represent 1σ variability at sample scale. Grey line represents compositional field of abyssal peridotites.*

Looking at Cr# vs. Mg# diagram, samples appear slightly shifted to lower Mg# with respect to the compositional field of abyssal peridotites (grey line). Samples with higher Cr# plot out from the compositional field of the residual abyssal peridotites in the direction of melt/rock interaction (sample S2318-31 and sample S2317-135).

In figure 3.3.3.2, Cr# vs. Ti oxide are reported along with the compositional field of abyssal peridotites (grey line). As commonly observed in spinel from plagioclase-bearing peridotites (DICK & BULLEN, 1984; DICK, 1989; SEYLER & BONATTI, 1997; TARTAROTTI ET AL, 2002), spinels in these samples are Ti enriched. Marked trends of increasing both Cr# and Ti content are

readable at the dredge scale. Almost all samples show a Ti content >0.2wt%, while lot of them display a Ti content >0.3wt%, up to 0.85wt% of Ti in sample S2318-31.

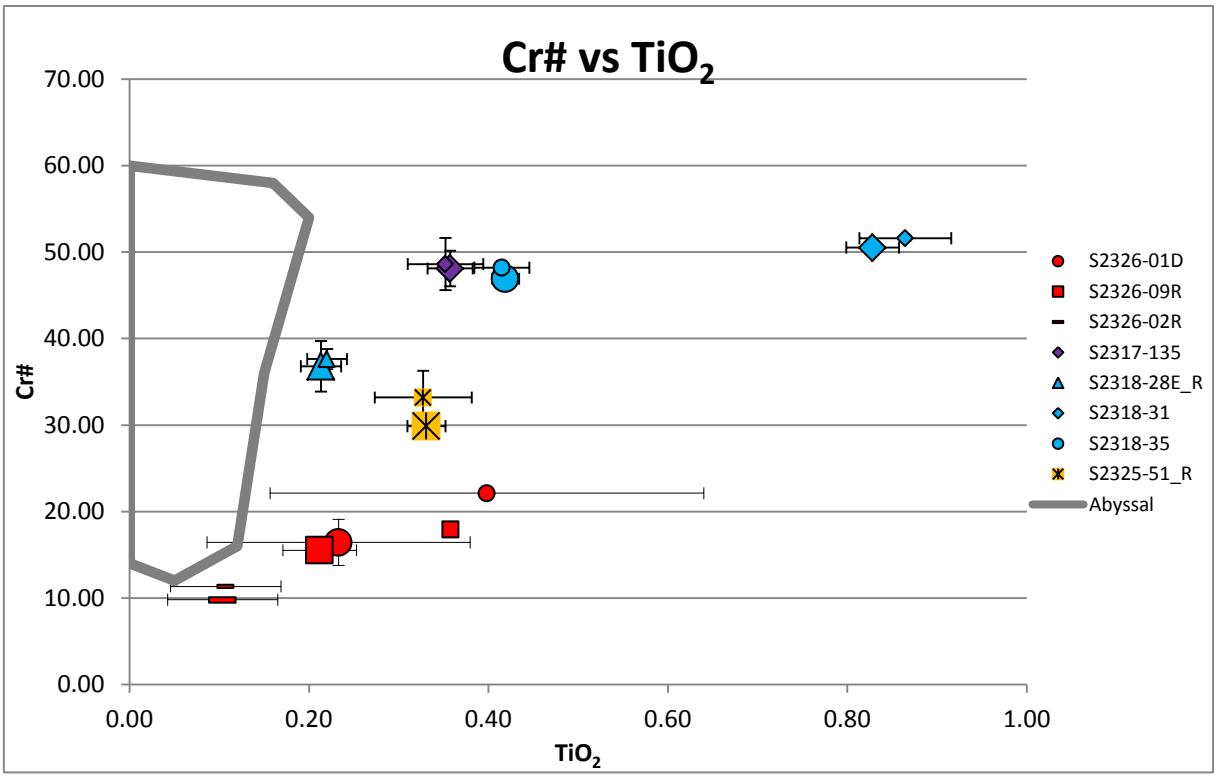

Figure 3.3.3.2 *Cr# vs. TiO_2 in spinel. Small symbols represent crystal rims, coarse symbols represent crystal cores. Error bars represent 1σ variability at sample scale. Grey line represents compositional field of abyssal peridotites.*

3.3.4 Concluding remarks

1. Except some minor elements as Ti and Na, mineral major element composition of plagioclase-bearing peridotites from ABFZ plot inside the compositional field of other plagioclase-bearing abyssal peridotites.
2. Only few samples fit the compositional field of the spinel-equilibrated peridotites from ABFZ.
3. Looking to major element composition, dredge S2318 and dredge S2326 are well distinguishable, plotting usually at both ends of the compositional field.
4. Looking to indicators of the degree of melting, it seems that peridotites sampled along the ridge axis (dredge S2318) have undergone a higher degree of melting with respect to peridotites sampled in the transform wall (dredge S2326).

3.4 – Mineral equilibrium in peridotites from ABFZ

In the following graphs, Cr# of clinopyroxene, orthopyroxene and spinel are reported. In figure 3.4.1, Cr# values from spinel-peridotites are reported; values from mylonites have been omitted. The overall positive Cr# correlations record equilibrium under spinel field mantle conditions. Observed values span the abyssal peridotite field.

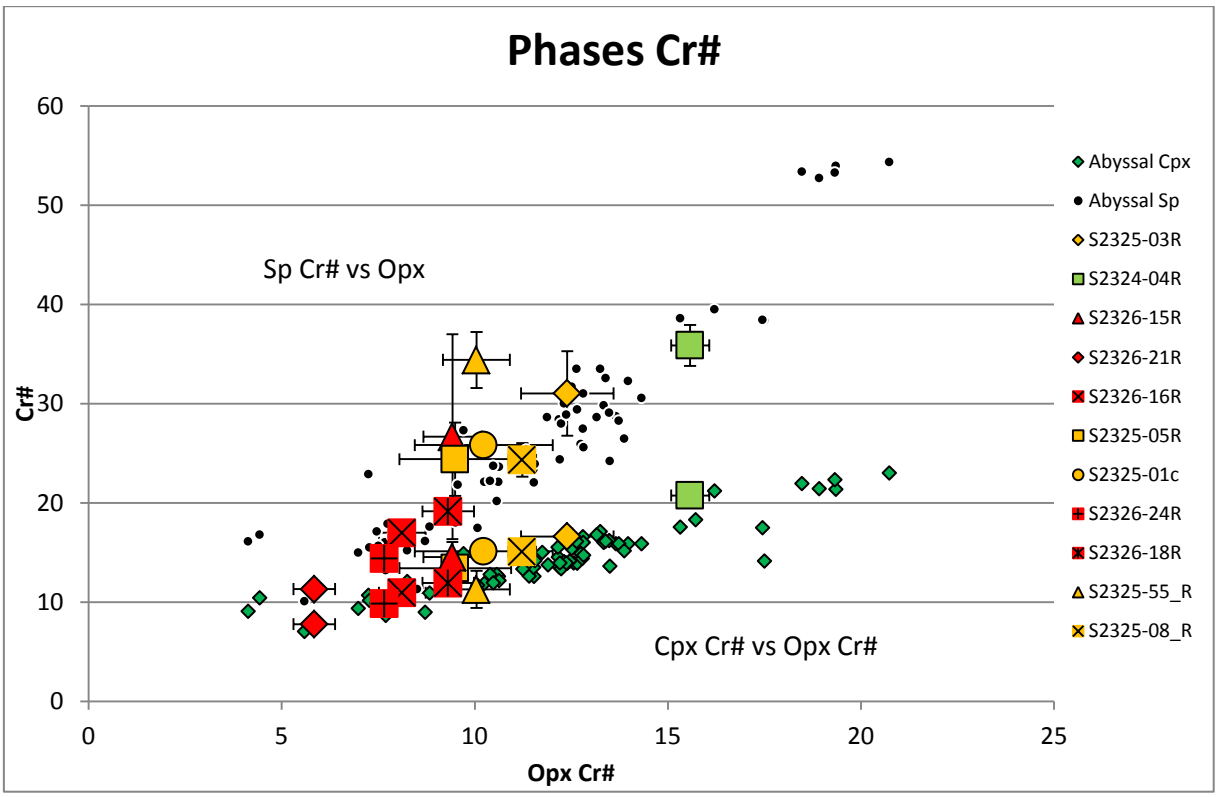

Figure 3.4.1 *Orthopyroxene vs. spinel and clinopyroxene Cr-number [100 x Cr/(Cr + Al)] in plagioclase-free peridotites from ABFZ. Symbols represent crystal cores. Error bars represent 1σ variability at sample scale. Black dots are spinel Cr# of abyssal peridotites and green dots are cpx Cr# of abyssal peridotites.*

At the thin section scale large compositional variation are observed attesting for an equilibrium at the grain scale. The observed 1σ variability is however comparable with that observed on the other samples of the abyssal peridotite record (BRUNELLI ET AL., 2006; SEYLER ET AL., 2003). Considering a single dredge haul, the inter-sample variability is usually higher than the 1σ intrasample one thus suggesting the equilibration length to be higher than the sample dimension (10-20 cm) but lower than the dredge length (<1 km).

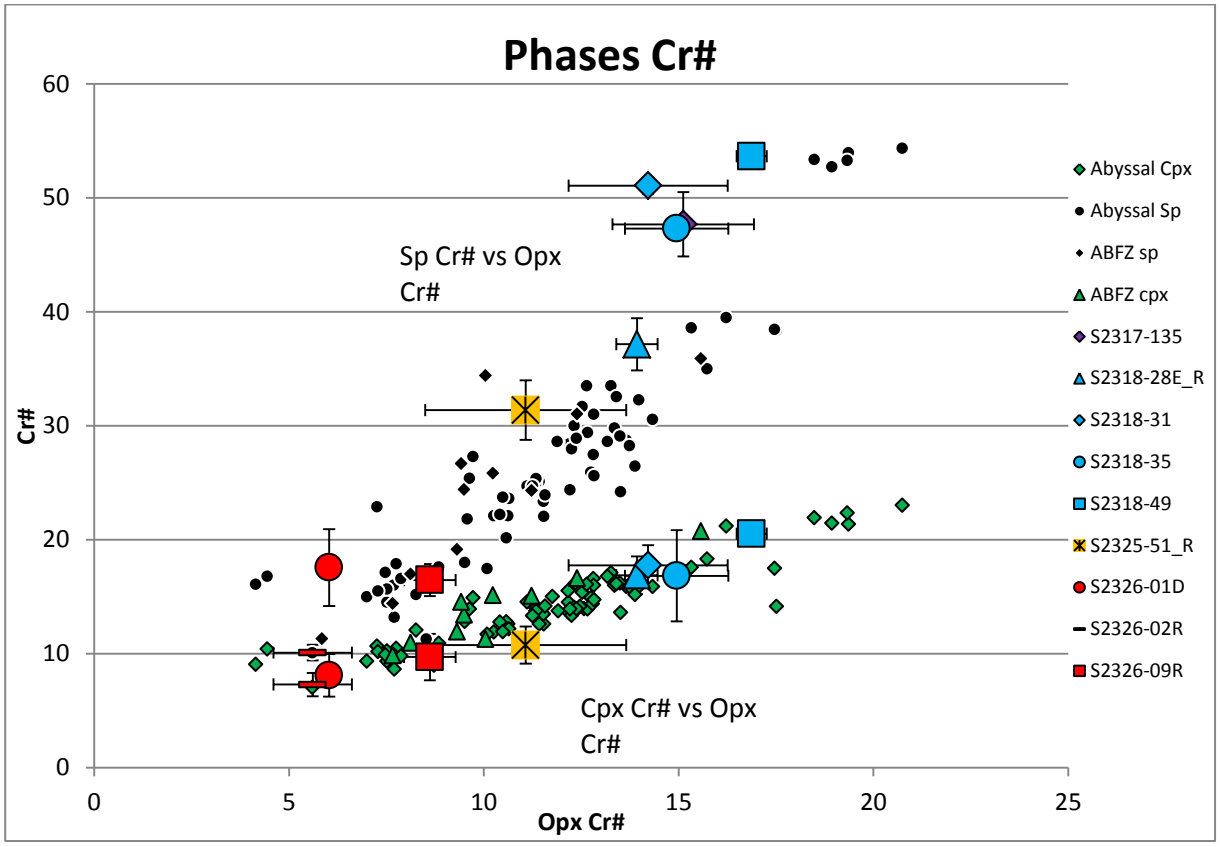

Figure 3.4.2 *– Orthopyroxene vs. spinel and clinopyroxene Cr-number [100 x Cr/(Cr + Al)] in plagioclase-bearing peridotites from ABFZ. Error bars represent 1σ variability at sample scale. Black dots are spinel Cr# of abyssal peridotites and green dots are cpx Cr# of abyssal peridotites.*

In figure 3.4.2, Cr# values from plagioclase-bearing peridotites are reported; values from mylonites have been omitted. Black dots are Cr# values of spinel peridotites from the abyssal peridotite record. Unlike spinel peridotites the mineral Cr# values in the plagioclase-bearing peridotites are more dispersed, especially concerning spinel Cr#. The intrasample 1σ variability is comparable to that observed for spinel field equilibrated peridotites.

However looking to the two-elements plot, as for instance the TiO_2 vs. Cr# for spinels (Fig. 3.3.3.2) it appears that samples from a single dredge define trends of progressive equilibration with plagioclase (and/or melt/rock interaction extent) where the single sample compositional fields are well separated. This suggests that even in the presence of a different equilibration process the equilibration lengthscale is probably comparable between the spinel and plagioclase equilibrated samples. The exception represented by dredge S2326, where Ti contents of grain rims span over the whole dredge variability of the related grain cores, attests for this dredge to represent an intermediate step toward re-equilibration possibly due to very low amount of melt in a cold thermal setting.

3.4.1 Equilibrium temperature of ABFZ peridotites

Temperature of equilibrium of ABFZ peridotites have been estimated using the geothermometer proposed by TAYLOR (1998), that can estimate equilibrium temperature using composition of clinopyroxene and associated orthopyroxene. In figures below results of equilibrium temperature are reported, for spinel peridotites and for plagioclase-bearing peridotites.

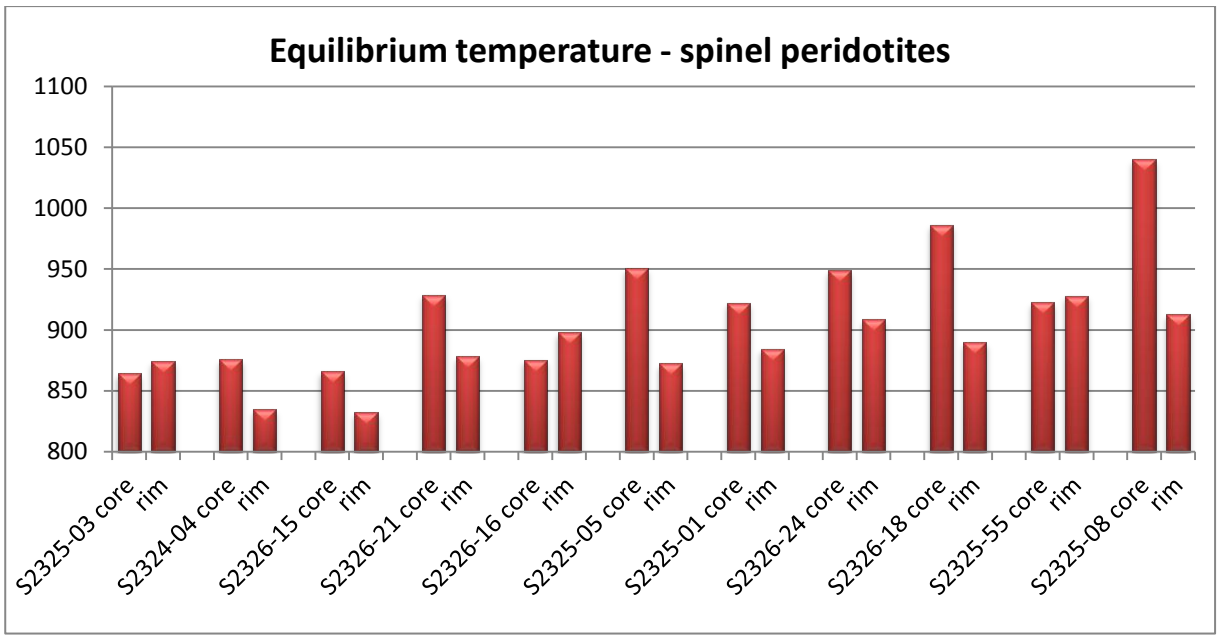

Figure 3.4.1.1 *– Equilibrium temperature of plagioclase-free peridotites computed in according to Taylor, 1998. The majority of the rocks shows a lower rim-temperature.*

Except samples S2325-55, S2325-03 and S2326-16, all spinel-peridotite samples show a lowering in temperature moving from core to rim. Core equilibrium temperatures range from ~850°C to ~1000°C.

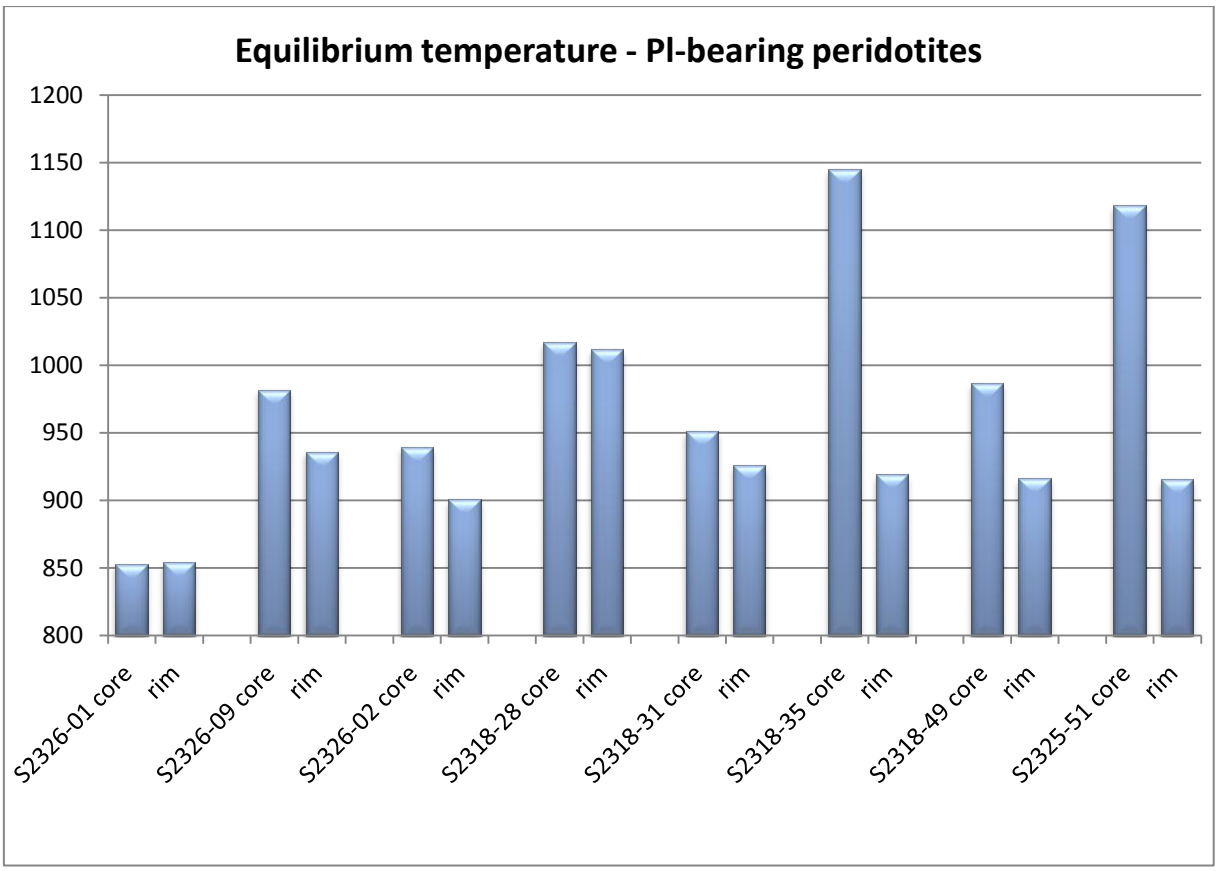

Figure 3.4.1.2 *– Equilibrium temperature of plagioclase-bearing peridotites computed in according to Taylor, 1998. The majority of the rocks shows a lower rim-temperature. The mean temperature of equilibrium is higher for plagioclase-bearing peridotites.*

Except sample S2326-01, all samples show a lowering in temperature moving from core to rim. Core equilibrium temperatures range from ~900°C to ~1150°C.

Plagioclase-bearing peridotites show equilibrium at slightly higher temperature compared to the spinel peridotites. In fact, looking at figure 3.4.1.3, except sample S2326-01, the mean values of thermal equilibrium for plagioclase-bearing peridotites appears to be higher with respect value of thermal equilibrium of spinel-peridotites.

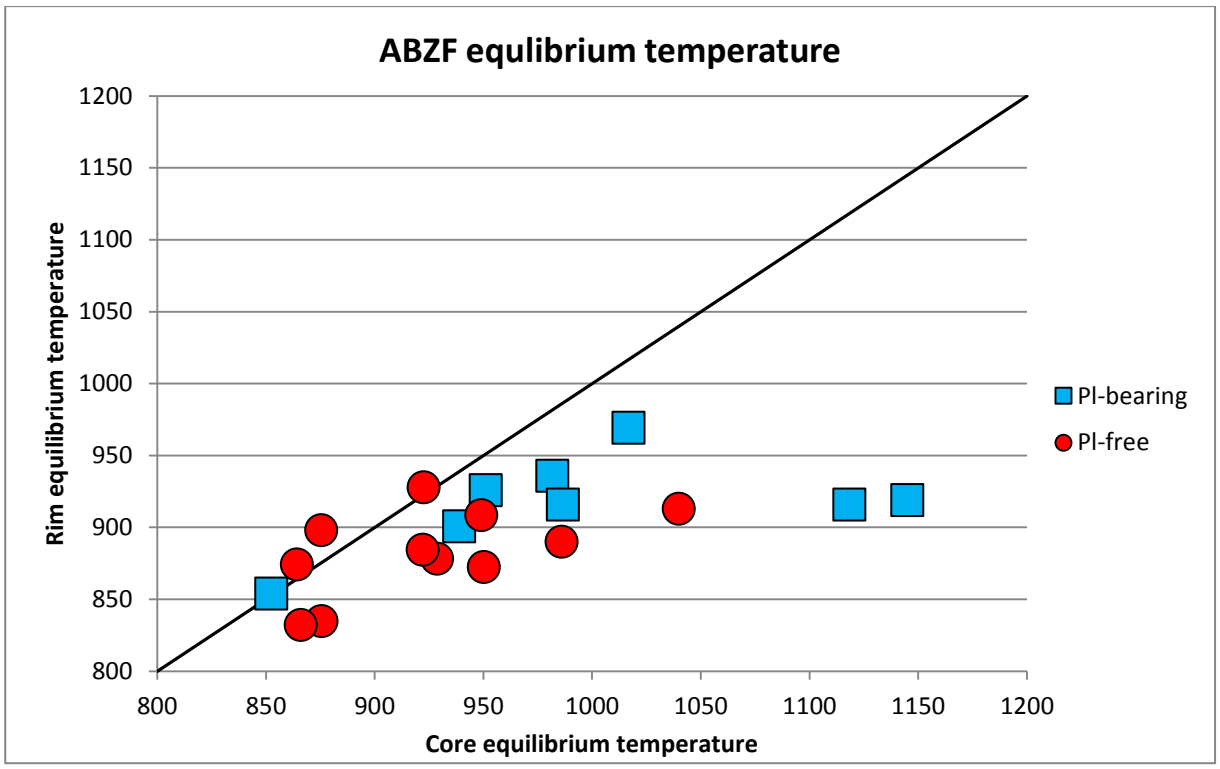

Figure 3.4.1.3 *– Rim-T vs. core-T. Red dots represent spinel peridotites, whereas blue squares represent plagioclase bearing peridotites. Figure shows that the majority of the sample is characterized by higher temperature for cores, and that plagioclase bearing peridotites seem to have equilibrated to higher temperature, although the number of samples is too small to be conclusive.*

In figure 3.4.1.3 it is possible also to see core/rim different equilibrium temperature. Samples fitting lower the right part of the plot represent samples where cores show a higher equilibrium temperature than the rims, and vice versa in the upper left corner. Moreover, samples from dredge S2326, even when plagioclase is present, show a core-rim behavior similar to their counterpart in the spinel-equilibrated peridotites, suggesting a cooling rate similar to the one shown by spinel peridotites. On the other hand, samples from dredge S2318 do not show such intense difference from core to rim concentration, suggesting a

more rapid cooling (or a shallower melt/rock interaction). This feature is strictly linked with the distribution and occurrence of plagioclase-bearing peridotites at ABFZ domain: all the peridotites sampled at the ridge axis are characterized by modal plagioclase, whereas plagioclase-bearing peridotites sampled at the transform wall are the minority. This can be explained by the occurrence of ancient and cold lithospheric contrasting the fracture zone: the enhanced cold-edge effect cools more the upwelling mantle close to the fracture zone. This can also explain what can be seen in previous graph: plagioclase-bearing peridotites, being characterized by modal plagioclase, need a shallower supply of melt to be percolated.

Chapter 4

Trace elements

4.1 Inter-laboratory calibration and setting of Modena LA-ICP-MS

Trace element data have been collected at the University of Montpellier 2 (France), with a Cameca IMS4F ion probe, and at Modena University with a Thermo Finnigan X-Series II ICP-MS coupled with a laser ablation system (LA-ICP-MS)

The Modena LA-ICP-MS was installed soon before the starting of the present thesis. In order to rapidly bring the probe to reproduce the values obtained by other international laboratories, I decided to perform a two step calibration:

1. Internal calibration: able to ensure high accuracy and low detection level based on a set of international standards.
2. External calibration: thought to build a reference curve for each element able to make each measured element comparable with a set of chosen laboratories worldwide.

To reach the first point a large number of test concerning spot size, fire frequency, laser power and helium flux have been performed based on standard reference material NIST 610, 612 and 614 (working values after PEARCE ET AL., 1997). All these tests are not reported here, they however allowed to define the correct operating procedures for the concentration range and matrix typical of the analysed material.

The resulting procedure is reported here: ICP-MS data have been collected using a 100 µm diameter pre-ablation beam for a period of 5 seconds and with a frequency of 2Hz. Laser fluency is about 25 J/cm^2. Once pre-ablation has finished, measurements starts with an 80 µm diameter ablation beam that works for a period of 30 seconds and with a fire frequency of 20 Hz. A flux of helium of 600 ml/min is used to transport ablated aerosol from laser ablation sample holder to the plasma torch. Plasma is produced by a flux of argon cooling gas of 13 liters/min plus an auxiliary flux of 0.9 l/min and a nebulizer flux of 0.8 l/min, using a RF power set up at 1400 Watts. Acquisition lasts 30 seconds during which the quadrupole analyses all the chosen analytes, changing potential configuration each 30 msec. These working conditions are mean values because the day by day instrumental tuning slightly differs. Machine tuning is performed by maximizing the ^{139}La and ^{232}Th signals, keeping oxides formations under 1%.

^{43}Ca	^{45}Sc	^{49}Ti	^{51}V	^{53}Cr	^{59}Co	^{60}Ni	^{65}Cu
^{85}Rb	^{88}Sr	^{89}Y	^{90}Zr	^{93}Nb	^{95}Mo	^{133}Cs	^{137}Ba
^{139}La	^{140}Ce	^{141}Pr	^{146}Nd	^{149}Sm	^{151}Eu	^{157}Gd	^{159}Tb
^{163}Dy	^{165}Ho	^{167}Er	^{169}Tm	^{173}Yb	^{175}Lu	^{177}Hf	^{181}Ta
^{182}W	^{205}Tl	^{208}Pb	^{232}Th	^{238}U			

Table 4.1.1 *– List of analytes calibrated for Modena ICP-MS.*

Evaluating the instrumental accuracy requires testing the reproducibility through time. Uncorrected measures over known standards have been followed to check for measure and error reproducibility. It appears that the overall temporal variability plots inside the 5% error around the expected value. For instance the typical 1σ error is 2.543 for Sr (equal to 3.23% relative error) and 1.337 for La (equal to 3.49% relative error), and 95% expected value plot inside the 5% error area.

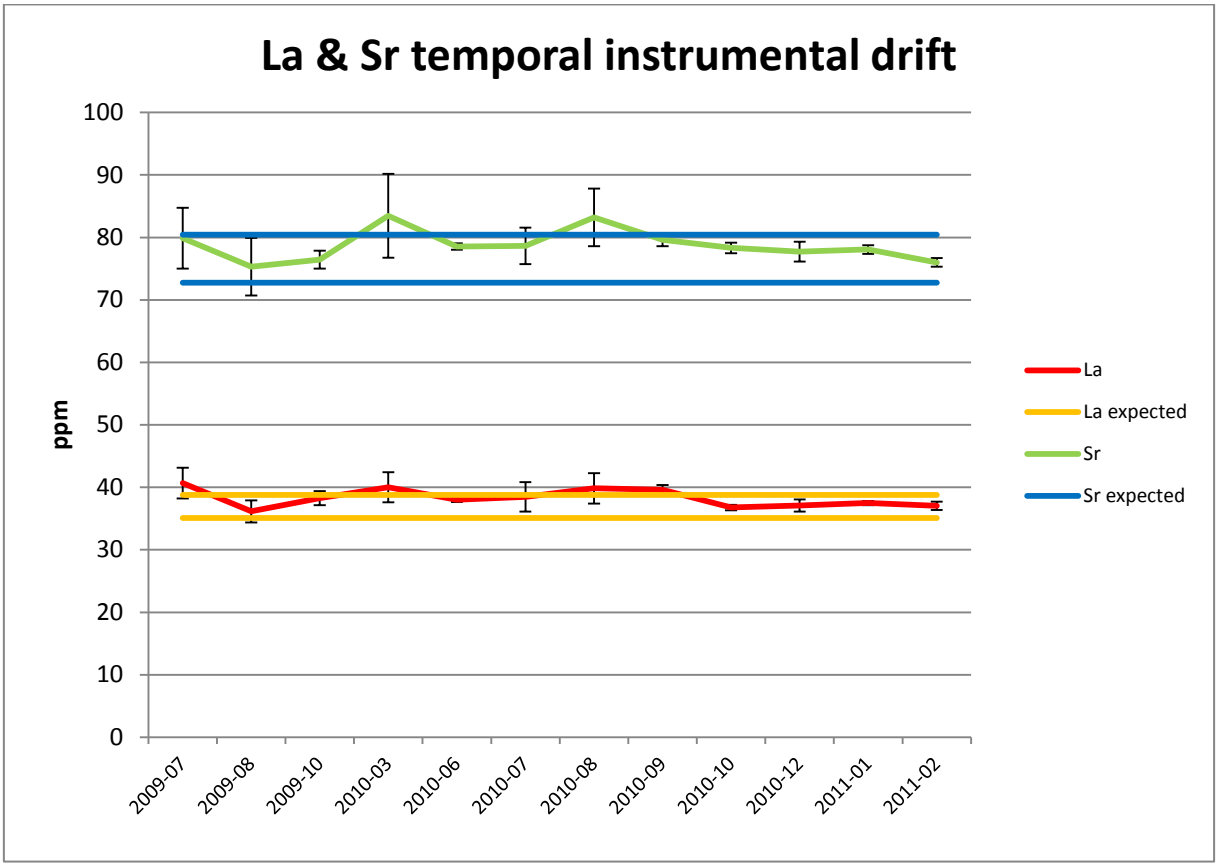

Figure 4.1.1 *– Uncorrected Sr and La temporal instrumental drift in Modena LA-ICP-MS. Mean values are value of STD NIST 612, with a tolerance of ±5%.*

The second point, i.e. the external calibration, has been reached by measuring a set of known basaltic, mafic and ultramafic materials. The samples have been chosen among a

collection of rocks analyzed at the laboratories of Lamont-Doherty Earth Observatory of Columbia University – New York, USA, University of Montpellier 2, France, University of Pavia, Italy, and Pisa CNR, Italy.

The rationale of our work has been to build a calibration curve able to correct the measured values to an interlaboratory calibrated concentration value. The curve for each element describes the yield of our instrumental configuration with respect to values obtained from the other selected laboratories. In this way we ensure to bring as close as possible the measured value on a 1:1 correlation with respect to the other labs. Example of the calibration curves are reported in following graphs, where only two of the total amount of 35 calibrated elements compare (the complete list of calibrated analytes is reported in Table 4.1.1). Dotted line represents the 1:1 correlation, while solid line is the regression curve that characterizes Modena instrument. Pearson product-moment correlation coefficient is also reported in figure. All data obtained with the instrument have been re-calculated based on the regressed equations.

Based on the reported curves it appears that at low concentration values the regression approaches 1:1. This is the region of interest of our sample set therefore telling the assumed correction is negligible for our data.

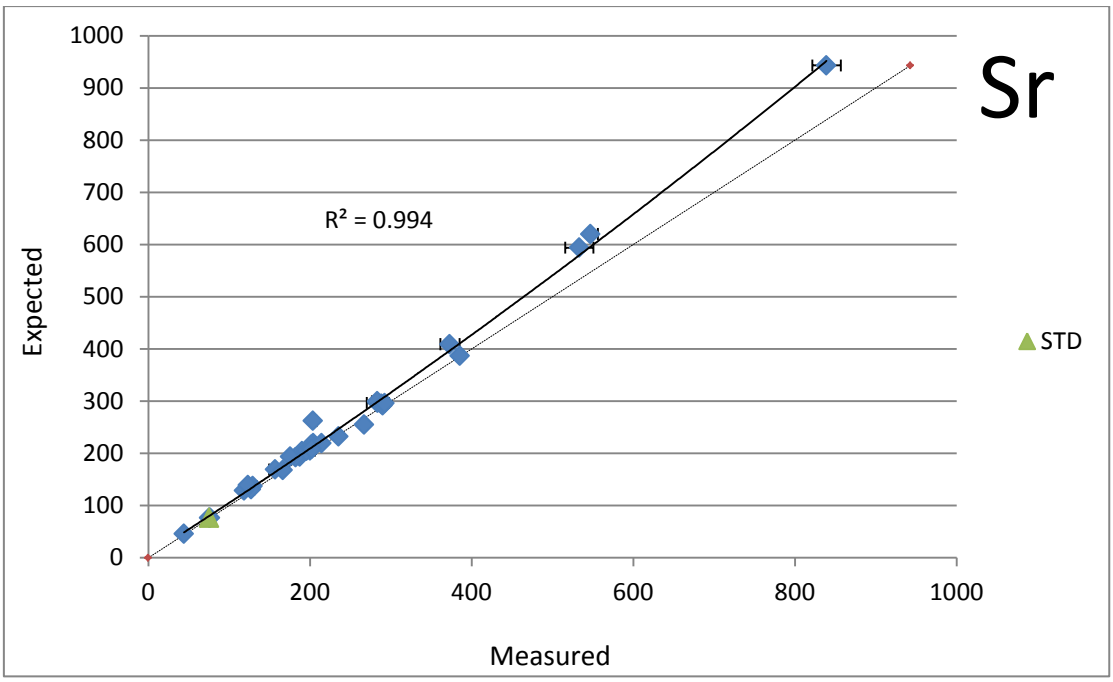

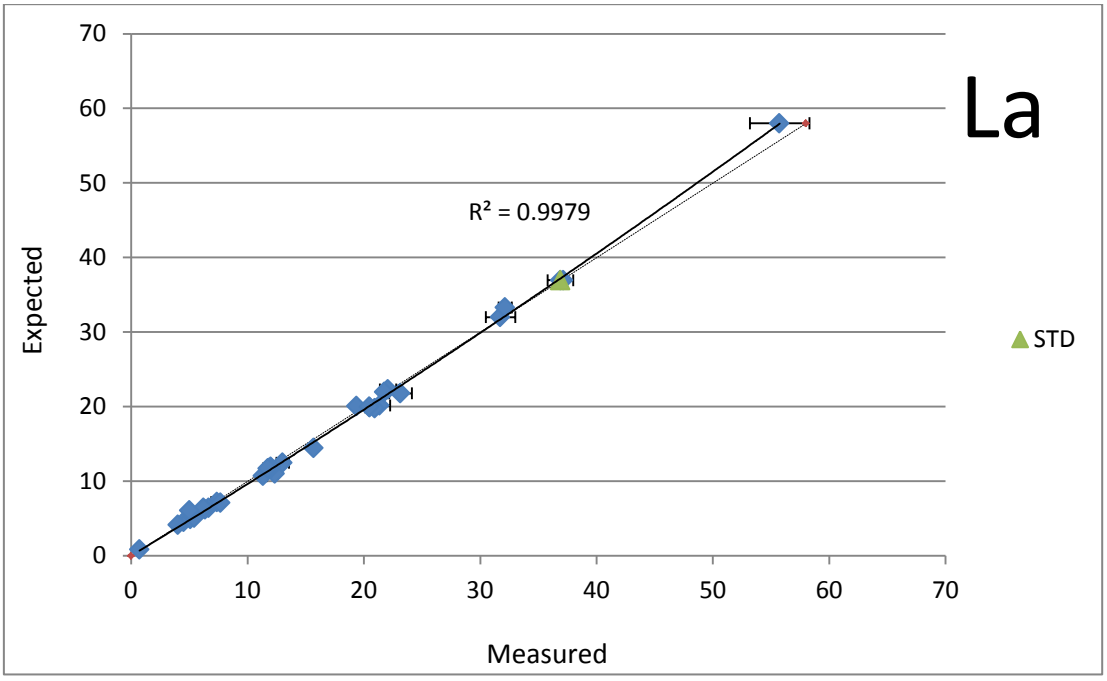

Figure 4.1.2 *– Sr and La calibration curves for Modena LA-ICP-MS. STD represents standard NIST 612 and each blue diamond represents a single analysis.*

Concerning SIMS analysis, samples and standards were polished to provide a flat surface for sputtering of secondary ions. Surface of samples was carbon-coated to prevent charging during SIMS. 19 species were analysed by secondary ion mass spectrometry (SIMS) on a Cameca IMS4F at the University of Montpellier 2 by Bernard Boyer.

Negative oxygen ions with an accelerating potential of 15 kV, were used as primary ions. A 20 nA O_2 primary beam was focused to sputter a 35 micron diameter flat-bottomed crater on the sample. Before collecting secondary ions, the surface was sputtered during five minutes in order to remove the carbon coating from the spot area. The surrounding carbon coating was enough to keep the surface from charging. Positive secondary ions for mass analysis were extracted with a 4.5 kV accelerating voltage. Secondary ions were detected by means of an electron multiplier operating in the ion counting mode. For the quantitative measurements of REEs, the energy filtering technique was adopted (SHIMIZU ET AL., 1978) with a 30 eV energy window, a high-energy offset of 80 eV, and fully open entrance and exit slits. This technique was adopted to overcome the problem of molecular interferences. Two different analytical methods are largely used: high mass resolution and high energy filtering. High mass resolution utilizes secondary ions with low initial kinetic energies, whereas energy filtering uses secondary ions with high initial kinetic energies. Energy filtering utilizes the fact that the energy distribution of molecular ions is much narrower than that of atomic ions, so the proportion of molecular species relative to atomic species decreases with increasing secondary ion kinetic energy. For low energy secondary ions, mass bias is very sensitive to the energy of the ion, and thus, high mass resolution analyses are very sensitive from sample charging. The use of energy filtering allows the mass spectrometer to be operated at low mass resolution, consequently simplify instrument tuning and stable analytical conditions can be achieved more easily with insulator samples. Each measurement consisted of a ten cycles routine where the magnet was cyclically peak-switched through the masses. Isotopes chosen to be measured in each spot consist of 25.7, 30Si+, 45Sc+, 47Ti+, 88Sr+, 89Y+, 90Zr+, 93Nb+, 137Ba+, 139La+, 140Ce+, 143Nd+, 147Sm+, 151Eu+, 159Tb+, 160Gd+, 163Dy+, 167Er+, 174Yb+, 175Lu+. They were analysed, in that order. 25.7 is an arbitrary dummy mass used to control the background of the counting system. The counting

time for each peak varied from 2 seconds to 40 seconds depending on intensity level for each specie and each analysis point. A cycle through the spectrum taking between 4 min and 12 minutes, and a complete measurement comprising ten cycles takes 4 minutes to two hours. Quantitative REE analysis requires both good standards and good calibration to convert the measured peak intensities into concentrations. NIST SRM 610 silicate glasses were used for the calibration of all elements. The working values are the one proposed by ROCHOLL ET AL. (1997). Measurements of NIST 610 glass were carried out under the same analytical conditions to obtain the secondary ion yields of all trace elements. Since the Si concentration of the NIST 610 glass standard and samples silicates is known from electron microprobe analysis, the 30 Si+ is used as an internal standard. The 3.1% isotopic abundance of the 30Si, allow increasing the dynamic of the system. The secondary ion yields of mass M were obtained by dividing M+ /30Si+ by the concentration of element of mass M in the standard. The secondary ion yields were determined after correction for detector dead time (30 ns). The precision of the yields is typically 5% at 1σ over one year on the NIST 610 standard. This precision, estimated by the reproducibility of M+ /30Si+ ratios, is larger than the error calculated by ion counting statistics and takes into account standard charging and non homogeneity, apparatus drift, detector efficiency etc. The trend of the yield variation, agrees well with that obtained by various authors. The average of these secondary ion yields was used to determine the element concentration. In spite of the energy filtering technique reduces the effect of most molecular interferences; monoxides can produce significant interferences, and have to be corrected. The intensity of an interfering oxide is dependent of the element concentration of the interfering oxide, its isotopic abundance, and the oxide-to-element ratios of the interfering species. In our study, 28Si, 29Si, 30Si isotopes combinations produce interference on 88Sr, 89Y and 90Zr, and seven REEs oxides produce significant interferences: 135BaO+ with 151Eu+, 143NdO+ with 159Tb+, 144 NdO+ plus 144 SmO with 160Gd+ , 151 EuO+ with 167 Er+, 160 GdO+ with 174 Yb+, 159TbO+ with 175Lu+. To determine the Si-isotopes-combination-to-element ratios, a pure industrial silicon wafer was measured. To determine the REE-oxide-to-element ratios used for the corrections, Drake and Weill REE glass standards were measured precisely. Detailed descriptions of the data

reduction procedure were presented by many authors (ZINNER & CROZAZ, 1986; BOTTAZZI ET AL., 1992, FAHEY, 1997). In addition to the uncertainty resulting of the counting statistics on the analyzed masses, correction for interferences contributes to an overall reduction in the precision of the data. The counting statistics of all of the interference masses must be taking into account in the final counting statistics. For the calculation and in addition of the counting statistics, an uncertainty of 10% relative for each oxide-to-element ratios is used. This typical uncertainty larger than the precision obtained on the Drake and Weill REE glass standards, takes into account small difference on samples and standard resulting of matrix and charging effect. The increase of uncertainty is amplified for sample with high LREE/HREE ratios.

Data for this work has been produced in two of the previously mentioned labs (Montpellier 2 and Modena). The external calibration previously described would ensure the interlaboratory bias to be negligible. We verified the inter-laboratory analytical bias by checking all analyzed elements on a set of natural samples in both labs. As an example lanthanum values obtained in the two labs are reported in figure 4.1.3. It appears that values are on a 1:1 correlation in the 1 sigma variation well inside the 95% confidence bands.

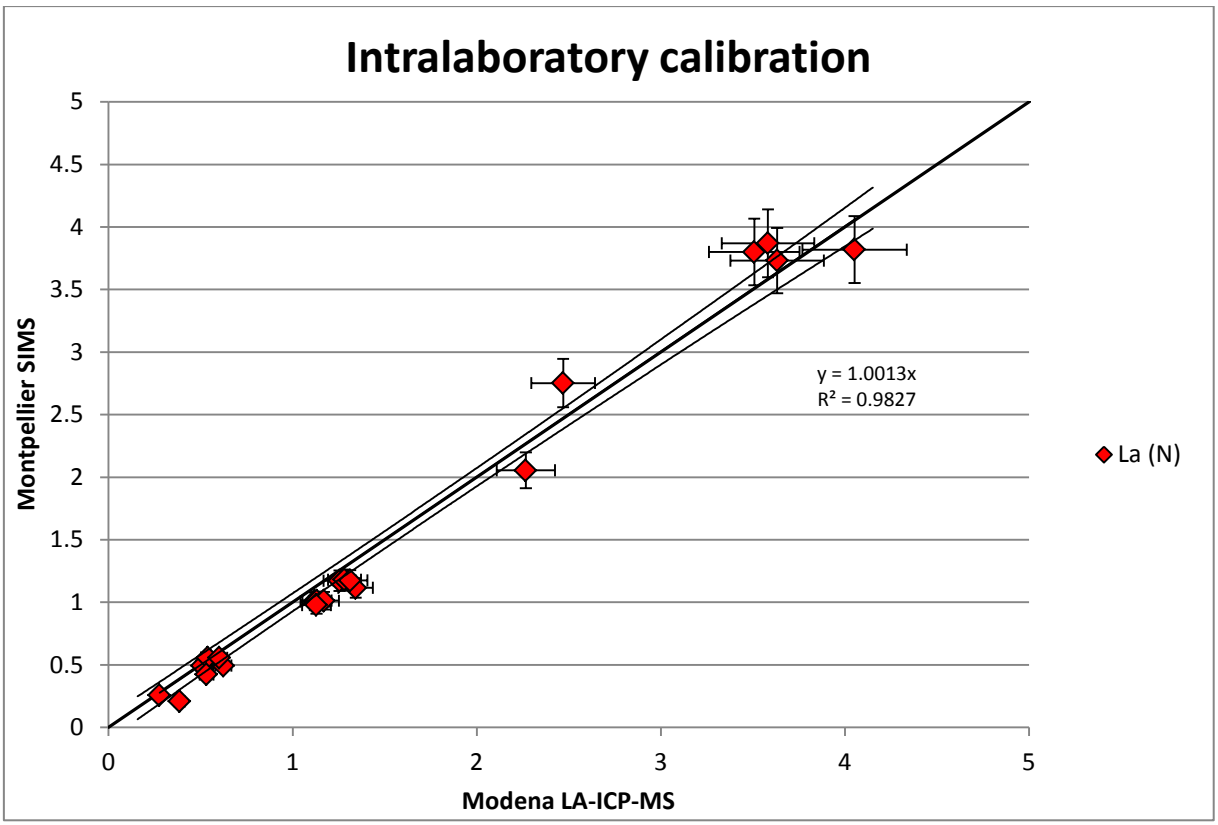

Figure 4.1.3 *– Inter-laboratory calibration curve for La concentrations. X-axis represents analysis done with Modena LA-ICP-MS, and Y-axis represents analysis done with Montpellier 2 SIMS. Each red diamond represents a single cpx analysis. Pearson product-moment correlation coefficient is also reported.*

4.2 Spinel-peridotites

For each clinopyroxene, at least six spots (three cores and three rims) have been performed. Concentrations represent the mean value for each sample. Error bars represent the 1σ intra-sample variability. In the following graphs, all concentration values have been normalized to chondrite composition (ANDERS & GREVESSE, 1989).

Samples do not show a significant variability from core to rim, suggesting all phases are equilibrated for the trace element analyses at the grain scale.

Extended trace element patterns are widely used as petrological tool being easily relatable to the total amount of partial melting, the depth extent of the melting column, the nature of the process (e.g. fractional vs. batch) and any possible metasomatic event affecting the system (JOHNSON ET AL., 1990; JOHNSON & DICK, 1992; HELLEBRAND ET AL., 2002). For instance melt retention following a near-fractional melting has been detected based on REE patterns by BRUNELLI and coworkers, 2006. The pattern morphology and relative fractionation among light and heavy REE also return information on selective fractionation due to progressive diffusion-controlled equilibration of transient melts with the host rock, a process known as chromatography (NAVON & STOLPER, 1987; VERNIERES ET AL., 1997; SUHR ET AL., 1999).

Extended trace element concentration patterns of ABFZ samples are characterized by negative Ti, Sr and Zr anomalies even though with variable extents (Fig. 4.2.1) a feature already described for abyssal residual pyroxenes (JOHNSON ET AL., 1991).

All other elements are difficultly orderable in a general trend even though the majority of the samples shows a general decrease of the L-REEs and a weak decrease even for the H-REEs moving from the intermediate REEs on. This weak to marked hump shape has been usually interpreted as garnet signature in several works (e.g. JOHNSON ET AL, 1990; HELLEBRAND ET AL, 2003).

To try distinguishing and ordering the different patterns, rare earth element (REE) spider along with element ratios diagrams have been used.

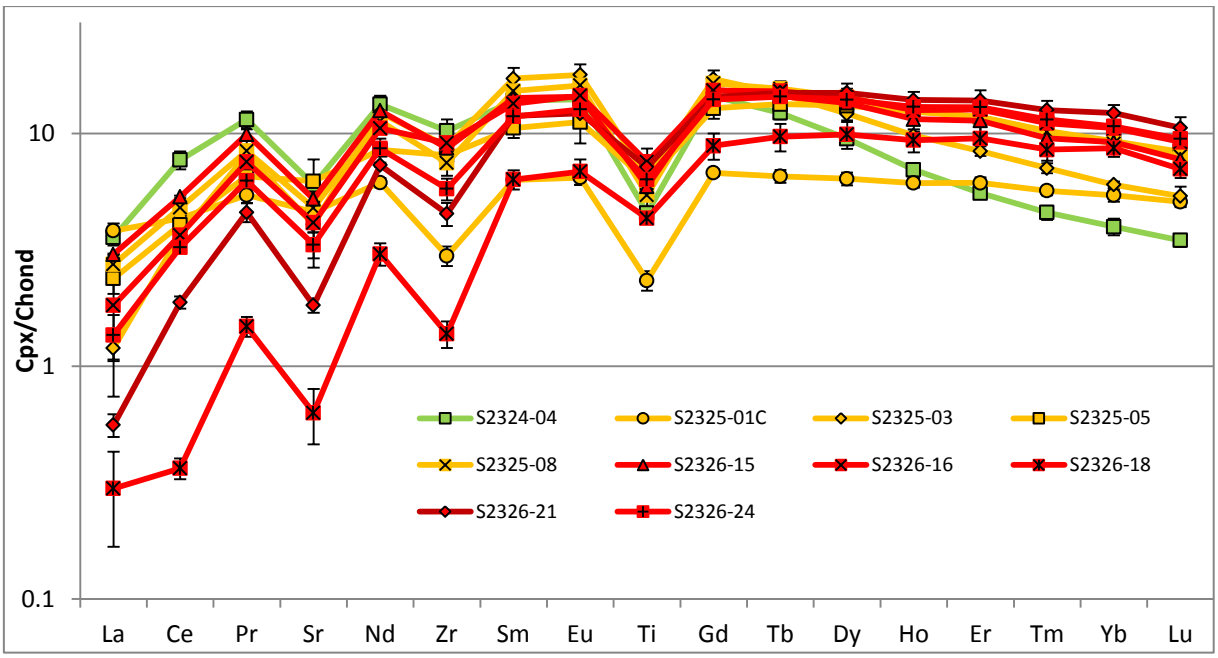

Figure 4.2.1 *– Extended trace element spiderdiagram for spinel peridotites. Samples are color coded by dredge: green S2324, yellow S2325, red S2326.*

A normal way to describe trace element behavior is to group the different samples based on "morphological" criteria, meaning grouping together all samples showing similar patterns, or alternatively, grouping those patterns reproducing the expected variation for a known process as, for instance, fractional melting. In this case an increase of LREE fractionation (depletion) with respect to HREE by progressing the melting process would be expected. However, our patterns form a bundle with no evident internal coherence. A better image results by separating the two lower concentration patterns (S2326-18 and S2325-01C). The remaining samples then show a minimum scatter around the Eu-Gd position, i.e. the intermediate REEs, while the heavier and the lighter REEs are strongly scattered (Fig. 4.2.2). An order can be anyway found being the patterns with highest heavy REE contents the ones showing the depleted-most light-REEs contents. For instance, sample S2324-04 shows the lowest concentrations in H-REEs (about 4 x Chond) and, at the same time, the highest L-REE concentrations (about 5-9 x Chond); while sample S2326-21 shows the highest H-REE

concentrations (about 11 x Chond) and, at the same time, the lowest L-REE concentrations (about 1 x Chond). Let's call this samples group as A-group.

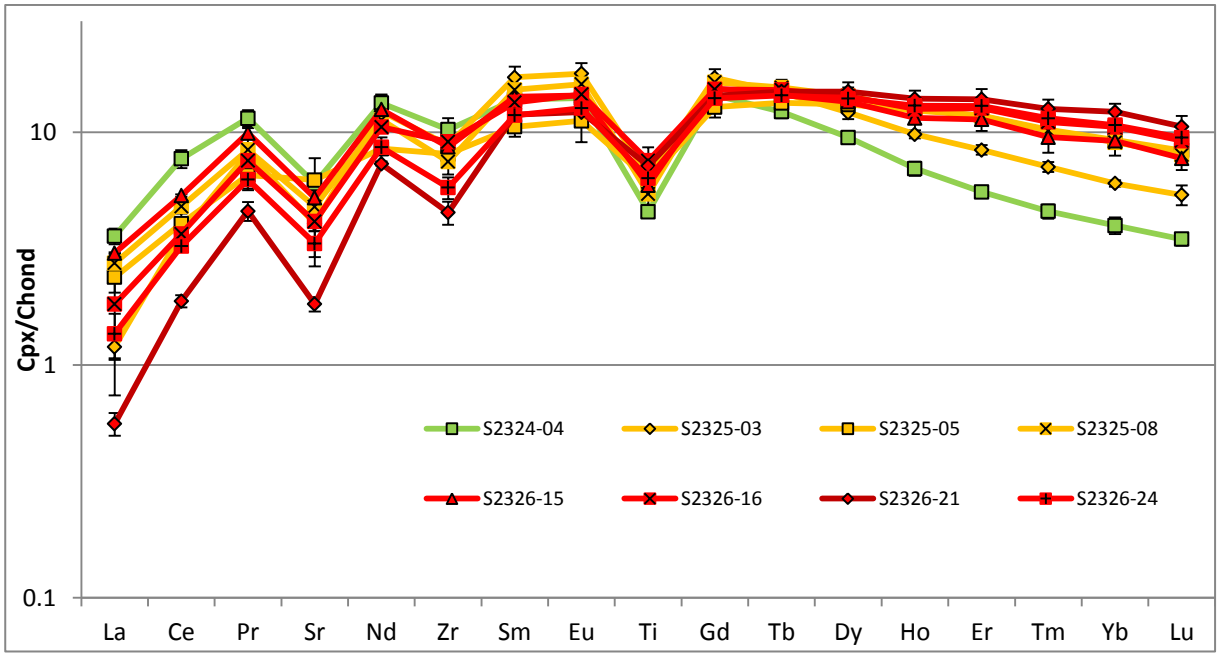

Figure 4.2.2 *– Extended trace element spiderdiagram for Group A spinel peridotites. Samples are color coded by dredge: green S2324, yellow S2325, red S2326. Samples S2326-18 and S2325-01C have been removed from figure to focus on the remaining samples.*

This behavior is well readable in a $Sm_{(N)}/Yb_{(N)}$ vs $Yb_{(N)}$ diagram (Fig. 4.2.3), where the A-group samples are aligned along a trend plotting at high angle with respect to the near-fractional expected melting trend (black line) for abyssal peridotites experiencing melting in the garnet (grt) and spinel facies (HELLEBRAND ET AL., 2002; BRUNELLI ET AL., 2006). This behavior is similar to the one described by SEYLER ET AL. (2011) for the eastern SWIR.

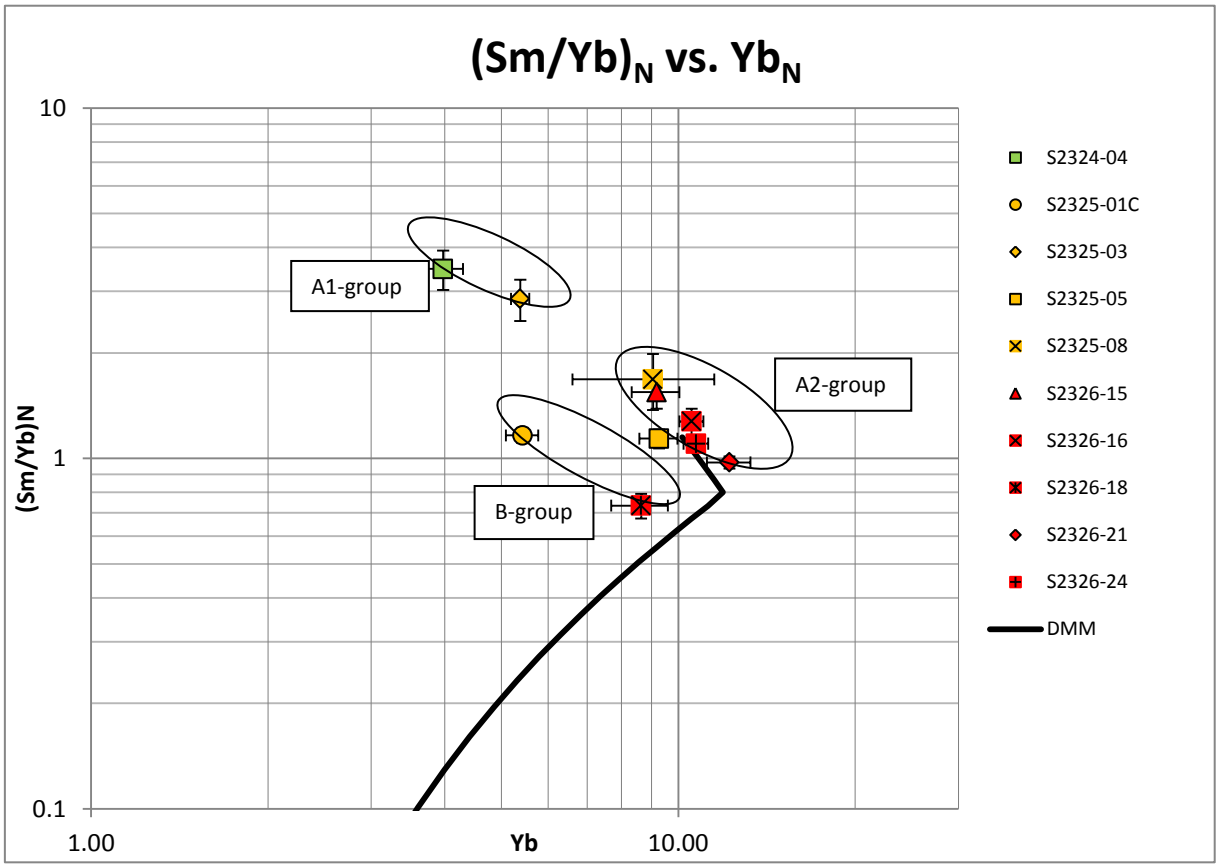

Figure 4.2.3 *– $Sm/Yb_{(N)}$ vs. $Yb_{(N)}$ for spinel-equilibrated peridotites. Errors bars indicate 1σ variability at sample scale. Black line indicates the near-fractional melting trend from a DMM for abyssal peridotites experiencing melting in the garnet facies (4%) and spinel facies.*

Looking at this diagram, A-group can be divided in two different sub-groups, according to the different Sm/Yb ratio: group A1 (Fig. 4.2.4) constituted by samples S2324-04 and S2325-03, samples that show a hump-shaped REEs pattern, and the remaining samples forming group A2, showing a less enhanced hump-shaped pattern (Fig. 4.2.5). Looking at these REE patterns, it is possible to see that A1-group samples cross each other at Nd and Sm concentrations, while A2-group samples cross each others around Tb and Dy.

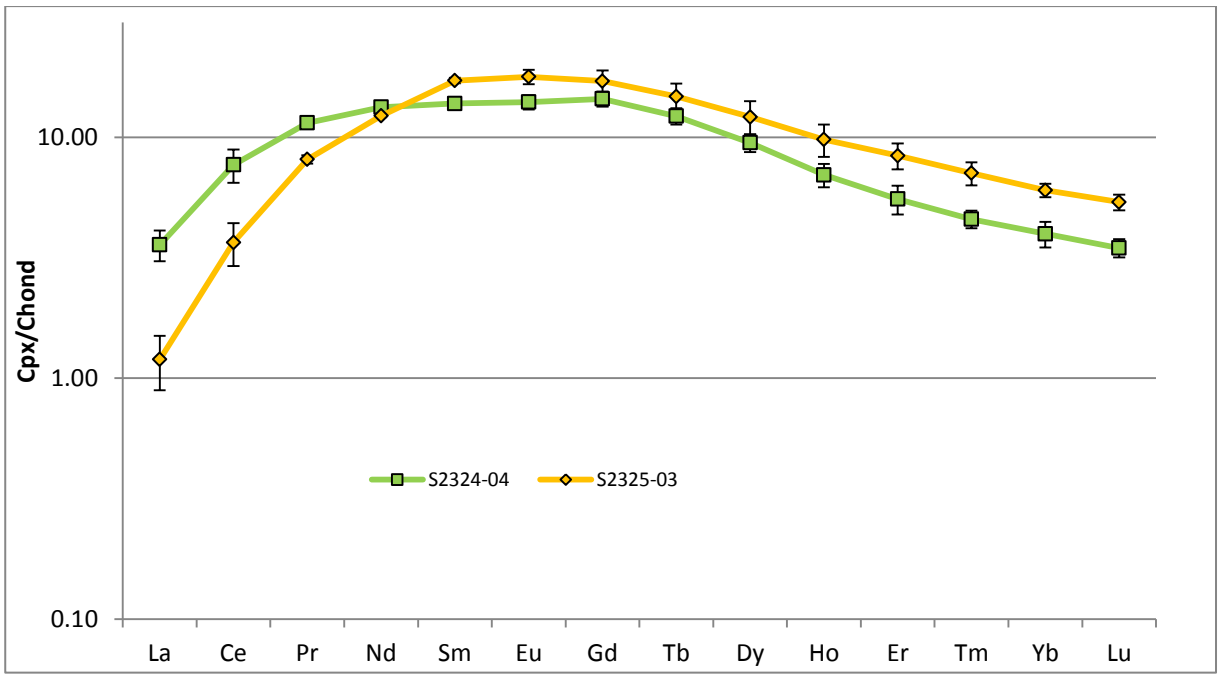

Figure 4.2.4 *– A1-group REEs patterns. Samples show an enhanced hump-shaped pattern and the two patterns crosscut each other at about Nd position. Errors bars indicate 1σ variability at sample scale.*

A1 patterns are characterized by a marked hump in the intermediate REEs (figure 4.2.4; samples S2324-04 and S2325-03) and a relative depletion of L-REE and H-REE. The samples that show this pattern are the richest in Cr_2O_3 content in both opx (0.88%) and cpx (1.85%) and the richest in Na_2O content in cpx (1.7%). Concerning spinels, they have the lowest Ni content (0.15%) and one of the higher Ti content. Similar patterns have been described by HELLEBRAND ET AL. (2003) and by SEYLER ET AL. (2011). Although A1 samples seem to be strictly linked to A2 group, in next chapter modeling will tell if they actually belong to this trend or if they can be explained by different computation condition.

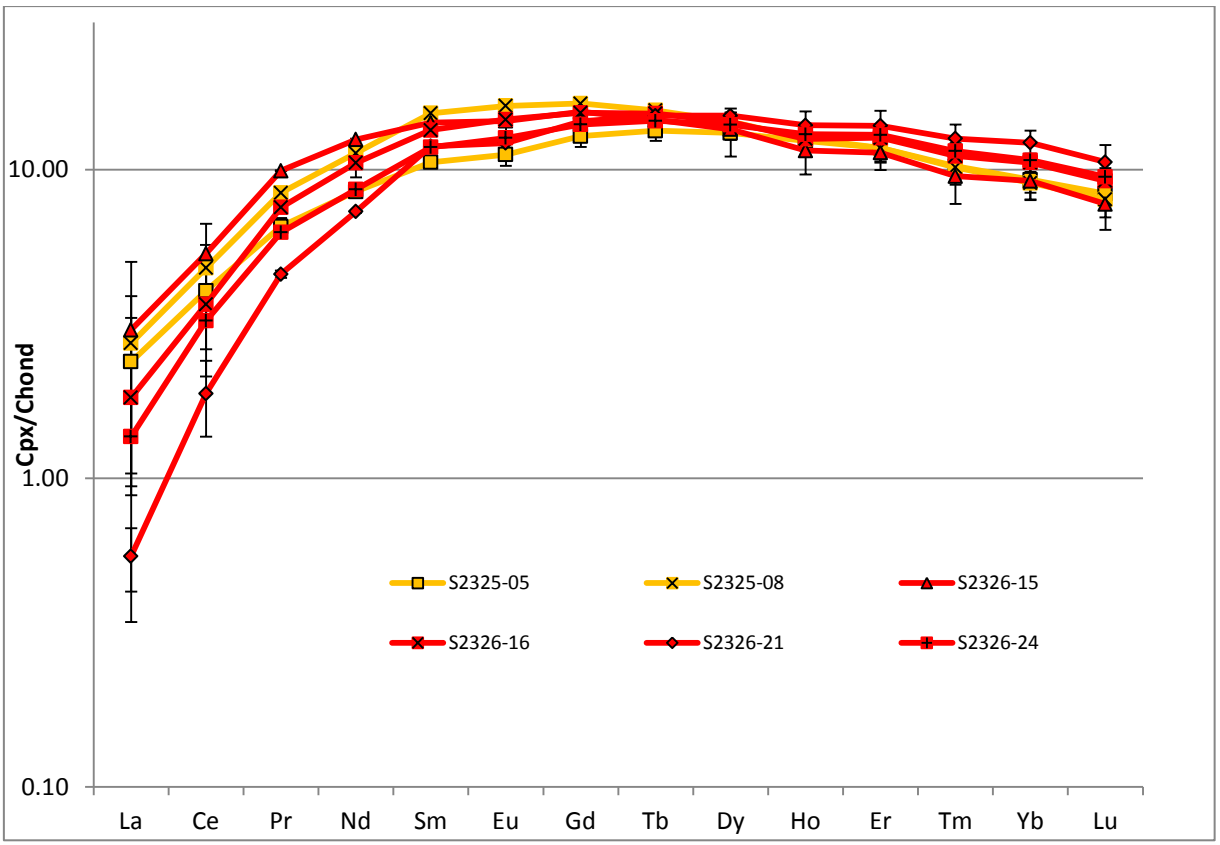

Figure 4.2.5 *– A2-group REEs patterns. Samples show a weak hump-shaped pattern and the patterns crosscut each other at about Tb-Dy position. Errors bars indicate 1σ variability at sample scale.*

A2-group samples present major element concentrations characterized by intermediate values between A1-group samples and sample S2326-21, that shows the lowest Cr# value in cpx, the lowest Cr# value in spinel and the highest NiO content value in spinel.

Looking again at the $Sm_{(N)}/Yb_{(N)}$ vs $Yb_{(N)}$ diagram (Fig. 4.2.2), it is possible to link also samples S2326-18 and sample S2325-01C by a trend sub-parallel to the one characterizing A-group. We define these two samples as B-group. Their REE patterns crosscut each other at Sm-Eu position (Fig. 4.2.6).

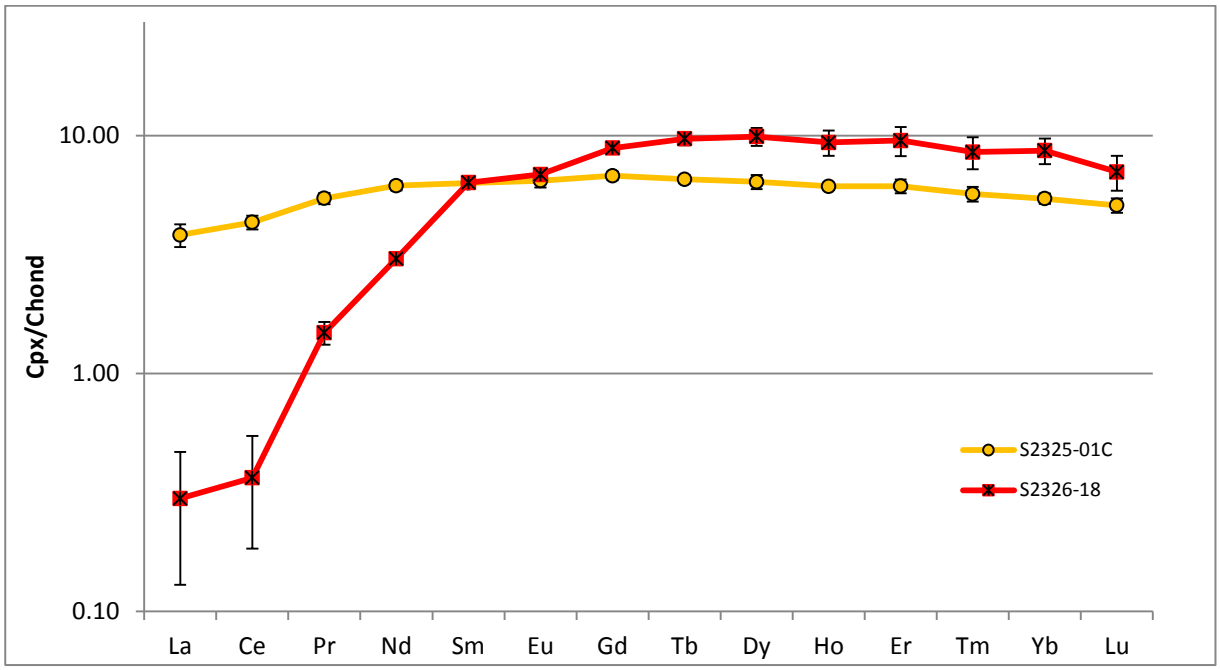

Figure 4.2.6 *– B-group REE patterns of samples S2326-18 and S2325-01C. Errors bars indicate 1σ variability at sample scale.*

Sample S2325-01C is characterized for the extremely low abundance of Ti: Ti contents in opx are the lowest (0.05%), same in cpx (0.15%) and in sp (0.05%), while opx from S2325-01C are among the most enriched in Ca (1.5%). Sample S2326-18 is the only sample which plots the compositional fields of abyssal and SWIR peridotites in the Na_2O vs. TiO_2 diagram. It shows also the highest Ca content in opx.

The groups that have been found show also a common behavior in Cr# values for all the analyzed mineral phases. In A-group, S2325-21 sample is characterized by the lowest Cr# values, that increase moving to S2324-04 sample, that shows its highest content. Also in B-group, the sample that is close to the near-fractional melting curve show the lowest Cr# value, that increases moving away from the melting curve (diagrams in figures 3.2.2.1, 3.2.3.2 and 3.2.4.1). Same behavior is also shown by Ni content in spinel, Ni content that

decreases moving away from melting curve (Fig. 3.2.4.3). An opposite trend is shown by Al and Ti contents in pyroxenes: samples S2326-21 and S2326-18, that are respectively A-group and B-group closest samples to the melting curve, are characterized by the highest contents in Al, Ca and Ti. These element concentrations progressively decrease moving away from the melting curve (figures 3.2.2.1, 3.2.2.3, 3.2.3.2, 3.2.3.3). Na behavior is not completely clear: it increases moving away from the melting trend, but samples S2325-08 and S2326-15 show a sodium content that is slightly lower with respect to the sample S2326-21 one (Fig. 3.2.3.3).

This way of grouping the trace element patterns although counterintuitive is justified by the existence of trends in the $(Sm/Yb)_{(N)}$ vs. $Yb_{(N)}$ diagram that move REE concentrations outside theoretical residual compositions.

As a result the chosen groups show trace element patterns characterized by a rotation around a mid-point situated on a specific REE for each group. Group A1 patterns characterized by a pronounced hump in the L-M REEs region rotate around the Nd position. Group A2 samples rotate around the Tb-Dy position. They are characterized by a less pronounced hump affecting the intermediate REEs. Group B patterns rotate around Sm position, however they show a strong difference in the pattern morphology, being the group characterized by a near-flat pattern and by a residual-like pattern.

Observed trends are in general not relatable to known models of deep processes, as depletion by partial melting and melt extraction. Exploring its viability by other processes is the goal of next chapter.

4.3 Plagioclase-peridotites

Plagioclase-bearing peridotites from ABFZ seem to be less heterogeneous than associated spinel peridotites. Trace element concentrations show concentration anomalies for Sr, Zr and Ti, and also concerning Eu, as expected for cpx being equilibrated with plagioclase. Looking at M-REEs and H-REEs, concentrations show a range of distribution of one order of magnitude, spanning from 7 x Chond to 26 x Chond. The two dredge fields are well separated.

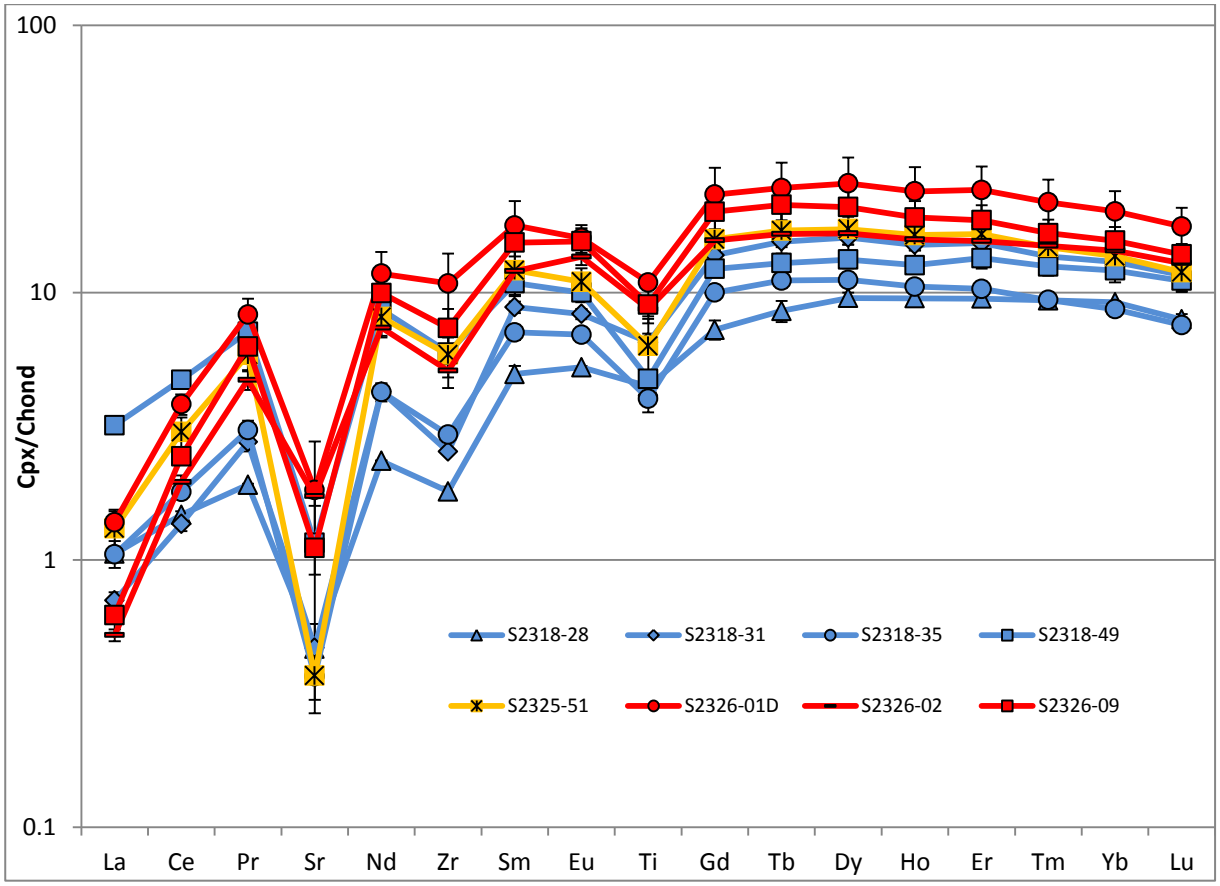

Figure 4.3.1 *– Extended trace element spiderdiagram for plagioclase-bearing peridotites. Samples are divided by dredge: blue S2318, yellow S2325, red S2326.*

Looking at the REE patterns, it is possible to distinguish two different groups, although compositional variations in plagioclase peridotites are less marked than in spinel peridotites. Each group represents a different dredge: group 1 (Fig. 4.3.2) is constituted by dredge S2326 samples, where samples show high chondritic concentrations for almost all the REEs, values that cannot be obtained considering only a fractional melting process, although curves show a depletion in L-REE with respect to M-REE and H-REE. The strong enrichment of these rocks is well marked looking at the $Sm/Yb_{(N)}$ vs. $Yb_{(N)}$ graph (Fig. 4.3.4), where group I samples occupy an area that is completely out from the melting curve. A weak or none Eu anomaly is commonly present and group 1 shows subparallel patterns.

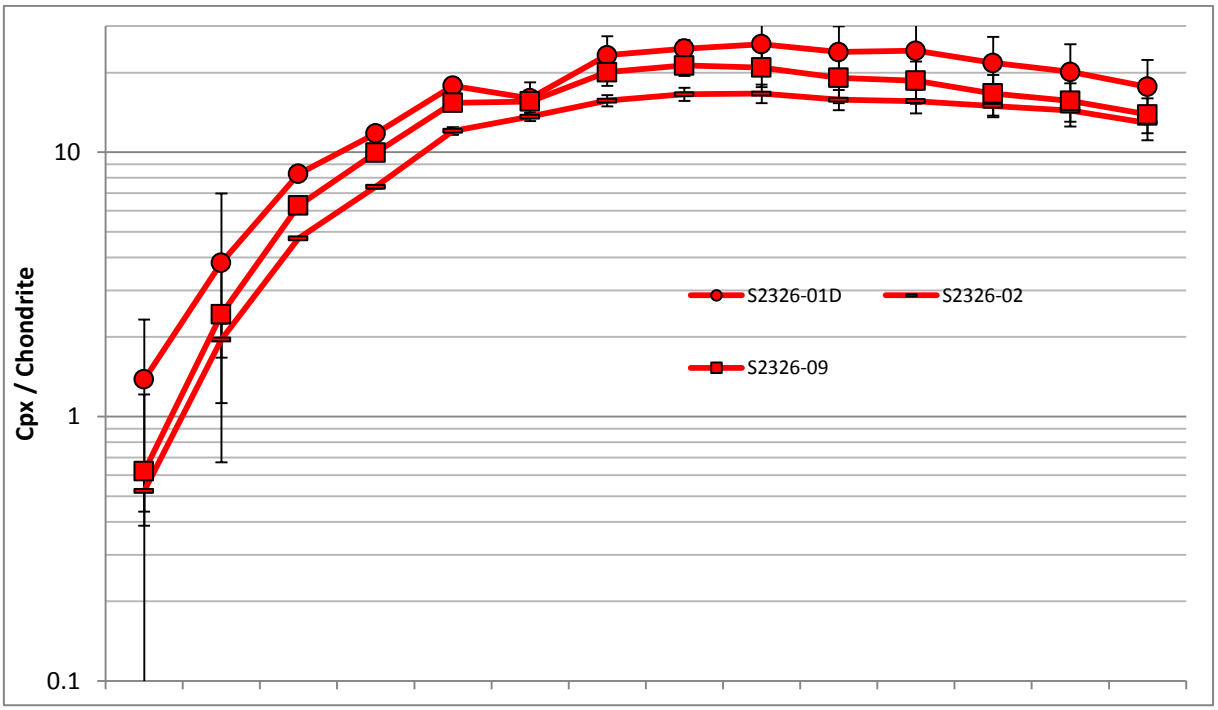

Figure 4.3.2 *– REE spiderdiagram for plagioclase-bearing peridotites. Group I.*

Group 2 (Fig. 4.3.3), on the other hand, appears to be more heterogeneous. While it is possible to observe Eu anomaly, as in Group 1, a general trend is, again, a depletion in light

REEs with respect to the heavy and medium REEs, but the extent of this fractionation seems to be very variable. In fact, samples seem to be arranged in two sub-groups when looking at $Sm/Yb_{(N)}$ vs $Yb_{(N)}$ diagram (Fig. 4.3.5).

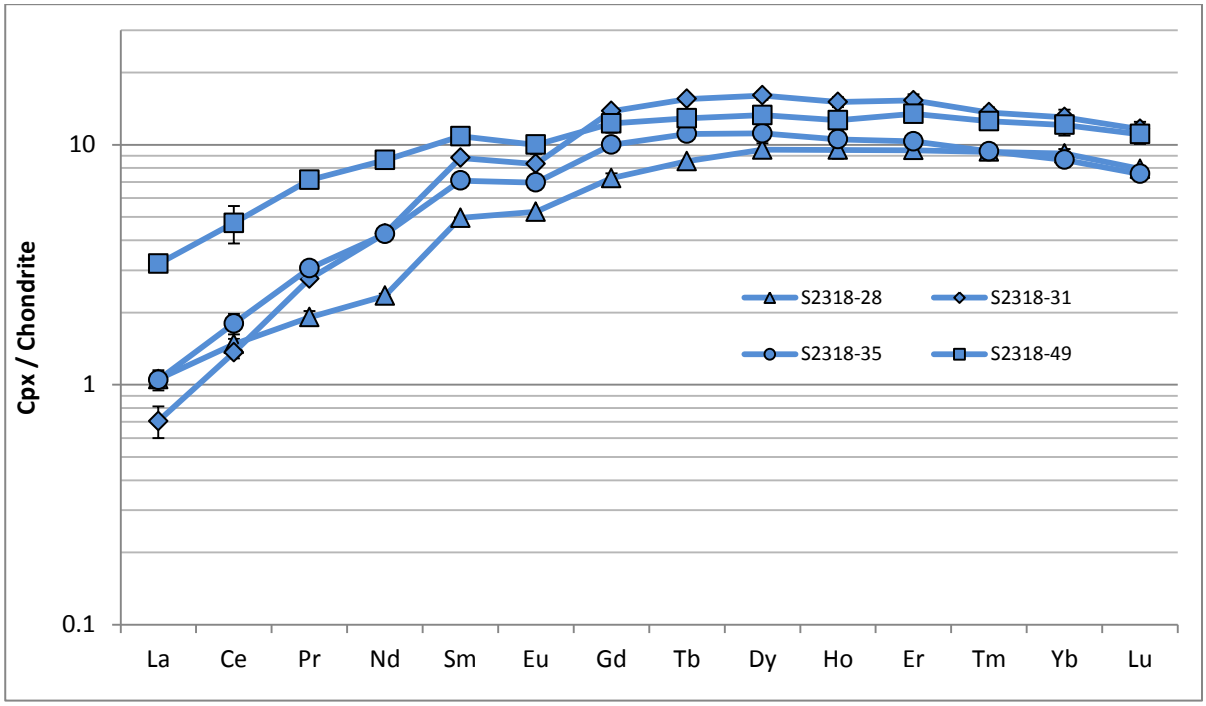

Figure 4.3.3 *– REE spiderdiagram for plagioclase-bearing peridotites. Group 2.*

Concerning major element concentrations, group 1 shows the lowest Cr# values for all the analyzed mineral phases, while shows higher Ti and, less marked, Na concentrations in cpx with respect to group 2. Ti content in spinels is lower in group I, and very high in group II. Moreover, opx from group I shows lower values in Ca content.

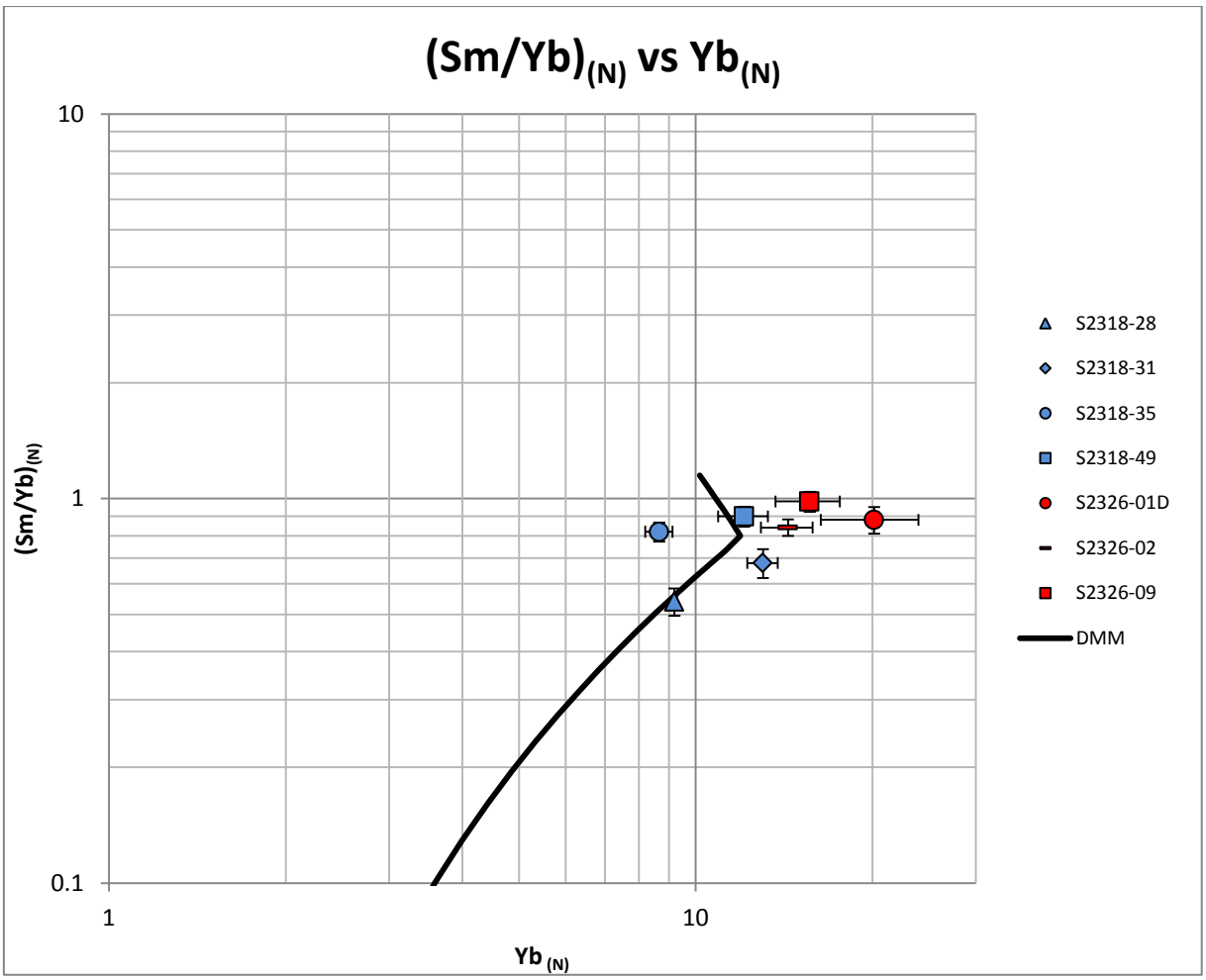

Figure 4.3.4 *– $Sm/Yb_{(N)}$ vs. $Yb_{(N)}$ for plagioclase-bearing peridotites. Errors bars indicate 1σ variability at sample scale.*

4.4 Mylonites

Sample S2325-51 closely resembles sample S2325-55, a spinel-peridotite mylonite. Nevertheless, looking at REE spiderdiagram (Fig. 4.3.3), they strictly resemble one each other both differing from other samples: concerning H-REEs and L-REEs, they show almost the same concentration, and slightly different concentrations looking at M-REEs. Moreover, sample S2325-55 spinels are characterized by a high content in Ti (up to 0.4 wt%), suggesting plagioclase to be present, as already seen in previous chapter. These observations suggest they both pertain to a common group, possibly representing rocks that have been impregnated but also homogenized during mylonitization.

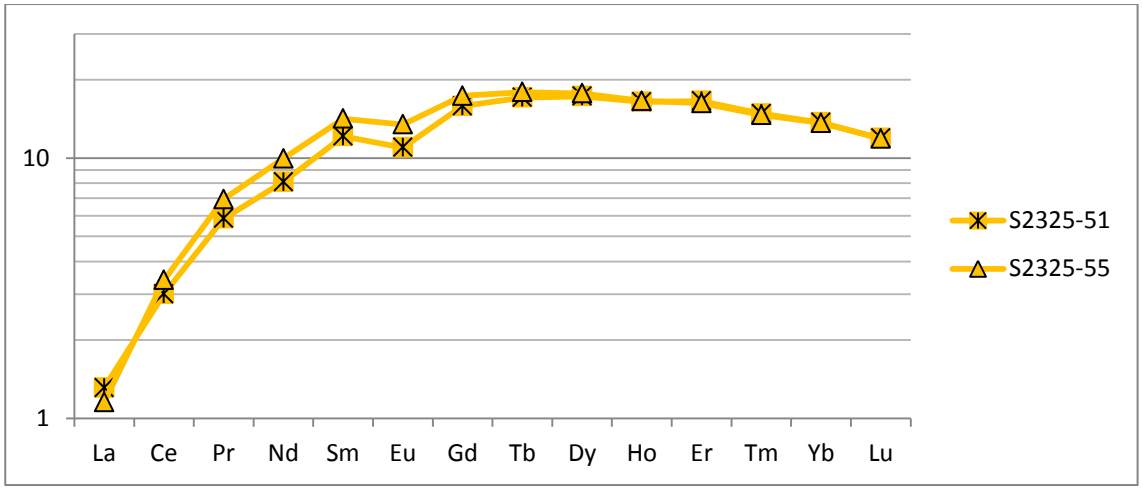

Figure 4.3.3 *– REE spiderdiagram for mylonitc samples, S2325-51 and 55.*

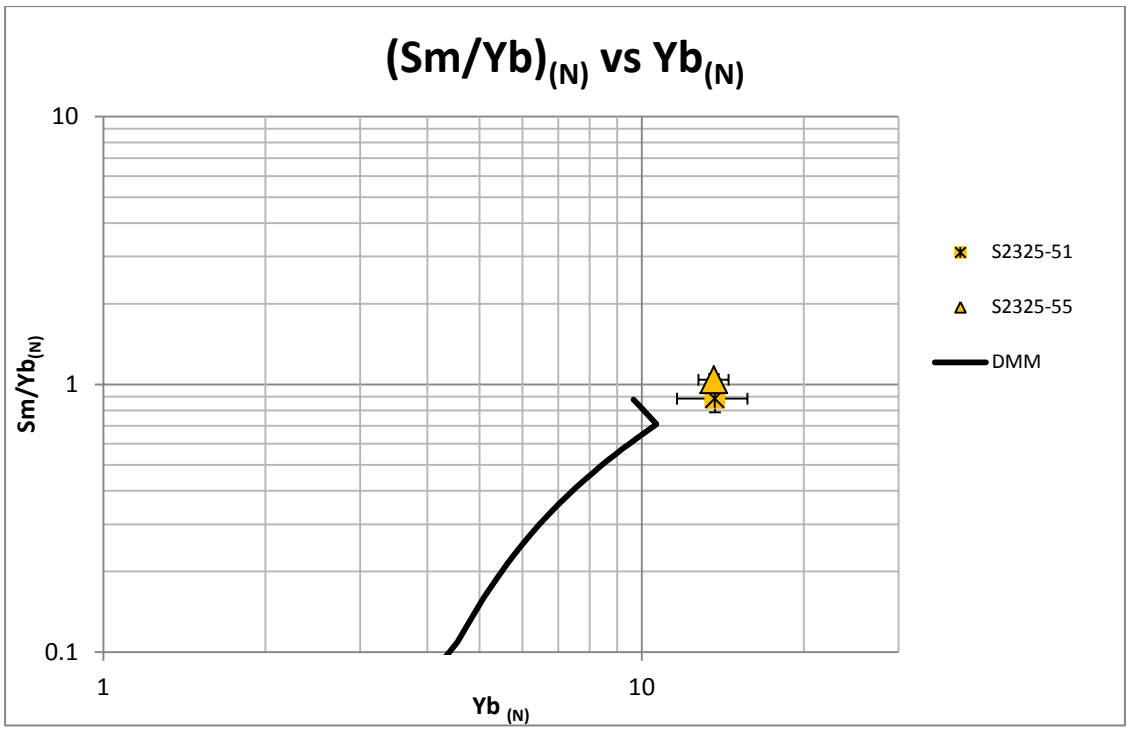

Figure 4.3.3 *– $Sm/Yb_{(N)}$ vs. $Yb_{(N)}$ for mylonitic samples. Errors bars indicate 1σ variability.*

4.5 Concluding remarks

1. Spinel-bearing peridotites and plagioclase-bearing peridotites show well marked differences in trace element contents, reflecting their modal differences by the occurrence of plagioclase.
2. Spinel equilibrated peridotites show trace element normalized patterns characterized by marked humps in intermediate REEs. They can be grouped on the base of the trends shown in the $(Sm/Yb)_{(N)}$ vs. $Yb_{(N)}$ diagram that correspond to a rotation of the patterns around a defined mid-point. The samples showing the highest contents in H-REEs show the lowest contents in L-REEs and vice versa. A1-group patterns appear to rotate around Nd position, A2-group patterns appear to rotate around Tb-Dy position and B-group patterns seem to rotate around Sm/Eu position.
3. The pattern rotation does not appear in the plagioclase-bearing peridotites.
4. In spinel peridotites, the trends observed for trace elements are also present in major element concentrations. Chromium (in all phases) and sodium in cpx increase moving away from the melting curve, while other elements, such as aluminum, calcium and titanium in cpx decrease moving away from melting curve in the same way as Sm/Yb increases and Yb decreases moving away from the melting curve. Moreover, nickel content in spinel decreases moving away from melting curve.
5. Plagioclase-bearing peridotites show an opposite behavior: chromium content, in all phases, and calcium content in pyroxenes decrease moving away from the melting trend, while aluminum, titanium and, less, sodium contents in pyroxenes increases moving away from the curve, although titanium in spinel seems to decrease.
6. Majority of the samples shows REEs trends not in agreement with a near-fractional melting process, but they need a different melting process or refertilization to explain such trends.
7. Mylonites, irrespective of carrying fresh modal plagioclase or not, seem to have undergone a homogenization during deformation process. REEs confirm that the spinel mylonite indeed bears plagioclase.

Chapter 5

Model

5.1 – Partial melting, melt extraction and refertilization

Earth mantle, during its upwelling beneath mid-ocean ridges, can experience different petrological processes, namely partial melting and melt extraction, leading to strong modification of chemical element concentrations and ratios. Mantle partial melting is a fundamental process for the differentiation and evolution of the Earth. Modeling of partial melting using trace element concentrations is required to understand the melt generation and extraction processes and to understand the chemical composition of primary melts. There are three general processes describing the mantle melting: batch melting, fractional melting (SCHILLING & WINCHESTER, 1967; GAST, 1968; SHAW, 1970), and dynamic melting (LANGMUIR ET AL., 1977; MCKENZIE, 1985; LIANG, 2008; SHAW, 2000; ALBARÈDE, 1995; JOHNSON & DICK, 1992; LANGMUIR ET AL., 1977; ZOU, 1998). Batch melting assumes that melt remains in

equilibrium with the solid throughout the melting event whereas the fractional melting assumes that the melt is removed from the initial source as it is formed and only the last drop of melt is in equilibrium with the residue. Dynamic melting accounts for a critical threshold for melt extraction: when the melt mass fraction in the residue is less than the critical value for melt separation, there is no melt extraction (as in batch melting), when the melt fraction in the residue is greater than the critical value for melt separation, any infinitesimal excess of melt will be extracted from the matrix. At the end of the process the melt mass corresponding to the critical mass fraction is retained in the mantle residue.

The simplest and at the same time more realistic process that mantle can experience is a dynamic melting, in which the system porosity presents a minimum value that allows segregation of melt. Here we describe the effect of partial melting using trace element concentrations in residual clinopyroxene. This mineral phase hosts the majority of the incompatible trace elements and can be used as a proxy of whole rock composition. It is also the mineral phase that is less affected by serpentinization and low-temperature alteration.

Mantle melting can be well pictured in a $(Sm/Yb)_{(N)}$ vs. $Yb_{(N)}$ plot (Fig. 5.1.1) where both the relative enrichment of a mildly incompatible element (Yb) and its fractionation with respect to a more incompatible element (Sm) are described. At the same time the Sm/Yb ratio images the steepness of the REE pattern thus allowing a rapid translation of this information in a morphological aspect. In this compositional space data are compared with model melting curves showing the behavior of Sm and Nd in cpx during the melting of a depleted mantle parcel (DM).

Beneath ocean ridges, mantle melting can start in the garnet-stability field or in spinel-stability field depending on the correlation between mantle potential temperature and peridotite solidus. If starting in the garnet facies, melting possibly continues in the spinel facies where it usually ends (NIU, 1997; ASIMOW ET AL., 1995; AHEARN & TURCOTTE, 1979; KLEIN & LANGMUIR, 1987; MCKENZIE & BICKLE, 1988; NIU & HÉKINIAN, 1997A; ZHANG & TANIMOTO, 1993). Therefore cpx undergoes re-equilibration in spinel-facies either during melting or during

cooling. Due to this fact all sampled residual peridotites are equilibrated in the spinel facies, so the model curves must be.

Model melting curves hereafter reported in $(Sm/Yb)_N$ vs. Yb_N diagram are therefore projected in the spinel field accounting for the redistribution of the trace elements among the spinel field phases during garnet breakdown reaction. Solid lines in figure 5.1.1 show the melting trend calculated by HELLEBRAND ET AL., 2002) followed by cpx in equilibrium with the whole rock and during a pure-fractional melting.

Based on this representation (figure 5.1.1), HELLEBRAND and coworkers (2002) suggested that the observed scatter in Sm/Yb for a given Yb concentration in residual mantle equilibrated clinopyroxenes from the Central Indian Ridge (CIR) can be explained considering melting to have started at different pressures, i.e. at different depth in the garnet stability field. This results in different degrees of melting undergone by the upwelling mantle in the garnet facies and ultimately a variable shift in Sm/Yb for a given Yb value. However the whole reasoning is based on a pure fractional melting model thus assuming melt to be perfectly extracted per each infinitesimal increment during its production.

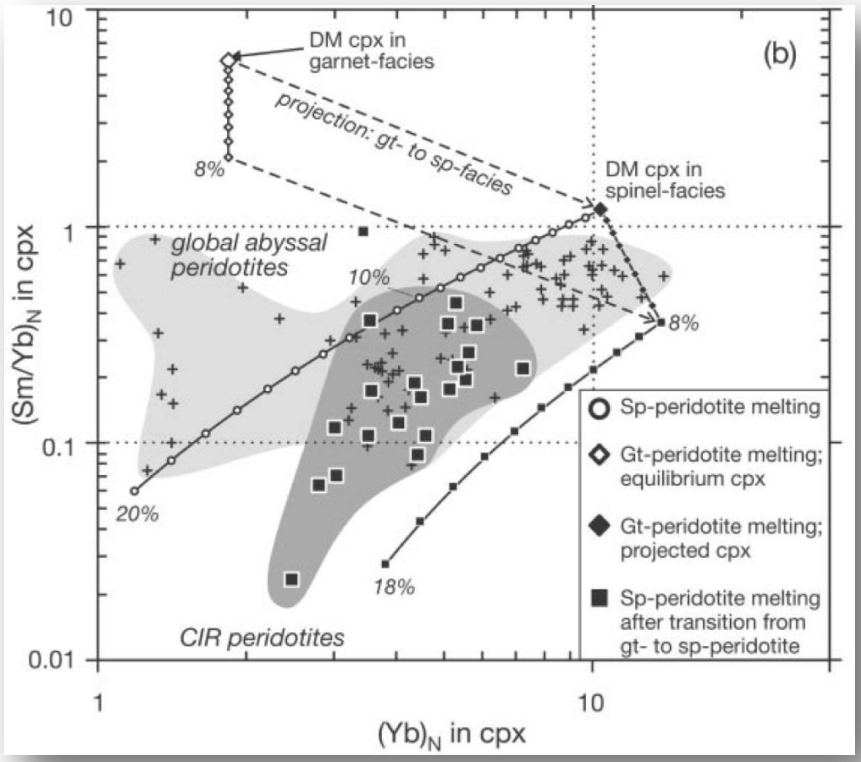

Figure 5.1.1 *– $(Sm/Yb)_{(N)}$ vs. $Yb_{(N)}$ diagram from HELLEBRAND ET AL, 2002. White diamonds represent cpx composition during melting in the garnet stability field. When mantle enters spinel stability field, clinopyroxenes re-equilibrate in these new conditions, and their composition is projected in spinel stability field (black diamonds). Now, melting can continue in spinel stability field (black squares). If there is no melting in garnet stability field, melting will start at DM cpx in spinel-facies and it will continue following this melting curve (white circles).*

Considering a more realistic melting scenario accounts for melt not being extracted before an interconnected network is developed. At the same time the end of melting is characterized by a certain amount of melt to be retained in the rock. In the simple case in which the two quantities are assumed to be the same the model evolves to the known dynamic melting model. In this scenario accounting for a finite residual porosity (critical mass porosity, cmp) reveals that the observed compositional scatter has not anymore a

unique interpretation. In fact, the dispersion can be partly explained by varying the critical mass porosity of the system because part of the most incompatible elements are buffered during melting and partially retained in the rock being hosted in the critical porous melt fraction. The compositional contribution of the critical mass porosity is redistributed among the solid phases during recrystallization and subsolidus cooling. BRUNELLI ET. AL. (2006) showed how varying the cmp results in progressive shift of the melting curves to cover part of the observed scatter (Fig. 5.1.2). The modeled shift refers to the simple variation of the cmp in a melting scenario where retained melts are those corresponding to the last melt increment.

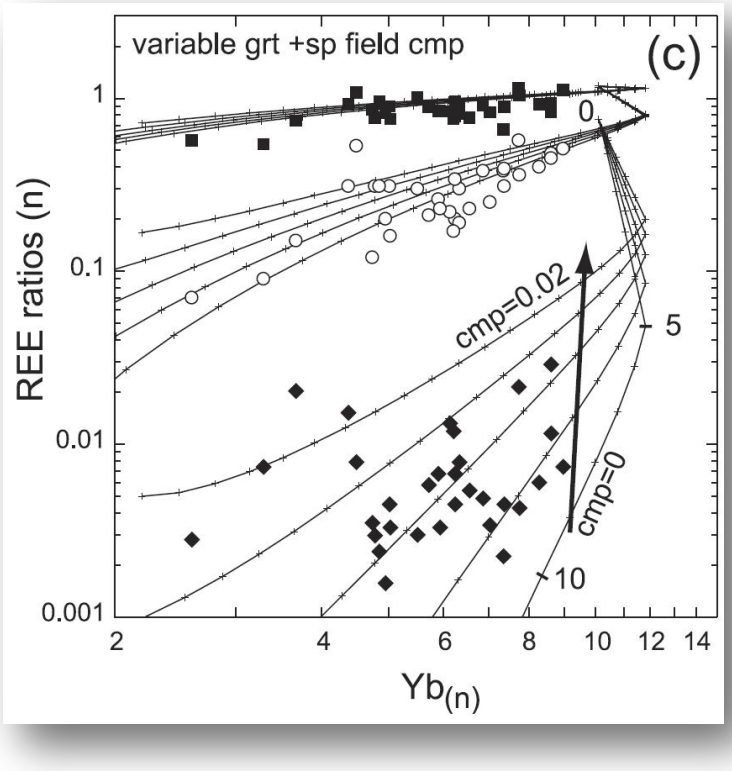

Figure 5.1.2 *– Model dynamic (non-modal) melting paths varying the critical mass porosity (cmp) compared with clinopyroxene composition for the Vema Lithospheric Section peridotites; $(Dy/Yb)_n$ (black squares), $(Sm/Yb)_n$ (white circles) and $(Ce/Yb)_n$ (black diamonds) vs. $Yb_{(n)}$. Variation of the cmp in both garnet and spinel fields for the same cmp values. Tick marks on the model curve are 1% melting steps. The total extent of melting (5% increments) is reported for reference on the (Sm/Yb)n melting curve. Diagram from BRUNELLI ET AL. (2006).*

However, SEYLER ET AL.(2001) showed that residual abyssal peridotites carry textural evidence for interstitial mineral phases crystallized from unextracted melt. BRUNELLI ET AL., 2006 observed that in some peridotite samples the volume of the interstitial phases (>1%) is larger than the volumes assumed as realistic for the critical mass porosity, that for abyssal peridotites are well below 1%. This fact suggests that melt retention at the end of the melting region locally overcomes the simple cmp network volume, and possibly represents a different mechanism of melt retention. Melt transport in a melting mantle parcel can be achieved by porous flow in an interconnected network. This is the case assumed when considering models of melting as dynamic previously described. However, melt percolation through a partially molten region in upwelling is an unstable process due to preferential pyroxene dissolution and heterogeneous small-scale porosity distribution (KELEMEN ET AL., 1995a, 1995b). Consequently an upwelling partially molten mantle parcel invariably leads to a focused melt transport resulting in channeling. Preferential pyroxene dissolution and ± olivine +spinel precipitation (reaction) leading to dunite formation and rapid transport of large volume melts to shallow depths. SPIEGELMAN & KELEMEN, 2003, showed that the transport in such a double-porosity system may explain extreme compositional variations of the carried melts ranging from highly enriched quasi instantaneous endmembers to more depleted variably aggregated melts. This mechanism allows for an extreme variable composition of the melt to be accounted for when considering a possible re-injection or retention of melts in the rising mantle peridotite. On this base BRUNELLI and coworkers (2006) considered the possible chemical influence of refertilization due to retention of melts at the top of the melting region in the case of this melts were not in local equilibrium with the residual paragenesis (Fig 5.1.3). Cpx composition plotting outside the melting trends can thus be reached.

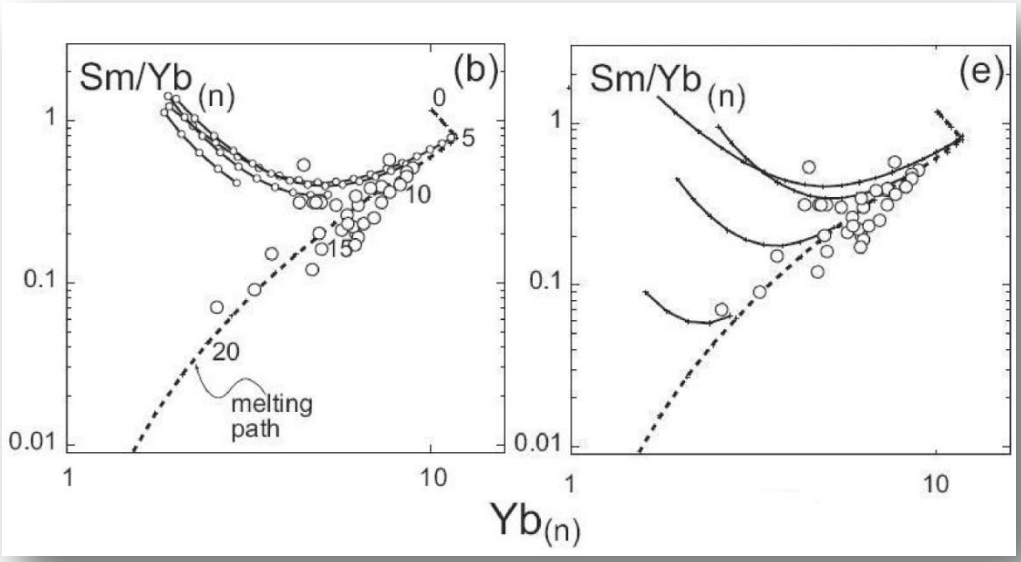

Figure 5.1.3 *– from* BRUNELLI ET AL, *2006. Iso-refertilization. $(Sm/Yb)_n$ vs. $Yb_{(n)}$ compared with model iso-refertilization paths for a residual peridotite-hosted clinopyroxene. Curves show how a variably aggregated (b) or quasi-instantaneous (e) melt can modify the clinopyroxene REE element contents after crystallizing 0.5% melt in a variably depleted source. All curves refer to 5% non-modal fractional melting in the garnet field followed by melting in the spinel field. Quasi-instantaneous (continuous lines, small ticks) and variably aggregated (continuous lines, open circles) melts are extracted after 5, 10, 15 and 20% source partial melting and added back to a rock that has undergone further melting. The composition of residual clinopyroxenes not affected by refertilization follows the normal melting path (dashed line).*

Nevertheless, melting and re-enrichment processes do not explain the trends seen in ABFZ samples, given that only a minority of ABFZ samples fits the modeled curves (Fig. 4.2.3).
Most samples occupy an enriched area impossible to be reproduced by these conventional melting and melt extraction processes. Moreover, the observed enrichments in the element ratios are coupled to an increase in Cr# of the residual phases. Cr# is commonly considered as a good indicator of the degree of depletion experienced by a mantle parcel, increasing during melting and decreasing during refertilization by addition of alumina-rich melts.

Therefore a simple refertilization by melt entrapment resulting in compositional mixing between rock and melt cannot be accounted for because addition of Al-bearing melts while rising the incompatible/compatible element ratio (e.g. Sm/Yb) would result in lowering of the whole rock Cr# resulting in negative trends that are the opposite to the effect of a near fractional melting process (McDonough & Frey, 1989; Downes et al,. 1991; Takazawa et al., 1992).

It is necessary, then, to introduce another process able to explain and to reproduce the REE compositional trends observed in the ABFZ samples.

5.2 – Open system melting

Open system melting (OSM) represents a more general formulation for melting and melt extraction: along with the degree of melting experienced by the system and the amount of melt extracted it accounts for the possible amount of exotic melt entering the system. Batch, fractional and dynamic melting represent particular cases of the general formulation. In fact, fractional melting represents the particular case in which there is no melt left in the system because it is completely extracted simultaneously to melting (critical mass porosity ϕ=0). When the critical mass porosity equals the degree of melting (ϕ = 1), all the melt is retained inside the rock and the system is representative of a pure-batch melting.

Open system melting can be modeled based on the equation sets of OZAWA & SHIMIZU, 1990 or ZOU, 1998 that derived equations for melting in presence of melt influx. The model here developed aims to reproduce the case of a mantle parcel, equilibrated in the spinel field, experiencing melting while a variable amount of exotic melt enters the system. To reproduce this case a stepwise incremental model has been adopted in which the composition of a depleting source, the extracted and residual melts and the phase elemental compositions are calculated based on a dynamic melting approximation. The open system case is reproduced by mixing the residual melt with a given amount of incoming melt and calculating the new solid bulk in equilibrium with the modified melt. By assuming small-enough increments in degree of melting ($\Delta F \rightarrow 0$) and melt influx the model approaches a true fractional melting in an open-system. However the chosen formulation allows for assuming variable residual porosity profiles and influxing rates along the melting column.

5.2.1 Equations and parameters

The equation set proposed by ZOU (1998) has been adopted. To compute and simulate trace element behavior in melting and refertilization process due to influx of an enriched melt, a stepwise calculation procedure has been used. For each step, compositions of bulk residue, residual phases and extracted melt have been computed, as well as bulk distribution

coefficient, melting and residual modes. We have considered the case of a non-modal melting in which the melting mode differs from the actual mode of the source.

The concentration of a trace element in the residue (residual solid + residual melt) C_{res} is expressed as:

$$C_{res} = \frac{1}{D_0 + \Phi(1-P)} C_0 \left\{ 1 - \frac{X\,P + \Phi(1-P)}{D_0 + \Phi(1-P)} \right\}^{1/\Phi + (1-\Phi)P - 1}$$

While the concentration of a trace element in the extracted melt C_L is expressed by:

$$C_L = \frac{C_0}{X} \left\{ 1 - \left[1 - \frac{X\,P + \Phi(1-P)}{D_0 + \Phi(1-P)} \right]^{1/\Phi + (1-\Phi)P} \right\}$$

Where:

C_0 concentration of a trace element in the source;

P weighted liquid partition coefficient: $P = \sum kd_i/l\ p_i$, where p_i is the melting mode of the phase i;

D_0 initial bulk distribution coefficient of the source: $D_0 = \sum Kdi/l\ X_0,i$, where X_0,i is the mode of the phase i in the source;

Φ critical mass porosity, i.e. the minimum 'critical' amount of partial melting required to allow segregation of the melt from the source; this also represents the amount of melt retained in the source after extraction;

X fraction of extracted melt, where $X = 0$ for $F \leq \Phi$, $X = \frac{F - \Phi}{1 - \Phi}$ for $F > \Phi$

Fractional (non-modal) melting represents the particular case in which there is no residual porosity (Φ = 0), i.e. all the melt is perfectly extracted from the source (X = F) as soon as is

produced. By setting Φ = 0 equations become that of the fractional melting equations of Shaw (1970). Modal melting corresponds to the particular case in which $P = D_0$.

When melting starts in the garnet stability field, breakdown of residual garnet (at the boundary between garnet stability filed and spinel stability field) during the transition to the spinel stability field has been computed according to the following reaction (JOHNSON ET AL., 1990)

1.0 Ol + 1.0 Gt = 2.5 Opx + 1.0 Sp + 0.75 Cpx in wt%

Model has been run with a DMM bulk composition (MCDONOUGH & SUN, 1995).
Initial mode composition, melting mode composition and partition coefficients between mineral phase and melt are from HELLEBRAND ET AL. (2002) and BRUNELLI ET AL., 2006. Partition coefficients for all minerals and all elements were compiled based on BLUNDY ET AL. (1998) and SUHR ET AL. (1998), with the exception of Gd obtained by averaging adjacent element values. Initial and melting modes are from JOHNSON ET AL. (1990), KINZLER (1997), JOHNSON (1998) and WALTER (1998). Parameters are reported in table 5.2.1.1.

	Ol	Opx	Cpx1	Cpx2	Grt	Sp	Source C/C1
Source mode	0.57	0.21		0.13	0.09		
Melting mode - grt	0.04	-0.19		1.05	0.11		
Melting mode - sp	-0.06	0.28	0.67			0.11	
Partition coefficient							
La	0.000007	0.0025	0.06	0.09	0.0035	0.0006	0.91
Ce	0.00001	0.005	0.1	0.16	0.008	0.0006	1.4
Nd	0.00007	0.01	0.2	0.36	0.05	0.0006	1.97
Sm	0.001	0.02	0.3	0.67	0.22	0.001	2.23
Eu	0.001	0.03	0.37	0.8	0.45	0.001	2.34
Gd	0.0025	0.04	0.405	0.95	1.225	0.0015	2.39
Dy	0.004	0.05	0.44	1.1	2	0.002	2.44
Er	0.009	0.07	0.43	1.44	3.5	0.003	2.46
Yb	0.014	0.09	0.41	1.43	5	0.005	2.5

Table 5.2.1.1 *– Parameters used in the models. Cpx1, partition coefficients in the spinel stability field, Cpx2, partition coefficients in the garnet stability field.*

5.2.2 Model geometry

The model aims to reproduce a mantle parcel experiencing melt influx during progressive decompressional melting. Model input (Fig. 5.2.2.1) consists in a variably depleted, spinel-field equilibrated, mantle parcel with a bulk C_0 trace element concentration.
Each calculation step consists of the following stages:

1- The rock experiences a finite small amount of melting (F) and melt extraction (X)
2- Solid residue, residual mode, phase compositions and residual melt are calculated for a given cmp (ϕ).
3- The residual melt composition is modified by assuming mixing with an exotic melt influx.
4- A new bulk solid is recalculated in equilibrium with the new residual melt.
5- Goto 1

This geometry describes a process in which (see figure 5.2.2.1) a mantle parcel melts, and a compositionally m_1 liquid is extracted (Fig. 5.2.2.1-1). An exotic melt (m_{ex}) enters the system and mixes with the residual melt (Fig. 5.2.2.1-2) then equilibrating with the bulk residual solid (Fig. 5.2.2.1-3). The new bulk concentration is now C_1, and melting takes place, producing an m_2 melt exiting the system (Fig. 5.2.2.1-4). At step n, the same exotic m_{ex} melt enters the system and modifies C_n bulk, that melts resulting in a new C_{n+1} bulk plus m_{n+1} escaping melt.

By setting $\Phi \neq 0$ the exact Φ melt volume is retained in the system at each melting step. In this case an incoming exotic melt entering the system can mix with the resident. This is expressed in terms of ratio between exotic and residual melt volumes. Ratio between incoming melt and residual melt is defined as dilution factor (D_f = exotic melt / [residual melt + exotic melt]). For D_f=1 the exotic melt is not diluted by the resident melt, thus it

completely replaces it. This case is of course unrealistic but represents the endmember for the complete substitution of an in-situ-equilibrium melt with an exotic out-of-equilibrium component. For D_f=0.1 the exotic melt is diluted by 10 times. And when D=0 there is no melt influx. To ensure mass conservation the net amount of melt has been keep constant = ϕ assuming perfect isenthalpic mixing. The D_f ratio is expressed in vol%, considering negligible the difference in density between the two melts.

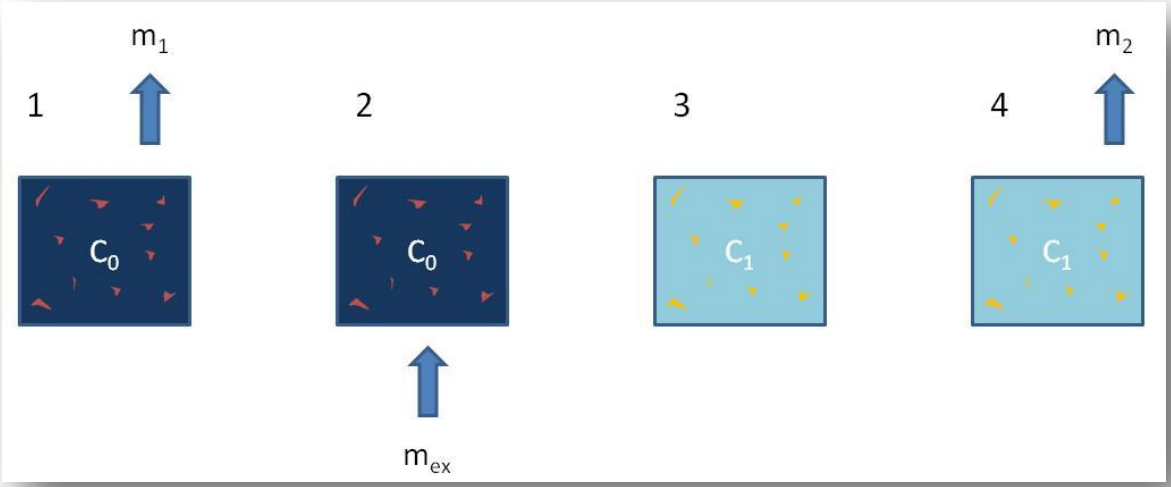

Figure 5.2.2.1 *– Geometry of the proposed model.* 1) A C_0 *composition mantle parcel melts, and a compositionally* m_1 *liquid is extracted. Red shapes represent the retained melt in the system porosity. 2) The exotic melt* m_{ex} *enters the system and mixes with the residual melt; 3) the new melt formed at previous step (yellow interstitial melt in figure) now equilibrates with the (old) bulk residual solid forming the new residual solid (light blue in figure). 4) The new bulk concentration is now* C_1*, and melting takes place, producing an* m_2 *melt exiting the system. At this point, another step of melting can start, considering the composition of residual solid at first step* C_1*.*

The model considers a peridotite melting in the spinel stability. In the real case, an exotic melt entering a spinel-field melting peridotite can be thought to derive from a garnet-bearing source or from a higher pressure spinel-bearing source. The majority of the cpx REE patterns from our samples are better fitted considering melt derived after few degrees of melting in the garnet-facies, as it will be discussed in next paragraphs.

In order to reproduce the case of maximum system perturbation the entering melt is assumed with a constant composition for all the computational steps. A constant composition of the influxing melt acting on a progressively modified mantle parcel corresponds to postulating an infinite melt reservoir. In a true melting mantle this configuration corresponds to mantle parcels in contact with, or close to melt conduits as dunitic channels.

5.2.3 Closed-system melting of DMM peridotite in the spinel stability field

In this section pure-fractional, pure-batch and dynamic melting are discussed. Diagrams represent REEs concentrations in equilibrated cpx at different degrees of melting. All patterns are normalized to CI chondrite values (ANDERS & GREVESSE, 1998)

Pure-fractional melting in a closed-system in the spinel field (Fig. 5.2.3.1) leads to a progressively strong depletion in L-REEs and a less enhanced depletion in H-REEs, due to their different partition coefficients between cpx and melt. This behavior has been widely described in literature and represents the current base for estimating the degree of depletion of a residual mantle parcel (see for instance JOHNSON ET AL., 1990 and references therein).

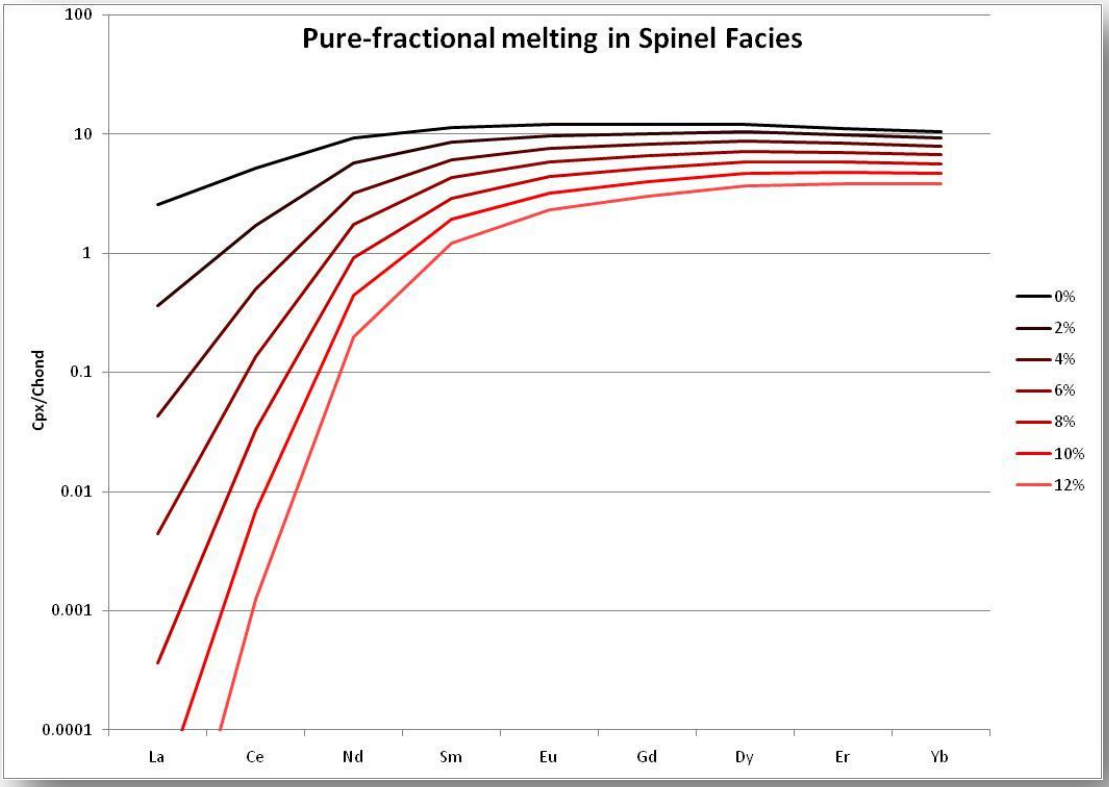

Figure 5.2.3.1 *– Cpx REE patterns of a pure-fractional melting system from a DMM source. Each pattern represents a 2% step of melting. It is possible to see the enhanced fractionation between L-REE and H-REE.*

In a dynamic melting scenario the degree of depletion in the LREEs also depends on Φ, that controls the type of melting. The presence of melt in the residual porosity has a buffering effect proportional to the trace element incompatibility; this results in a lesser depletion of the LREEs with respect to the HREEs relative to fractional melting. In the next figure is reported as example a case of melting in the spinel stability field (Fig. 5.2.3.2) in which ϕ value is set at 0.003, where step values of F are 0.01.

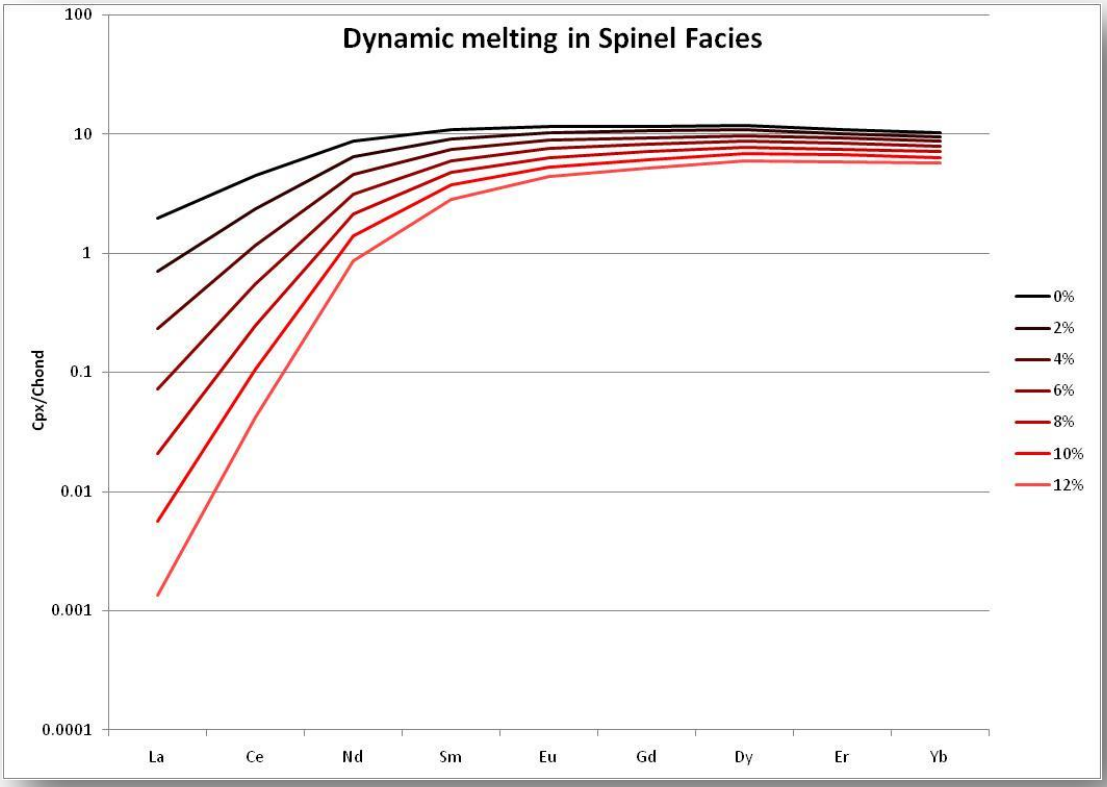

Figure 5.2.3.2 *– Cpx REE patterns of a dynamic melting system from a DMM source. Each pattern represents a 2% step of melting. It is possible to see the different degree of fractionation between L-REE and H-REE occurring in this case if compared to previous figure. In this example, computation steps are 0.01 for F and 0.003 for* Φ*.*

Setting ϕ=F indicates a pure batch melting where all produced melt F is retained in the rock. Under this regime of melting resulting equilibrated cpx appears to be more enriched in incompatible elements than in the previous melting models (Fig. 5.2.3.3). In fact the buffering effect is the maximum possible because the liquid is always in contact with the residual solid. In this case batch melting is of course thought to be followed by the complete extraction of the whole volume of produced melt at the end of the melting event.

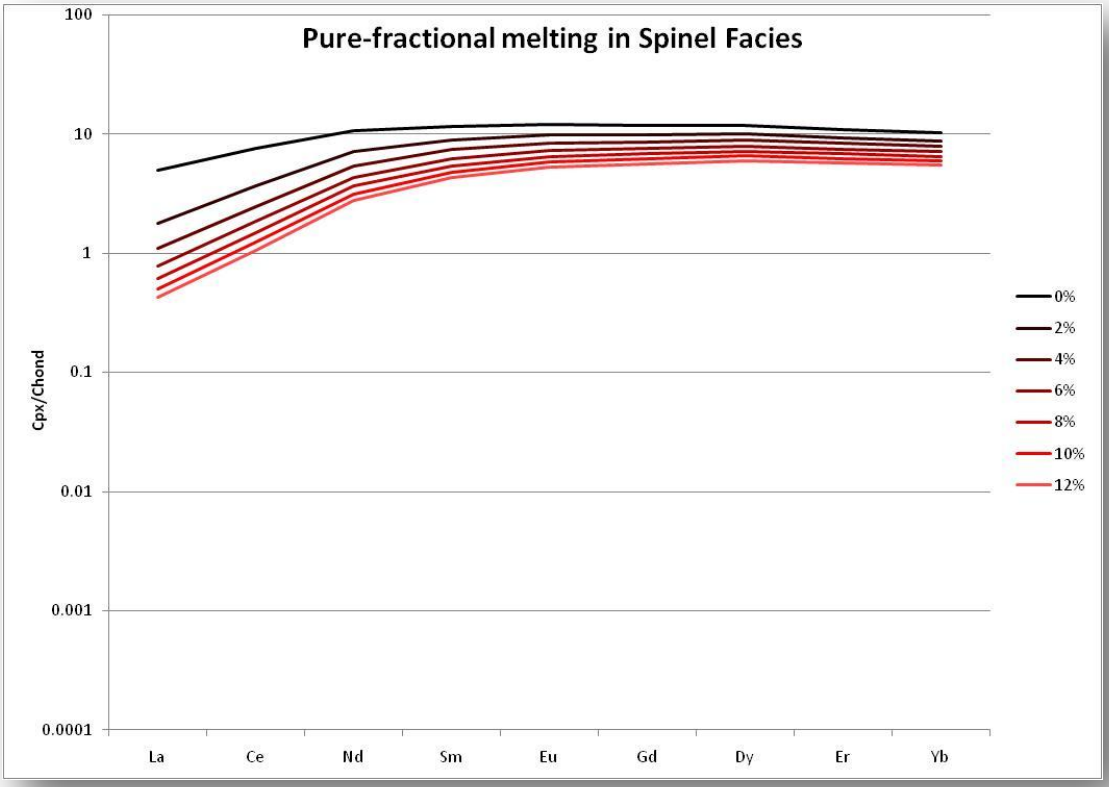

Figure 5.2.3.3 *– REE patterns of a pure-batch melting system from a DMM source. Each pattern represents a 2% step of melting. Note that after the first degrees of melting, fractionation between L-REE and H-REE stops.*

In conclusion, the result that is possible to obtain varying ϕ with respect to F is to vary the type of the melting process: when ϕ<<F the resulting melting regime assumes a near-fractional character, where only a minor part of the produced melt is retained inside the rock, being the majority extracted (possibly leading to results similar to those for pure-fractional melting); when ϕ→F, the melting regime can be defined as near-batch melting, where the majority of melt is retained in the rock and the melt extraction is negligible (leading to results similar to those observed in pure-batch melting). This behavior will be discussed in detail in the next paragraphs.

5.2.4 Open system melting

The influx of an exotic melt dramatically changes the behavior of the trace element during melting. In this paragraph the parameters governing open system melting (OSM) are discussed. The incoming melt composition plays the key role. Two different melts are used in this section to be representative of the possible compositional variability of the percolating melt trough a mantle melting system: an incompatible enriched melt, similar to that produced by low degrees of melting in the garnet field, and an aggregated-like melt similar to a N-MORB flat pattern (Fig. 5.2.4.1). The composition of the two has been estimated by modeling 1% melting in the garnet field of a DMM source (for the composition of the enriched melt) and aggregating from 1% up to 5% melting in the spinel field (for the N-MORB like melt). Hereafter they will be designed as “enriched” and “aggregated” melts respectively.

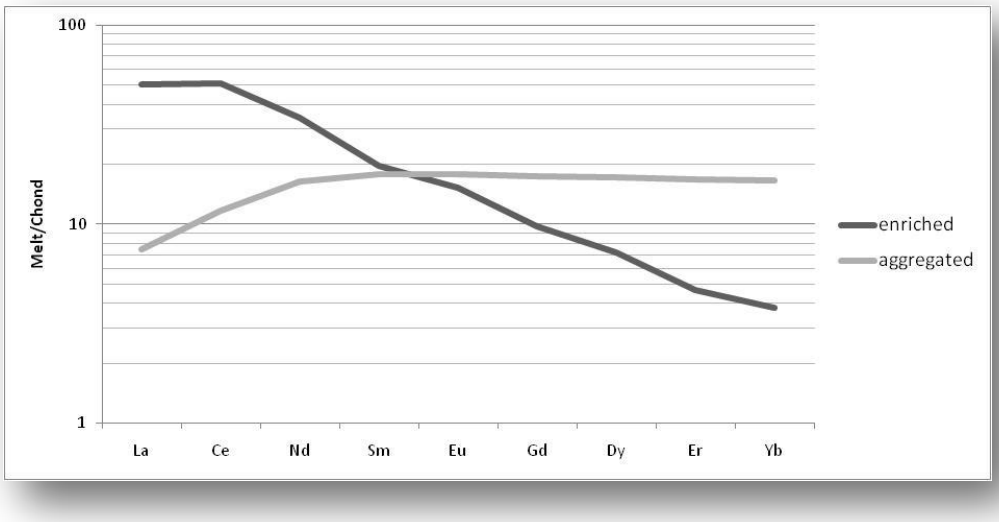

Figure 5.2.4.1 *– REE patterns of the melt used in this section. Concentration values are normalized to CI chondrite concentration (ANDERS & GREVESSE, 1989). “Enriched” composition has been estimated by modeling 1% melting in the garnet field of a DMM source and “aggregated” composition has been estimated by aggregating DMM-derived melt from 1% up to 5% melting in the spinel field.*

The obtained OSM trends are reported in green in the next figures always compared with the expected dynamic (ϕ=0.02) melting trends for garnet and spinel field melting in a closed system. As seen before, all patterns are projected in the spinel compositional field to be comparable with the recovered spinel-field equilibrated ABFZ peridotites.

Varying D_f in a near-fractional melting model

Melting in an open-system results in a trend that is different if compared to that defined by dynamic closed-system melting. In the first example (Fig. 5.2.4.2), melting of the DM source in presence of an enriched melt influx is computed by step of 1% with ϕ = 0.001 and a D_f = 1 per each step. Under these conditions, i.e. ϕ<<F, the system reproduces a near-fractional melting process.

The compositions of the residual clinopyroxene then follow a trend crosscutting the expected trend for spinel field melting due to the marked increase of Sm/Yb while Yb progressively decreases.

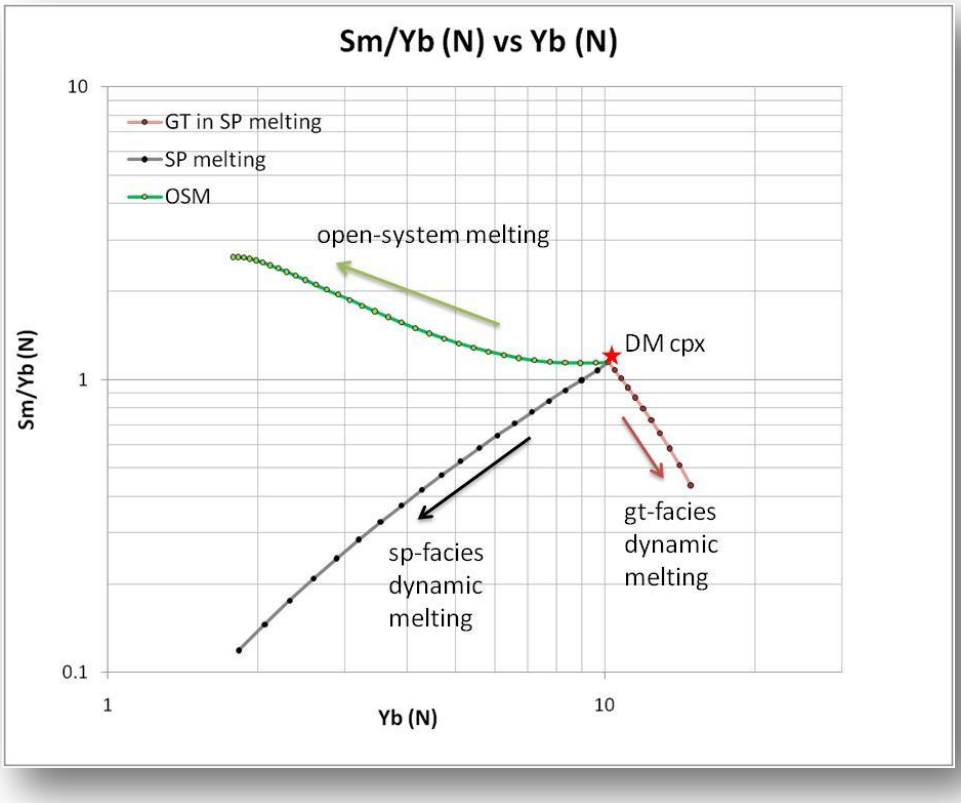

Figure 5.2.4.2 *– $(Sm/Yb)_N$ vs. $Yb_{(N)}$ in OSM from a DM source in the spinel stability field with influx of garnet-derived melt (green). Concentration values are normalized to CI chondrite concentrations (ANDERS & GREVESSE, 1989). Trend represents the evolution of the cpx normalized concentrations in Sm and Yb. For comparison, also DM in garnet-facies melting projected in spinel-facies (red) and DMM in spinel-facies (black) are reported. Each point on each curve represents step of 1% of melting. Other parameters are* $\phi = 0.001$ *and* $D_f = 1$.

Progressively varying the volume of melt entering the system (D_f :1 - 0.2), keeping the same configuration, results in trends progressively approaching the curve of dynamic spinel field melting (Fig. 5.2.4.3 and Fig. 5.2.4.4). This reflects the progressive dilution of the incoming melt with the equilibrium melt locally produced.

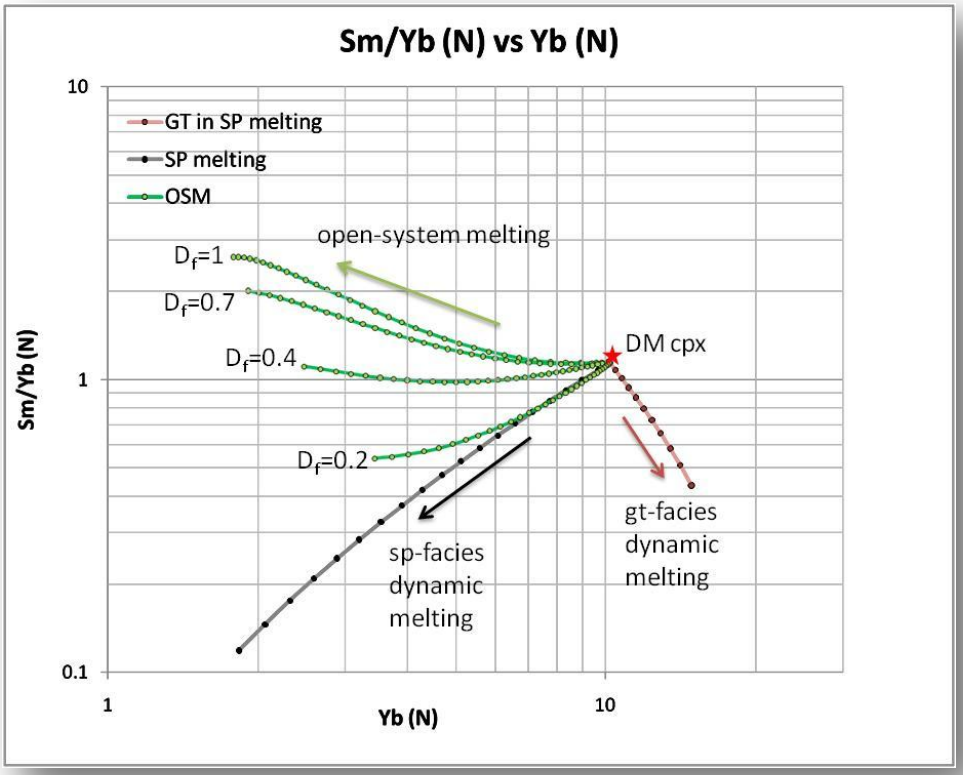

Figure 5.2.4.3 *– OSM with variable D_f and enriched influxing melt: $(Sm/Yb)_N$ vs. $Yb_{(N)}$ in OSM of a DM source in the spinel stability field with influx of garnet-derived melt. Concentration values are normalized to CI chondrite concentration (ANDERS & GREVESSE, 1989). In this example, the only varying parameter is D_f (exotic melt/[resident melt + exotic melt]) as reported in figure. All other parameters are the same as in figure 5.2.4.2. For comparison, also DM in the garnet-facies melting projected in the spinel-facies (red) and DM in spinel-facies (black) are reported. Each point on each curve represents step of 1% of melting.*

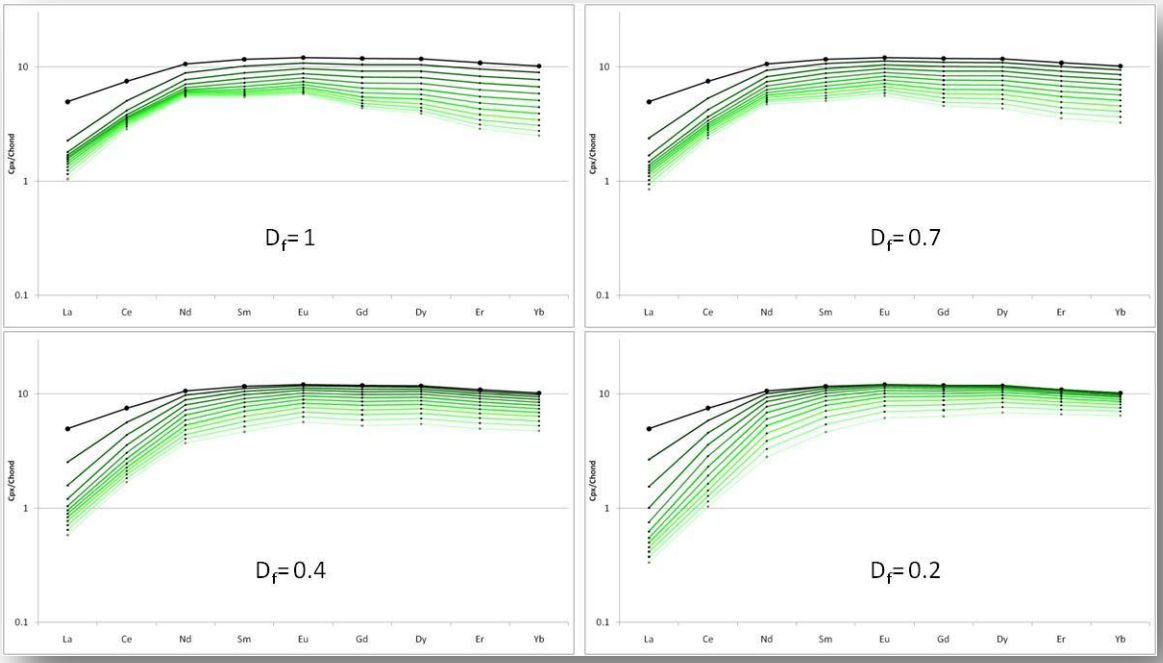

Figure 5.2.4.4 *– OSM with variable D_f and enriched influxing melt: REEs patterns in OSM from a DM source in spinel stability field with influx of a garnet derived melt. Concentration values are normalized to CI chondrite concentration (ANDERS & GREVESSE, 1989). REEs patterns show the effect of OSM for different values of D_f on a melting mantle parcel. All computation parameters are the same as in figure 5.2.4.2. In this example, the only parameter that changes in every spidergram is D_f ([exotic melt/(resident melt + exotic melt] in vol%) as reported in figure. Each green pattern on each spidergram represents step of 2% of melting. Black line is the DM-equilibrated cpx.*

The compositional effect can be dramatic. For instance in the next figures (5.2.4.5 and 5.2.4.6) using an aggregated melt gives a very different behavior. In this case by varying F over a wide range gives only minor compositional variation on the residue. This fact results from adding a “flat” component that strongly resembles the compositional pattern of the equilibrium melt produced in situ because both the melts are produced in the spinel field facies. A significant fractionation results only at very high degrees of melting.

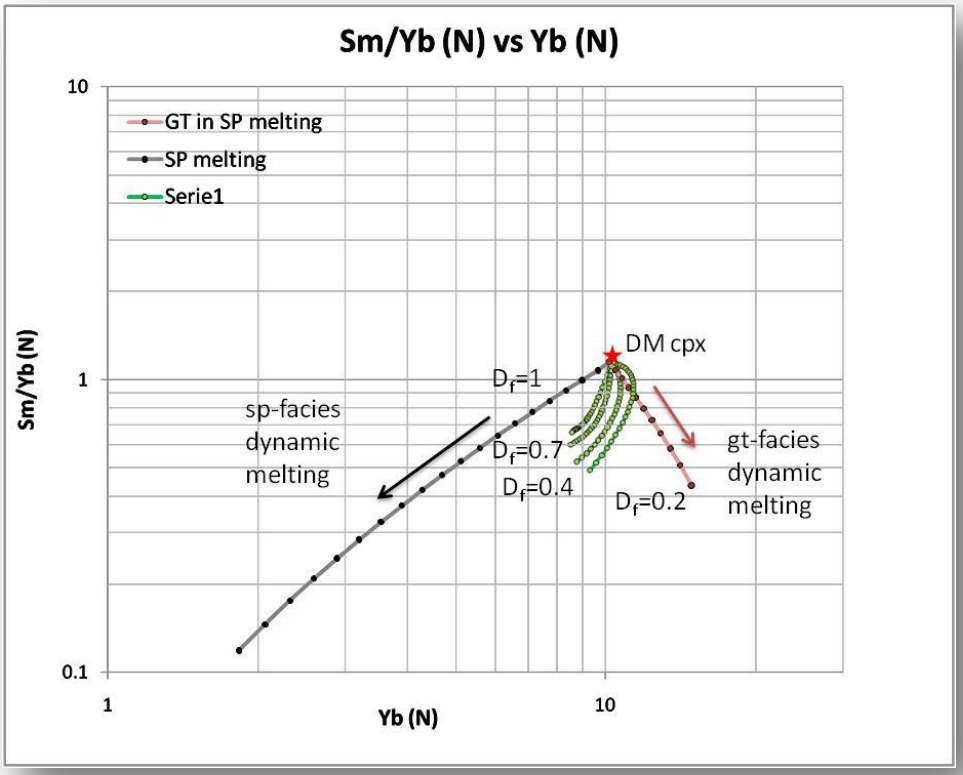

Figure 5.2.4.5 *– OSM with variable D_f and aggregated influxing melt: $(Sm/Yb)_N$ vs. $Yb_{(N)}$ in OSM of a DM source in the spinel stability field with influx of a spinel-derived melt. Concentration values are normalized to CI chondrite concentration (ANDERS & GREVESSE, 1989). In this example, the only varying parameter is D_f (exotic melt/[resident melt + exotic melt]) as reported in figure. All other parameters are the same as in figure 5.2.4.1. For comparison, also DM in the garnet-facies melting projected in the spinel-facies (red) and DM in the spinel-facies (black) are reported. Each point on each curve represents step of 1% of melting.*

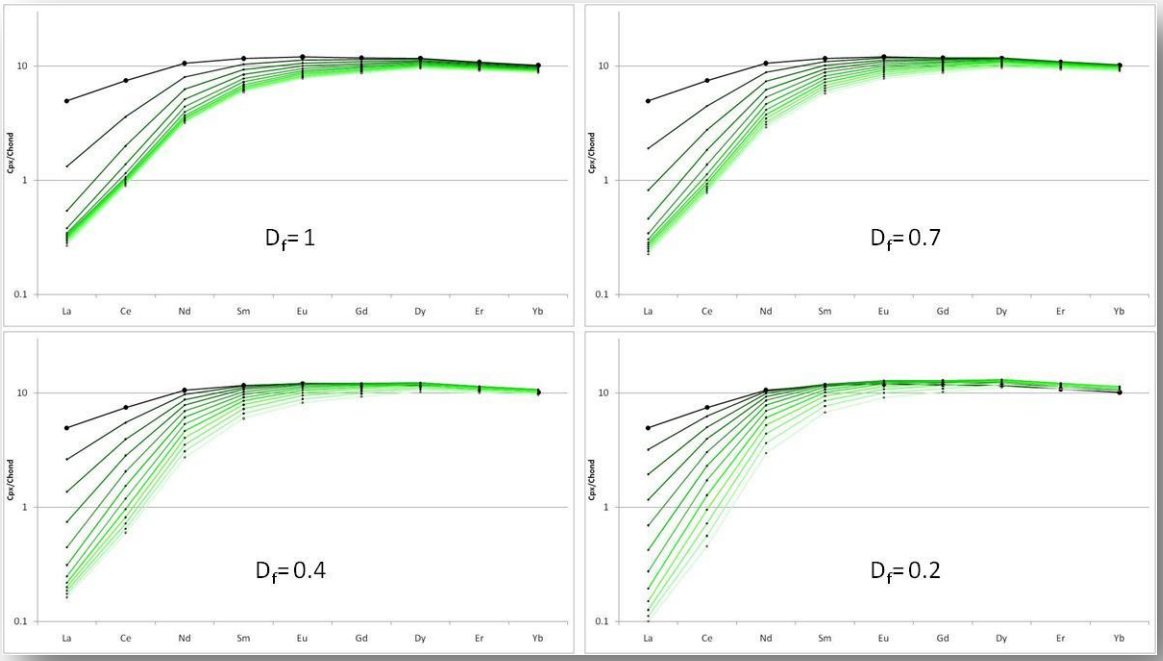

Figure 5.2.4.6 *– OSM with variable D_f and aggregated influxing melt: REEs patterns in OSM from a DM source in spinel stability field with influx of a garnet derived melt. Concentration values are normalized to CI chondrite concentration (ANDERS & GREVESSE, 1989). REEs patterns show the effect of OSM for different values of D_f on a melting mantle parcel. All computation parameters are the same as in figure 5.2.4.2. In this example, the only parameter that changes in every spidergram is D_f ([exotic melt/(resident melt + exotic melt] in vol%) as reported in figure. Each green pattern on each spidergram represents step of 2% of melting. Black line is the DM-equilibrated cpx.*

Varying the type of melting from near-fractional to near-batch

As for dynamic melting, varying the critical mass porosity, ϕ, strongly modifies the model OSM trends. Hereafter the ratio between F and ϕ will be indicated as α = ϕ/F. In the following figures the effect of varying α is shown for OSM with influx of an enriched (Fig. 5.2.4.7 and 5.2.4.8) and aggregated melt (Fig. 5.2.4.9 and 5.2.4.10). The α ratio varies

between 0, indicating that melting runs in a pure-fractional melting regime, and 1, indicating that melting runs in a pure-batch melting regime.

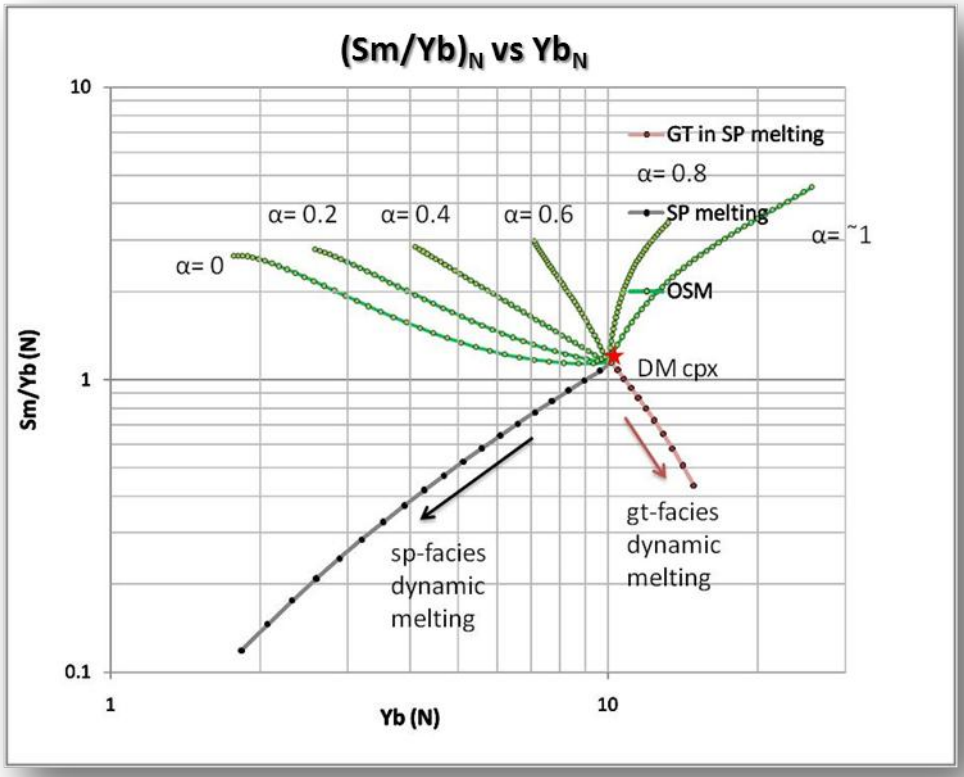

Figure 5.2.4.7 *– OSM with a variable value of α (as reported in the figure) and enriched influxing melt: $(Sm/Yb)_N$ vs. $Yb_{(N)}$ in OSM from a DM source in spinel stability field with influx of a garnet derived melt. Concentration values are normalized to CI chondrite concentration (ANDERS & GREVESSE, 1989). In this example, the only parameter that changes from one OSM trend to another is α (ϕ /F) as reported in figure. All other parameters are the same of figure 5.2.4.2. For comparison, also DMM in the garnet-facies melting projected in the spinel-facies (red) and DM in spinel-facies (black) are reported. Each point on each curve represents step of 1% of melting.*

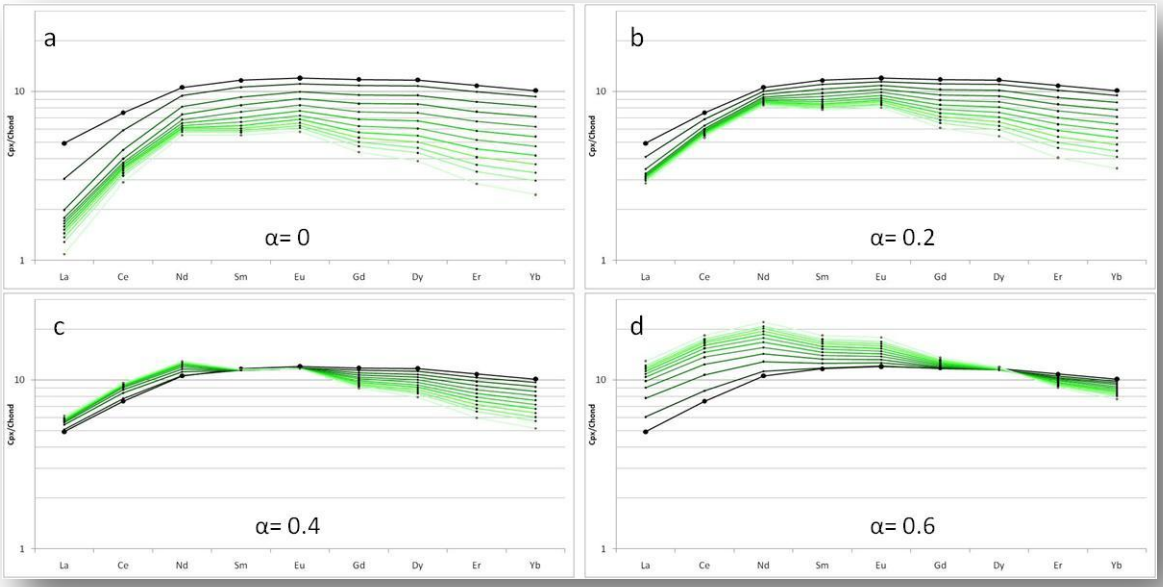

Figure 5.2.4.8 *– OSM with a variable value of α (as reported in the figure) and enriched influxing melt: REEs patterns in OSM from a DM source in the spinel stability field with influx of a garnet derived melt. Concentration values are normalized to CI chondrite concentration (ANDERS & GREVESSE, 1989). REEs patterns show the effect of OSM for different values of α on a melting mantle parcel. All computation parameters are the same used for examples in figure 5.2.4.4 and 5.2.4.5. In this example, the only parameter that changes in every spidergram is α (ϕ /F) as reported in figure. It gives an information about the type of melting regime and about the retention and stagnation of melt in the bulk rock. Each green pattern on each spidergram represents step of 2% of melting.*

The effect on the whole REE pattern is shown in figures 5.2.4.8. The figure is divided in four parts, where melting is characterized by a different α value.

The near batch to purely batch character shows up in the observed trends and pattern evolution. When an enriched melt is accounted for the effect of buffering on the incompatible most elements is visible even for very low α values (Fig. 5.2.4.8 a and b). A counter enrichment appears for the LREEs with respect to the HREEs resulting from the progressive equilibration with the incoming melt even at very low α values. Increasing α,

dramatically increases this effect on the REEs: the L-REEs rebound becomes large enough to over enriches the residual solid during melting. On the contrary, the H-REE concentrations decrease because of the negative net depletion during melting due to the low HREE contents in the influxing melt. The overall effect is that of a pattern rotation around a particular REE. The position of the rotation point is related to ϕ (Sm and Eu in Fig. 5.2.4.8c and Dy in Fig. 5.2.4.8d).

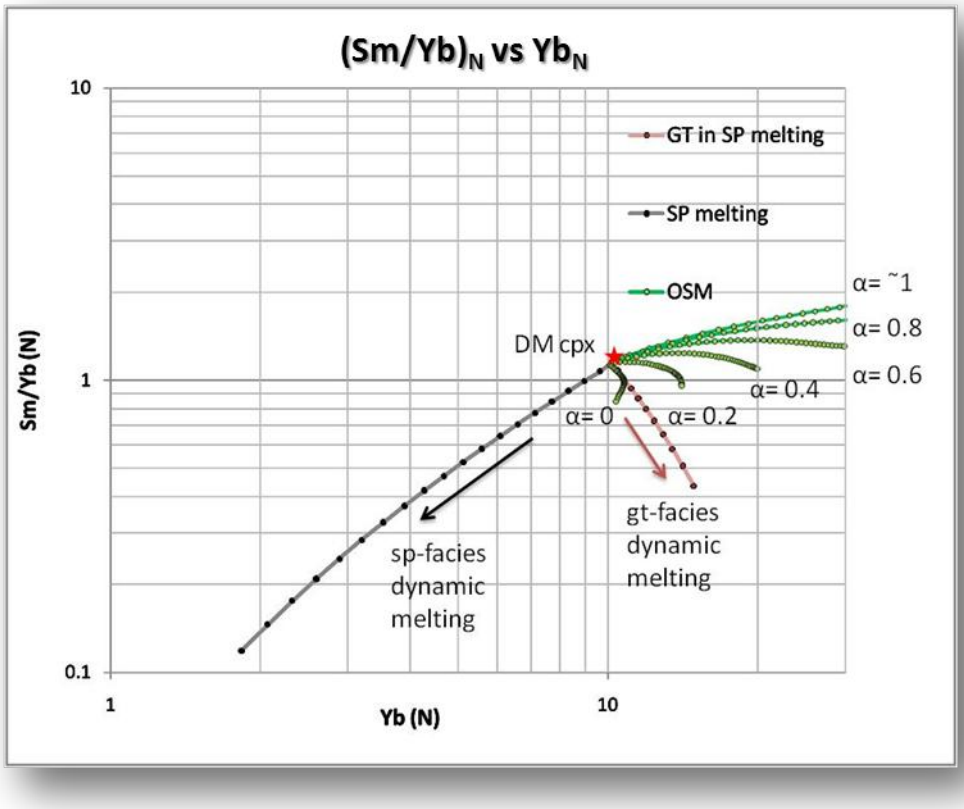

Figure 5.2.4.9 *– OSM with a variable value of α (as reported in the figure) and aggregated influxing melt: $(Sm/Yb)_N$ vs. $Yb_{(N)}$ in OSM from a DM source in the spinel stability field with influx of a spinel-derived melt. Concentration values are normalized to CI chondrite concentrations (ANDERS & GREVESSE, 1989). In this example, the only parameter that changes from one OSM trend to another is α (ϕ /F) as reported in figure. All other parameters are the same of figure 5.2.4.2. For comparison, also DM in the garnet-facies melting projected in the spinel-facies (red) and DM in spinel-facies (black) are reported. Each point on each curve represents step of 1% of melting.*

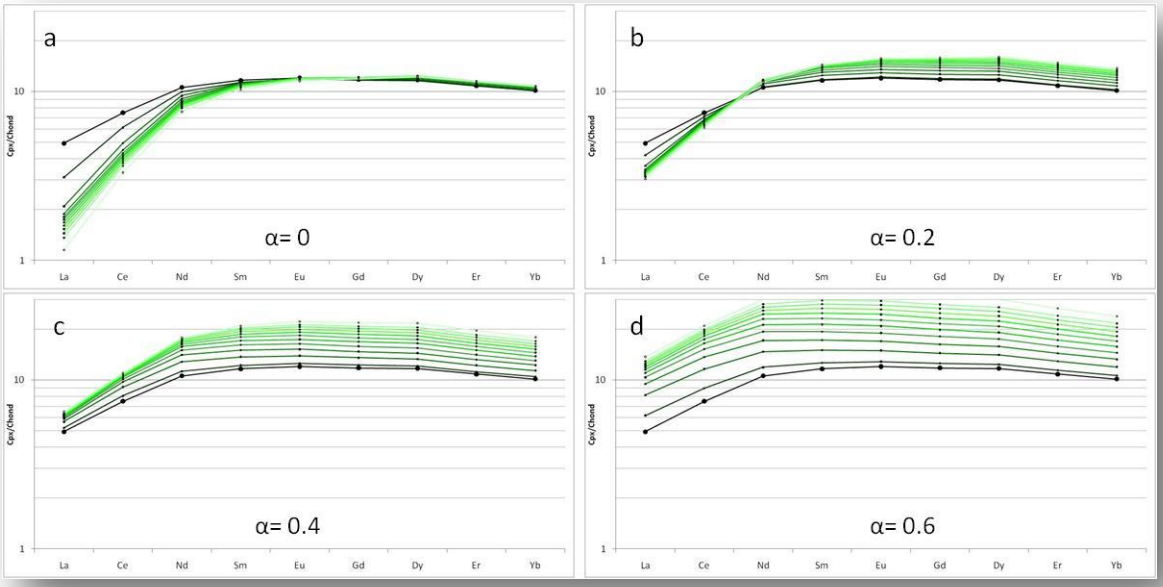

Figure 5.2.4.10 *– OSM with variable α and aggregated influxing melt: REEs patterns in OSM from a DM source in spinel stability field with influx of a spinel-derived melt. Concentration values are normalized to CI chondrite concentrations (ANDERS & GREVESSE, 1989). REE concentration patterns show the effect of OSM for different values of α on a melting mantle parcel. All computation parameters are the same used for examples in figure 5.2.4.4 and 5.2.4.5. In this example, the only parameter that changes in every spidergram is α (ϕ /F) as reported in figure. Each green pattern on each spidergram represents step of 2% of melting.*

An aggregated melt causes a different migration of the model REE patterns (Fig. 5.2.4.9 and 5.2.4.10). The preferential enrichment of the heaviest REEs makes the model patterns to rotate in the counter direction with respect to that previously observed. Moreover the net rotation is weaker than the previous one. As a result the rotation point moves toward the LREEs while the influxing of an enriched melt forces it to move toward the HREEs.

As for the previous case one can consider that the last equilibrated pattern tends to the composition of the incoming melt. This fact is due to the geometry of the model that considers an infinite melt reservoir of a constant compositionally melt instead of a

progressively modified melt percolating trough the rock. Thus the ultimate pattern strongly resembles that of the cpx equilibrated with the percolating melt.

As another example, an open system melting is now considered to occur after the peridotite has undergone some degrees of melting in the garnet stability field followed by a few more in the spinel stability field. Model REE behavior is described in the following figures.
In this model, a mantle portion has undergone melting both in the garnet and spinel facies. More precisely, the total amount of melting experienced by the mantle portion is 7%, 3% in the garnet stability field and 4% in the spinel stability field. At this point, an enriched melt enters the OSM system (Fig. 5.2.4.11 and 5.2.4.12).

In this case the result mimics that previously observed for a DM source. However the effect is more pronounced due to the depleted nature of the percolated residue and the lower amount of residual clinopyroxene interested by the process.

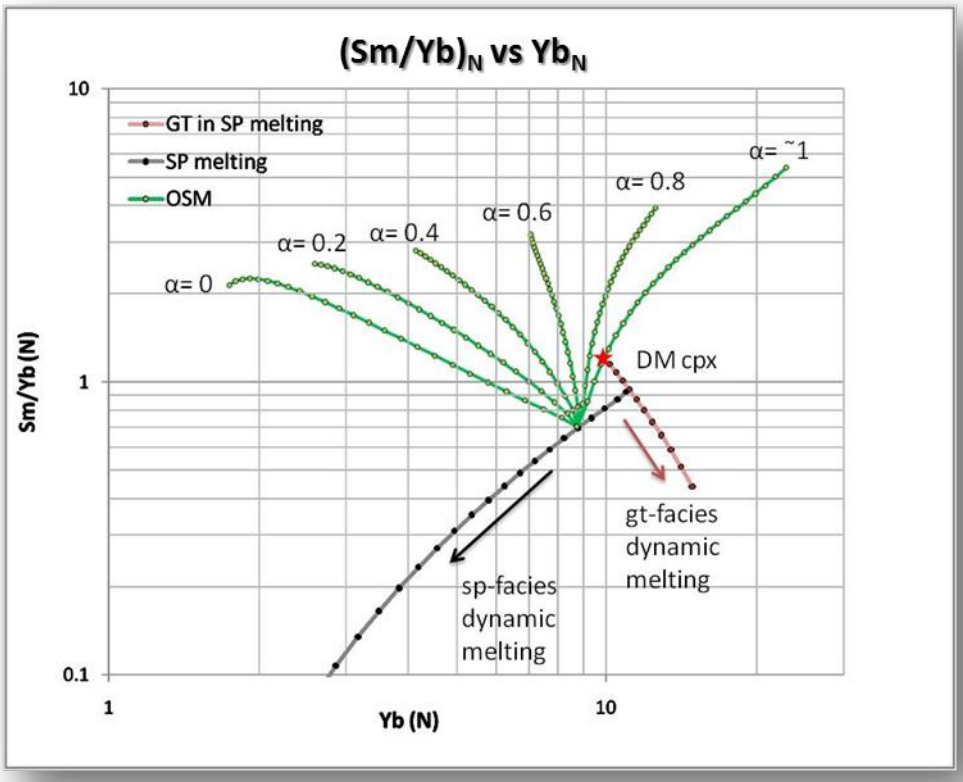

Figure 5.2.4.11 *– OSM with variable value of α (as reported in the figure) and enriched influxing melt: $(Sm/Yb)_N$ vs. $Yb_{(N)}$ in OSM from a DM source in spinel stability field with influx of a spinel derived melt. Concentration values are normalized to CI chondrite concentration (ANDERS & GREVESSE, 1989). DM source has undergone 3% melting in the garnet-stability field followed by 4% melting in the spinel stability field. The six OSM trends have been obtained varying value of α (ϕ/F) as reported in figure. All other parameters are the same as in figure 5.2.4.1. For comparison, also DM in the garnet-facies melting projected in the spinel-facies (red) and DM in the spinel-facies (black) are reported. Each point on each curve represents step of 1% of melting.*

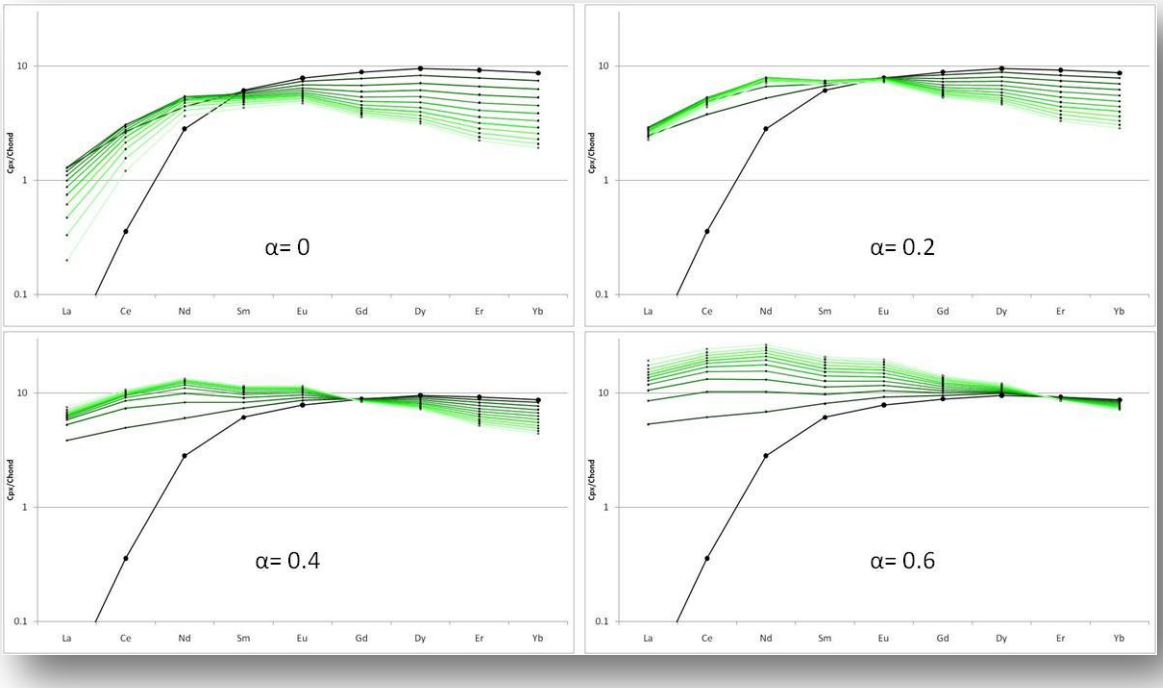

Figure 5.2.4.12 *– OSM with variable α and aggregated influxing melt: REEs patterns in OSM from a DM source in the spinel stability field with influx of a spinel-derived melt. Concentration values are normalized to CI chondrite concentrations (ANDERS & GREVESSE, 1989). REE patterns show the effect of OSM for different values of α on a melting mantle*

parcel. All computation parameters are the same described in figure 5.2.5.11. In this example, the only parameter that changes in every spidergram is α (ϕ/F) as reported in figure. Each green pattern on each spidergram represents step of 2% of melting.

Resulting trends in figures 5.2.4.11 and 5.2.4.12 are very similar to those described in figures 5.2.4.7 and 5.2.4.8. The major difference is that in this case residual cpx composition approaches the melt composition quicker than in previous case (Fig. 5.2.4.12): this is due to the different degree of modal depletion of the source that undergoes OSM as said before. In this case, cpx modal composition is lower than previous case, because the DMM has undergone 7% dynamic melting before OSM, while in the other case, DMM has undergone no dynamic melting.

A case significant to the modeling that will be applied later on the measured patterns is that of an influxing melt deriving from large degrees of melting of a DMM garnet equilibrated source. Irrespective to the significance of such a melt the resulting liquid is characterized by a strong hump in the intermediate REE (Fig. 5.2.5.13).

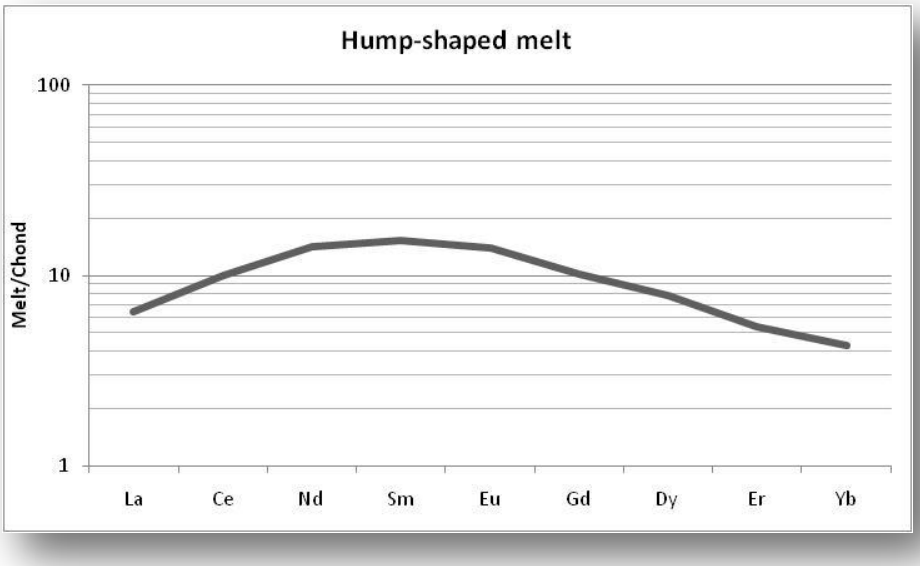

Figure 5.2.5.13 *–REE patterns of the melt used in this last model. Concentration values are normalized to CI chondrite concentration (ANDERS & GREVESSE, 1989). This hump-shaped composition has been estimated by modeling 14% melting in the garnet field of a DMM source.*

As observed in the previous examples, in case of OSM with such a melt influxing, this would be the REE pattern shape to which the system evolves. Therefore one can expect that REE humped shapes can easily be the result of such a configuration (Fig. 5.2.4.14 and 5.2.4.15).

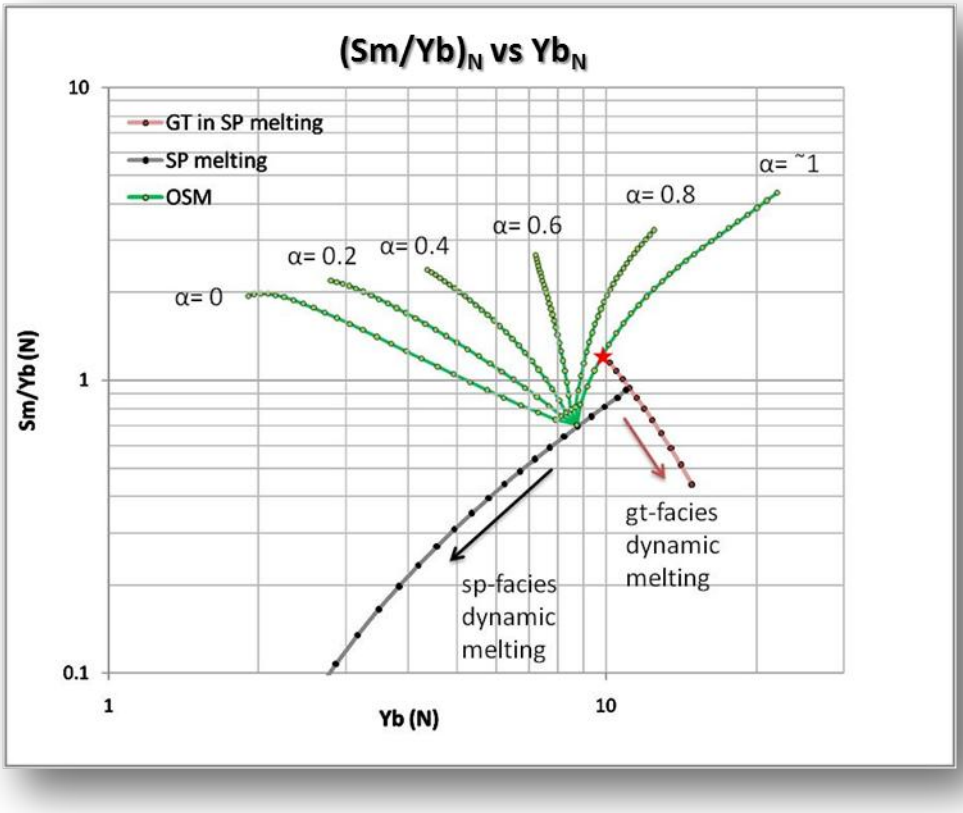

Figure 5.2.4.14 *– OSM with variable α and hump-shaped influxing melt: $(Sm/Yb)_N$ vs. $Yb_{(N)}$ in OSM from a DM source in the spinel stability field with influx of a spinel derived melt. Concentration values are normalized to CI chondrite concentrations (ANDERS & GREVESSE, 1989). DM source has undergone 3% melting in the garnet-stability field followed by 4%*

melting in the spinel stability field. The six OSM trends have been obtained varying value of α (ϕ/F) as reported in figure. All other parameters are the same of figure 5.2.5.2. For comparison, also DM in the garnet-facies melting projected in the spinel-facies (red) and DM in the spinel-facies (black) are reported. Each point on each curve represents step of 1% of melting.

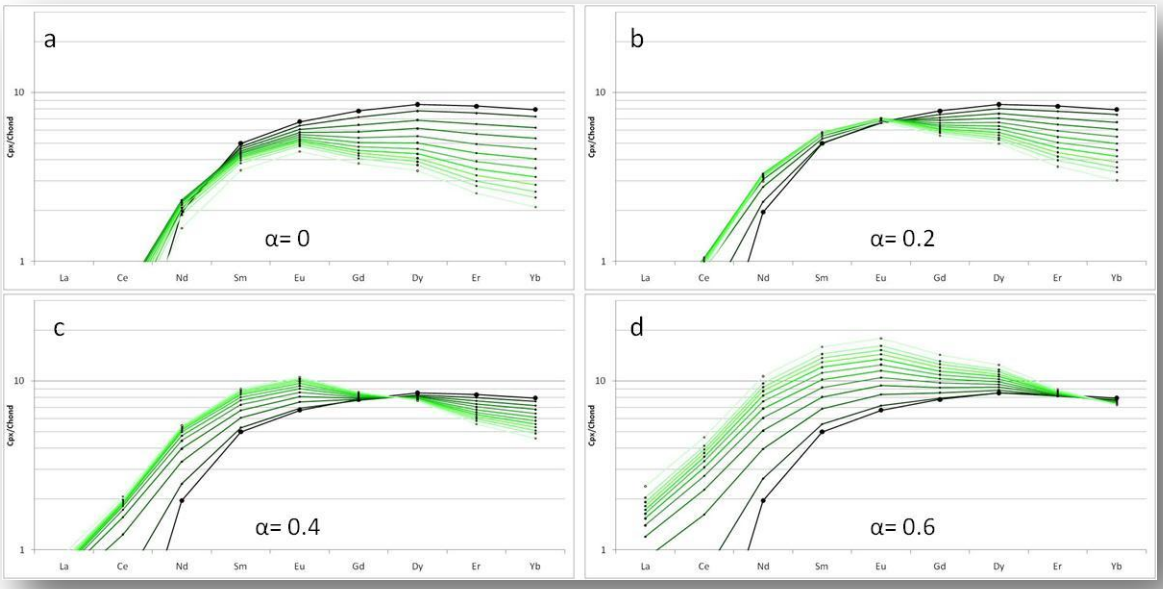

Figure 5.2.4.15 *– OSM with variable α and hump-shaped influxing melt: REEs patterns in OSM from a DM source in spinel stability field with influx of a garnet derived melt. Concentration values are normalized to CI chondrite concentration (ANDERS & GREVESSE, 1989). REEs patterns show the effect of OSM for different values of α on a melting mantle parcel. In this example, the only parameter that changes in every spidergram is α (ϕ/F) as reported in figure. Each green pattern on each spidergram represents step of 2% of melting. See figure 5.2.4.14 for other computation parameters.*

Also in this case, the REE patterns change drastically varying α. In figure 5.2.5.15 a REE pattern is reported for each value of α. Again, it is possible to see how α controls the REE

rotation point (Nd-Sm in Fig. 5.2.5.15a, Eu in Fig. 5.2.5.15b, Gd-Dy in Fig. 5.2.5.15c and Er-Yb in Fig. 5.2.5.15d) and how this can affect the displacement of the hump on these REE patterns. The enriched nature of the melt forces the rotationpoint to shift toward the HREEs.

5.3 Spinel-equilibrated peridotites from the ABFZ

REE patterns and element correlation measured in the clinopyroxenes of ABFZ peridotite are modeled in this paragraph based on the open system melting presented in the previous paragraphs.

Applying the OSM model to the real patterns also asks for adapting the composition of the influxing melt to obtain the best fit to the measured pattern. In principle one can consider the composition of the incoming melt as a completely free parameter. However while fancy patterns can be suggested, the better case is to assume as possible only those patterns that can be obtained by dynamic melting of a normal DMM. This means assuming instantaneous melt compositions as end members for the fractionated most patterns. On the other hand smoothed patterns are represented by aggregated melts. A set of synthetic melts have been calculated accordingly. The whole set of chosen melts will be discussed at the end of this chapter, in paragraph 5.5.

In all following graphs REE concentrations are reported normalized to CI chondrite values (ANDERS & GREVESSE, 1989). Hereafter, position of DM-cpx and direction of the dynamic melting curves in garnet and spinel stability field on $Sm/Yb_{(N)}$ vs. $Yb_{(N)}$ graphs have been omitted (see paragraph 5.2 for details).

B-Group samples: S2326-18 and S2325-01

Only one ABFZ sample (S2326-18) plots on a near-fractional melting curve. Using the calibration of BRUNELLI ET AL. (2006), the REE contents of this sample can be reproduced by 3% degree melting in the garnet stability field followed by 4% melting in the spinel stability field of a DMM source, with a very low critical mass porosity (ϕ = 0.002). The total amount of melting is thus 7%. Figure 5.3.1 and 5.3.2 show the best fit for the model patterns with the measured one. The La rebound of the sample has been neglected during this modeling. In fact such enrichment (often extended to Ce) is common in abyssal peridotites and is usually

attributed to local weak chromatographic effects (HELLEBRAND ET AL., 2002; BRUNELLI ET AL., 2006). Accordingly the observed La enrichment is strongly variable at the sample scale as reported in Chapter 4 (Fig. 4.2.6).

Significantly this sample is the only one for which the Na and Cr contents fall inside the compositional field of the abyssal residual peridotites (Figs. 3.2.3.3 and 3.2.3.5).

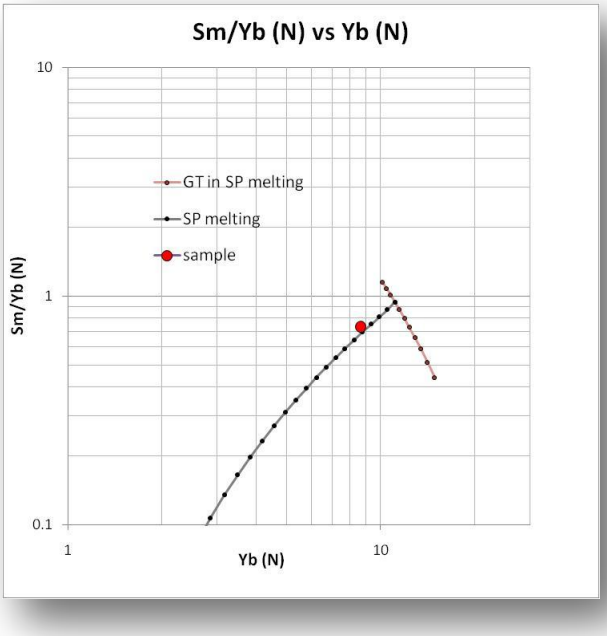

Figure 5.3.1 *– $Sm/Yb_{(N)}$ vs. $Yb_{(N)}$ for Sample S2326-18. Sm and Yb concentrations are normalized to CI chondrite concentrations (ANDERS & GREVESSE, 1989). Red line represents garnet-facies melting of a DMM source after re-equilibration in spinel-facies. Black line represents second stage melting in spinel-field. Ticks represent 1% step of melting. Red dot represents the sample. 3% dynamic melt in garnet stability field and 4% dynamic melt in spinel stability field with a very low critical mass porosity (φ = 0.002) fits well the sample.*

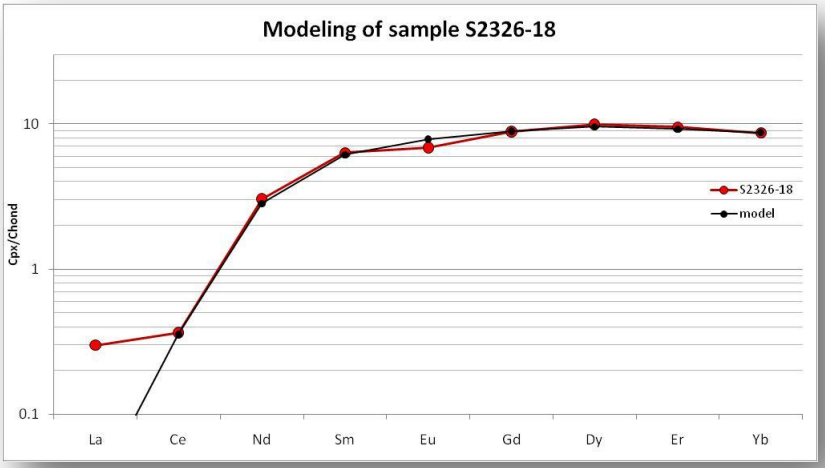

Figure 5.3.2 *– Modeling of Sample S2326-18. Red REE pattern represents sample S2326-18, black REE patterns represent model obtained using parameters reported in text. 3% dynamic melt in garnet stability field and 4% dynamic melt in spinel stability field with a very low critical mass porosity (φ = 0.002) fits well the sample. The La rebound of the sample has been neglected during this modeling: see text for details.*

Assuming that sample S2326-18 has the closest composition of a pure residue, the composition of sample S2325-01C can be modeled using S2326-18 as starting point for an OSM system (Fig. 5.3.3 and 5.3.4). The best fit to the observed pattern is given by influx of a garnet-derived melt (GRT1 in paragraph 5.5) into a melting peridotite. Assuming S2326-18 as starting point means considering a similar compositional source to be affected by OSM when it has experienced a partial melting of the same degree as shown by S2326-18, i.e. 7%. α was risen up to 0.5 and D_f is 0.5. Melting of the solid residue then continues up to 12% melting, during which the exotic melt is continuously added to the system. Considering the two samples as a single process means that porosity has increased during melting (from 0.002 for sample S2326-18 to 0.005 for sample S2325-01C). This process has for effect to decrease the HREEs and increase the LREEs, forcing the REE pattern to rotate around the Sm position (Figure 5.3.4). Then, the REE shape of sample S2325-01c can be reproduced. During this

rotation, $(Sm/Yb)_N$ increase whereas $Yb_{(N)}$ decreases, reproducing theoretical OSM trend (Fig. 5.3.3).

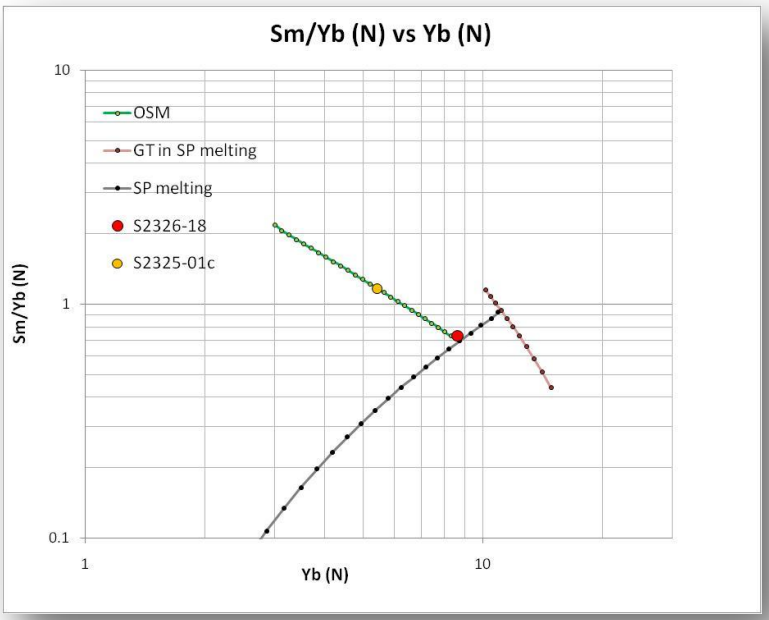

Figure 5.3.3 *– $Sm/Yb_{(N)}$ vs. $Yb_{(N)}$ in samples S2326-18 and S2325-01c. Both samples plot on the trend that has been modeled above. Red line represent garnet-facies melting projected in spinel facies, black line represents spinel-facies melting and green line is OSM. Tick points represent melting step of 1%. It is possible to notice that $(Sm/Yb)_N$ increase whereas $Yb_{(N)}$ decreases.*

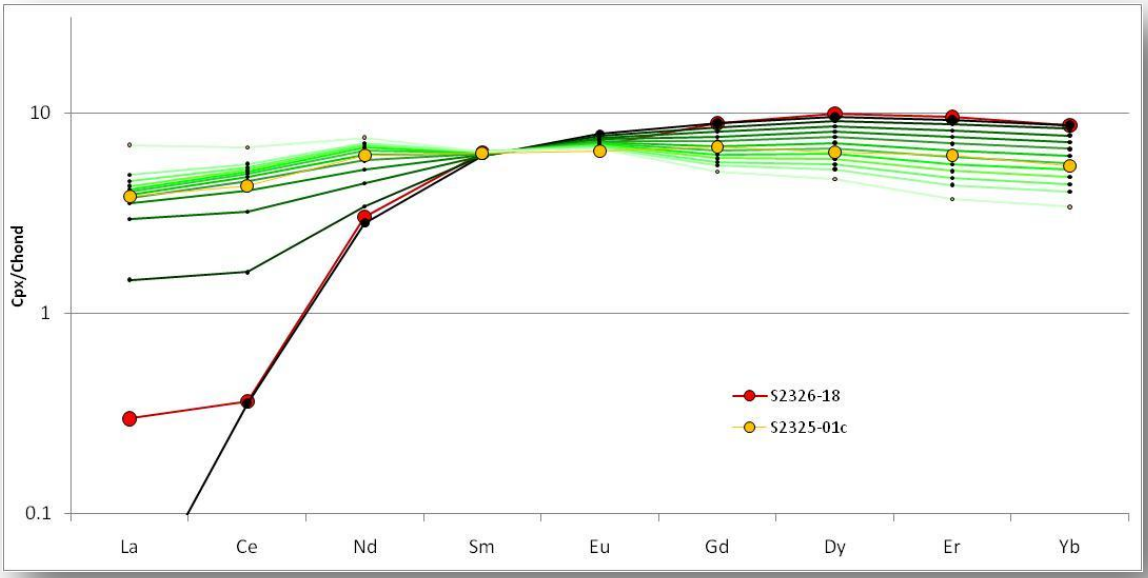

Figure 5.3.4 *– REE patterns showing modeling for B-group in spinel peridotites. Red sample is sample S2326-18 and yellow line is sample S2325-01c. Black pattern represent the modeling of sample S2326-18 as described in text: this residual composition has been considered the point where the OSM started. Green lines represent steps of 1% melting in open system: OSM starts from the black patter in figure and follows the green lines, from the darkest green to the lighter green. This process has for effect to decrease the HREEs and increase the LREEs, forcing the REE pattern to rotate around the Sm position. Both samples are fitted by the modeled trend.*

Group A2: Samples S2325-08, S2326-15 S2326-16 and S2326-24

REE compositions in cpx from group A2 peridotites can be fitted considering a DM parcel that have melted in closed-system of 5% in the garnet stability field, followed by the melt influx of exotic melt with a garnet-derived melt composition (GRT2 in paragraph 5.5, see paragraph for explanation), then OSM has continued up to further 8% melting, where the two endmembers of this group plot, (S2326-24 and S2325-08 see figure 5.3.5). GRT2 melt composition is necessary to reproduce the L-REE concentration values: more enriched melt would lead to too high L-REE concentrations, whereas more depleted melt would lead to too

low L-REE values. α value is 0.6, that means that the stagnation of melt inside the mantle parcel is higher than normal, while D_f is 0.9, suggesting a low degree of mixing between exotic melt and resident melt. The process has for effect to decrease the HREEs and increase the LREEs, forcing the REE pattern to rotate around the Dy position (Figure 5.3.7). Then, the REE shape of B-Group samples can be reproduced.

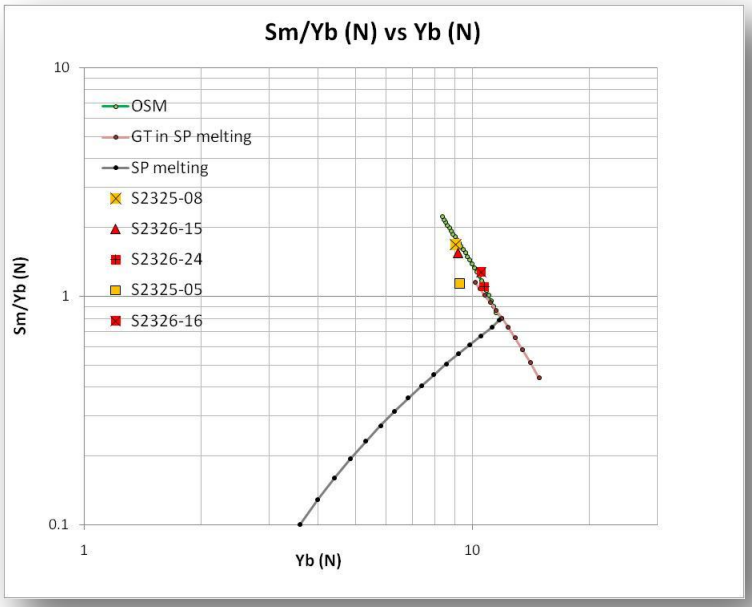

Figure 5.3.5 *– $Sm/Yb_{(N)}$ vs. $Yb_{(N)}$ in samples from A2-Group. All samples plot on the trend that has been modeled and described in text above. Red line represent garnet-facies melting projected in spinel facies and black line represents spinel-facies melting, and tick points represent melting step of 1%. Green line is OSM and tick points represent melting step of 0.5%. It is possible to notice that $(Sm/Yb)_N$ increases whereas $Yb_{(N)}$ decreases.*

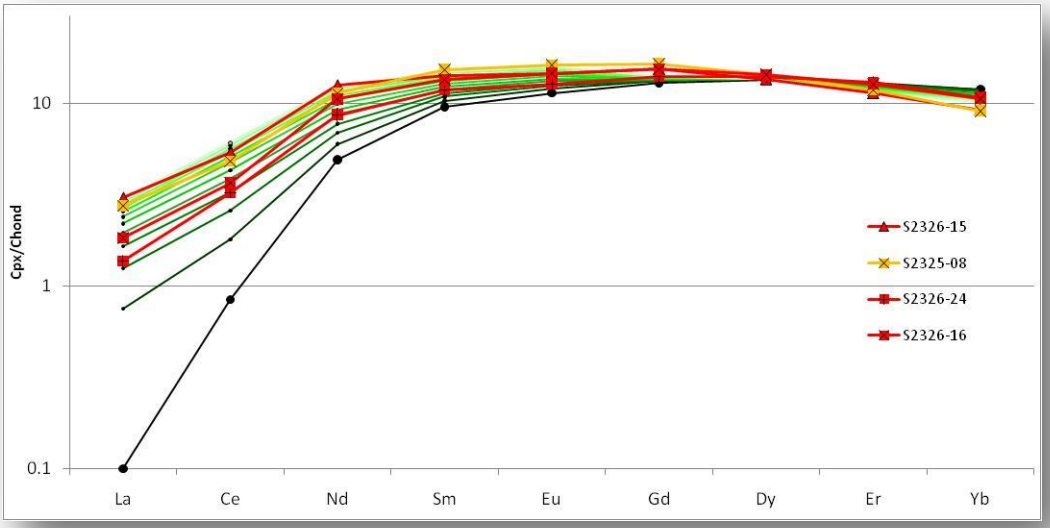

Figure 5.3.6 *– REE patterns showing modeling for A2-group in spinel peridotites. Samples reported in figure are the ones representative of this group. Black pattern represent the point at which OSM took place, i.e. after 5% melting in garnet stability field. Green lines represent steps of 1% melting in open system: OSM starts from the black pattern in figure and follows the green lines, from the darkest green to the lighter green. This process has for effect to decrease the HREEs and increase the LREEs, forcing the REE pattern to rotate around the Dy position. A2-group samples are fitted by the modeled trend.*

A1-Group: Samples S2324-01 and S2325-03

Samples S2324-01 and S2325-03 are the furthest ABFZ samples from the fractional melting trend. In Chapter 4 they have been proposed as possibly pertaining to the same trend of A2-group samples (see figure 4.2.3 and related description in text). However they need a more H-REE depleted residue to justify the low concentration of H-REE. For this reason, they can no more be considered linked to A2-group, a high degree of melting in spinel stability field being necessary to decrease H-REE content.

Starting from sample S2324-01 (figure 5.3.7 and 5.3.8), its REE concentration can be obtained considering, first of all, a mantle parcel that has underwent a high degree of melting, more precisely a mantle portion that has underwent 1% melting in garnet stability

field and 12% melting in the spinel stability field at closed system melting, for a total of 13% melting. Then, a first influx of a garnet-derived melt (GRT2 in paragraph 5.5) has occurred, and OSM continued for other 8% melting in spinel stability field. The critical mass porosity has risen from low values (0.2%) till higher values (0.5%), α being 0.5 at the end of the process.

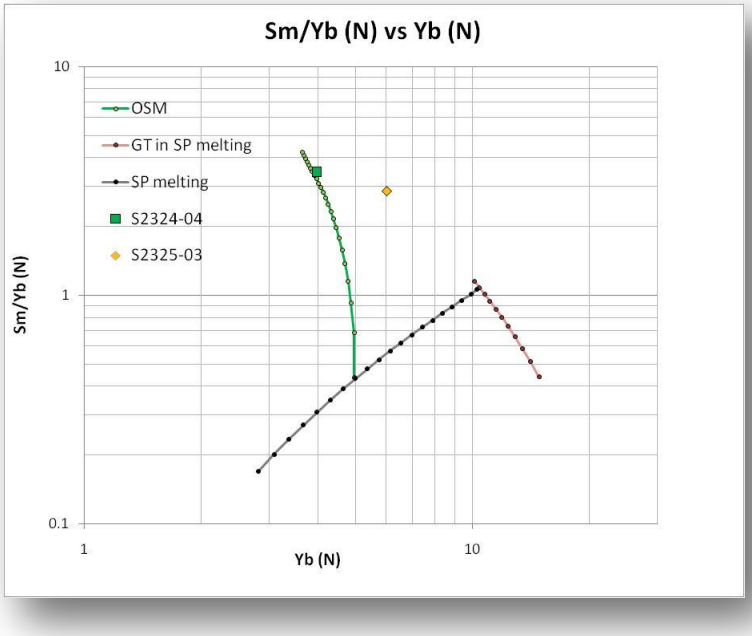

Figure 5.3.7 *– $Sm/Yb_{(N)}$ vs. $Yb_{(N)}$ in cpx of sample S2324-01 from A1-Group. Sample plot on the trend that has been modeled and described in text above. Red line represent garnet-facies melting projected in spinel facies and black line represents spinel-facies melting, and tick points represent melting step of 1%. Green line is OSM and tick points represent melting step of 0.5%. It is possible to notice that $(Sm/Yb)_N$ strongly increases whereas $Yb_{(N)}$ slightly decreases.*

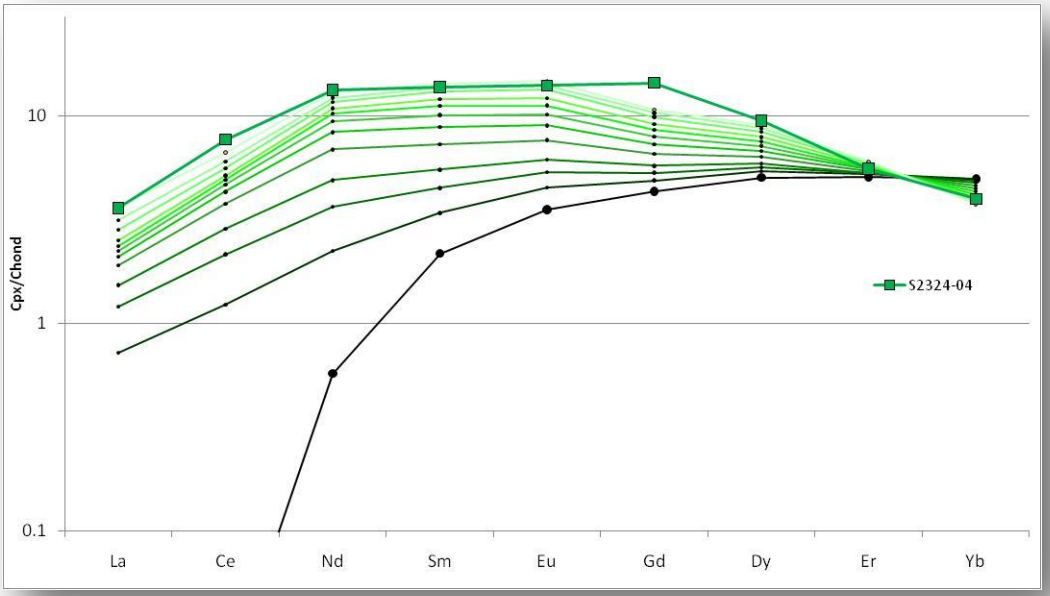

Figure 5.3.8 *– REE patterns showing modeling for cpx of S2324-01 sample in spinel peridotites. Black pattern represents the point at which OSM in this case took place, i.e. after 1% melting in garnet stability field and 12% melting in spinel stability field. Green lines represent steps of 1% melting in open system: OSM starts from the black patter in figure and follows the green lines, from the darkest green to the lighter green. This process has for effect to produce an enrichment in M-REE, resulting in a hump-shaped patter. In this case a depleted starting point for OSM is necessary to obtain the depletion in H-REE. Moreover, a relatively L-REE depleted melt guarantees only M-REE to be enriched.*

Considering now sample S2325-03, to reproduce its REE composition a depleted residue is also needed, because the H-REEs are strongly depleted. Its cpx REE pattern, in fact, can be fitted considering a mantle parcel that underwent 1% melting in garnet stability field followed by 10% melting in spinel-facies. After this close-system melting, a first influx of a L-REE depleted garnet derived melt (GRT3 in paragraph 5.5), then OSM continued for 9% melting in spinel stability field (Fig. 5.3.9 and 5.3.10). In this case, ϕ value was raised from 0.002 to 0.006, and α was 0.6.

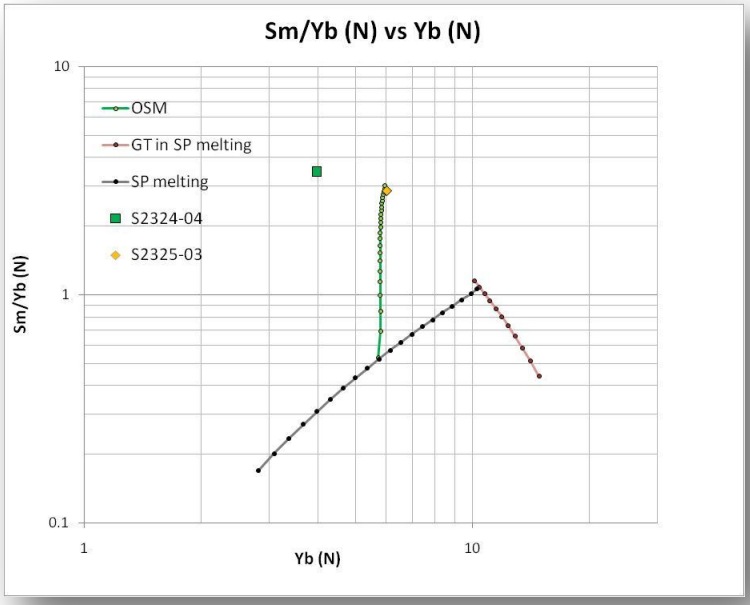

Figure 5.3.9 *– $Sm/Yb_{(N)}$ vs. $Yb_{(N)}$ in sample S2325-03 from A1-Group. Sample plot on the trend that has been modeled and described in text above. Red line represent garnet-facies melting projected in spinel facies and black line represents spinel-facies melting, and tick points represent melting step of 1%. Green line is OSM and tick points represent melting step of 0.5%. It is possible to notice that $(Sm/Yb)_N$ strongly increases whereas $Yb_{(N)}$ is stables. All computation parameters are very similar to those used in modeling of sample S2324-01 (see text for details).*

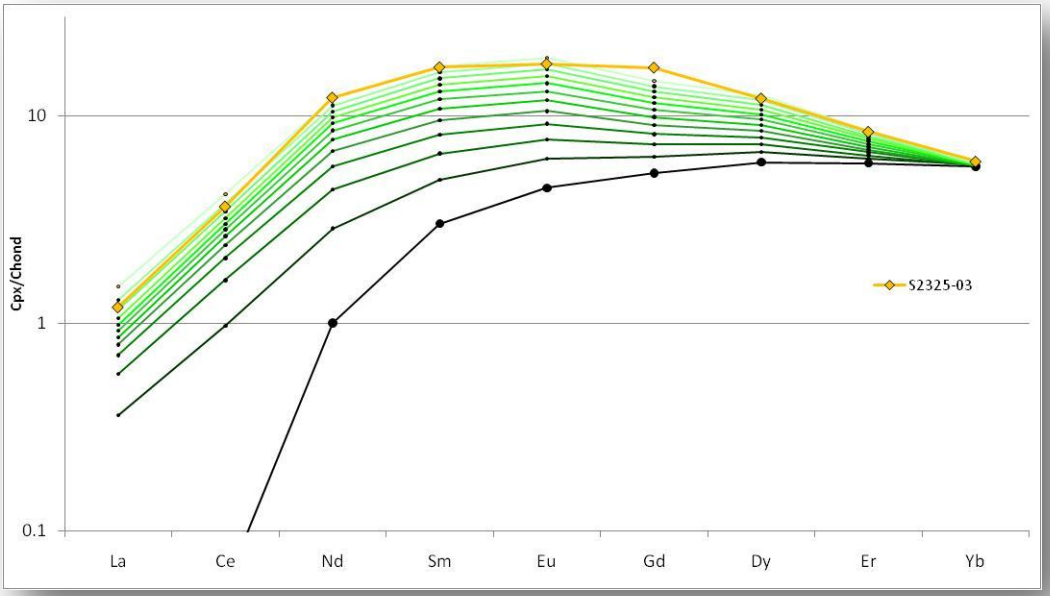

Figure 5.3.10 *– REE patterns showing modeling for cpx of S2325-03 sample in spinel peridotites. Black pattern represents the point at which OSM in this case took place, i.e. after 1% melting in garnet stability field and 10% melting in spinel stability field. Green lines represent steps of 1% melting in open system: OSM starts from the black patter in figure and follows the green lines, from the darkest green to the lighter green. This process has for effect to produce an enrichment in M-REE, resulting in a hump-shaped patter. In this case a depleted starting point for OSM is necessary to obtain the depletion in H-REE. Moreover, a L-REE depleted melt guarantees only M-REE to be enriched. All parameters of computation are the very similar to S2324-01 modeling.*

These calculations show that cpx REE hump-shaped patterns of the two samples can be reproduced only if they underwent high degree of melting in dynamic melting regime before infiltration of exotic melt. Mineral major element compositions also suggest that both samples have undergone a high degree of melting, higher degree of melting needed for sample S2324-01 relative to sample S2325-03 (for example, considering an indicator of degree of melting as Cr# in spinel, respectively 35.88 and 31.20, see figure 3.2.4.1). The main

difference between the two samples is represented by the α value of the OSM, accompanied by a slightly different influxing melt composition, L-REE depleted for sample S2325-03. This means the two mantle parcels to have experienced a similar process only differing slightly in the fractional character being melt extraction more effective for sample S2324-01 than for sample S2325-03.

5.4 Plagioclase-bearing peridotites from the ABFZ

Reactive percolation and refertilization in the plagioclase field

The textural relationships of the plagioclase equilibrated samples tells that recovered samples undergone percolative reaction and extensive melt retention (see paragraph 2.3.3 for details). The petrographic relationships never show evidence for consumption of the plagioclase phase suggesting that no melting has undergone under plagioclase facies conditions. Instead plagioclase crystallization always occurs interstitially or vein like assemblages.

Accordingly plagioclase equilibrated samples have been modeled by simple melting followed by spinel breakdown and then refertilization of a basaltic component.

Computational steps followed for this model are the following:

1. Dynamic melting of a DMM bulk composition over the garnet and spinel fields using the calibration proposed in the previous section. The total amount of melting is tuned for each sample in order to obtain the composition better approaching the measured one;
2. Addition of a variable amount of melt: defining R the total amount in volume of refertilizing melt added, solid volume has been considered 1-R and source enrichment has been calculated. The liquid is assumed to crystallize pl and cpx in the same proportion.
3. Re-equilibration of the residue from spinel-stability field to plagioclase-stability field, using reaction proposed by TAKASAWA ET AL, 1996:

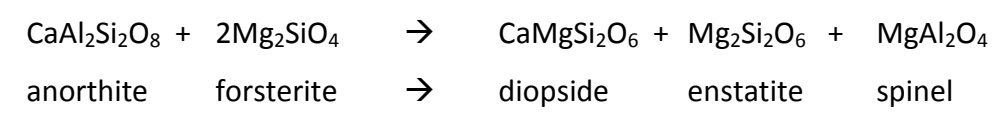

This sequence does not cast interpretation on the true sequence of events experienced by the rock. In fact the spinel to plagioclase breakdown is probably forced by the impregnation event itself. Accordingly plagioclase coronas around spinel are always accompanied by

textural evidence for melt percolation in the plagioclase field (e.g. interstitial plagioclase, see chapter 2). Assuming the two events are separated does not affect the actual trace element distribution.

The estimated degrees of melting of the rock before plagioclase field impregnation are less striking than those estimated for spinel equilibrated peridotites. There is a major incertitude due to the fact that the amount of melt retained in the source is usually large as shown by petrography (chapter 2). The large melt retention tends to mask the former compositional variability then reducing the significance of any reconstructed composition. In the proposed approach the amount of estimated retained melt is minimized by assuming the residual composition to be the closest to the measured one prior the plagioclase melt retention occurred. This approach while underestimating the melt retention also results in underestimating the degree of melting because part of the late stage refertilization can be unresolved. Thus the estimated degrees of melting should be taken as minima, as well as the degree of refertilization, for any given refertilizing composition. Inferences after this modeling have thus a more qualitative character than those obtained after modeling of spinel field equilibrated rocks.

In all following graphs cpx REE concentrations are reported normalized to CI chondrite (ANDERS & GREVESSE, 1989). Hereafter, position of DM-cpx and direction of the dynamic melting curves in garnet and spinel stability field on $Sm/Yb_{(N)}$ vs. $Yb_{(N)}$ graphs have been omitted (see paragraph 5.2 for details).

In the following modeling results, it can be noticed that spinel breakdown causes a shift toward higher Yb contents in the composition of residual cpx in a $(Sm/Yb)_{(N)}$ vs. $Yb_{(N)}$ diagram (Fig. 5.4.1). The shift is an effect of the LREEs being more compatible than HREEs in plagioclase resulting in an increase of H-REEs with respect to L-REEs in associated cpx also causing the formation of a weak Eu negative anomaly (Fig. 5.4.2). However the observed shifts is not always large enough to make the measured values plot out of the compositional region related to partial melting. Similarly some REE patterns closely resemble those obtainable from simple (or complex) melting processes. If from one side this makes hard to

recognize cryptic plagioclase impregnation events, on the other side may induce to underestimate the degree of re-equilibration in the plagioclase facies. For that reason, also considering the large uncertainty in the modeling process itself, all the samples showing modal plagioclase are considered to be fully equilibrated in the plagioclase field and consequently modeled following the proposed procedure.

Sample S2326-02 representative of dredge S2326 bearing peridotites

The best fit for the S2326 plagioclase-bearing peridotites is given by a mantle parcel melted up to 3% in the garnet stability field, followed by 2% melting in the spinel field and plagioclase field impregnation by an aggregated melt produced in the spinel stability field characterized by a weak garnet fingerprint (GT-SP melt in paragraph 5.5). Estimated volume of melt that has crystallized in the host peridotites ranges 1-9 % varying from sample to samples.

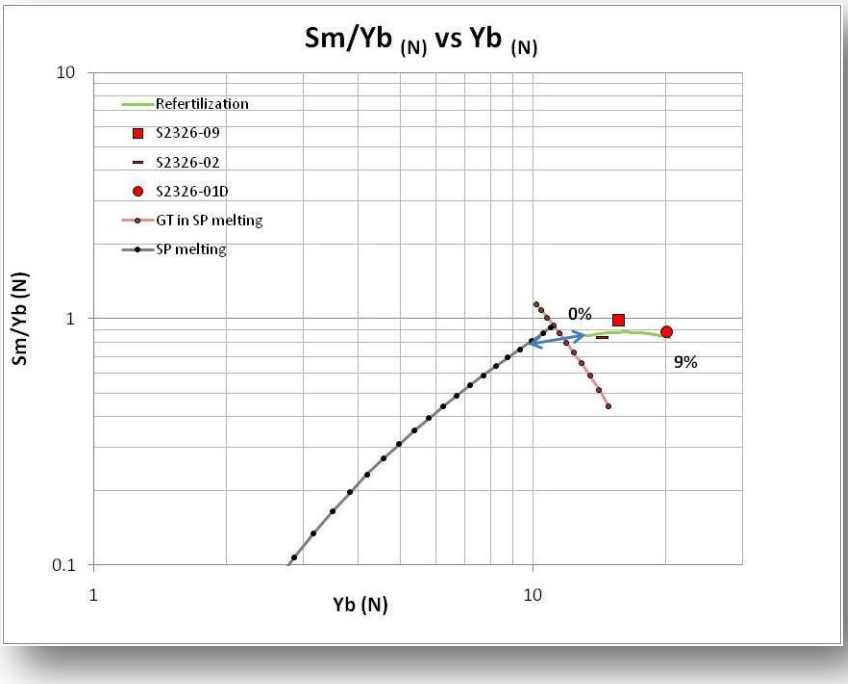

Figure 5.4.1 *– $Sm/Yb_{(N)}$ vs. $Yb_{(N)}$ in plagioclase-bearing samples from dredge S2326. All samples plot on the trend that has been modeled and described in text above. Red line*

represent garnet-facies melting projected in spinel facies and black line represents spinel-facies melting, and tick points represent melting step of 1%. Blue arrow represents the projection of a spinel-equilibrated cpx into the plagioclase-facies, starting from the residual cpx composition to the composition of spinel-equilibrated cpx projection in plagioclase-facies. Green line is the refertilization trend that moves away from the melting trend: 0% and 9% indicate the total mass fraction added to the residual solid. It is possible to notice that $(Sm/Yb)_N$ *is constant, whereas* $Yb_{(N)}$ *increases.*

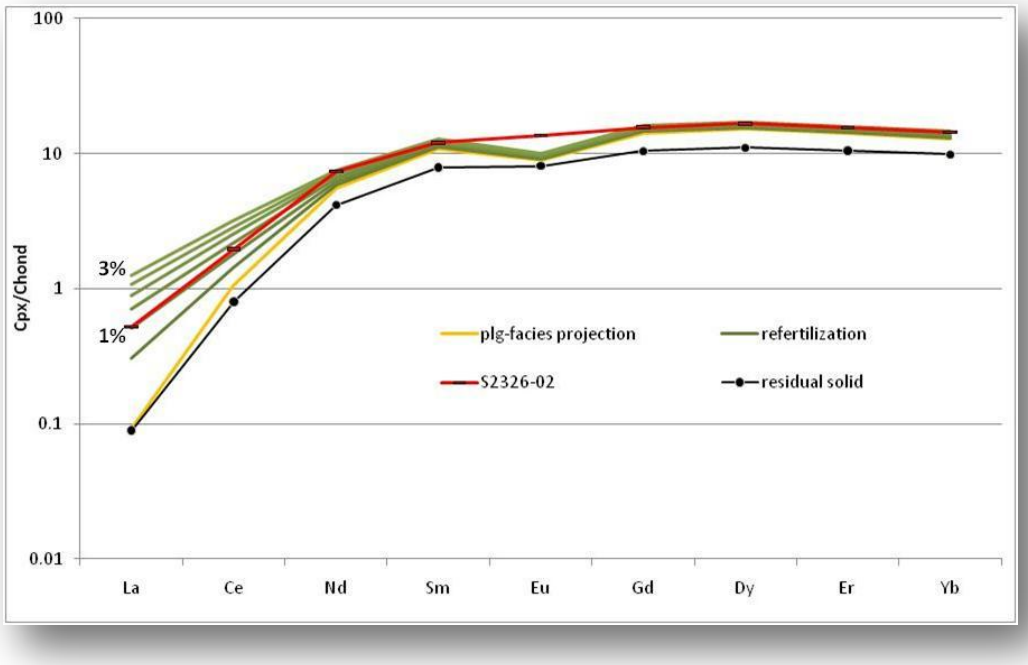

Figure 5.4.2 *– REE patterns showing modeling for sample S2326-02, representative of the plagioclase-bearing peridotites from dredge S2326. Black pattern represent the cpx REE pattern composition of residual cpx after 3% melting in garnet stability field followed by 2% melting in spinel stability field. Yellow line represent the REE shifting occurring during the reaction of spinel breakdown in plagioclase facies. Red pattern represents the sample S2326-02. Green patterns represent 0.5% steps of refertilization: for simplicity, in figure only the patterns needed to model sample S2326-02 have been reported. Although sample S2326-02 does not show the Eu negative anomaly proposed by the model patterns, other plagioclase-*

bearing peridotite from this dredge are characterized by such a feature (see figure 4.3.2 in chapter 4).

Dredge S2318 plagioclase-bearing peridotites

Sample S2318-31

Cpx composition of sample S2318-31 has been modeled considering the best fit for a mantle parcel after 5% melting in garnet-stability field followed by 3% melting in spinel stability field. At this point, spinel breakdown has been accounted for, followed by refertilization by an aggregated melt produced in spinel stability field characterized by a weak garnet fingerprint (GT-SP melt in paragraph 5.5). Sample cpx composition values can be reached after adding 2% in volume of the considered melt (Fig. 5.4.3 and 5.4.4).

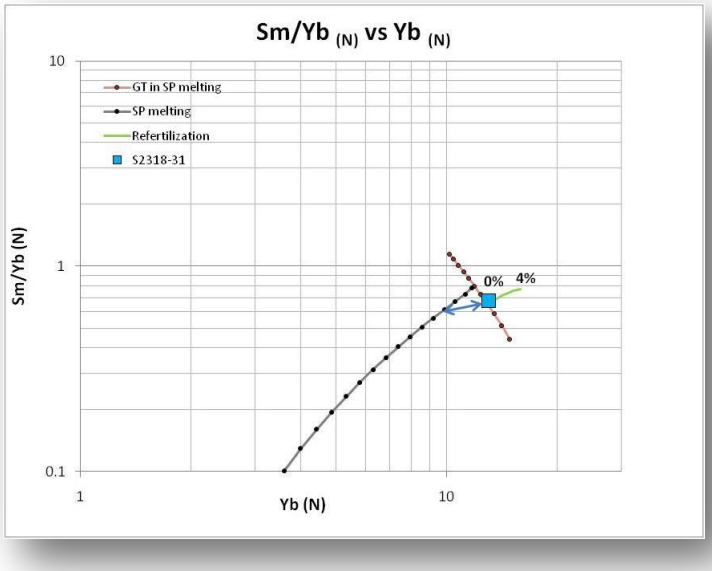

Figure 5.4.3 *– $Sm/Yb_{(N)}$ vs. $Yb_{(N)}$ in cpx from sample S2318-31. All samples plot on the trend that has been modeled and described in text above. Red line represent garnet-facies melting projected in spinel facies and black line represents spinel-facies melting, and tick points represent melting step of 1%. Blue arrow represents the projection of a spinel-equilibrated*

cpx into the plagioclase-facies, starting from the residual cpx composition to the composition of spinel-equilibrated cpx projection in plagioclase-facies. Green line is the refertilization trend that moves away from the melting trend: 0% and 4% indicate the total mass fraction added to the residual solid.

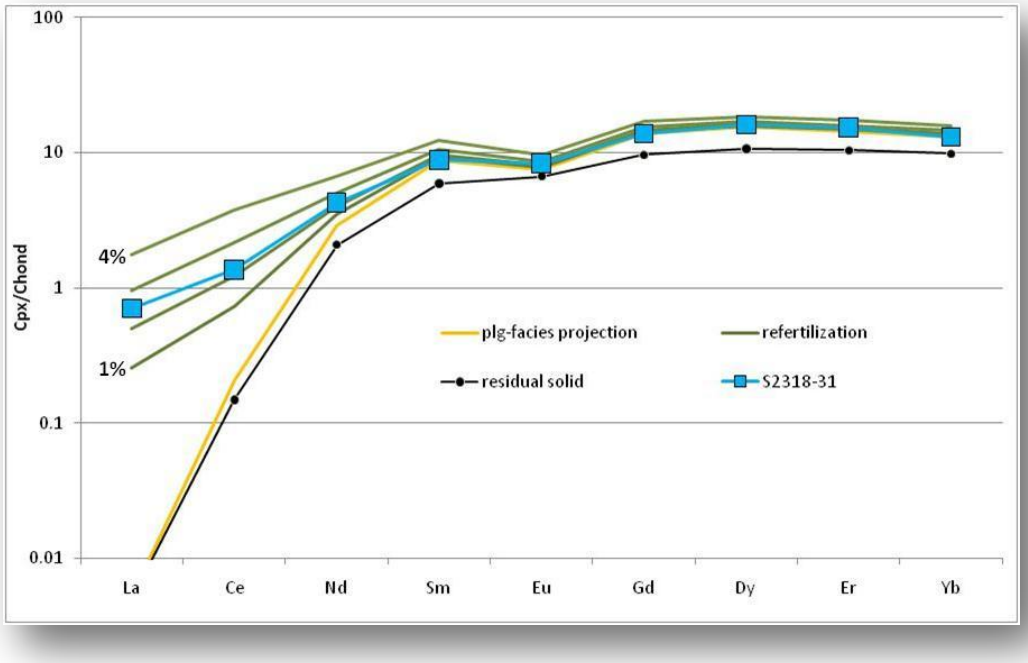

Figure 5.4.4 *– Cpx REE patterns showing modeling for sample S2318-31. Black pattern represents the cpx REE pattern composition of residual cpx after 5% melting in garnet stability field followed by 3% melting in spinel stability field. Yellow line represent the REE shifting occurring during the reaction of spinel breakdown in plagioclase facies. Blue patters represent the modeled sample. Green patterns represent 1% steps of refertilization.*

Sample S2318-35

Sample S2318-35 is the only sample from dredge S2318 that can be best modeled accounting for no melting in garnet-stability field. In fact, its cpx concentration can be modeled starting from a DMM that underwent 10% melting in spinel-stability field. After this

melting event, spinel breakdown has occurred, followed by an interaction of an aggregated melt produced in spinel stability field (SP melt in paragraph 5.5). Sample cpx composition values can be reached adding 2% in volume of the considered melt (Fig. 5.4.5 and 5.4.6).

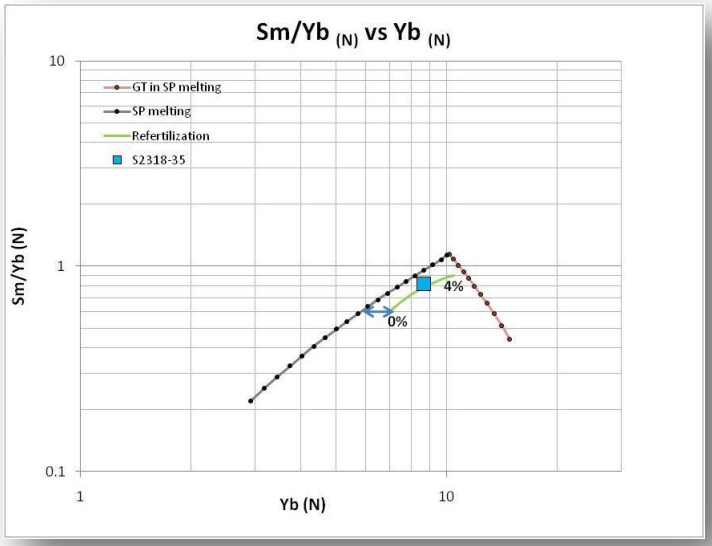

Figure 5.4.5 *– $Sm/Yb_{(N)}$ vs. $Yb_{(N)}$ in cpx from sample S2318-35. All samples plot on the trend that has been modeled and described in text above. Red line represent garnet-facies melting projected in spinel facies and black line represents spinel-facies melting, and tick points represent melting step of 1%. Blue arrow represents the projection of a spinel-equilibrated cpx into the plagioclase-facies, starting from the residual cpx composition to the composition of spinel-equilibrated cpx projection in plagioclase-facies. Green line is the refertilization trend that moves away from the melting trend: 0% and 4% indicate the total mass fraction added to the residual solid during model runs.*

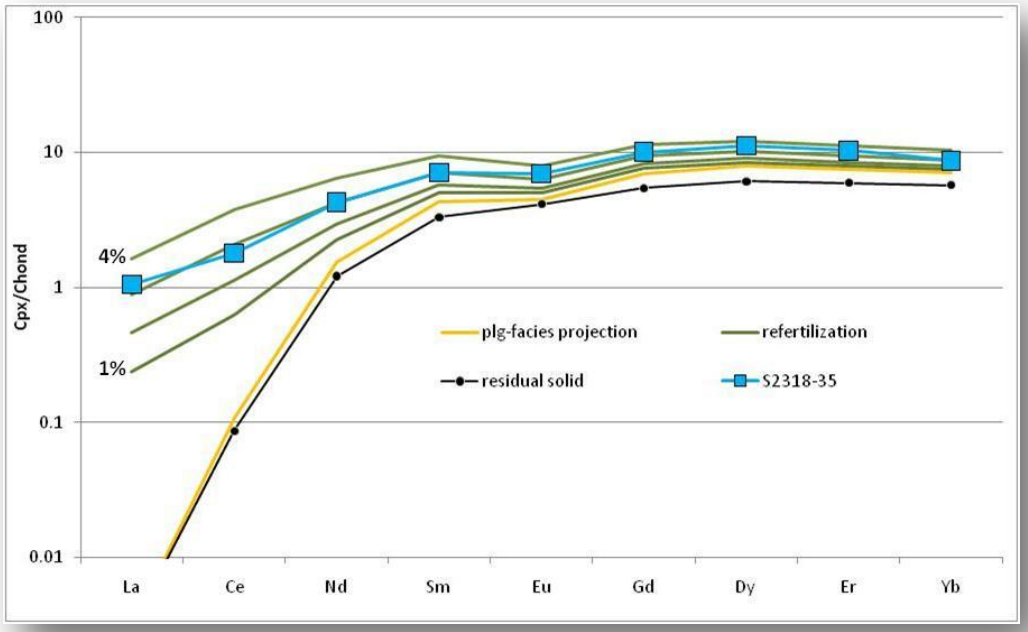

Figure 5.4.6 *– Cpx REE patterns showing modeling for sample S2318-35. Black pattern represents the cpx REE pattern composition of residual cpx after 10% melting in spinel stability field. Yellow line represent the REE shifting occurring during the reaction of spinel breakdown in plagioclase facies. Blue patters represent the modeled sample. Green patterns represent 1% steps of refertilization.*

Sample S2318-28 and sample S2318-49

Inside the dredge S2318 peridotites, these two samples can be modeled using the same parameters. The two cpx REE patterns, in fact, appear very similar (figure 4.3.3 in chapter 4). To obtain the best fit of their cpx compositions, a residual source has been obtained considering a mantle parcel after 6% melting in the garnet-stability field and 10% melting in the spinel-stability field. After this melting event, spinel breakdown has been calculated, followed by interaction with an aggregated melt produced in spinel stability field characterized by a weak garnet fingerprint (GT-SP melt in paragraph 5.5). Model has run for an amount of melt considered for residue refertilization up to 9%: sample S2318-28

composition can be reached after 4% addition of the considered melt and sample S2318-49 composition can be reached considering an addition of 8% (Fig. 5.4.7 and 5.4.8).

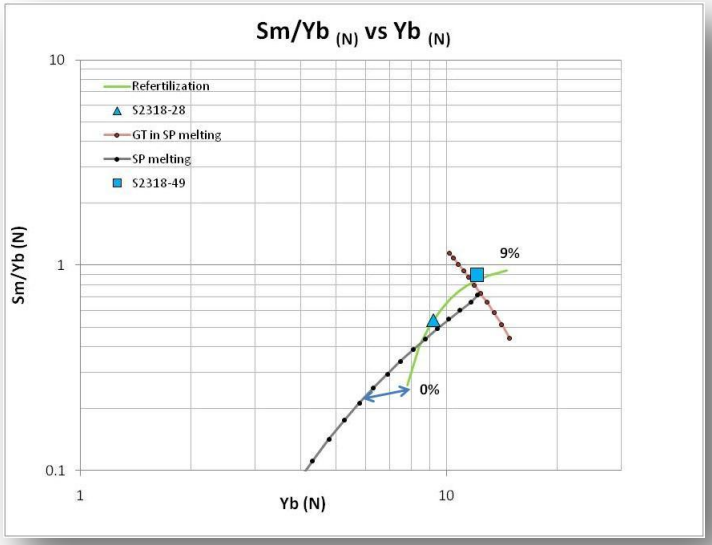

Figure 5.4.7 *– $Sm/Yb_{(N)}$ vs. $Yb_{(N)}$ in samples S2318-28 and S2318-49 from dredge S2326. All samples plot on the trend that has been modeled and described in text above. Red line represent garnet-facies melting projected in spinel facies and black line represents spinel-facies melting, and tick points represent melting step of 1%. Blue arrow represents the projection of a spinel-equilibrated cpx into the plagioclase-facies, starting from the residual cpx composition to the composition of spinel-equilibrated cpx projection in plagioclase-facies. Green line is the refertilization trend that moves away from the melting trend: 0% and 9% indicate the total mass fraction added to the residual solid. It is possible to notice that both $(Sm/Yb)_N$ and $Yb_{(N)}$ increase.*

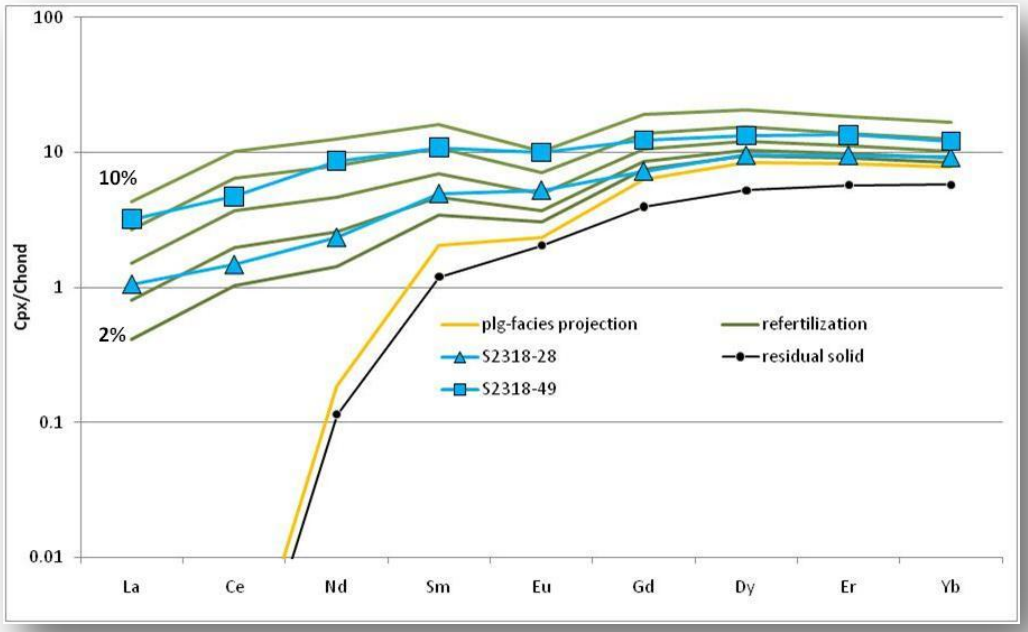

Figure 5.4.8 *– REE patterns showing modeling for samples S2318-28 and S2318-49. Black pattern represent the cpx REE pattern composition of residual cpx after 6% melting in garnet stability field followed by 10% melting in spinel stability field. Yellow line represent the REE shifting occurring during the reaction of spinel breakdown in plagioclase facies. Blue patters represent the two modeled samples. Green patterns represent 2% steps of refertilization.*

5.5 Compositions of the melts used during modeling

Modeling with OSM required assuming the composition of the influxing melt. Considering the ensemble of the used melts may give some constrain on the melting process itself. As introduced at the beginning of the paragraph 5.3 the composition of the melts has been forced to a realistic case of DMM derived melts. It is worth noting that the choice of a melt composition is constrained from the observed enrichment and ultimately from the observed rotation of the pattern pertaining to a same group.

In table 5.5.1 all REE concentration values (ppm) are reported, while in figure 5.5.2 their REE patterns have been normalized to CI chondrite concentration (ANDERS & GREVESSE, 1989).

	La	Ce	Nd	Sm	Eu	Gd	Dy	Er	Yb
GRT1	11.99	31.13	15.7	2.89	0.86	1.93	1.77	0.75	0.61
GRT2	2.72	10.69	9.93	2.59	0.83	1.97	1.85	0.8	0.65
GRT3	1.53	6.1	6.43	2.25	0.79	2.02	1.94	0.86	0.69
GR-SP	1.85	6.06	5.39	1.98	0.79	2.89	3.6	2.31	2.32
SP	1.78	7.12	7.5	2.64	1	3.48	4.22	2.67	2.68

Table 5.5.1 *– REE concentrations (ppm) in melts used during modeling. Coded names of liquids are arranged as follow: "GRT1", "GRT2", "GRT3" represent garnet-derived melt instantaneously extracted from a DMM source that has already experienced respectively 1%, 8% and 14% melting in garnet stability field. "SP" represents a spinel derived melts that has been aggregated over a range of melting of 1% to 15% of a DMM source. "GR-SP" represent an aggregated melt formed by aggregation of a garnet-derived melt produced in the melting range of 1% to 5% melting in the garnet stability field and by aggregation of a spinel-derived melt produced in the melting range of 1% to 15% melting in the spinel stability field of the same DMM source. For observation about concentrations, see text and caption of figure 5.2.4.2.*

The melts used during modeling are divided in two different families (Fig. 5.5.2).

Garnet-derived melts are red coded: they show an enrichment in L-REE in case of few degrees of melting and an enrichment in M-REE for large degrees of melting. H-REE are constant, regardless of the degree of melting. Liquids produced in the garnet stability field are only fractionated for the LREE being the HREE balanced by the opposite behavior of the coexisting garnet and clinopyroxene phases. HREE are in fact compatible in garnet and incompatible in cpx (WESTRENEN ET AL., 2001; JOHNSON, 1998; NICHOLLS & HARRIS; 1980). High degrees of melting of a DMM source in the garnet stability field are unrealistic, but this feature will be discussed in the next chapter.

Black and grey (Fig, 5.2.2) aggregated melts that account for a spinel-field derived component, differ mainly by the degree of enrichment shifting parallel depending on the aggregation length. Melts generated by a garnet-free source are characterized by flat (or near-flat) HREEs, even if they are mix with a small volume of garnet-derived melt, as the case of melt of composition GT-SP in figure 5.5.2.

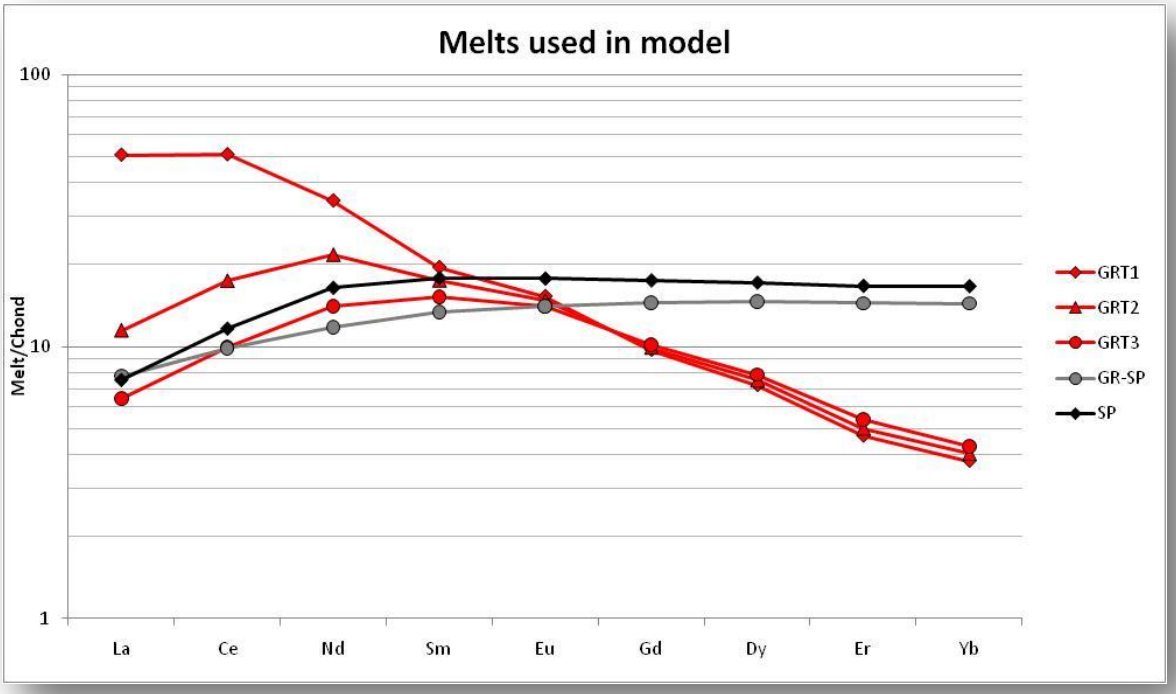

Figure 5.5.2 *– Normalized REE spidergrams of melts used during modeling. For codes meaning, see caption of figure 5.5.1. Red coded patterns represent concentrations of garnet-derived melts: H-REE are stable because these trace elements are retained inside the garnet, leading to a relative depletion in cpx composition; L-REE concentration progressively decreases because during melting (1%, 8% and 14% degrees of melting for respectively GRT1, GRT2 and GRT3in figure) most incompatible elements are preferentially extracted, leaving cpx with less incompatible elements. Other patterns represent (more evolved) aggregated melts over different degree of melting, in particular from spinel-facies (SP melt in figure) that show flat H-REEs even if mixed with small amount of garnet-derived melts (GT-SP in figure).*

5.6 Concluding remarks

1. Almost all samples started to melt in the garnet stability field. Moreover, majority of samples has experienced a low degree of partial melting, as expected by areas with anomalously thick lithosphere and strong cold-edge effects (LIGI ET AL., 2006;)
2. Samples collected at ridge axis have undergone an overall higher degree of melting with respect to the samples collected at transform wall.
3. Melts that have interacted with the peridotites often come from the garnet stability field or have a garnet-derived component.
4. Spinel field equilibrated rocks from the transform wall have interacted with primitive melts, suggesting that this interaction took place deeper in the melting region.
5. Plagioclase field equilibrated samples collected from the ridge axis, have interacted with more evolved, aggregated melts, according with a melt/rock interaction occurring in the shallower part of the melting column.
6. Some of the plagioclase-bearing peridotites of dredge S2326 have interacted with evolved melts even in a mega-transform environment.
7. Open System Melting modeling of the spinel field equilibrated peridotites reveals high values of ϕ/F, suggesting that melt extraction was inhibited and stagnation of melt beneath ABFZ is extremely high. The absence of a continuous basaltic crust would possibly be paired by melt retention at depth.

Chapter 6

Conclusion

6.1 – General discussion and conclusion

Model results overall suggest that the majority of samples from ABFZ have started melting very deep beneath the sea-floor. Observed element pattern agrees with melting starting in the garnet stability field then continuing in the spinel field. Modeling also suggests that after a variable (although restricted) amount of melting, an exotic and variably enriched melt entered the system. Computed melt compositions requires the exotic melt to be generated in the garnet facies. The source of the enriched melt is however not defined because of the required composition cannot be unequivocally produced by a given lithology. The incompatible enriched trace element pattern can in fact be generated by extensive melting of a lithological heterogeneity or by low degrees of melting of a DMM source. A first kind of

liquid (for example, GRT1, see paragraph 5.5 in chapter 5) possibly derives from a normal DMM while a second kind of melt (for example, GRT3, see paragraph 5.5 in chapter 5) requiring such a large extent of melting cannot be formed from a DMM lherzolite because there is not enough heat to reach such high degrees of melting. Instead it can be produced by a fertile grt/cpx rich heterogeneity. Such a high melting degree is not allowed for a normal thermal setting, instead this possibly represents an evidence for an enriched heterogeneity to be melted extensively in presence of garnet. Those kinds of heterogeneities are possibly represented by garnet pyroxenites, inherited remnants of ancient subducted crust, present as veins in peridotitic mantle or as eclogites (HIRSCHMANN & STOLPER, 1996; BODINIER ET AL., 2008; MACGREGOR & MANTON, 1986; TAYLOR & NEAL, 1989; SOBOLEV ET AL., 2007, HANAN ET AL., 2004, REHKAMPER & HOFMANN, 1997).

These observations are suggestive of a melting scenario where a lithology with a solidus lower than DMM, melts deeper with respect to the ambient mantle peridotite and generates the exotic melts that flow through the observed mantle portion. Considering the simplest example, i.e. a double lithology source, the component characterized by the lowest solidus will melt first. Usually these low-solidus lithologies are assumed to be pyroxenites or eclogites but blobs of more fertile peridotites resulting from metasomatic reactions can be also considered (WARREN ET AL., 2009) (Figure 6.1.1). This mechanism gives the melt supply needed for an OSM scenario.

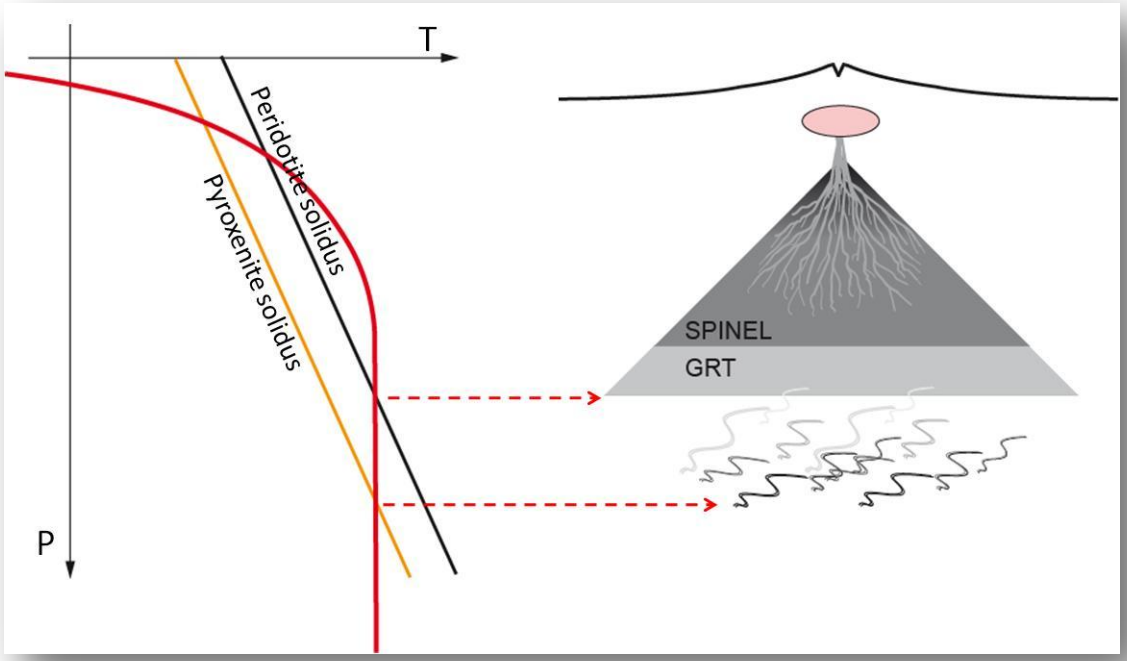

Figure 6.1.1 *– Cartoon showing the relationship between the solidii of mantle peridotite (black line in the left part) and a general heterogeneity (yellow line in the left part). The latter will start melting deeper, and melts here produced can easily interact with the mantle peridotite in the deepest part of the melting region. In the right part of the figure, triangle represents the mantle melting region and grey stripes represent general heterogeneities. Light grey area represents garnet stability field and dark grey represents spinel stability field. Pink circle represents the magma chamber.*

The second important aspect deriving from this modeling is that, in the majority of cases, a near-batch melting regime (i.e. high values of ϕ/F, up to 0.6) is needed to fit the observed alignment crosscutting the fractional melting trends. A high value of ϕ/F indicates a very high retention and stagnation of melt in a spinel field-equilibrated mantle, thus much deeper than plagioclase stagnation reported for analogous ridge settings (TARTAROTTI ET AL., 2002). This observation represents an unexpected situation for the oceanic mantle upwelling in the melting region (LIANG ET AL., 2009; KELEMEN ET AL., 1997; NIU, 1997; BAKER ET AL., 1995).

To allow melt production and concomitant stagnation encompassing the minimal ϕ values for melt interconnectivity (ϕ/F=0.5, NIU, 1997; ZOU, 1998), a permeability barrier needs to be accounted for, able to deny melt extraction and allow melt stagnation.

A permeability barrier at such depth can be the result of several synergic factors in mantle melting region.

The first is represented by the thermal negative anomaly of the whole system, as described in previous chapters: ABFZ is part of a slow-to-ultraslow spreading ridge considered to represent a cold-spot in the oceanic ridge system (CANNAT ET AL., 2006; DICK ET AL., 2003; MICHAEL ET AL., 2003; DEMETS ET AL., 1990). However modeling the extent of melting of the recovered samples do not show a marked difference concerning the estimated degree of melting in the garnet field with respect to hotter sections of the mid oceanic ridges as for instance the Vema FZ in the Atlantic (BRUNELLI ET AL., 2006). This observation suggests that the onset of melting occurs at comparable depth in the two systems and therefore that a negative anomaly cannot be ascribed to a lower mantle potential temperature.

Instead the overall low degree of melting results from a lower extent of melting in the spinel stability field suggesting deeper thermal boundary layer and thicker lithosphere for the ABFZ region. The thicker ABFZ lithosphere would possibly result from the lower spreading rate associated to an enhanced cold-edge effect. The mega-transform geometrical setting where a 50 Ma old, 70 km thick lithosphere (PASINI, 2009) fronts the tip of the present-day ridge axis plays a key role in lowering the temperature of the upwelling mantle and inhibiting melting and melt extraction (MORGAN & FORSYTH, 1988; LIGI ET AL., 2006). This ultimately creates a thermal permeability barrier from above (Fig. 6.1.2).

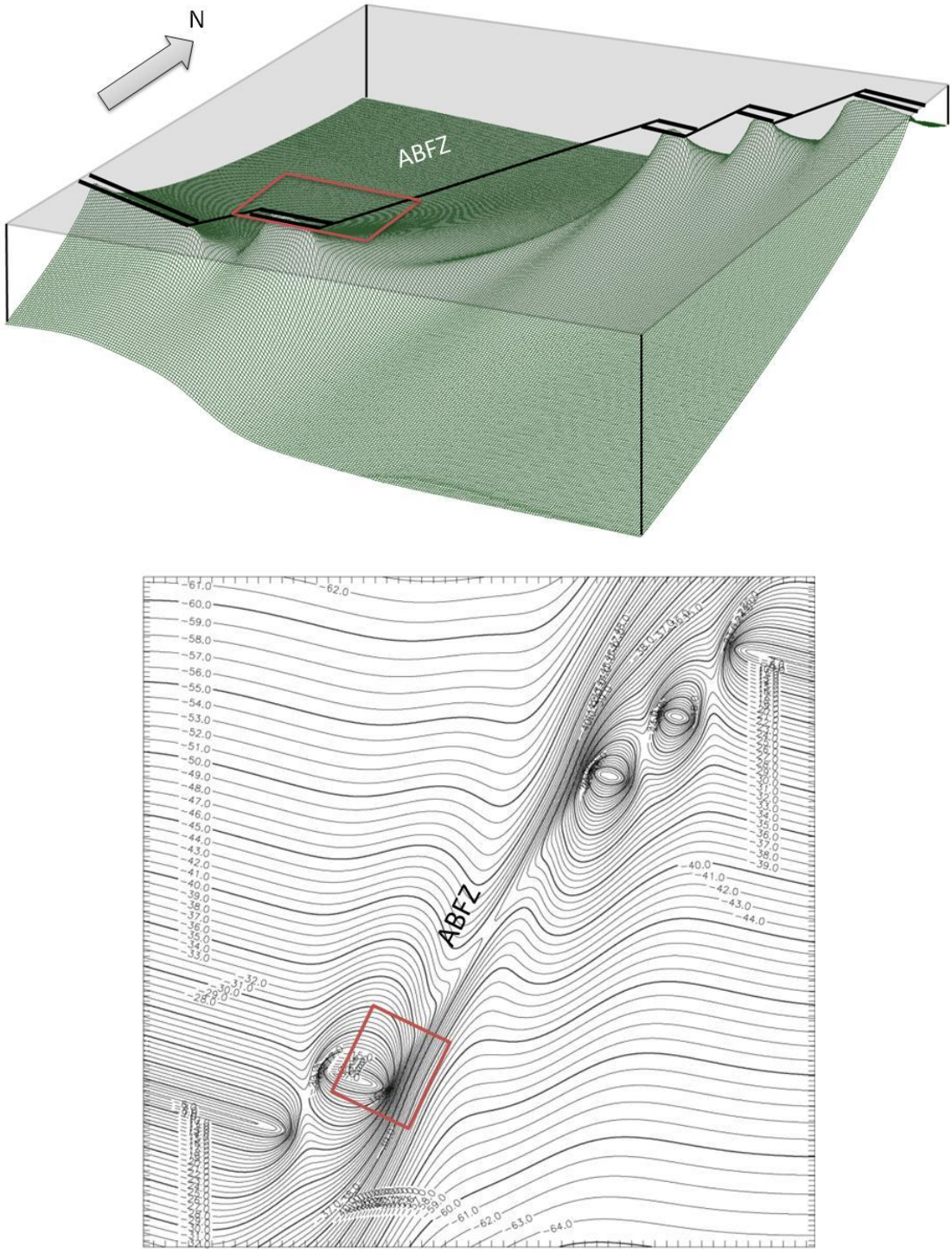

Figure 6.1.2 *– Lithospheric thickness modeled by* PASINI *(2009) for ABFZ: 3D representation (upper part) and map (down) of the depth of the lithosphere have been reported. In first figure, green level represents the bottom of the lithosphere and red rectangle indicates the*

studied area. In second figure, red rectangle represents the studied area and numbers indicate the lithospheric depth in km. Lithosphere depth decreases beneath ridge axis and steeply increases under the large fracture zone. In such a situation, this old and cold lithosphere plays a key role in lowering the temperature of the upwelling mantle and inhibiting melting and melt extraction.

The steep thermal gradient and related lithospheric thickness near the southern ridge axis can also explain the occurrence of the majority of plagioclase-bearing peridotites at the ridge axis. Cooling due to the thick/old lithosphere close to the transform can stop melting in the upwelling mantle earlier and deny percolation of melt at shallow lithospheric levels. This feature is also noticeable in the equilibrium temperatures discussed in major element chapter: plagioclase-bearing peridotites show higher equilibrium temperatures than spinel-equilibrated peridotites. Plagioclase bearing peridotites are concentrated on the ridge axis centre. The higher temperature of equilibration may in part reflect the higher temperature expected for the ridge centre than for the tips. However higher equilibration temperatures may also reflect a kinetic component. For systems undergoing high cooling rates the recorded closure temperatures are higher than for slow cooling temperatures (Lasaga, 1983). Let consider two parcels: one situated in the spinel field at the ridge tip, the other situated in the plagioclase field at the ridge centre. The plagioclase impregnation asks for liquid to be retained in the plagioclase field, this liquid is at solidus temperature thus once thermally equilibrated the plagioclase impregnated peridotite should be slightly hotter, or close to that of the spinel field (subsolidus) equilibrated peridotite at the axis tip. The impregnation of the plagioclase peridotites occurring at shallower levels than the spinel field equilibrated plagioclase-free peridotites imposes the upwelling length to be shorter for the peridotites at the ridge axis thus for these latter to experience a higher cooling rate. Consequently even assuming the two peridotite sets to have the same temperature kinetics assures higher closure temperatures for the plagioclase bearing peridotites. Overall the plagioclase bearing peridotites are therefore related to hotter, lithospheric thinner, regions

of the spreading system. While the spinel field equilibrated peridotites are related to colder regions where mantle melting is inhibited earlier, deeper, allowing permeability barriers to form deep in the mantle.

Although a thermal permeability barrier always occurs in a suboceanic mantle environment entering in conductive cooling region (CHEN, 1996), in ABFZ case this permeability barrier seems to occur deeper.

Let consider the melt flow pattern through the mantle: several mechanisms act based on the rheology and P/T conditions of the melting mantle. Usually melt transport starts as porous flow at the bottom of the melting region (TURCOTTE & AHERN, 1978; IWAMORI, 1993; LUNDSTROM ET AL., 1995) and progressively changes to a focused porous flow till channeling into dunitic conduits (KELEMEN ET AL., 1995; AHARONOV ET AL., 1995; MORGAN & LIANG, 2005; MAZZUCCHELLI ET AL., 2008; LIANG ET AL., 2010). The transition to high flow rates through dunite channels allows melt transport to bypass the conductive cooling barrier and to provide melt supply to magma chambers beneath MOR. In figure 6.1.3 a thermally "normal" situation is reported: here the enriched melts coming from melting of heterogeneities and enriched material deep in the melting region are collected by the melt network system inside the ambient peridotite and transported till the magma chamber at the base of the crust by focused flow and trough dunite channels; at this level magma experiences several stages of mixing (Fig. 6.1.3). In fact, dunite channel can preserve in their inner part this deep and enriched heterogeneities-derived melt, keeping them separated by depleted and shallower melt produced in the upper part of the melting region (Fig. 6.1.4).

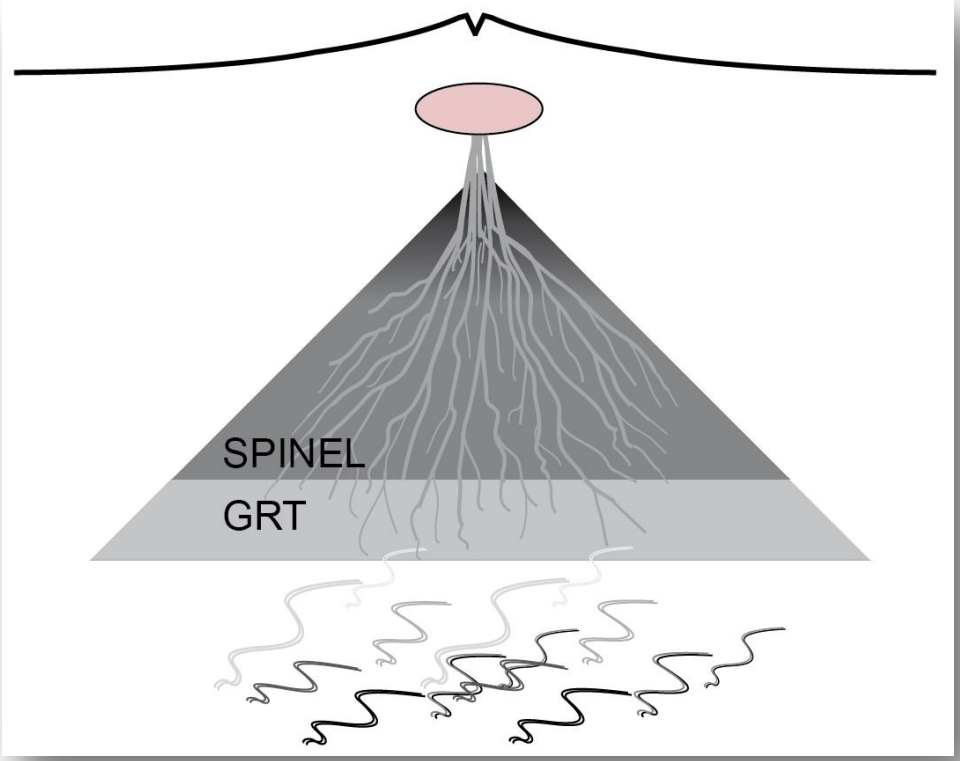

Figure 6.1.3 *– Cartoon showing the melting region beneath "normal" MOR. Triangle represents the mantle melting region. Light grey area represents garnet stability field and dark grey represents spinel stability field. The enriched melts coming from melting of heterogeneities (black and grey strips) and enriched material deep in the melting region are collected by the melt network system inside the ambient peridotite and transported till the magma chamber (pink circle) at the base of the crust before by focused flow and then trough dunite channels; at this level magma experiences several stages of mixing. In fact, dunite channel can preserve in their inner part this deep and enriched heterogeneities-derived melt, keeping them separated by depleted and shallower melt produced in the upper part of the melting region*

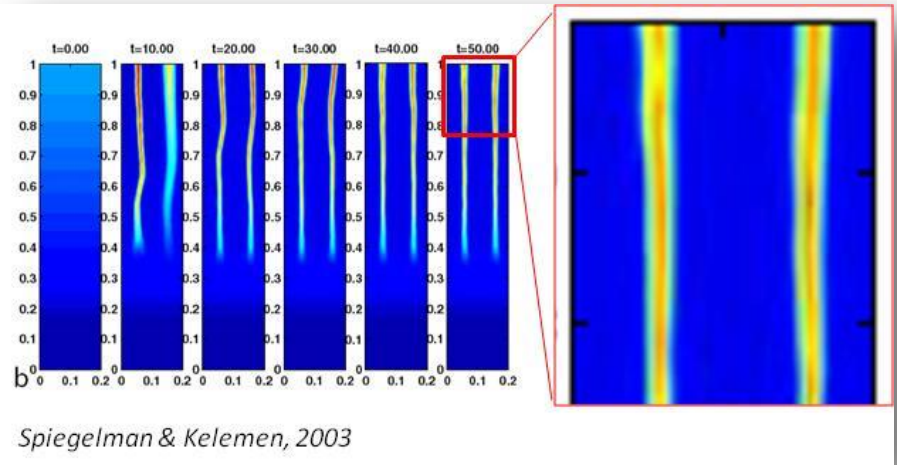

Figure 6.1.4 *– Model of enriched melt transport in dunite conduits (from Spiegelman & Kelemen, 2003). Figure shows the mechanism of melt transport by dunite channels, that can preserve in their inner part this deep and enriched heterogeneities-derived melt, keeping them separated by depleted and shallower melt produced in the upper part of the melting region.*

The enhanced deeper cooling in the case of ABFZ mantle lowers the conductive cooling to a region where melt is possibly not yet organized in a channelized flow. This results in melt retention at depth and lower, if nothing, melt supply at ridge axis. This mechanism can be responsible of the lack of a continuous basaltic crust in this and similar regions as Romanche FZ (BONATTI ET AL., 1991).

The second factor that can lead to a permeability barrier can be related to the composition of the exotic melt. Here the term exotic is simply related to a melt that is out of equilibrium with a given portion of the melting region and does not mean it is generated in markedly different melting conditions (i.e. with strict reference with source composition).
Compositions of exotic melts that interact with mantle can spread over a wide compositional range. The effect of percolation of melts in disequilibrium with the percolated parcel of mantle may cause dramatic effects as for instance the formation of dunitic conduits due to

dissolution instabilities when olivine normative basalts percolate through a harzburgite or lherzolite matrix (QUICK, 1981; KELEMEN, 1990; KELEMEN ET AL. 1992, 1995A, B, 1997, 2000; ASIMOW & STOLPER 1999; MORGAN & LIANG, 2005). MAZZUCCHELLI ET AL. (2008) give also a numerical example of a melt/rock interaction in the case of a silica under-saturated melt. In this case, dunite channels form very quickly due to enhanced dissolution of pyroxenes and crystallization of olivine.

The effect of an exotic melt flowing through a rock depends upon the relative relations of element saturation. Reducing the discussion to the simpler case, i.e. silica saturation, it can be suggested that if the exotic melt added to the system is silica over-saturated with respect to the melts in local equilibrium, olivine reacts with the melt inducing pyroxenes (especially orthopyroxene) crystallization in the peridotite (KOGISO ET AL., 2003, 2004, 2006; SOBOLEV ET AL., 2005, 2007), lowering the critical mass porosity of the system and possibly forming a permeability barrier that denies (or obstructs) melt segregation according to the following reactions (SOBOLEV ET AL., 2007):

Peridotite + SiO2 (eclogitic melt) → opx

opx + eclogitic melt → cpx.

The last factor that can play an important role in the formation of this anomalously deep permeability barrier derives from thermodynamical constraints. ASIMOW and coworkers, 1995, showed as the garnet breakdown reaction reduces the total amount of entropy of the system: solid-solid transition between garnet and spinel is characterized by a positive Clapeyron slope, that can inhibit melt or even freeze it during isentropic pressure-released melting. If normally this reaction does not affect the melting processes that occur deeply in the melting region, in a low thermal setting, as the ABFZ domain, the breakdown related heat-loss can have a synergic effect to the creation of a permeability barrier.

In figure 6.1.5, all these causes are summarized.

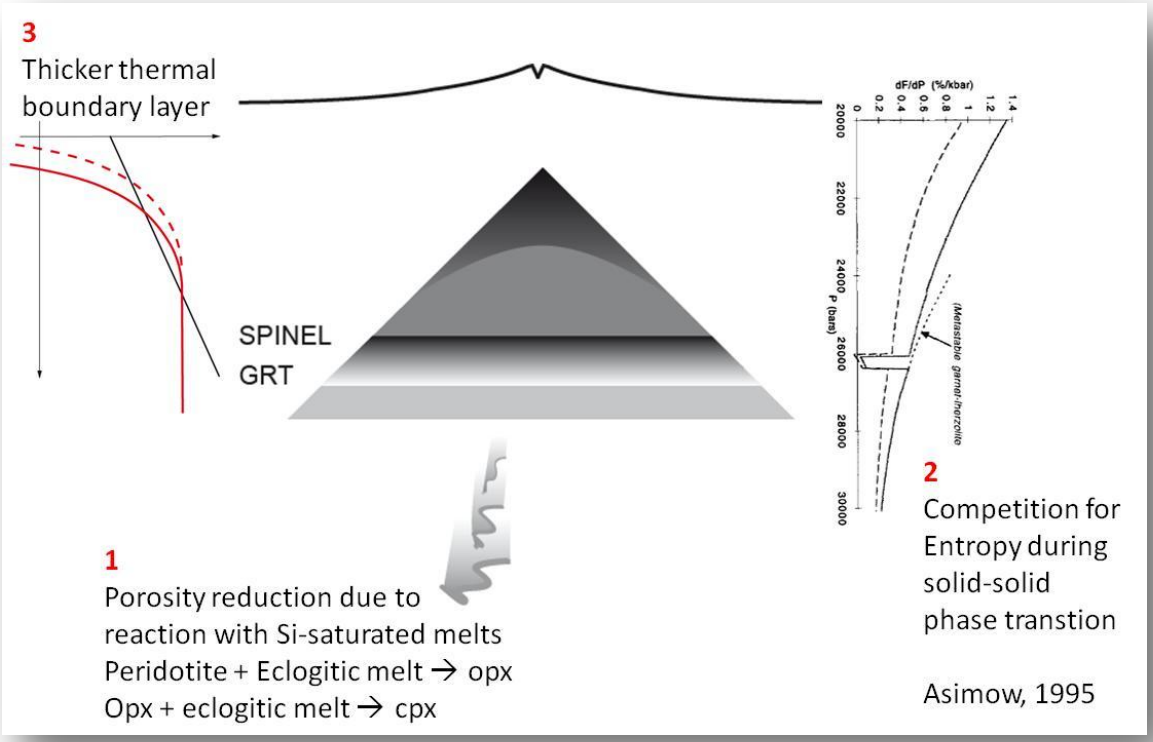

Figure 6.1.5 *– Cartoon showing the three different causes leading to the formation of a deep permeability barrier: 1) porosity reduction due to reaction with over-saturated melts; 2) competition for entropy during phase-phase transition in garnet breakdown reaction; 3) enhanced cooling from above due to the anomalous thick lithosphere.*

References

AHARONOV, E., J. WHITEHEAD, P. B. KELEMEN, AND M. SPIEGELMAN, Channeling instability of upwelling melt in the mantle, J. Geophys. Res., 100, 20,433–20,450, 1995.

AHERN, J.L., AND TURCOTTE, D.L., 1979, Magma migration beneath an ocean ridge: Earth and Planetary Science Letters, v. 45, p. 115–122.

ALBARÈDE E., Introduction to Geochemical Modeling, Cambridge Univ. Press, 1995

ANDERS, E. & GREVESSE, N. (1989). Abundances of the elements: meteoritic and solar. Geochimica et Cosmochimica Acta 53, 197.

ASIMOW P. D., HIRSCHMANN M. M., GHIORSO M. S., O'HARA M. J., STOLPER E. M., The effect of pressure-induced solid-solid phase transitions on decompression melting of the mantle, Geochimica et Cosmochimica Acta, Vol. 59, No. 21, pp. 4489-4506, 1995

ASIMOW P. D., STOLPER E. M., Steady-state Mantle–Melt Interactions in One Dimension: I. Equilibrium Transport and Melt Focusing, J. Petrology (1999) 40 (3): 475-494. doi: 10.1093/petroj/40.3.475, 1999

BENCE, A. E. & ALBEE, A. L., Empirical correction factors for the electron microanalyses of silicates and oxides. *Journal of Geology,* **76**, 382–403, 1968.

BERNARD, A., MUNSCHY, M., ROTSTEIN, Y., SAUTER, D., Refined spreading history at the Southwest Indian Ridge for the last 96 Ma, with the aid of satellite gravity data, *Geophys. J. Int.*, **162,** 765–778, 2005

BLUNDY, J., ROBINSON, J. A. C. & WOOD, B. (1998). Heavy REE are compatible in clinopyroxene on the spinel lherzolite solidus. Earth and Planetary Science Letters 160, 493–504.

BODINIER JEAN-LOUIS, GARRIDO CARLOS J., CHANEFO INGRID, BRUGUIER OLIVIER, GERVILLA FERNANDO, Origin of Pyroxenite–Peridotite Veined Mantle by Refertilization Reactions: Evidence from the Ronda Peridotite (Southern Spain), Journal of Petrology, 49 (5): 999-1025, 2008

BONATTI E., BRUNELLI D., BUCK W. R., CIPRIANI A., FABRETTI P., FERRANTE V., GASPERINI L., LIGI M., Flexural uplift of a lithospheric slab near the Vema transform (Central Atlantic): Timing and mechanisms, *Earth and Planetary Science Letters*, **240**, 642–655, 2005

BONATTI, E., D. BRUNELLI, P. FABRETTI, M. LIGI, R.A. PORTARO AND M. SEYLER, Steady-state creation of crust-free lithosphere at cold spots in mid-ocean ridges**,** *Geology,* **29**, 979-982, 2001.

BONATTI, E., LIGI, M., CARRARA, G., GASPERINI, L., TURKO, N., PERFILIEV S., PEYVE, A., SCIUTO, P.F., Diffuse impact of the Mid-Atlantic Ridge with the Romanche transform: An ultracold ridge/transform intersection, *Journal of Geophysical Research*, **101**, 8043-8054, 1996.

BONATTI E., M. LIGI**,** L.GASPERINI, A.MAZAROVICH, Y.RAZNITSIN, Y.J.CHEN, Transform migration and vertical tectonics at the Romanche fracture zone, equatorial Atlantic, *Journal of Geophysical Research*, **99**, 21779-21802, 1994.

BONATTI, E., HANNOREZ, J., Sections of the earth's crust in the equatorial Atlantic, *Journal of Geophysical Research*, **81**, 4104-4116, 1976.

BOTTAZZI P., OTTOLINI L., VANNUCCI R., SIMS Analyses of Rare Earth Elements in Natural minerals and glasses: An investigation of structural matrix on ion yelds. Scanning vol 14, 160-168, 1992

BRUNELLI D., CIPRIANI A., OTTOLINI L., PEYVE A., BONATTI E., Mantle peridotites from the Bouvet Triple Junction Region, South Atlantic, doi: 10.1046/j.1365-3121.2003.00482.x, Terra Nova, 15, 194–203, 2003

BRUNELLI, D., SEYLER, M., CIPRIANI, A., OTTOLINI, L., BONATTI, E., Discontinuous Melt Extraction and Weak Refertilization of Mantle Peridotites at the Vema Lithospheric Section (Mid-Atlantic Ridge), *Journal of Petrology*, **47**(4), 745–771, 2006.

BRUNELLI, D., & SEYLER, M., Asthenospheric percolation of alkaline melts beneath the St. Paul region (Central Atlantic Ocean), Earth and Planetary Science Letters 289 (2010) 393–405, 2010

BUCK, W.R., A.N.B. POLIAKOV, Abyssal hills formed by stretching oceanic lithosphere, *Nature*, **392**, 272-275, 1988.

CANNAT M., SAUTER D., MENDEL V., RUELLAN E., OKINO K., ESCARTIN J., COMBIER V., BAALA M., Modes of seafloor generation at a melt-poor ultraslow-spreading ridge, *Geology*, **34**; no. 7; p. 605-608; DOI: 10.1130/G22486.1, 2006

CANNAT M., How thick is the magmatic crust at slow spreading oceanic ridges?, *Journal of Geophysical Research*, **101** (B2), 2847-2857, 1996.

CANNAT, M., SEYLER, M.,Transform tectonics, metamorphic plagioclase and amphibolitization in ultramafic rocks of the Vema transform fault (Atlantic Ocean), *Earth and Planetary Science Letters*, **133**, 283-298, 1995.

CANNAT M., Emplacement of mantle rocks in the seafloor at mid-ocean ridges, *Journal of Geophysical Research*, **98**, 4163–4172, 1993.

CANNAT, M,. BIDEAU, D., BOUGAULT, H,. Serpentinized peridotites and gabbros in the Mid-Atlantic Ridge axial valley at 15°37′N and 16°52′N, Earth and Planetary Science Letters, Volume 109, Issues 1-2, Pages 87-106, March 1992

CANNAT, M., MAMALOUKAS-FRANGULIS, V., AUZENDE, J.-M., BIDEAU, D., BONATTI, E., HONNOREZ, J., LAGABRIELLE, Y., MALAVIEILLE, J. & MEVEL, C., A geological cross-section of the Vema fracture zone transverse ridge, Atlantic Ocean. Journal of Geodynamics 13, 97–118, 1991

CARESS, D., CHAYES, D., MB-SYSTEM Release 5, 2005, URL: www.ldgo.columbia.edu/MB-System.

CHEN Y. J., Constraints on melt production rate beneath the mid-ocean ridges based on passive flow models, Pure and Applied Geophysics, Volume 146, Numbers 3-4, 589-620, DOI: 10.1007/BF00874735, 1996

CHRISTENSEN, N. I. & SMEWING, J. D., Geology and seismic structure of the northern section of the Oman ophiolite, *Journal of Geophysical Research*, **86**, 2545−2556, 1981

CHRISTENSEN, N. I., Ophiolites, seismic velocities and oceanic crustal structure, *Tectonophysics* **47**, 131−157, 1978.

CHU, D., GORDON, R., Evidence for motion between Nubia and Somalia along the Southwest Indian ridge, Nature 398, 64-67, DOI:10.1038/18014; 1999

COOGAN L.A., THOMPSON G.M., MACLEOD C.J.,. DICK H.J.BEDWARDS, S.J., HOSFORD SCHEIRER A., T.L. BARRYG, A combined basalt and peridotite perspective on 14 million years of melt

generation at the Atlantis Bank segment of the Southwest Indian Ridge: evidence for temporal changes in mantle dynamics?, Chemical Geology Volume 207, Issues 1-2, 28 Pages 13-30, 2004

CUNDALL, P.A., Numerical experiments on localization in frictional materials, *Ingenieur Archives*, **58**, 148–159, 1989.

DEMETS C., GORDON R. G., ARGUS D. F., STEIN S., Current plate motions, Geophysical Journal International, Volume 101, Issue 2, pages 425–478, May 1990

DICK, H., LISSENBERG, J., WARREN, J., Mantle Melting, Melt Transport, and Delivery Beneath a Slow-Spreading Ridge: The Paleo-MAR from 23°15′N to 23°45′N, J. Petrology, 51 (1-2): 425-467, 2010

DICK H. J. B., LIN J., SCHOUTEN H., An ultraslow-spreading class of ocean ridge, *Nature*, **426**, 405-412, 2003

DICK, H. J. B., Abyssal peridotites, very slow spreading ridges and ocean ridge magmatism. In: Saunders, A. D. & Norry, M. J. (eds) Magmatism in the Ocean Basins. Geological Society, London, Special Publications 42, 71–105, 1989

DICK H. J. B. & BULLEN T., Chromian spinel as a petrogenetic indicator in abyssal and alpine type peridotites and spatially associated lavas. Contributions to Mineralogy and Petrology 86, 54–76. 1984

DICK, H.J.B., FISHER, R.L., BRYAN, W.B., Mineralogical variability of the uppermost mantle along mid-ocean ridges, *Earth and Planetary Science Letters*, **69**, 88–106, 1984

DOWNES H, BODINIER JL, THIRLWALL MF, LORAND JP, FABRIEÁS J (1991) REE and Sr-Nd isotopic geochemistry of Eastern Pyrenean peridotite massifs: sub-continental lithospheric mantle modi®ed by continental magmatism. J Pet Spec Lherzolites Issue: 97-115

DRAKE M.J. AND WEILL D.F., New rare earth element standards for electron microprobe analysis. Chem.. geol., 10: 179-181, 1972

DUNN T., SEN C., Mineral/matrix partition coefficients for orthopyroxene, plagioclase, and olivine in basaltic to andesitic systems: A combined analytical and experimental study, Geochimica et Cosmochimica Acta, Volume 58, Issue 2, January, Pages 717-733, 1994

EBINGER, C. J., T. YEMANE, D. J. HARDING, S. TESFAYE, S. KELLEY, D. C. REX, Rift deflection, migration, and propagation: Linkage of the Ethiopian and Eastern rifts, Africa, *Geol. Soc. Am. Bull*., **112**(2), 163–176, 2000.

EDGERTON H.E., Sub-bottom penetrations in Boston Harbour, *Journal of Geophysical Research*, **68**, 9, 1963.

ENGELN, J.F., D.A. WIENS, S. STEIN, Mechanisms and depths of Atlantic transform earthquakes, *Journal of Geophysical Research,* **91**, 548–577, 1986.

ENGLAND, P., HOUSEMAN, G., SONDER, L., Length scales for continental deformation in convergent, divergent, and strike-slip environments: Analytical and approximate solutions for a thin viscous sheet model, *Journal of Geophysical Research*, **90**, 3551-3557.

EWING J.I., TIREY G.B., Seismic profiler, *Journal of Geophysical Research*, **66**, 5, 1961.

FAHEY A.J., Details of the measurements of rare earth and other trace element abundances by secondary ion mass spectrometry: International Journal of Mass Spectrometry 176, 63-76, 1998

FISHER, R. L., A. M. GOODWILLIE, The physiography of the Southwest Indian Ridge, Mar, *Journal of Geophysical Research*, **19**, 451–455, 1997.

FOX, J.P., D.G. GALLO, A tectonic model for ridge-transform-ridge plate boundaries; implications for the structure of oceanic lithosphere, *Tectonophysics*, **104**, 205–242, 1984.

GASPERINI, L., STANGHELLINI, G., SEISPRO, a processing software for high resolution seismic data, ISMAR Tecnical Report in preparation, 2005.

GAST, P.W., 1968. Trace element fractionation and the origin of tholeiitic and alkaline magma types. Geochim. Cosmochim. Acta 32, pp. 1057–1086

GEBCO, IHO-UNESCO, General Bathymetric Chart of the Oceans, Digital Edition, 2003, www.ngdc.noaa.gov/mgg/gebco.

GEORGEN, J.E., J. LIN, H.J.B. DICK, Evidence from gravity anomalies for interactions of the Marion and Bouvet hotspots with the Southwest Indian Ridge: effects of transform offsets, *Earth and Planetary Science Letters,* **187**, 283-300, 2001.

GRINDLAY, N.R., J.A. MADSEN, C. ROMMEVAUX, J.G. SCLATER, A different pattern of ridge segmentation and mantle Bouguer gravity anomalies along the ultra-slow spreading Southwest Indian Ridge (15 degrees 30 ' E to 25 degrees E), *Earth and Planetary Science Letters,* **161**, 243-253, 1998.

GRINDLAY, N. R., J. A. MADSEN, C. ROMMEVAUX-JESTIN, J. SCLATER, S. MURPHY, Southwest Indian Ridge 15E-35E: A geophysical investigation of an ultra-slow spreading midocean ridge system*, InterRidge News*, **5**, 7-12 , 1996.

HANAN B., BLICHERT-TOFT J., PYLE D., CHRISTIE D., Contrasting origins of the upper mantle revealed by hafnium and lead isotopes from the Southeast Indian Ridge, Nature 432, 91-94 (4 November 2004) | doi:10.1038/nature03026; 2004

HELLEBRAND, E., SNOW, J.E., DICK, H.J.B., HOFMANN, A.W., Coupled major and trace-element melting indicators in mid-ocean ridge peridotites, *Nature*, **410**, 677–681, 2001.

HELLEBRAND, E., SNOW, J. E., HOPPE, P. & HOFMAN, A. W., Garnet-field melting and late-stage refertilization in 'residual' abyssal peridotites from the Central Indian Ridge. Journal of Petrology 43, 2305–2338, 2002

HELLEBRAND, E. & SNOW, J. E., Deep melting and sodic metasomatism underneath the highly oblique-spreading Lena Trough (Arctic Ocean). Earth and Planetary Science Letters 216, 283–299, 2003

HIRSCHMANN M. M., STOLPER E. M., A possible role for garnet pyroxenite in the origin of the "garnet signature" in MORB, Contributions to Mineralogy and Petrology, Volume 124, Number 2, 185-208, DOI: 10.1007/s004100050184, 1996

HORNER-JOHNSON, B. C., GORDON, R., COWLES, S., ARGUS, D., The angular velocity of Nubia relative to Somalia and the location of the Nubia–Somalia–Antarctica triple junction, Geophysical Journal International, Volume **162**, Issue 1, pages 221–238, 2005

ILDEFONSE, B., BLACKMAN, D. K., JOHN, B. E., OHARA, Y., MILLER, D. J., MACLEOD, C. J., Oceanic core complexes and crustal accretion at slow-spreading ridges, *Geology*, **35**, 623-626, 2007

IWAMORI H, A model for disequilibrium mantle melting incorporating melt transport by porous and channel flows, Nature 366, 734 - 737; doi:10.1038/366734a0, 1993

JOHNSON, K. T. M. (1998). Experimental determination of partition coefficients for rare-earth and high-field-strength elements between clinopyroxene, garnet and basaltic melt at high pressures. Contributions to Mineralogy and Petrology 133, 60–68.

JOHNSON, K. T. M. & DICK, H. J. B.. Open system melting and spatial variation of peridotite and basalt at the Atlantis II Fracture Zone. Journal of Geophysical Research 97, 9219–9241, 1992

JOHNSON, K., DICK, H., SHIMIZU, N., Melting in the Oceanic Upper Mantle: An Ion Microprobe Study of Diopsides in Abyssal Peridotites, doi:10.1029/JB095iB03p02661, JOURNAL OF GEOPHYSICAL RESEARCH, VOL. 95, NO. B3, PP. 2661-2678, 1990

KELEMEN, P. B., Reaction Between Ultramafic Rock and Fractionating Basaltic Magma I. Phase Relations, the Origin of Calc-alkaline Magma Series, and the Formation of Discordant Dunite, J. Petrology (1990) 31 (1): 51-98. doi: 10.1093/petrology/31.1.51, 1990

KELEMEN, P. B., N. SHIMIZU, AND V. J. M. SALTERS, Extraction of mid-ocean-ridge basalt from the upwelling mantle by focused flow of melt in dunite channels, Nature, 375, 747– 753, 1995a.

KELEMEN, P. B., J. A. WHITEHEAD, E. AHARONOV, AND K. A. JORDAHL, Experiments on flow focusing in soluble porous media, with applications to melt extraction from the mantle, J. Geophys. Res., 100, 475, 1995b.

KELEMEN, P.B., G. HIRTH, N. SHIMIZU, M. SPIEGELMAN AND H.J.B. DICK, A review of melt migration processes in the asthenospheric mantle beneath oceanic spreading centers, Phil. Trans. Roy. Soc. London A355, 283-318, 1997

KELEMEN, P.B., BRAUN M., HIRTH G., Spatial distribution of melt conduits in the mantle beneath oceanic spreading ridges: Observations from the Ingalls and Oman ophiolites, Geochemistry, Geophysics Geosystems, vol 1, ISSN 1525-2027, 2000

KINZLER, R. J. (1997). Melting of mantle peridotites at pressure approaching the spinel to garnet transition: application to mid ocean ridge basalt petrogenesis. Journal of Geophysical Research 102,953–974.

KLEIN, E. M. & LANGMUIR, C. H., 1987. Global correlations of ocean ridge basalt chemistry with axial depth and crustal thickness. Journal of Geophysical Research **92,** 8089–8115.

KOGISO T., HIRSCHMANN M.M., FROST D.J., High-pressure partial melting of garnet pyroxenite: possible mafic lithologies in the source of ocean island basalts, Earth and Planetary Science Letters 216 (2003), pp. 603–617

KOGISO T., HIRSCHMANN M.M., PERTERMANN M., High pressure partial melting of mafic lithologies in the mantle, Journal of Petrology 45 (2004), pp. 2407–2422

KOGISO T., HIRSCHMANN M.M., Partial melting experiments of bimineralic eclogite and the role of recycled mafic oceanic crust in the genesis of ocean island basalts, Earth and Planetary Science Letters 249 (2006), pp. 189–199.

LABRECQUE, J. L., D. E. HAYES, Seafloor spreading history of the Aguhlas Basin, *Earth and Planetary Science Letters*, **45**(2), 411–428, 1979.

LANGMUIR C.H., BENDER J.F., BENCE A.E., HANSON G.N., TAYLOR S.R., Petrogenesis of basalts from the FAMOUS area: Mid-Atlantic Ridge, Earth and Planetary Science Letters, Volume 36, Issue 1, 1977, Pages 133-156

LASAGA A., Geospeedometry: an extension of geothermometry, Advances in Physical Geochemistry"(SK Saxena, ed.), 1983

LAXON, S., MCADOO, D., Satellites provide new insights into polar geophysics, *Eos, Transactions American Geophysical Union*, **79**, 69-69, 1998.

LEMAUX, J., GORDON, R. G., ROYER, J. Y., Location of the Nubia-Somalia boundary along the Southwest Indian Ridge, *Geology*, **30**(4), 339–342, 2002.

LENOIR, X., GARRIDO, C.J., BODINIER, J. L., DAUTRIA, J. M., Contrasting lithospheric mantle domains beneath the Massif Central (France) revealed by geochemistry of peridotite xenoliths, *Earth Planet. Sci. Lett.* **181**, 359–375, 2000.

LIANG, Y., Simple models for dynamic melting in an upwelling heterogeneous mantle column: Analytical solutions, Geochimica et Cosmochimica Acta, Volume 72, Issue 15, 1 August 2008, Pages 3804-3821

LIANG, Y,. PENG Q., Non-modal melting in an upwelling mantle column: Steady-state models with applications to REE depletion in abyssal peridotites and the dynamics of melt migration in the mantle, Geochimica et Cosmochimica Acta, Volume 74, Issue 1, 1, Pages 321-339, 2010

LIGI, M., BONATTI, E., BORTOLUZZI, G., CARRARA, G., FEBRETTI, P., GILOD, D., PEYVE, A., SKOLOTNEV, S., TURKO, N., BOUVET TRIPLE JUNCTION IN THE SOUTH ATLANTIC: GEOLOGY AND EVOLUTION, JOURNAL OF GEOPHISICAL RESEARCH, SOLID EARTH, DOI:10.1029/1999JB900192 VOL. **104**, NO. B12, PP. 29,365-29,385, 1999

LIGI, M., E. BONATTI, A. CIPRIANI, L. OTTOLINI, Water-rich basalts at mid-ocean-ridge cold spots, *Nature*, **434**, 66-69, 2005.

LIGI, M., E. BONATTI, L. GASPERINI, A.N.B. POLIAKOV, Oceanic broad multifault transform plate boundaries, *Geology*, **30**, 11-14, 2002.

LIGI, M., E. BONATTI, S. SKOLOTNEV, A. PEYVE, N.R. GRINDLAY, J.G. SCLATER, G. BORTOLUZZI, D. BRUNELLI, A. CIPRIANI, R. MERCURI, F. MUCCINI, E. PAGANELLI, F. ZAFFAGNINI, C. TAKEUKI, Y. BARAMYKOV, N. CHAMOV, S. EROFEEV, A. ESKIN, S. KOLODYAZHNY, A. PERTSEV, V. SEMENOV, V. RASTORGYEV, N. TSUKANOV, N. TURKO, V. YEFIMOV, L. ZOTOV, Report on the morphobathymetric, magnetometric, gravimetric, multichannel reflection seismic and dredging investigations during cruise S23-AB06 aboard R/V A.N.Strakhov, *ISMAR-BO Technical Report*, **100**, 48, 2006.

LIGI, M., E. BONATTI, S. SKOLOTNEV, A. PEYVE, N.R. GRINDLAY, J.G. SCLATER, G. BORTOLUZZI, D. BRUNELLI, A. CIPRIANI, R. MERCURI, F. MUCCINI, E. PAGANELLI, F. ZAFFAGNINI, C. TAKEUKI, Y. BARAMYKOV, N. CHAMOV, S. EROFEEV, A. ESKIN, S. KOLODYAZHNY, A. PERTSEV, V. SEMENOV, V. RASTORGYEV, N. TSUKANOV, N. TURKO, V. YEFIMOV, L. ZOTOV, Andrew Bain Transform: Multiple Continental-type Transform Boundaries at Mid-Ocean Ridges, *Poster from InterRidge meeting*, Sestri Levante, 2006.

LIVERMORE, R.A., HUNTER, R.J., Mesozoic seafloor spreading in the SouthernWeddell Sea, in Weddell Sea Tectonics and Gondwana Break-up, **108**, 227–241, *eds Storey, B.C., King, E.C. & Livermore, R.A., Geol. Soc., London*, 1996.

LUGUET, A; ALARD, O; LORAND, J P; PEARSON, N J; RYAN, C; OREILLYY, S Y, Laser-Ablation microprobe (LAM)-ICPMS unravels the highly siderophile element geochemistry of the oceanic mantle, EARTH PLANET SCI LETT, vol 189, pages, 285-294, 2001

LUNDSTROM C. C., GILL J., WILLIAMS Q., PERFIT M. R., Mantle Melting and Basalt Extraction by Equilibrium Porous Flow, Science, Vol. 270 no. 5244 pp. 1958-1961, DOI: 10.1126/science.270.5244.1958, 1995

LUNDSTROM, C. C., GILL, J., WILLIAMS, Q., A geochemically consistent hypothesis for MORB generation, *Chemical Geology*, **162**, 105–126, 2000.

MACGREGOR D., MANTON W., Roberts Victor Eclogites: Ancient Oceanic Crust, Journal of Geophisical Research, VOL.91, NO.B14, PP.14,063-14,079, doi:10.1029/ JB091iB14p 14063, 1986

MASINI L. LIGI M., Sistema di controllo e sincronizzazione cannoni sismici ad aria compressa, Rapporto Tecnico IGM N.**37**, 126pp, 1995.

MAZZUCCHELLI M., RIVALENTI G., BRUNELLI D., ZANETTI A., BOARI E., Formation of Highly Refractory Dunite by Focused Percolation of Pyroxenite-Derived Melt in the Balmuccia Peridotite Massif (Italy), Journal of Petrology, 50 (7): 1205-1233. doi: 10.1093/petrology/egn053, 2009

MCDONOUGH, W. F,. FREY, F. A., 1989, REE in the upper mantle rocks, In: B. Lipin and G. R. McKay, Geochemistry and mineralogy of rare earth elements, 99-145, Mineralogical Society of America

MCDONOUGH, W. F., SUN, S., The composition of the Earth, Chemical Geology, Volume 120, Issues 3-4, 1995, Pages 223-253

MCKENZIE, D., The generation and compaction of partially molten rock, Journal of Petrology, 1985, 25(3), 713-65 CODEN: JPTGAD; ISSN: 0022-3530.

MCKENZIE, D. & BICKLE, M. J., 1988. The volume and composition of melt generated by extension of the lithosphere. Journal of Petrology **29,** 625–679.

MENARD H. W., ATWATER T., Change in direction in sea floor spreading, *Nature*, **216**, 1276-1280, 1968

MERCIER, J. C. C., NICOLAS, A., Textures and Fabrics of Upper-Mantle Peridotites as Illustrated by Xenolith from Basalts, *Journal of Petrology*, **16** (2), 454-487, 1975.

MEVEL, C., Serpentinization of abyssal peridotites at mid-ocean ridges, Comptes Rendus Geosciences, doi:10.1016/j.crte.2003.08.006, Volume 335, Issues 10-11, Pages 825-852, 2003

MICHAEL, P.J., BONATTI, E., Peridotite composition from the north Atlantic: Regional and tectonic variations and implications for partial melting, *Earth and Planetary Science Letters*, **73**, 91–104, 1985.

MICHAEL P. J., LANGMUIR C. H., DICK H. J. B., SNOW J. E., GOLDSTEIN S. L., GRAHAM D. W., LEHNERT K., KURRAS G., JOKAT W., MÜHE R., EDMONDS H. N., Magmatic and amagmatic seafloor generation at the ultraslow-spreading Gakkel ridge, Arctic Ocean, Nature 423, 956-961 (26 June 2003) | doi:10.1038/nature01704; 2003

MORGAN, P. J., Thermodynamics of pressure released melting of a veined plum pudding mantle, *Geochem. Geophys. Geosys*., **2**, 2000GC000049, 1525-2027, 2001.

MORGAN P., FORSYTH J., D. W., Three-dimensional flow and temperature perturbations due to a transform offset: Effects on oceanic crustal and upper mantle structure, Journal of Geophysical Research, **93**, 2955–2966, 1988.

MORGAN, Z., LIANG Y., An experimental study of the kinetics of lherzolite reactive dissolution with applications to melt channel formation, Contributions to mineralogy and petrology, Volume 150, Number 4, 369-385, DOI: 10.1007/s00410-005-0033-8, 2005

MORITZ H., Geodetic reference System, The Geodesist Handbook, *Bull.Geod*., **53**, 388-398, 1980-1984.

NAVON O. AND STOLPER E., Geochemical consequence of melt percolation: the upper mantle as a chromatographic column, J. Geol. 95 (1987), pp. 285–307.

NICHOLLS I. A., HARRIS K. L., Experimental rare earth element partition coefficients for garnet, clinopyroxene and amphibole coexisting with andesitic and basaltic liquids, Geochimica et Cosmochimica Acta, Volume 44, Issue 2, Pages 287-308, 1980

NIU, Y., Mantle Melting and Melt Extraction Processes beneath Ocean Ridges: Evidence from Abyssal Peridotites, *Journal of Petrology*, **38**, 1047–1074, 1997.

NIU, Y. & HE´KINIAN, R., 1997*A*. Spreading rate dependence of the extent of mantle melting beneath ocean ridges. *Nature* **385,** 326–329.

NIU, Y. & HE´KINIAN, R., 1997*B*. Basaltic liquids and harzburgitic residues in the Garrett transform: a case study at fast-spreading ridges. Earth and Planetary Science Letters **146,** 243–258.

NOAA, National Oceanic and Atmospheric Administration, www.noaa.gov

OZAWA, K., SHIMIZU, N., Open-system melting in the upper mantle: Constraints from the Hayachine-Miyamori ophiolite, northeastern Japan, Journal of Geophysical Research, Vol. 100, No. B11, PP. 22,315-22,335, 1995

PANTELEEV V.L., Foundations of Marine gravimetry, *Nedra*, Moscow, 1983.

PARSON, B., SCLATER, J. G., An analysis of the variation of ocean floor bathymetry and heat flow with age, *Journal of Geophysical Research*, **80**, 4417-4424, 1977.

PASINI, V., Studio Geofisico della trasforme Andrew Bain: Oceano Sudovest Indiano, bechelor degree, 2009

PATRIAT, P., SLOAN, H., SAUTER, D., From slow to ultraslow: a previously undetected event at the Southwest Indian Ridge at ca. 24 Ma, Geology, doi: 10.1130/G24270A.1 v. 36 no. 3 p. 207-210

PEARCE J.G., PERKINS T. , WESTGATE A.,. GORTON M.P, A Compilation of New and Published Major and Trace Element Data for NIST SRM 610 and NIST SRM 612 Glass Reference Materials, Geostandards Newsletter, vol. 21, N. 1, pages 115-144, 1997

PERTERMANN, M., HIRSCHMANN, M. M., Partial melting experiments on a MORB-like pyroxenite between 2 and 3 GPa: Constraints on the presence of pyroxenite in basalt source

regions from solidus location and melting rate, *Journal of Geophysical Research*, **108** (B2), 2125, doi:10.1029/2000JB000118, 2003.

QUICK, J. E., The origin and significance of large, tabular dunite bodies in the Trinity peridotite, northern California, Controbution to Mineralogy and Petrology, 78, 413-422, 1981

RAMPONE E., PICCARDO G.B., VANNUCCI R., BOTTAZZI P., OTTOLINI L., Subsolidus reactions monitored by trace element partitioning: the spinel-to plagioclasi-facies transitino in mantle peridotites. *Contrib Mineral Petrol* **115**, 1-17, *1993*

REHKAMPER M., HOFMANN A. W., Recycled ocean crust and sediment in Indian Ocean MORB, Earth and Planetary Science Letters, Volume 147, Issues 1-4, March, Pages 93-106, 1997

ROCHOLL A.B.E., SIMON K., JOCHUM K.P., BRUHN F.,GEHANN R., KRAMAR U., LUECKE W., MOLZAHN M., PERNICKA E., SEUFERT M., SPETTEL B. AND STUMMEIER J. Chemical characterisation of NIST silicate glass certified reference material SRM 6 10 by ICP-MS, TIMS, LIMS, SSMS, INAA, AAS and PIXE. Geostandards Newsletter:The Journal of Geostandards and Geoanalysis, 21,101-114., 1997

ROSS, K. & ELTHON, D., 1997, Extreme incompatible trace-element depletion of diopside in residual mantle from south of the Kane Fracture Zone. In: KARSON, J. A., CANNAT, M., MILLER, D. J. & ELTHON, D. (eds) Proceedings of the Ocean Drilling Program, Scientific Results, 153. College Station, TX: Ocean Drilling Program, pp. 277–284.

ROYER, J.Y., PATRIAT, P., BERGH, H.W. & SCOTESE, C.R., Evolution of the Southwest Indian Ridge from the Late Cretaceous (anomaly 34) to the Middle Eocene (anomaly 20), *Tectonophysics,* **155,** 235–260, 1988.

SALTERS, V., & DICK, H., Mineralogy of the mid-ocean-ridge basalt source from neodymium isotopic composition of abyssal peridotites, Nature, vol. 418, July 2002

SANDWELL, D.T., SMITH, W.H.F., Marine gravity anomaly from Geasat and ERS-1 satellite altimetry, *Journal of Geophysical Research,* **102**, 10 039–10 054, 1997.

SCHILLING J. C., RUPPEL C., DAVIS A. N., MCCULLY B., TIGHE S. A., KINGSLEY R. H., LIN J., Thermal structure of the mantle beneath the equatorial; Mid-Atlantic Ridge: Inferences from the spatial variation of dredged basalt glass compositions, *Journal of Geophysical Research*, **100**, 10057-10076. 1995.

SCHILLING, J.G. AND WINCHESTER, J.W., 1967. Rare-earth fractionation and magmatic processes. In: Runcorn, F.R.S.S.K., Editor, , 1967. Mantles of Earth and Terrestrial Planets, Interscience, pp. 267–283.

SCLATER, J. G., M. MUNSCHY, R. L. FISHER, P. A. WEATHERALL, S. C. CANDE, P. PATRIAT, H. BERGH, R. SCHLICH, Geophysical synthesis of the Indian/Southern Oceans; Part 1, The Southwest Indian Ocean, *Scripps Institution of Oceanography Reference*, **97-06**, 45, 1997

SCLATER, J.G., N.R. GRINDLAY, J.A. MADSEN, C. ROMMEVAUX, Tectonic interpretation of the Andrew Bain transform fault: Southwest Indian Ocean, *Geochem. Geophys. Geosys*., **6**, Q09K10, 2005.

SEYLER, M., CANNAT, M., MÉVEL, C., Evidence for major-element heterogeneity in the mantle source of abyssal peridotites from the Southwest Indian Ridge (52° to 68°E), Geochem. Geophys. Geosyst., **4**(2), 9101, doi:10.1029/2002GC000305, 2003.

SEYLER, M., BONATTI, E., Regional-scale melt-rock interaction in lherzolitic mantle in the Romanche Fracture Zone (Atlantic Ocean), *Earth and Planetary Science Letters*,**146**, 273-287, 1997.

SEYLER, M., LORAND, J., TOPLIS, M., GODARD, G., Asthenospheric metasomatism beneath the mid-ocean ridge: evidence from depleted abyssal peridotites, Geology; v. 32; no. 4; p. 301–304; April 2004

SEYLER, M., LORAND, J., DICK, H., DROUIN, M., Pervasive melt percolation reactions in ultra-depleted refractory harzburgites at the Mid-Atlantic Ridge, 15° 20' N: ODP Hole 1274A, Contrib. Mineral Petrol DOI 10.1007/s00410-006-0148-6, 2006

SEYLER, M., BRUNELLI, D., TOPLIS, M., MEVEL, C., Multiscale chemical heterogeneities beneath the eastern Southwest Indian Ridge (52°E–68°E): Trace element compositions of along-axis dredged peridotites, Geochemistry Geophysics Geosystems, Volume 12, Number 9, 2011

SHAW, D., Trace element fractionation during anatexis, Geochimica et Cosmochimica Acta, Volume 34, Issue 2, February 1970, Pages 237-243

Shaw, D., 2000, CONTINUOUS (DYNAMIC) MELTING THEORY REVISITED. CANADIAN MINERALOGIST 38, 1041–1063.

SHIMIZU H., SEMET M. ALLEGRE CJ: Geochemical application of quantitative ion- microprobe analysis Geochimica et cosmochimica acta 42, 1321-1334, 1978

SIMPSON, E. S. W., J. G. SCLATER, B. PARSONS, I. O. NORTON, L. MEINKE, Mesozoic magnetic lineations in the Mozambique Basin, *Earth and Planetary Science Letters*, **43**(2), 260–264, 1979.

SOBOLEV ALEXANDER V., HOFMANN ALBRECHT W., SOBOLEV STEPHAN V., NIKOGOSIAN IGOR K., An olivine-free mantle source of Hawaiian shield basalts, Nature, VOL 434, page 590, 2005

SOBOLEV ALEXANDER V., ALBRECHT W. HOFMANN, DMITRY V. KUZMIN, GREGORY M. YAXLEY, NICHOLAS T. ARNDT, SUN-LIN CHUNG, LEONID V. DANYUSHEVSKY, TIM ELLIOTT, FREDERICK A. FREY, MICHAEL O. GARCIA, ANDREY A. GURENKO, VADIM S. KAMENETSKY, ANDREW C. KERR, NADEZHDA A. KRIVOLUTSKAYA, VLADIMIR V. MATVIENKOV, IGOR K. NIKOGOSIAN, ALEXANDER ROCHOLL, INGVAR A. SIGURDSSON, NADEZHDA M. SUSHCHEVSKAYA, MENGIST TEKLAY, The Amount of Recycled Crust in Sources of Mantle-Derived Melts, Science: Vol. 316 no. 5823 pp. 412-417, DOI: 10.1126/science. 1138113, 2007

SPIEGELMAN, M., KELEMEN, P,. Extreme chemical variability as a consequence of channelized melt transport, Geochemistry Geophysics Geosystems, Volume 4, Number 7, 1055, doi:10.1029/2002GC000336, ISSN: 1525-2027, 2003

SUHR, G., SECK, H. A., SHIMIZU, N., GU¨NTHER, D. & JENNER, G. (1998). Infiltration of refractory melts into the lowermost oceanic crust: evidence from dunite- and gabbro-hosted clinopyroxenes in the Bay of Islands Ophiolite. Contributions to Mineralogy and Petrology 131,136–154.

SUHR, G,. Melt Migration under Oceanic Ridges: Inferences from Reactive Transport Modelling of Upper Mantle Hosted Dunites, Journal Of Petrology, volume 40, number 4, pages 575–599, 1999

TAKASAWA E., FREY F. A., SHIMIZU N., OBATA M., BODINIER J. L., Geochemical evidence for melt migration and reaction in the upper mantle, Nature 359, 55-58, 1992; doi:10.1038/359055a0

TAKEUCHI C.S., SCALTER J., GRINDLAY N.R., J MADSEN.A, ROMMEAVAUX-JESTIN C.,. Segmentation and accretionary process near the Andrew Bain transform fault: Soutwest Indian Ridge. Geochem. Geophys. Geosys., 2010.

TARTAROTTI, P., SUSINI, S., NIMIS, P., OTTOLINI, L., Melt migration in the upper mantle along the Romanche Fracture Zone (Equatorial Atlantic), *Lithos*, **63**, 125– 149, 2002.

TAYLOR, L.A., NEAL, C.R., 1989. Eclogites with oceanic crustal and mantle signatures from the Bellsbank kimberlite, South Africa, Part I: Mineralogy, petrography, and whole rock chemistry. J. Geol. 97, pp. 551–567

TAYLOR, W.R., An experimental test of some geothermometer and geobarometer formulations for upper mantle peridotites with application to the thermobarometry of fertile lherzolite and garnet websterite. N Jb Min Abh 172:381–408, 1998

TORGE W., DE GRUYTER, W, Gravimetry, Berlin-NY, 1989.

TURCOTTE, D.L., Are transform fault thermal contraction cracks?, Journal of Geophysical Research, **79**, 2573-2577, 1974.

TURCOTTE D. L., AHERN J. L., A Porous Flow Model for Magma Migration in the Asthenosphere Journal of Geophysical Research, VOL. 83, NO. B2, PP. 767-772, 1978

VERNIÈRES J., GODARD M. AND BODINIER J.-L., A plate model for the simulation of trace element fractionation during partial melting and magma transport in the earth's upper mantle, J. Geophys. Res. 102 (1997), pp. 24771–24784

WALTER, M. J. (1998). Melting of garnet peridotite and the origin of komatiite and depleted lithosphere. Journal of Petrology 39, 29–60.

WARREN J. M., SHIMIZU N., SAKAGUCHI C., DICK H. J. B., NAKAMURA E., An assessment of upper mantle heterogeneity based on abyssal peridotite isotopic compositions, Journal of geophysical research, VOL. 114, B12203, doi:10.1029/2008JB006186, 2009

WARREN, J., & SHIMIZU, N., Cryptic Variations in Abyssal Peridotite Compositions: Evidence for Shallow-level Melt Infiltration in the Oceanic Lithosphere, JOURNALOF PETROLOGY, VOLUME 51 NUMBERS 1 & 2 PAGES 395^423 2010

WESSEL P., SMITH W.H.F., New version of the Generic Mapping Tool released, EOS Trans. **AGU**, 329, 1995. See also URL: gmt.soest.hawaii.edu.

WESTRENEN W., WOOD B., BLUNDY J., A predictive thermodynamic model of garnet-melt trace element partitioning, Contributions to Mineralogy and Petrology, Volume 142, Number 2, 219-234, DOI: 10.1007/s004100100285, 2001

WILSON, J.T., A new class of faults and their bearing on continental drift, *Nature*, **207**, 343-347, 1965.

WILSON T.J., Transform faults, Oceanic ridges, and magnetic anomalies of southwest Vancouver Island, *Science,* **150**, 482-485, 1965.

WORKMAN, R. K., STANLEY R. H., Major and trace element composition of the depleted MORB mantle (DMM), *Earth and Planetary Science Letters*, **231**, 53-72, 2005.

YODER, H.S., Generation of basaltic magma, *Washington DC: National Academy of Sciences*, 1976.

ZHANG, Y.-S. & TANIMOTO, T., 1993. High resolution global upper mantle structure and plate tectonics. Journal of Geophysical Research **98,** 9793–9823.

ZINNER E., CROZAZ G., A method for quantitative measurement of rare earth elements in the ion microprobe. International Journal of Mass Spectrometry ion Proc 69, 17-38, 1986

ZOU, H., 1998, Trace element fractionation during modal and nonmodal dynamic melting and open-system melting: a mathematical treatment. Geochimica et Cosmochimica Acta 62, 1937–1945.

Appendix A

Sampling

Sampling of ABFZ during AB06_S23 oceanographic expedition

Dredge	Sample	Size (cm)	rock type	Description
S2317	S2317-01	30x20x20	basalt	Sector of pillow basalt with fresh glassy crust. Rare plagioclase phenocrysts. Slightly vesicular. Vesicles are empty/clean.
S2317	S2317-02	27x20x13	basalt	Sector of pillow basalt with fresh glassy crust. Rare plagioclase phenocrysts. Plg up to 2-3 mm. Slightly vesicular. Vesicles are empty/clean. Thick rim of alteration
S2317	S2317-03	30x15x15	basalt	sector of pillow basalt with fresh glassy crust. Rare plg phenocryst up to 0.5 cm. slightly vesicular. Vesicles are empty.
S2317	S2317-04	15x20x12	basalt	same as S2317-03
S2317	S2317-05	22x12x12	basalt	same as S2317-03
S2317	S2317-06	16x15x10	basalt	sector of pillow basalt, aphyric with rare small plg, glassy crust, slightly vesicular. Thick rim of alteration
S2317	S2317-07	20x15x15	basalt	same as S2317-06 but fresh
S2317	S2317-08	15x10x10	basalt	rather fresh aphyric pillow sector with fresh glassy crust
S2317	S2317-09	12x10x8	basalt	same as S2317-08
S2317	S2317-10	11x7x9	basalt	pillow basalt with glassy crust
S2317	S2317-11	16x7x7	basalt	aphyric pillow basalt with glassy crust, slightly vesicular

S2317	S2317-12	12x10x8	basalt	same as S2317-11
S2317	S2317-13	11x8x8	basalt	pillow basalt with glassy crust
S2317	S2317-14	11x11x8	basalt	same as S2317-03
S2317	S2317-15	12x11x6	basalt	same as S2317-03
S2317	S2317-16	19x10x7	basalt	same as S2317-03
S2317	S2317-17	11x5x4	basalt	same as S2317-03
S2317	S2317-18	8x5x5	basalt	same as S2317-03
S2317	S2317-19	10x9x7	basalt	same as S2317-03
S2317	S2317-20	11x6x5	basalt	same as S2317-03
S2317	S2317-21	18x5x5	basalt	same as S2317-03
S2317	S2317-22	12x11x6	basalt	same as S2317-03
S2317	S2317-23	12x11x9	basalt	same as S2317-03
S2317	S2317-24	17x10x5	basalt	same as S2317-03
S2317	S2317-25	11x7x7	basalt	same as S2317-03
S2317	S2317-26	12x7x8	basalt	same as S2317-03
S2317	S2317-27	11x11x7	basalt	same as S2317-03
S2317	S2317-28	13x8x4	basalt	same as S2317-03
S2317	S2317-29	15x8x7	basalt	same as S2317-03
S2317	S2317-30	10x9x4	basalt	same as S2317-03
S2317	S2317-31	8x6x4	basalt	same as S2317-03
S2317	S2317-32	11x9x5	basalt	same as S2317-03
S2317	S2317-33	6x5x4	basalt	same as S2317-03
S2317	S2317-34	7x6x5	basalt	same as S2317-03
S2317	S2317-35	8x8x5	basalt	same as S2317-03
S2317	S2317-36	8x7x7	basalt	same as S2317-03
S2317	S2317-37	9x8x4	basalt	same as S2317-03
S2317	S2317-38	18x11x7	basalt	same as S2317-03
S2317	S2317-39	11x8x6	basalt	same as S2317-03
S2317	S2317-40	10x9x7	basalt	same as S2317-03
S2317	S2317-41	12x6x6	basalt	same as S2317-03
S2317	S2317-42	13x7x7	basalt	same as S2317-03
S2317	S2317-43	9x7x5	basalt	same as S2317-03
S2317	S2317-44	9x8x6	basalt	same as S2317-03
gap in numeration (error in numeration)				
S2317	S2317-50	9x6x5	basalt	same as S2317-03
S2317	S2317-51	9x6x5	basalt	same as S2317-03
S2317	S2317-52	7x6x5	basalt	same as S2317-03
S2317	S2317-53	5x5x3	basalt	same as S2317-03
S2317	S2317-54	5x5x4	basalt	same as S2317-03
S2317	S2317-55	6x5x4	basalt	same as S2317-03
S2317	S2317-56	2x2x3	basalt	glassy crust with plagioclase phenocrysts
S2317	S2317-57	7x6x4	basalt	same as S2317-03
S2317	S2317-58	5x5x3	basalt	same as S2317-03
S2317	S2317-59	7x5x5	basalt	same as S2317-03
S2317	S2317-60	7x4x2	basalt	same as S2317-03
S2317	S2317-61	4x3x2	basalt	fresh glassy nodule
S2317	S2317-62	4x4x2	basalt	fresh glassy nodule
S2317	S2317-63	17x14x14	basalt	aphyric pillow basalt, slightly vesicular, no glass
S2317	S2317-64	10x9x9	basalt	same as S2317-63

S2317	S2317-65	9x8x8	basalt	aphyric pillow basalt with rare vesicles, variolitic structure
S2317	S2317-66	14x7x5	basalt	aphyric pillow basalt with strongly altered domains
S2317	S2317-67	8x6x5	basalt	same as S2317-63
S2317	S2317-68	8x7x6	basalt	aphyric pillow basalt, rare vesicles, rare plg phenocrysts up to 0.5 cm
S2317	S2317-69	8x6x4	basalt	same as S2317-68
S2317	S2317-70	7x5x4	basalt	same as S2317-63
S2317	S2317-71	6x5x4	basalt	same as S2317-68
S2317	S2317-72	11x7x6	basalt	altered aphyric basalt
S2317	S2317-73	14x7x6	basalt	same as S2317-68
S2317	S2317-74	9x7x6	basalt	vesicular basalt similar to S2317-63
S2317	S2317-75	8x7x5	basalt	same as S2317-65
S2317	S2317-76	8x5x5	basalt	same as S2317-65
S2317	S2317-77	8x5x4	basalt	vesicular basalt with vesicles filled by secondary minerals
S2317	S2317-78	8x6x4	basalt	same as S2317-74 but more altered
S2317	S2317-79	4x3x2	basalt	same as S2317-74
S2317	S2317-80	9x4x3	basalt	plg poprhyric basalt. Plg up to 0.4 cm
S2317	S2317-81	11x8x4	basalt	aphyric basalt with red rim of alteration
S2317	S2317-82	6x4x4	basalt	plg porphyric basalt. Slightly vesicular with vesicles filled by secondary minerals. Plg phenocrysts up to 7 mm
S2317	S2317-83	3x3x2	basalt	aphyric altered basalt cut by secondary veins
S2317	S2317-84	6x3x3	dolerite	dolerite with rare plg, altered
S2317	S2317-85	8x6x5	basalt	glass nodule, fractured
S2317	S2317-86	11x7x7	basalt	aphyric basalt partially altered
S2317	S2317-87	2x2x2	basalt	slightly vesicular fresh basalt with fresh glassy crust
S2317	S2317-88	3x2x2	basalt	fresh aphyric basalt
S2317	S2317-89	1x1x1	dolerite	dolerite
S2317	S2317-90	4x3x2	basalt	aphyric basalt
S2317	S2317-91	4x3x2	basalt	aphyric basalt
S2317	S2317-92	6x5x1	basalt	rare plg porphyric basalt, slightly vesicular and altered
S2317	S2317-93	6x5x5	basalt	pillow basalt with huge plg xenocryst. Fresh glassy crust
S2317	S2317-94	4x3x3	basalt	altered basalt
S2317	S2317-95	4x3x2	basalt	altered porphyric basalt
S2317	S2317-96	6x3x2	basalt	same as S2317-95
S2317	S2317-97	4x3x2	basalt	same as S2317-95
S2317	S2317-98	5x3x2	basalt	same as S2317-95
S2317	S2317-99	5x3x2	basalt	same as S2317-95
S2317	S2317-100	2x1x1	basalt	same as S2317-95
S2317	S2317-101	10x5x4	basalt	same as S2317-95
S2317	S2317-102	8x5x1	dolerite	altered
S2317	S2317-103	7x4x4	basalt	same as S2317-95
S2317	S2317-104	8x4x4	basalt	same as S2317-95
S2317	S2317-105	16x11x3	basalt	altered brecciated porphyric basalt
S2317	S2317-106	5x3x1.5	basalt	brecciated altered basalt
S2317	S2317-107	5x4x4	basalt	altered basalt with sulphides filling the vesicles
S2317	S2317-108	5x5x1	basalt	altered aphyric basalt
S2317	S2317-109	4x2x1.5	basalt	altered basalt
S2317	S2317-110	4x2x1	basalt	altered basalt
S2317	S2317-111	3x2x1	basalt	altered basalt

S2317	S2317-112	3x2x1	basalt	altered basalt
S2317	S2317-113	5x3x2	breccia	altered basaltic breccia
S2317	S2317-114	4x3x2	basalt	altered basalt
S2317	S2317-115	8x5x5	breccia	altered basaltic breccia
S2317	S2317-116	6x4x2	basalt	strongly altered basalt
S2317	S2317-117	8x6x1	basalt	strongly altered basalt
S2317	S2317-118	3x2x2	breccia	altered basaltic breccia
S2317	S2317-119	12x10x3	basalt	strongly altered basalt
S2317	S2317-120	6x5x1.5	basalt	altered poprhyroclastic basalt
S2317	S2317-121	6x2x1	basalt	altered vesicular basalt
S2317	S2317-122	3x2x2	dolerite	altered dolerite
S2317	S2317-123	2x1x1	dolerite	same as S2317-122
S2317	S2317-124	6x4x1.5	basalt	altered vesicular basalt
S2317	S2317-125	6x4x3	dolerite	altered
S2317	S2317-126	8x5x5	gabbro	medium grained
S2317	S2317-127	5x3x2	gabbro	coarse grained, slightly brecciated
S2317	S2317-128	2x1x1	gabbro	altered
S2317	S2317-129	3x3x2	gabbro	very altered
S2317	S2317-130	4x1x1	gabbro	fine grained, altered
S2317	S2317-131	3x2x1	gabbro	fine grained
S2317	S2317-132	2.5x15x1	gabbro	altered
S2317	S2317-133	1.5x0.5x0.5	basalt	Plg poprhyric altered basalt
S2317	S2317-134	various small		various small pieces of altered basalt
S2317	S2317-135	6x4x3	peridotite	serpentinized peridotite. Relics of opx fresh up to 1 cm. relics of spinels. Black type serpentine.
S2317	S2317-136	5x4x2	breccia	basaltic breccia covered with Fe-Mn crust
S2317	S2317-137	5x3x2	breccia	basaltic breccia covered with Fe-Mn crust
S2317	S2317-138	7x4x3	breccia	basaltic breccia with small pieces of fresh glass in the matrix
S2317	S2317-139	6x4x1.5	crust	Fe-Mn crust
S2318	S2318-01	14x11x9	basalt	aphyric
S2318	S2318-02	22x17x14	gabbro	fresh, coarse to medium grained gabbro, olivine
S2318	S2318-03	18x14x12	gabbro	pegmatitic to coarse grained gabbro, large px oikocrysts up to 3 cm. fresh
S2318	S2318-04	14x10x7	gabbro	coarse to medium grained, slightly altered
S2318	S2318-05	8x7x5	gabbro	same as S2318-04
S2318	S2318-06	7x4x4	gabbro	same as S2318-04
S2318	S2318-07	6x3x3	gabbro	same as S2318-04
S2318	S2318-08	12x6x6	gabbro	same as S2318-04
S2318	S2318-09	9x7x6	gabbro	same as S2318-04
S2318	S2318-10	10x6x5	gabbro	same as S2318-04
S2318	S2318-11	7x5x5	gabbro	same as S2318-04
S2318	S2318-12	8x5x6	gabbro	same as S2318-04
S2318	S2318-13	6x6x4	gabbro	fine grained
S2318	S2318-14	9x7x4	gabbro	same as S2318-12
S2318	S2318-15	11x7x4	gabbro	olivine bearing gabbro/gabbro contact. Grain size decreases with olivine content. Olivine is altered
S2318	S2318-16	8x6x4	microgabb	

			ro	
S2318	S2318-17	6x5x4	dolerite	pebble with ice marks
S2318	S2318-18	8x6x6	microgabbro	altered
S2318	S2318-19	8x6x6	gabbro	same as S2318-04
S2318	S2318-20	13x10x7	gabbro vein	leucogabbro vein in altered peridotite. There is a large altered reaction zone around the leucovein. Late oxide rich ore levels
S2318	S2318-21	8x5x4	anorthosite	altered, sulphides
S2318	S2318-22	6x6x5	gabbro	ol-bearing gabbro. One 7-cm pyroxene oikocryst ebclosing pl chadocrysts. Altered
S2318	S2318-23	7x6x4	breccia	breccia of altered gabbroic and basaltic fragments
S2318	S2318-24	6x5x4	gabbro	altered leucogabbro
S2318	S2318-25	8x6x3	gabbro	altered
S2318	S2318-26	8x4x4	troctolite	altered
S2318	S2318-27	6x6x3	peridotite-gabbro contact	fresh cpx in peridotite
S2318	S2318-28	16x15x11	harzburgite	harzburgite cut by a 1-cm thick gabbroic vein. Serpentinized up to 80%
S2318	S2318-29	7x4x4	lherzolite	px-rich lherzolite cut by 3mm thick gabbroic veinlet. Cpx forms aggregates policrystalline cutting opx foliation by 20 degrees. Impregnated peridotite
S2318	S2318-30	11x10x8	lherzolite	px-poor lherzolite. Cpx forms aggregates elongated to form chains cutting peridotite foliation. Strongly altered
S2318	S2318-31	11x9x5	lherzolite	px-poor lherzolite same as S2418-30
S2318	S2318-32	13x10x10	harzburgite	
S2318	S2318-33	11x9x9	lherzolite	lherzolite, cpx forms aggregated after impregnation. Plg? Cpx + plg aggregates. But plg seems more scattered
S2318	S2318-34	10x7x6	harzburgite	small veins of altered stuff possibly replacing 1 mm thick gabbroic (plg bearing) vein
S2318	S2318-35	11x5x4	lherzolite	cpx is possibly present because of impregnation. Round opx
S2318	S2318-36	10x6x5	harzburgite	same as S2318-35
S2318	S2318-37	7x5x4	harzburgite	
S2318	S2318-38	13x9x6	lherzolite	cpx aggregates cuttin rock foliation. Cpx+plg scattered aggregates
S2318	S2318-39	10x7x6	lherzolite	same as previous S2318-38. Cut by 1 mm thick gabbroic vein
S2318	S2318-40	10x8x5	lherzolite	same as S2318-38
S2318	S2318-41	11x6x5	lherzolite	same as S2318-38
S2318	S2318-42	10x4x3	peridotite-dunite contact	the dunite is cut by thin veins (?)
S2318	S2318-43	8x5x3	lherzolite	same as S2318-38
S2318	S2318-44	6x5x4	lherzolite	same as S2318-38; possibly no plagioclase
S2318	S2318-45	6x6x3	lherzolite	plagioclase?
S2318	S2318-46	10x8x5	lherzolite	cpx aggregates
S2318	S2318-47	8x7x4	harzburgite	
S2318	S2318-48	10x8x4	harzburgite	

S2318	S2318-49	8x7x7	lherzolite	high cpx/opx ratio. Opx poor peridotite. Locally cpx/opx=1
S2318	S2318-50	8x7x5	harzburgitic mylonite	strong mineral lineation marked by policrystalline aggregates of opx (altered?). Small dark green garins associated with opx (possibly amph?). Opx aggregates look like recrystallized after deformation
S2318	S2318-51	9x7x4	harzburgitic mylonite	same as previous sample cut in the foliation plane
S2318	S2318-52	7x5x3	harzburgite	harzburgite impregnated by abundant Pl patches
S2318	S2318-53	7x5x2	peridotite	altered
S2318	S2318-54	6x5x4	harzburgite	abundant plg patches; possibly cpx elongated aggregates
S2318	S2318-55	10x6x5	dunite	large spn patches possibly surrounded by Pl (or Chl). A set of thin iddingsite veins cut the Ol foliation
S2318	S2318-56	6x6x4	lherzolite	cpx-rich lherzolite with or without plagioclase. Large policrystalline cpx aggregates cut opx foliation. Small scattered Pl grains, associated with cpx. High px/ol ratio
S2318	S2318-57	6x5x4	lherzolite	same as S2318-56
S2318	S2318-58	9x6x5	lherzolite	same as S2318-56, plus Pl rich vein parallel to cpx foliation
S2318	S2318-59	6x5x4	lherzolite	same as S2318-56
S2318	S2318-60	6x4x3	lherzolite	same as S2318-56
S2318	S2318-61	6x5x4	lherzolite	same as S2318-56
S2318	S2318-62	17x15x13	breccia	dunitic breccia. Breccia is cemented by carbonatic ooze. Clasts of variably altered dunite. Large sp patches. The largest clast is probably fresh.
S2319	S2319-01	12x8x7	gabbro	leucogabbro or plagiogranite. Possibly erratic.
S2319	S2319-02	11x7x7	breccia	erratic breccia chert
S2323	S2323-01	28x18x4	mylonite	mylonitic peridotite
S2323	S2323-02	18x15x10	granitoid	quartz-garnet erratic
S2323	S2323-03	14x15x14	granitoid	quartz-kfeldspar (?) erratic
S2324	S2324-01	13x8x8	lherzolite	lherzolite, large cpx-spn. Spinel up to 3 mm. dark green cpx. Protogranular texture
S2324	S2324-02	9x5x4	lherzolite	lherzolite same as 24-01
S2324	S2324-03	13x6x6	harzburgite	harzburgite, no residual cpx
S2324	S2324-04	13x6x5	lherzolite	lherzolite. Large spinels
S2324	S2324-05	13x8x8	harzburgite	harzburgite cut by gabbroic veins
S2325	S2325-01	25x2421	lherzolite	lherzolite with high T foliation, marked by opx and cpx lineation. Cpx forms chains possibly by melt percolation ± sp. Maybe possible olivine. Opx 20%, cpx 5-10%. Opx 4-12 mm
S2325	S2325-02	25x19x11	harzburgite	strongly foliated harzburgite. Deeply altered, fractured. Fractures are filled with serpentine and calcite/aragonite
S2325	S2325-03	21x15x13	lherzolite	lherzolite with low opx content. Opx 10-15%; cpx is present as discrete grains. No evident lineation. Weak foliation. Large spinel up to 3 mm
S2325	S2325-04	12x11x8	lherzolite	weakly foliated lherzolite. Gabbroic vein in contact (be careful)
S2325	S2325-05	18x14x10	lherzolite	lherzolite with protomilonitic texture. Cpx rich bands in the center of the sample. Cpx forms elongated policrystalline patches associated with large rare spinel grains up to 2 mm
S2325	S2325-06	15x10x4	lherzolite	weakly foliated lherzolite, pyroxene poor, opx 10-15%. Opx and cpx grains are rounded
S2325	S2325-07	11x10x4	lherzolite	lherzolite similar to S2325-05, large elongated opx

S2325	S2325-08	10x9x4	lherzolite	lherzolite similar to S2325-05. look at the sp-pl (?) intergrowth marked on the sample
S2325	S2325-09	16x7x4	lherzolite	lherzolite similar to S2325-05
S2325	S2325-10	21x10x8	lherzolite	lherzolite similar to S2325-05; rounded small opx and cpx, strongly foliated
S2325	S2325-11	14x10x4	lherzolite	lherzolite, opx poor, very large spinel marked on the surface. Fresh olivine (?)
S2325	S2325-12	30x9x8	lherzolite	lherzolite, pyroxene poor, large spinels
S2325	S2325-13	10x10x4	lherzolite	lherzolite similar to S2325-06
S2325	S2325-14	6x4x4	lherzolite	lherzolite with large spinel (0.5 cm). Elongated cpx and rounded opx
S2325	S2325-15	6x4x4	lherzolite	lherzolite, rounded cpx and opx
S2325	S2325-16	8x7x3	lherzolite	lherzolite, granular to weakly foliated texture, px rich, spinel trains
S2325	S2325-17	13x8x4	lherzolite	lherzolite, px poor, 2-3 mm spinels, fresh olivine, weak foliation
S2325	S2325-18	13x7x5	lherzolite	foliated lherzolite, px poor, cpx is dark green
S2325	S2325-19	17x11x9	lherzolite	lherzolite, px rich, opx up to 1 cm, cpx are generally smaller (0.5 cm), granular texture
S2325	S2325-20	12x10x6	lherzolite	lherzolite similar to S2325-05, cpx forms elongated policrystalline patches. Small sp
S2325	S2325-21	12x6x6	lherzolite	lherzolite, px rich, granular to foliated texture. Cpx is dark green
S2325	S2325-22	15x10x7	lherzolite	lherzolite similar to S2325-21, px rich, gabbroic (?) impregnation
S2325	S2325-23	14x12x6	lherzolite	lherzolite similar to S2325-21
S2325	S2325-24	14x10x7	lherzolite	lherzolite similar to S2325-04
S2325	S2325-25	16x10x8	lherzolite	lherzolite similar to S2325-04, weak foliation
S2325	S2325-26	24x12x9	harzburgite	harzburgite with layers rich in cpx. Cpx is small or elongated in policrystalline aggregates. 30-40% opx. Weak foliation. Aragonite veins cut the upper portion of the sample which can be considered an oficalcite.
S2325	S2325-27	13x8x3	lherzolite	lherzolite similar to S2325-05
S2325	S2325-28	11x7x4	lherzolite	lherzolite, px poor
S2325	S2325-29	18x11x8	lherzolite	lherzolite similar to S2325-10 but with less px. Aragonite veins replacing milonitic domain?
S2325	S2325-30	26x22x8	lherzolite	lherzolite similar to S2325-10. more altered
S2325	S2325-31	17x10x8	lherzolite	altered peridotite, foliated similar to S2325-30
S2325	S2325-32	11x7x7	lherzolite	peridotite similar to S2325-31
S2325	S2325-33	30x17x13	lherzolite	altered foliated peridotite similar to S2325-32 but more foliated and strongly weathered
S2325	S2325-34	19x10x8	lherzolite	lherzolite similar to S2325-01, with less cpx and more weathered
S2325	S2325-35	16x10x5	lherzolite	lherzolite similar to S2325-05
S2325	S2325-36	13x10x6	lherzolite	lherzolite similar to S2325-02, less weathered; fresh cpx
S2325	S2325-37	19x18x9	lherzolite	lherzolite similar to S2325-01, less cpx. Domains enriched in opx up to 1 cm associated with 0.5 cm spn. 2 cm thick gabbroic vein.
S2325	S2325-38	7x6x5	lherzolite	lherzolite strongly foliated, dark green cpx
S2325	S2325-39	17x14x8	lherzolite	lherzolite similar to S2325-01
S2325	S2325-40	15x10x10	lherzolite	lherzolite similar to S2325-03, big spn
S2325	S2325-41	10x6x5	lherzolite	lherzolite similar to S2325-03 (looks like a piece of # S2325-03)
S2325	S2325-42	14x6x4	lherzolite	lherzolite similar to S2325-03, big spn
S2325	S2325-43	13x6x5	lherzolite	lherzolite weakly foliated, fine grain size of cpx and opx
S2325	S2325-44	10x7x6	lherzolite	lherzolite same as S2325-18, foliated, less cpx
S2325	S2325-45	11x10x4	harzburgite	harzburgite similar to S2325-44, foliated
S2325	S2325-46	9x8x8	lherzolite	altered foliated peridotite similar to S2325-33

S2325	S2325-47	21x10x10	lherzolite	altered foliated peridotite similar to S2325-46
S2325	S2325-48	13x10x2	lherzolite	lherzolite similar to S2325-10. plg patches.
S2325	S2325-49	13x5x4	harzburgite	harzburgite with plagioclase patches
S2325	S2325-50	7x6x5	lherzolite	lherzolite with milonitic texture
S2325	S2325-51	10x6x5	lherzolite	lherzolite, dark green cpx similar to S2325-21
S2325	S2325-52	12x6x5	dunite	
S2325	S2325-53	12x7x4	dunite	strongly weathered
S2325	S2325-54	11x6x6	pyroxenite	Ol-pyroxenite, fresh dark green cpx, small spn
S2325	S2325-55	8x6x3	pyroxenite	same as S2325-54
S2325	S2325-56	8x5x4	gabbro	gabbro hydrothermally altered, noce green amph (Chl?)
S2325	S2325-57	8x3x2	pyroxenite	same as S2325-54
S2325	S2325-58	8x5x4	siltstone?	siltstone with 2 mm thick cemented mud
S2325	S2325-59	17x7x7	oficalcite	brecciated peridotite cemented by calcite/aragonite
S2325	S2325-60	9x7x5	oficalcite	same as S2325-60
S2325	S2325-61	9x3x2	oficalcite	same as S2325-60
S2325	S2325-62	6x4x1	oficalcite	same as S2325-60
S2325	S2325-63	8x3x2	oficalcite	same as S2325-60
S2325	S2325-64	7x4x3	oficalcite	same as S2325-60
S2325	S2325-65	8x5x3	oficalcite	same as S2325-60
S2325	S2325-66	5x4x2	peridotite	strongly altered serpentinite
S2325	S2325-67	8x4x3	pyroxenite	strongly altered ortopyroxenite
S2325	S2325-68	7x3x3	peridotite	strongly altered peridotite with hydrogarnet (? pink mineral)
S2325	S2325-69	10x7x5	granite	erratic granit (Qtz+Plg)
S2325	S2325-70	8x6x4	granite	biotite rich erratic granite
S2326	S2326-01	40x30x30	lherzolite	lherzolite cut by pyroxenite vein. Altered Pl patches dispersed in the matrix. Cpx is shut. Opx relics. Pl is more abundant closer to the vein. Granular texture
S2326	S2326-02	15x9x4	lherzolite	lherzolite similar to S2326-01, with more abundant Pl (3 %) scattered in the matrix
S2326	S2326-03	9x6x4	lherzolite	lherzolite similar to S2326-01, Pl is associated with spinel
S2326	S2326-04	7x6x6	lherzolite	lherzolite similar to S2326-03
S2326	S2326-05	6x5x4	lherzolite	lherzolite similar to S2326-03
S2326	S2326-06	7x6x3	lherzolite	lherzolite similar to S2326-03, Px are bigger, up to 1 cm
S2326	S2326-07	9x6x5	lherzolite	lherzolite similar to S2326-03, cpx is fresh
S2326	S2326-08	11x7x6	lherzolite	lherzolite similar to S2326-07, Pl scattered in the matrix
S2326	S2326-09	9x7x6	lherzolite	lherzolite similar to S2326-08, less Pl
S2326	S2326-10	6x5x4	lherzolite	lherzolite similar to S2326-08, abundant Px
S2326	S2326-11	9x8x5	lherzolite	lherzolite similar to S2326-10, Pl is associated with spn, some is scattered in the matrix
S2326	S2326-12	14x11x8	lherzolite	lherzolite similar to S2326-02, Pl is associated with spn, some scattered
S2326	S2326-13	11x8x6	lherzolite	strongly altered lherzolite similar to S2326-01, Pl is scattered
S2326	S2326-14	12x10x6	lherzolite	lherzolite similar to S2326-01, more weathered. Pl is associated with Px
S2326	S2326-15	11x10x9	lherzolite	lherzolite similar to S2326-01 but very fresh and no Pl
S2326	S2326-16	9x7x5	lherzolite	lherzolite with fresh cpx similar to S2326-15
S2326	S2326-17	8x6x5	lherzolite	lherzolite similar to S2326-16
S2326	S2326-18	11x8x4	lherzolite	lherzolite similar to S2326-16, more weathered, cpx shut

S2326	S2326-19	10x5x4	lherzolite	lherzolite. Most cpx and opx are rounded. Some elongated cpx form elogated chains
S2326	S2326-20	10x4x3	lherzolite	lherzolite; fresh px but serpentine is strongly weathered
S2326	S2326-21	8x5x4	lherzolite	lherzolite; pyroxenes look "readsorbed"; intergranular texture?; cpx is dark green
S2326	S2326-22	8x5x4	peridotite	serpentinized peridotite, weathered, fresh opx. Ol?
S2326	S2326-23	10x6x3	lherzolite	weathered lherzolite. Some cpx and opx are fresh. Lots of serpentine veins
S2326	S2326-24	8x6x4	lherzolite	lherzolite similar to S2326-21, dark serpentine and very abundant green cpx. Intergranular texture?
S2326	S2326-25	9x9x4	lherzolite	lherzolite similar to S2326-24, more altered. Cpx shut
S2326	S2326-26	13x10x6	lherzolite	lherzolite with gabbroic intrusion or some sort of high T melt intrusion. Cpx is still fresh. Intrusion seems altered.
S2326	S2326-27	10x6x6	lherzolite	serpentinized peridotite with gabbroic intrusion similar to S2326-26. more weathered. Rare pl associated with pyroxene.
S2326	S2326-28	9x6x4	lherzolite	fresh lherzolite cut by lots of serpentine veins
S2326	S2326-29	12x10x6	lherzolite	fresh lherzolite surrounded by serpentine veins (?) similar to S2326-28. maybe after a system of cracks in fresh peridotite filled with tardive serpentine
S2326	S2326-30	10x8x5	peridotite	weathered peridotite cut by serpentine veins
S2326	S2326-31	11x6x5	lherzolite	lherzolite with stretched opx and cpx; milonite (?)
S2326	S2326-32	8x7x5	peridotite	peridotite similar to S2326-30
S2326	S2326-33	6x5x5	basalt	vesicular aphyric basalt; vesicles are bundant and have irregular shape,
S2326	S2326-34	4x4x3	basalt	vesicular aphyric basalt; very fine vesicles
S2326	S2326-35	6x5x4	basalt	aphyric basalt; very fine vesicles; rare small plg
S2326	S2326-36	18x14x8	basalt	altered basalt
S2326	S2326-37	9x7x5	basalt	altered basalt
S2326	S2326-38	22x12x11	dolerite	
S2326	S2326-39	30x20x15	basalt	Pl-porphyric basalt; Pl crystals up to 4mm. Slightly vesicular. Vesicles are empty and have irregular shape
S2327	S2327-01	8x7x6	basalt	basalt pebble. Rounded shape. Aphyric with rare vesicles. Thick alteration rim
S2327	S2327-02	28x15x15	erratic granitoid	erratic granitoid
S2329	S2329-01	14x11x8	gabbro	rounded sample of Ol gabbro partially covered by thin FeMn film. Probably erratic material
S2330	S2330-01	22x18x12	dolerite	erratic
S2330	S2330-02	20x20x12	dolerite	erratic
S2330	S2330-03	5x3x2	dolerite	erratic
S2330	S2330-04	11x9x8	basalt	erratic
S2330	S2330-05	30x25x25	granit	erratic

Appendix B

Major element analysis

Major element analysis of ABFZ samples

Olivine

Sample	'SiO2'	'TiO2'	'Al2O3'	'FeO'	'MnO'	'MgO'	'CaO'	'Na2O'	'K2O'	'Cr2O3'	'NiO'	'Totals'
S2325-03R	41.52	0.00	0.00	8.05	0.13	50.03	0.02	0.01	0.00	0.00	0.38	100.14
S2325-03R	41.51	0.00	0.01	8.18	0.12	50.13	0.04	0.00	0.00	0.01	0.31	100.31
S2325-03R	41.58	0.00	0.00	8.24	0.11	50.39	0.03	0.01	0.00	0.00	0.40	100.75
S2325-03R	41.33	0.03	0.00	8.27	0.13	50.48	0.01	0.01	0.00	0.00	0.40	100.66
S2324-04R	41.13	0.00	0.00	9.21	0.17	49.69	0.04	0.00	0.00	0.04	0.38	100.67
S2324-04R	41.05	0.01	0.01	9.18	0.14	49.81	0.04	0.01	0.00	0.00	0.37	100.62
S2324-04R	41.02	0.02	0.03	9.29	0.13	49.87	0.03	0.00	0.01	0.00	0.38	100.78
S2325-05R	41.68	0.00	0.00	7.91	0.11	50.40	0.01	0.00	0.00	0.00	0.40	100.51
S2325-05R	41.64	0.00	0.01	7.93	0.09	50.30	0.01	0.01	0.00	0.02	0.37	100.38
S2325-05R	41.72	0.01	0.02	8.21	0.12	50.16	0.00	0.00	0.00	0.00	0.37	100.61
S2325-05R	41.92	0.00	0.00	7.75	0.13	50.44	0.01	0.00	0.01	0.00	0.41	100.68
S2325-01c	41.42	0.05	0.00	9.19	0.12	49.62	0.02	0.01	0.01	0.01	0.37	100.82
S2325-01c	41.73	0.00	0.00	9.19	0.13	49.50	0.03	0.00	0.00	0.00	0.36	100.95

S2325-01c	41.67	0.01	0.00	9.13	0.13	49.64	0.01	0.01	0.01	0.00	0.39	101.01
S2325-01c	41.75	0.01	0.00	9.09	0.16	49.71	0.01	0.01	0.00	0.00	0.38	101.13
S2318-49	39.88	0.01	0.00	13.39	0.25	46.51	0.02	0.02	0.01	0.00	0.32	100.43
S2325-55_R	41.05	0.00	0.00	9.64	0.12	49.16	0.05	0.00	0.00	0.00	0.38	100.41
S2325-55_R	41.11	0.00	0.01	9.74	0.16	49.27	0.03	0.01	0.01	0.00	0.41	100.76
S2325-55_R	40.92	0.02	0.02	9.78	0.19	49.14	0.04	0.04	0.02	0.00	0.38	100.56
S2325-55_R	40.83	0.00	0.00	8.45	0.14	49.83	0.02	0.03	0.00	0.10	0.40	99.81
S2325-55_R	41.29	0.00	0.00	8.46	0.11	50.25	0.01	0.01	0.00	0.17	0.43	100.73
S2325-51_R	41.36	0.02	0.00	8.59	0.13	49.95	0.01	0.00	0.00	0.11	0.41	100.59

Orthopyroxene

Sample	Spot	'SiO2'	'TiO2'	'Al2O3'	'FeO'	'MnO'	'MgO'	'CaO'	'Na2O'	'K2O'	'Cr2O3'	'NiO'	'Totals'
S2325-03R	core	55.81	0.11	3.86	5.26	0.14	33.09	0.94	0.08	0.00	0.88	0.10	100.28
S2325-03R	rim sp1	56.45	0.12	2.98	5.52	0.14	33.85	0.48	0.02	0.00	0.71	0.08	100.35
S2325-03R	core	55.69	0.11	4.09	5.28	0.11	33.07	0.73	0.06	0.00	0.94	0.12	100.20
S2325-03R	rim ol	56.86	0.11	2.69	5.38	0.11	33.93	0.64	0.03	0.01	0.44	0.08	100.27
S2325-03R	rim sp2	56.44	0.14	3.30	5.42	0.10	33.48	0.91	0.04	0.00	0.67	0.09	100.59
S2325-03R	core	56.06	0.12	3.72	5.38	0.11	33.50	0.68	0.07	0.01	0.81	0.08	100.54
S2325-03R	rim ol	56.66	0.13	3.08	5.51	0.13	33.88	0.54	0.02	0.00	0.61	0.07	100.61
S2325-03R	core	56.21	0.13	3.58	5.29	0.11	33.24	0.89	0.07	0.01	0.78	0.06	100.36
S2325-03R	rim ol	56.07	0.15	3.61	5.31	0.12	33.11	1.25	0.11	0.00	0.74	0.10	100.57
S2324-04R	core	55.99	0.12	3.31	5.98	0.13	33.12	0.95	0.07	0.00	0.88	0.10	100.67
S2324-04R	rim cpx1	56.23	0.08	3.19	5.96	0.14	33.31	0.75	0.06	0.01	0.91	0.11	100.76
S2324-04R	rim ol	56.27	0.12	3.20	5.96	0.12	33.03	1.11	0.10	0.00	0.87	0.09	100.88
S2326-15R	rim cpx2	56.67	0.07	3.19	6.25	0.12	33.26	0.54	0.02	0.00	0.44	0.08	100.63
S2326-15R	core	55.43	0.09	4.86	6.20	0.14	32.07	1.15	0.05	0.00	0.80	0.13	100.91
S2326-15R	core	54.37	0.15	4.97	6.28	0.15	32.03	1.00	0.08	0.01	0.76	0.09	99.88
S2326-15R	rim ol	55.83	0.12	3.90	6.24	0.13	33.06	0.75	0.07	0.01	0.65	0.08	100.85
S2326-21R	core	54.87	0.18	5.79	6.47	0.14	30.98	1.50	0.13	0.01	0.60	0.09	100.79
S2326-21R	rim ol	55.84	0.15	4.29	6.79	0.15	31.98	0.83	0.07	0.00	0.35	0.09	100.56
S2326-21R	rim cpx	55.72	0.12	4.47	6.83	0.14	32.37	0.64	0.04	0.00	0.41	0.10	100.84
S2326-21R	core	55.16	0.17	5.02	6.68	0.13	31.64	1.03	0.38	0.01	0.46	0.09	100.78
S2326-21R	core	54.82	0.11	5.80	6.88	0.16	31.45	0.81	0.06	0.01	0.55	0.07	100.71
S2326-21R	core	55.01	0.15	5.70	6.59	0.14	31.58	1.03	0.09	0.00	0.57	0.08	100.95
S2326-21R	rim cpx4	56.01	0.07	4.11	6.54	0.14	32.44	0.67	0.05	0.00	0.40	0.08	100.52
S2326-21R	rim ol	56.51	0.12	3.63	6.72	0.16	32.67	0.62	0.03	0.00	0.28	0.06	100.80
S2326-16R	core	54.81	0.15	5.29	6.23	0.13	31.84	1.16	0.11	0.00	0.73	0.09	100.55
S2326-16R	core	55.01	0.15	5.25	6.20	0.13	31.89	1.07	0.09	0.01	0.72	0.08	100.59
S2326-16R	rim ol	55.75	0.11	4.08	6.40	0.13	32.68	0.88	0.10	0.01	0.49	0.07	100.70
S2326-01D	core	54.71	0.16	5.31	6.85	0.15	31.69	1.11	0.05	0.00	0.52	0.09	100.63
S2326-01D	rim cpx	53.07	0.17	5.62	6.97	0.15	32.21	0.67	0.05	0.00	0.54	0.09	99.54

S2326-01D	core	54.78	0.16	5.48	6.88	0.15	31.98	0.68	0.05	0.00	0.51	0.07	100.75
S2325-05R	core	55.48	0.14	4.54	5.07	0.10	32.85	1.29	0.12	0.00	0.84	0.10	100.55
S2325-05R	rim ol	56.62	0.09	2.91	5.36	0.13	34.13	0.57	0.06	0.00	0.36	0.09	100.33
S2325-05R	rim sp1	56.30	0.11	3.66	5.10	0.10	33.41	0.96	0.06	0.01	0.67	0.07	100.44
S2325-05R	core	55.55	0.13	4.62	5.10	0.10	32.80	1.10	0.09	0.01	0.85	0.11	100.44
S2325-05R	rim cpx1	56.91	0.08	3.21	5.33	0.13	33.61	0.61	0.03	0.01	0.50	0.12	100.52
S2325-05R	rim ol	56.66	0.10	3.44	5.30	0.12	33.82	0.65	0.05	0.01	0.52	0.07	100.73
S2325-05R	core	56.11	0.12	4.24	5.17	0.10	33.18	0.81	0.06	0.01	0.77	0.11	100.68
S2325-05R	rim ol	56.67	0.11	3.31	5.35	0.12	34.03	0.48	0.02	0.00	0.49	0.09	100.67
S2325-05R	rim cpx2	56.33	0.11	3.77	5.27	0.14	33.54	0.79	0.05	0.00	0.57	0.10	100.67
S2325-05R	core	56.29	0.11	3.77	5.25	0.12	33.53	0.89	0.08	0.00	0.60	0.07	100.70
S2325-05R	rim ol	57.35	0.07	2.52	5.42	0.13	34.16	0.42	0.01	0.00	0.26	0.11	100.46
S2325-01c	core	56.21	0.06	3.80	5.79	0.14	32.78	1.05	0.08	0.00	0.74	0.09	100.73
S2325-01c	rim ol	56.19	0.06	3.35	5.83	0.12	33.36	0.90	0.06	0.01	0.52	0.09	100.48
S2325-01c	core	55.64	0.05	4.11	5.65	0.13	32.36	1.41	0.10	0.00	0.86	0.11	100.41
S2325-01c	rim ol	56.82	0.04	2.91	5.95	0.14	33.85	0.60	0.03	0.00	0.38	0.08	100.80
S2325-01c	core	55.87	0.05	4.03	5.77	0.12	32.22	1.40	0.11	0.01	0.78	0.07	100.41
S2325-01c	rim ol	56.83	0.05	2.82	6.04	0.14	33.55	0.58	0.03	0.00	0.40	0.10	100.55
S2326-24R	core	54.86	0.15	5.55	6.16	0.14	31.65	1.15	0.10	0.00	0.69	0.10	100.56
S2326-24R	rim ol	56.36	0.14	4.04	6.34	0.14	32.38	0.76	0.10	0.01	0.50	0.07	100.84
S2326-18R	core	54.83	0.13	4.89	5.97	0.11	31.64	1.92	0.06	0.00	0.81	0.09	100.44
S2326-18R	rim ol	54.49	0.10	4.13	6.37	0.16	32.24	1.30	0.04	0.00	0.60	0.09	99.53
S2326-18R	core	54.95	0.12	4.96	6.15	0.13	32.19	1.15	0.05	0.00	0.80	0.09	100.60
S2326-18R	rim ol	55.97	0.10	3.84	6.31	0.14	32.54	1.19	0.03	0.01	0.54	0.07	100.74
S2326-09R	core	54.56	0.18	5.20	6.66	0.14	31.29	1.33	0.06	0.01	0.66	0.09	100.20
S2326-09R	rim ol	56.03	0.24	2.90	6.82	0.14	32.70	0.87	0.02	0.00	0.44	0.10	100.26
S2326-09R	core	55.47	0.18	4.50	6.77	0.14	31.57	1.24	0.04	0.00	0.60	0.08	100.59
S2326-09R	rim ol	56.64	0.19	2.97	6.97	0.16	32.62	0.75	0.02	0.00	0.44	0.08	100.86
S2326-02R	core	54.96	0.18	5.15	6.68	0.15	31.90	0.96	0.03	0.01	0.40	0.09	100.51
S2326-02R	rim sp1	55.54	0.31	3.89	6.97	0.15	32.70	0.46	0.01	0.00	0.44	0.06	100.53
S2326-02R	core	54.75	0.17	5.60	6.64	0.14	31.70	0.89	0.04	0.00	0.44	0.09	100.48
S2326-02R	rim sp	56.24	0.12	3.27	6.75	0.16	33.07	0.53	0.01	0.00	0.28	0.08	100.52
S2317-135	core	55.90	0.12	2.87	6.80	0.19	32.50	1.35	0.03	0.00	0.89	0.10	100.75
S2317-135	rim	55.12	0.11	3.91	6.88	0.17	31.89	1.58	0.04	0.00	0.92	0.10	100.73
S2317-135_R	core	55.61	0.13	2.61	6.89	0.18	32.61	1.36	0.02	0.00	0.79	0.07	100.27
S2317-135_R	rim	55.73	0.12	2.63	6.79	0.17	32.26	1.70	0.02	0.00	0.72	0.09	100.25
S2317-135	rim	55.41	0.13	3.35	6.72	0.16	31.98	1.88	0.03	0.00	0.86	0.08	100.61
S2317-135	core	54.75	0.11	4.32	6.84	0.17	32.05	1.32	0.03	0.00	0.93	0.10	100.62
S2318-28E_R	rim	55.30	0.10	3.48	6.35	0.16	32.54	1.55	0.03	0.00	0.84	0.11	100.46
S2318-28E_R	rim next to cpx incl	55.22	0.11	3.74	6.08	0.16	31.22	2.72	0.06	0.00	0.89	0.10	100.29
S2318-28E_R	core	54.78	0.16	4.09	6.14	0.16	31.36	2.82	0.07	0.00	0.93	0.10	100.61
S2318-28E_R	core	55.60	0.10	3.25	6.33	0.16	32.75	1.43	0.04	0.00	0.80	0.11	100.58
S2318-28E_R	rim	55.24	0.10	3.17	6.34	0.16	32.46	1.54	0.02	0.00	0.81	0.11	99.95

S2318-31	core	55.67	0.21	2.66	7.59	0.23	31.82	1.68	0.04	0.00	0.76	0.08	100.74
S2318-31	rim	55.79	0.21	2.28	7.86	0.21	32.25	1.06	0.03	0.00	0.62	0.08	100.40
S2318-31	core	54.86	0.13	3.88	7.79	0.18	31.74	1.01	0.03	0.00	0.89	0.09	100.60
S2318-31	rim	55.72	0.18	2.57	7.82	0.23	32.10	1.15	0.02	0.00	0.76	0.09	100.64
S2318-31	rim	54.18	0.13	4.37	7.72	0.16	31.47	1.20	0.03	0.00	0.87	0.09	100.23
S2318-31	core	54.52	0.14	3.99	7.69	0.18	31.50	1.41	0.03	0.00	0.83	0.09	100.38
S2318-35	core	55.28	0.13	3.62	6.24	0.16	31.82	2.09	0.04	0.00	0.93	0.11	100.43
S2318-35	rim	55.99	0.12	2.90	6.35	0.17	32.44	1.70	0.02	0.00	0.86	0.10	100.66
S2318-35	rim	55.24	0.13	3.47	6.35	0.18	31.86	2.10	0.04	0.00	0.92	0.09	100.40
S2318-35	core	54.54	0.13	4.13	6.24	0.14	31.21	2.85	0.05	0.01	0.95	0.09	100.35
S2318-49	rim	55.40	0.12	2.33	8.35	0.24	32.01	1.33	0.05	0.00	0.73	0.07	100.62
S2318-49	core	55.42	0.14	2.52	8.25	0.21	31.40	1.56	0.05	0.00	0.77	0.08	100.42
S2318-49	core	55.28	0.10	2.76	8.43	0.20	31.56	1.15	0.04	0.00	0.84	0.08	100.44
S2318-49	rim	56.01	0.16	1.92	8.41	0.26	32.38	0.78	0.02	0.00	0.56	0.06	100.56
S2325-08_R	core	55.02	0.14	4.69	4.93	0.12	32.03	2.59	0.12	0.00	0.91	0.11	100.66
S2325-08_R	rim next to spn1	55.68	0.15	3.80	5.19	0.12	33.54	1.05	0.04	0.00	0.73	0.09	100.40
S2325-08_R	in spn1	55.63	0.14	3.81	5.14	0.13	33.58	1.33	0.07	0.00	0.69	0.09	100.63
S2325-51_R	core	53.59	0.25	5.63	5.29	0.15	28.71	5.35	0.18	0.00	0.84	0.08	100.06
S2325-51_R	rim	56.17	0.15	2.58	6.26	0.14	33.47	0.97	0.02	0.00	0.63	0.09	100.50
S2325-51_R	core	54.29	0.12	5.56	6.12	0.14	31.89	1.12	0.03	0.00	0.80	0.10	100.16
S2325-51_R	rim	56.03	0.15	3.01	6.31	0.16	33.45	0.56	0.01	0.00	0.63	0.11	100.42
S2325-55_R	core	54.50	0.19	4.53	5.97	0.15	31.55	2.40	0.10	0.01	0.81	0.11	100.31
S2325-55_R	core	53.93	0.18	5.27	6.18	0.16	31.83	1.65	0.07	0.01	0.82	0.11	100.22

Clinopyroxene

Sample	Spot	'SiO2'	'TiO2'	'Al2O3'	'FeO'	'MnO'	'MgO'	'CaO'	'Na2O'	'K2O'	'Cr2O3'	'NiO'	'Totals'
S2325-03R	core	52.61	0.46	5.67	2.21	0.07	14.76	20.60	1.87	0.00	1.72	0.04	100.02
S2325-03R	rim opx1	53.06	0.49	5.33	2.17	0.08	15.21	21.27	1.41	0.01	1.51	0.06	100.60
S2325-03R	rim ol	53.30	0.48	5.16	2.30	0.07	15.59	20.93	1.49	0.00	1.43	0.05	100.80
S2325-03R	rim sp1	52.62	0.62	5.14	2.08	0.05	15.15	21.78	1.27	0.00	1.59	0.01	100.31
S2325-03R	core	52.61	0.43	5.68	2.21	0.08	14.85	20.93	1.58	0.00	1.74	0.04	100.16
S2325-03R	rim ol	53.18	0.45	4.98	2.25	0.07	15.35	20.81	1.53	0.00	1.52	0.03	100.17
S2325-03R	rim opx1	52.76	0.51	5.39	2.23	0.06	15.12	21.02	1.53	0.00	1.54	0.03	100.20
S2325-03R	core	52.85	0.40	5.96	2.24	0.07	14.73	20.68	1.75	0.00	1.96	0.04	100.68
S2325-03R	rim ol	53.33	0.52	5.09	2.19	0.05	15.37	21.28	1.44	0.00	1.41	0.05	100.73
S2324-04R	core	52.83	0.32	5.08	2.56	0.06	15.22	20.71	1.57	0.00	2.11	0.05	100.50
S2324-04R	rim ol	53.38	0.36	4.63	2.41	0.09	15.50	21.28	1.47	0.00	1.70	0.04	100.85
S2324-04R	rim opx1	53.36	0.34	4.60	2.12	0.07	15.12	21.25	1.58	0.00	1.89	0.04	100.36
S2324-04R	core	52.94	0.32	5.12	2.37	0.08	14.74	21.22	1.56	0.00	1.98	0.04	100.37
S2324-04R	rim ol	53.54	0.33	4.09	2.19	0.06	15.50	22.33	1.22	0.00	1.53	0.07	100.86
S2326-15R	core	51.93	0.40	6.70	2.54	0.07	14.26	21.47	1.48	0.01	1.56	0.04	100.45
S2326-15R	rim ol	52.84	0.50	4.54	2.47	0.06	15.48	22.26	1.13	0.00	1.29	0.03	100.60

S2326-15R	rim opx1	52.48	0.44	5.89	2.46	0.09	14.85	21.77	1.21	0.00	1.44	0.04	100.68
S2326-15R	core1	52.15	0.41	6.56	2.68	0.08	14.53	21.23	1.36	0.00	1.58	0.03	100.62
S2326-15R	core2	50.55	0.45	6.70	2.64	0.07	14.62	22.07	0.94	0.00	1.47	0.03	99.54
S2326-15R	rim ol	52.73	0.38	3.73	2.41	0.08	16.08	22.79	0.70	0.01	1.12	0.03	100.06
S2326-21R	core	52.19	0.57	6.17	2.99	0.10	15.19	21.05	1.31	0.01	0.82	0.05	100.45
S2326-21R	core	52.20	0.50	7.09	2.90	0.10	14.81	21.04	1.32	0.00	0.86	0.07	100.89
S2326-21R	core	51.95	0.49	7.49	2.82	0.10	14.62	20.92	1.31	0.00	0.96	0.02	100.68
S2326-21R	rim ol	52.54	0.47	5.92	2.84	0.10	15.37	21.50	1.14	0.00	0.70	0.03	100.61
S2326-21R	rim opx1 (cpx?)	51.87	0.56	6.69	2.40	0.10	14.67	22.42	1.04	0.01	0.86	0.03	100.65
S2326-21R	core	51.92	0.58	7.13	2.45	0.09	14.24	21.73	1.31	0.00	0.93	0.06	100.43
S2326-21R	core	52.02	0.54	7.47	2.69	0.08	14.60	20.80	1.47	0.00	0.98	0.07	100.72
S2326-21R	rim ol	52.94	0.56	5.86	2.82	0.08	15.17	21.46	1.18	0.01	0.67	0.04	100.79
S2326-21R	core	52.64	0.50	6.49	2.55	0.08	14.86	21.23	1.38	0.00	0.82	0.03	100.59
S2326-21R	rim ol	53.49	0.45	4.63	2.55	0.07	15.57	22.04	1.07	0.00	0.54	0.07	100.48
S2326-16R	rim sp1	52.49	0.60	6.03	2.59	0.10	15.11	21.17	1.39	0.01	1.18	0.05	100.72
S2326-16R	core	52.21	0.50	6.96	2.60	0.07	14.43	21.16	1.53	0.00	1.23	0.03	100.73
S2326-16R	core	52.25	0.48	6.88	2.63	0.09	14.45	21.31	1.52	0.00	1.22	0.03	100.87
S2326-01D	core	50.71	0.59	7.65	3.04	0.10	14.62	22.35	0.78	0.00	0.87	0.03	100.74
S2326-01D	core	51.85	1.06	5.28	2.58	0.07	15.39	23.16	0.65	0.00	0.90	0.04	100.99
S2326-01D	core	50.21	0.65	7.52	2.97	0.09	14.59	22.51	0.80	0.01	0.84	0.03	100.21
S2325-05R	core	52.32	0.42	6.02	2.20	0.08	15.14	20.78	1.52	0.01	1.47	0.05	100.01
S2325-05R	rim opx2	52.62	0.40	5.50	2.00	0.05	15.27	21.36	1.44	0.01	1.42	0.02	100.08
S2325-05R	core	53.38	0.47	5.90	2.22	0.06	15.52	20.49	1.42	0.00	1.27	0.04	100.78
S2325-05R	rim opx5	52.67	0.50	6.03	2.04	0.04	14.89	21.68	1.27	0.00	1.22	0.02	100.37
S2325-05R	rim ol	53.00	0.49	5.47	2.31	0.07	15.53	21.13	1.27	0.00	1.30	0.02	100.59
S2325-01c	core	52.71	0.16	5.49	2.32	0.08	15.32	21.53	1.15	0.00	1.47	0.03	100.26
S2325-01c	rim ol	52.88	0.20	5.23	2.39	0.08	15.53	21.33	1.18	0.00	1.35	0.04	100.21
S2325-01c	core	52.81	0.15	5.51	2.41	0.09	15.45	21.12	1.24	0.01	1.57	0.07	100.42
S2325-01c	rim ol	53.48	0.14	4.05	2.30	0.08	16.10	22.11	1.04	0.00	0.96	0.06	100.32
S2325-01c	core	53.27	0.16	5.34	2.20	0.07	15.14	21.53	1.27	0.00	1.47	0.03	100.49
S2325-01c	rim ol	53.23	0.20	4.87	2.22	0.06	15.53	21.80	1.14	0.00	1.32	0.04	100.41
S2326-24R	core	51.97	0.42	7.29	2.84	0.10	14.14	21.16	1.50	0.01	1.17	0.04	100.65
S2326-24R	rim ol	52.53	0.50	5.86	2.67	0.07	15.03	21.64	1.20	0.00	0.94	0.04	100.49
S2326-24R	core1	52.11	0.46	7.21	2.80	0.09	14.63	20.51	1.49	0.01	1.17	0.04	100.52
S2326-24R	core2	51.95	0.44	7.08	2.73	0.09	14.57	20.84	1.48	0.00	1.16	0.03	100.37
S2326-24R	core3	51.68	0.46	7.14	2.72	0.08	14.59	20.88	1.44	0.00	1.15	0.04	100.17
S2326-24R	core1	52.02	0.43	7.12	2.85	0.09	15.03	20.07	1.41	0.00	1.20	0.02	100.24
S2326-24R	rim ol	51.97	0.47	6.76	2.78	0.10	15.03	20.98	1.29	0.00	1.12	0.03	100.50
S2326-24R	core2	52.02	0.45	7.27	2.77	0.09	14.54	20.65	1.50	0.00	1.19	0.07	100.54
S2326-18R	core1	51.50	0.31	6.43	2.93	0.09	15.63	21.79	0.57	0.00	1.27	0.05	100.56
S2326-18R	core2	51.47	0.32	6.08	2.80	0.09	15.53	22.29	0.56	0.00	1.24	0.07	100.43
S2326-18R	core3	51.89	0.28	5.95	2.78	0.10	15.78	22.15	0.56	0.00	1.20	0.03	100.71
S2326-18R	rim ol (?)	52.33	0.32	5.00	2.70	0.07	15.73	22.85	0.55	0.00	1.05	0.01	100.62

S2326-18R	core1	51.74	0.29	6.19	2.89	0.09	15.86	21.53	0.58	0.00	1.30	0.07	100.54
S2326-18R	core2	51.38	0.32	6.17	2.78	0.11	15.30	22.09	0.57	0.00	1.25	0.06	100.04
S2326-18R	core	51.52	0.33	6.05	2.71	0.09	15.35	22.40	0.61	0.00	1.21	0.04	100.30
S2326-18R	rim ol	51.44	0.32	4.60	2.71	0.11	16.13	22.64	0.55	0.00	0.88	0.04	99.41
S2326-09R	core	51.37	0.55	7.07	3.29	0.10	15.19	21.64	0.70	0.00	0.90	0.03	100.86
S2326-09R	rim ol	51.96	0.85	4.98	3.16	0.09	15.96	21.64	0.65	0.00	1.00	0.05	100.34
S2326-09R	core1	50.89	0.60	7.09	3.19	0.10	15.07	21.78	0.66	0.01	0.99	0.05	100.44
S2326-09R	core2	50.69	0.60	7.52	3.25	0.09	14.68	22.13	0.64	0.00	0.92	0.05	100.57
S2326-09R	rim ol	52.88	0.72	4.54	2.85	0.08	15.88	22.45	0.63	0.00	1.00	0.02	101.05
S2326-09R	core1	51.24	0.59	7.10	3.21	0.12	15.23	21.50	0.74	0.00	0.99	0.04	100.77
S2326-09R	core2	51.21	0.59	6.57	3.12	0.10	15.48	21.33	0.75	0.00	0.95	0.03	100.14
S2326-09R	rim ol	53.73	0.60	3.25	3.04	0.08	16.45	22.29	0.55	0.00	0.63	0.06	100.67
S2326-02R	core	51.23	0.61	7.63	3.03	0.10	14.36	21.25	1.15	0.00	0.78	0.03	100.20
S2326-02R	rim ol	53.20	0.65	4.05	2.93	0.10	16.26	22.23	0.63	0.00	0.52	0.02	100.60
S2326-02R	rim opx	50.63	0.80	7.10	2.73	0.09	14.71	22.53	0.69	0.00	0.77	0.06	100.11
S2326-02R	core	51.20	0.59	7.21	3.15	0.11	14.85	21.58	0.91	0.01	0.76	0.03	100.39
S2326-02R	rim ol	52.89	0.52	3.76	2.87	0.10	16.49	22.37	0.57	0.00	0.54	0.06	100.17
S2318-28E_R	in opx1	51.70	0.31	4.79	2.78	0.10	16.85	21.82	0.55	0.00	1.45	0.07	100.42
S2318-31	rim	52.08	0.45	3.64	3.14	0.12	16.39	22.50	0.46	0.00	1.27	0.04	100.10
S2318-31	core	51.50	0.50	4.47	3.32	0.13	16.17	22.26	0.49	0.00	1.32	0.04	100.19
S2318-35	core	51.43	0.27	5.60	3.45	0.12	17.48	20.53	0.34	0.00	1.36	0.06	100.66
S2318-35	rim	52.48	0.31	3.56	2.66	0.10	16.72	23.02	0.37	0.00	1.30	0.04	100.55
S2318-49	core	52.37	0.37	3.58	3.61	0.14	16.46	21.74	0.58	0.00	1.37	0.05	100.28
S2318-49	rim	52.94	0.36	3.15	3.36	0.14	16.51	22.30	0.54	0.00	1.22	0.04	100.56
S2318-49	core	51.53	0.33	4.33	3.77	0.15	16.29	21.55	0.59	0.00	1.59	0.04	100.17
S2318-49	rim of opx2	52.77	0.34	3.01	3.32	0.14	16.49	22.55	0.57	0.00	1.22	0.05	100.45
S2325-08_R	core	51.97	0.38	6.23	2.41	0.09	16.19	20.70	1.13	0.00	1.60	0.06	100.76
S2325-08_R	rim	52.57	0.41	5.13	2.13	0.08	16.04	21.75	1.09	0.00	1.40	0.04	100.66
S2325-51_R	core	50.92	0.44	6.75	2.72	0.12	15.18	22.48	0.69	0.00	1.15	0.04	100.51
S2325-51_R	rim	51.22	0.55	5.37	2.69	0.09	16.06	22.19	0.62	0.00	1.21	0.05	100.06
S2325-51_R	core	51.23	0.34	6.56	3.48	0.14	19.43	17.62	0.55	0.00	1.08	0.07	100.48
S2325-51_R	core	50.24	0.35	7.30	2.88	0.11	15.62	21.48	0.67	0.00	1.16	0.07	99.88
S2325-55_R	core	50.43	0.48	7.19	2.80	0.09	14.79	22.89	0.64	0.01	1.15	0.05	100.53
S2325-55_R	rim	50.90	0.57	6.73	2.67	0.11	15.42	22.25	0.74	0.01	1.20	0.05	100.66
S2325-55_R	core	50.59	0.47	6.65	2.83	0.09	15.69	21.95	0.66	0.01	1.20	0.06	100.20
S2325-55_R	rim	51.96	0.55	5.29	2.57	0.12	15.74	22.47	0.70	0.00	1.29	0.03	100.72

Spinel

Sample	Spot	'SiO2'	'TiO2'	'Al2O3'	'FeO'	'MnO'	'MgO'	'CaO'	'Na2O'	'K2O'	'Cr2O3'	'NiO'	'Totals'
S2325-03R	core	0.04	0.17	42.77	13.66	0.08	17.66	0.01	0.01	0.00	25.84	0.20	100.45
S2325-03R	core	0.03	0.18	39.82	14.37	0.11	17.01	0.02	0.01	0.00	28.86	0.13	100.55
S2325-03R	core	0.01	0.18	43.47	13.30	0.07	18.04	0.00	0.02	0.01	25.64	0.22	100.95

S2325-03R	rim cpx3	0.00	0.14	43.83	13.50	0.06	17.44	0.04	0.01	0.00	25.67	0.17	100.87
S2325-03R	rim cpx3	0.04	0.12	43.81	13.45	0.07	17.49	0.01	0.02	0.00	25.78	0.17	100.96
S2325-03R	rim opx1	0.00	0.15	40.54	13.95	0.05	16.94	0.02	0.02	0.01	28.98	0.14	100.81
S2325-03R	rim opx1	0.03	0.07	44.86	13.15	0.08	17.81	0.00	0.03	0.01	24.27	0.20	100.52
S2325-03R	rim ol	0.01	0.13	45.33	13.41	0.06	17.82	0.00	0.00	0.00	23.42	0.21	100.39
S2325-03R	rim ol	0.03	0.16	44.13	13.58	0.09	17.67	0.02	0.01	0.00	24.60	0.21	100.49
S2325-03R	core	0.02	0.16	42.75	13.88	0.07	17.65	0.00	0.03	0.00	25.85	0.20	100.62
S2325-03R	core	0.02	0.23	39.82	13.56	0.04	17.25	0.00	0.01	0.00	29.54	0.21	100.69
S2325-03R	core	0.00	0.21	39.62	13.59	0.10	17.22	0.01	0.02	0.00	29.60	0.21	100.58
S2325-03R	core	0.01	0.21	39.81	13.66	0.09	17.40	0.01	0.03	0.00	29.30	0.16	100.68
S2325-03R	rim opx3	0.01	0.13	35.98	15.57	0.10	15.77	0.03	0.02	0.02	33.20	0.12	100.95
S2325-03R	rim opx3	0.02	0.10	34.32	15.96	0.09	15.10	0.03	0.01	0.00	34.71	0.16	100.49
S2324-04R	core	0.02	0.22	35.93	15.19	0.09	16.10	0.00	0.02	0.00	32.61	0.13	100.32
S2324-04R	core	0.02	0.19	36.36	15.03	0.10	16.12	0.00	0.01	0.00	32.56	0.12	100.51
S2324-04R	core	0.01	0.23	35.96	15.15	0.06	16.20	0.00	0.01	0.00	32.65	0.17	100.43
S2324-04R	core	0.02	0.16	38.43	14.82	0.04	16.48	0.00	0.02	0.00	30.20	0.10	100.27
S2324-04R	core	0.01	0.15	39.08	14.52	0.07	16.66	0.01	0.00	0.00	29.92	0.14	100.56
S2324-04R	core	0.01	0.17	39.32	14.44	0.09	16.59	0.00	0.00	0.00	29.64	0.15	100.42
S2326-15R	core	0.01	0.12	51.17	12.65	0.04	18.44	0.00	0.01	0.00	17.08	0.25	99.76
S2326-15R	core	0.01	0.13	50.39	13.35	0.10	17.90	0.00	0.00	0.00	17.69	0.30	99.88
S2326-15R	core	0.01	0.14	49.03	13.64	0.05	17.77	0.00	0.01	0.01	18.81	0.26	99.74
S2326-15R	core	0.03	0.38	33.78	17.68	0.09	14.10	0.02	0.07	0.00	34.02	0.12	100.31
S2326-15R	core	0.02	0.26	37.85	16.43	0.08	15.21	0.00	0.00	0.00	30.70	0.14	100.70
S2326-21R	core	0.04	0.12	57.10	11.64	0.08	19.43	0.00	0.00	0.00	10.62	0.33	99.36
S2326-21R	core	0.02	0.09	56.52	11.72	0.07	20.27	0.01	0.01	0.00	10.59	0.35	99.65
S2326-21R	core	0.02	0.07	55.62	11.75	0.07	20.42	0.00	0.01	0.00	10.79	0.36	99.12
S2326-21R	core	0.03	0.10	56.62	11.49	0.04	19.46	0.00	0.01	0.00	10.95	0.36	99.05
S2326-16R	core	0.01	0.15	51.72	11.69	0.04	19.26	0.00	0.01	0.00	16.29	0.34	99.51
S2326-16R	core	0.03	0.10	51.52	11.72	0.04	19.29	0.01	0.01	0.00	16.54	0.31	99.57
S2326-16R	core	0.04	0.16	51.49	11.57	0.07	19.21	0.00	0.00	0.00	16.60	0.35	99.50
S2326-16R	core	0.03	0.13	52.03	11.41	0.07	19.50	0.00	0.01	0.00	16.03	0.33	99.54
S2326-16R	core	0.01	0.13	52.94	11.18	0.06	19.53	0.00	0.00	0.00	15.09	0.34	99.28
S2326-16R	core/rim	0.00	0.11	52.56	11.32	0.07	19.52	0.01	0.01	0.00	15.69	0.35	99.64
S2326-16R	core	0.02	0.12	52.22	11.40	0.10	19.59	0.00	0.03	0.00	15.37	0.39	99.23
S2326-16R	core	0.02	0.13	52.04	11.45	0.07	19.47	0.00	0.34	0.02	15.42	0.43	99.38
S2326-01D	core	0.01	0.15	51.10	15.21	0.09	16.91	0.01	0.02	0.00	15.57	0.20	99.27
S2326-01D	core	0.00	0.21	51.83	15.33	0.08	16.93	0.02	0.00	0.00	15.63	0.32	100.35
S2326-01D	core	0.02	0.28	50.72	15.07	0.07	16.83	0.00	0.01	0.00	16.61	0.25	99.87
S2326-01D	core	0.02	0.58	50.00	14.04	0.06	17.91	0.00	0.01	0.00	17.28	0.29	100.18
S2326-01D	rim cpx	0.02	0.23	47.52	14.96	0.06	17.42	0.01	0.03	0.00	19.68	0.23	100.15
S2326-01D	rim cpx	0.02	0.57	46.56	14.96	0.10	17.37	0.01	0.02	0.00	20.15	0.24	100.00
S2326-01D	core	0.00	0.18	48.89	14.22	0.06	17.78	0.00	0.01	0.00	18.62	0.26	100.03
S2326-01D	core	0.00	0.12	54.55	13.22	0.11	18.53	0.01	0.01	0.00	12.87	0.26	99.68

S2326-01D	core	0.02	0.17	55.02	13.07	0.09	19.01	0.00	0.00	0.00	12.42	0.34	100.15
S2326-01D	core	0.01	0.18	54.36	13.41	0.10	18.58	0.00	0.01	0.01	12.79	0.35	99.79
S2325-05R	rim opx1	0.01	0.12	41.25	13.39	0.09	17.52	0.01	0.01	0.00	27.46	0.24	100.09
S2325-05R	rim opx1	0.01	0.12	41.99	12.95	0.02	17.71	0.01	0.00	0.00	27.00	0.15	99.95
S2325-05R	rim opx1	0.03	0.10	40.28	13.64	0.04	17.27	0.01	0.01	0.00	28.22	0.21	99.82
S2325-05R	core	0.05	0.10	46.02	12.33	0.10	18.34	0.00	0.00	0.00	22.58	0.27	99.80
S2325-05R	core	0.01	0.07	46.60	11.96	0.06	18.57	0.00	0.01	0.00	22.15	0.27	99.70
S2325-05R	core	0.01	0.15	46.65	12.12	0.09	18.42	0.00	0.03	0.00	22.31	0.22	100.01
S2325-05R	rim ol	0.02	0.05	48.66	12.11	0.10	19.11	0.00	0.00	0.00	19.63	0.20	99.89
S2325-05R	rim ol	0.00	0.06	45.46	14.09	0.04	17.22	0.03	0.00	0.00	22.35	0.17	99.42
S2325-05R	rim ol	0.01	0.06	47.81	12.68	0.06	18.23	0.00	0.02	0.00	19.98	0.23	99.09
S2325-05R	rim ol	0.01	0.04	49.17	12.75	0.07	18.22	0.01	0.01	0.00	18.89	0.25	99.42
S2325-05R	core	0.00	0.09	48.31	11.89	0.07	18.95	0.00	0.00	0.00	20.16	0.20	99.68
S2325-05R	core	0.02	0.10	47.54	12.11	0.06	18.88	0.01	0.00	0.00	20.37	0.22	99.31
S2325-05R	core	0.02	0.08	48.07	12.33	0.07	18.64	0.00	0.00	0.00	19.84	0.24	99.28
S2325-05R	rim opx	0.02	0.01	50.55	10.71	0.07	19.29	0.01	0.02	0.00	18.47	0.27	99.42
S2325-05R	rim opx	0.03	0.03	45.40	12.47	0.07	18.04	0.00	0.00	0.00	23.23	0.15	99.42
S2325-05R	rim opx	0.03	0.01	45.74	13.01	0.09	17.92	0.00	0.01	0.00	22.36	0.16	99.33
S2325-01c	core	0.01	0.05	46.16	12.82	0.05	17.83	0.01	0.00	0.00	22.78	0.25	99.98
S2325-01c	core	0.01	0.06	45.75	12.85	0.06	17.82	0.00	0.01	0.00	23.00	0.23	99.78
S2325-01c	core	0.00	0.05	46.04	13.12	0.08	17.43	0.00	0.01	0.00	22.52	0.22	99.47
S2325-01c	core	0.03	0.08	44.29	12.55	0.08	17.88	0.00	0.00	0.00	24.30	0.22	99.44
S2325-01c	core	0.02	0.06	44.13	12.66	0.07	17.79	0.00	0.01	0.01	24.64	0.22	99.59
S2325-01c	core	0.02	0.07	44.70	12.90	0.11	17.89	0.01	0.01	0.00	23.43	0.24	99.39
S2326-24R	core	0.02	0.11	54.08	11.65	0.07	19.53	0.00	0.01	0.00	13.61	0.31	99.39
S2326-24R	core	0.02	0.06	53.92	11.37	0.06	19.38	0.01	0.00	0.00	13.65	0.37	98.86
S2326-24R	core	0.03	0.11	53.98	11.73	0.07	19.37	0.00	0.01	0.01	13.66	0.38	99.34
S2326-24R	rim cpx	0.00	0.11	53.90	11.19	0.04	19.74	0.03	0.01	0.00	13.57	0.32	98.91
S2326-24R	rim cpx	0.03	0.05	54.17	11.39	0.04	19.67	0.04	0.01	0.00	13.58	0.31	99.29
S2326-24R	rim cpx	0.03	0.09	54.66	11.34	0.07	19.66	0.04	0.00	0.00	13.34	0.35	99.58
S2326-18R	core	0.01	0.10	49.68	12.89	0.10	18.90	0.01	0.02	0.00	17.36	0.29	99.36
S2326-18R	core	0.01	0.08	49.94	12.77	0.03	18.88	0.00	0.01	0.00	17.16	0.31	99.20
S2326-18R	core	0.02	0.09	49.70	12.71	0.09	18.76	0.00	0.00	0.00	17.64	0.28	99.29
S2326-18R	core	0.03	0.10	49.26	12.94	0.08	18.63	0.00	0.01	0.00	17.75	0.27	99.07
S2326-18R	core	0.02	0.05	49.89	12.89	0.06	18.70	0.00	0.01	0.01	17.61	0.35	99.59
S2326-18R	core	0.01	0.10	49.78	12.74	0.08	18.49	0.00	0.03	0.00	17.76	0.32	99.31
S2326-09R	core	0.03	0.19	52.48	13.60	0.07	18.91	0.01	0.03	0.01	14.27	0.32	99.92
S2326-09R	core	0.02	0.19	52.64	13.53	0.09	18.90	0.01	0.06	0.02	14.06	0.36	99.89
S2326-09R	core	0.01	0.26	52.08	13.66	0.07	18.71	0.00	0.02	0.00	14.70	0.34	99.83
S2326-09R	rim ol	0.02	0.35	50.51	13.92	0.07	18.65	0.01	0.00	0.00	15.75	0.31	99.59
S2326-09R	rim ol	0.02	0.36	49.64	14.03	0.07	18.39	0.04	0.01	0.00	16.83	0.25	99.63
S2326-02R	core	0.00	0.06	58.36	11.85	0.08	19.12	0.00	0.01	0.00	9.41	0.35	99.24
S2326-02R	core	0.02	0.05	58.13	11.87	0.08	19.17	0.00	0.03	0.00	9.58	0.34	99.26

S2326-02R	core	0.09	0.18	57.22	12.11	0.10	19.86	0.01	0.00	0.00	9.29	0.41	99.27
S2326-02R	core	0.01	0.13	57.59	12.13	0.08	19.80	0.00	0.01	0.00	9.17	0.37	99.28
S2326-02R	rim	0.04	0.11	56.52	11.83	0.05	19.80	0.01	0.01	0.00	10.77	0.34	99.48
S2317-135	core	0.05	0.38	27.09	20.34	0.44	12.37	0.00	0.00	0.00	39.82	0.15	100.64
S2317-135	core	0.02	0.40	27.04	20.38	0.46	12.31	0.00	0.03	0.00	39.84	0.10	100.58
S2317-135	core	0.04	0.33	26.28	20.67	0.42	11.88	0.00	0.01	0.00	40.60	0.16	100.38
S2317-135	core	0.04	0.34	27.12	21.18	0.44	11.93	0.00	0.00	0.00	39.42	0.08	100.55
S2317-135	core	0.04	0.38	27.27	21.07	0.47	11.79	0.00	0.01	0.00	38.75	0.11	99.89
S2317-135	core	0.10	0.38	27.94	19.74	0.42	12.70	0.02	0.04	0.00	38.59	0.17	100.10
S2317-135	core	0.02	0.37	27.98	19.81	0.43	12.80	0.01	0.03	0.01	38.82	0.13	100.42
S2317-135_R	core	0.04	0.34	30.15	19.30	0.48	12.58	0.00	0.00	0.00	36.68	0.16	99.72
S2317-135_R	core	0.04	0.34	28.83	20.39	0.46	12.17	0.00	0.01	0.00	37.88	0.12	100.24
S2317-135_R	core	0.29	0.33	30.10	19.55	0.44	12.97	0.01	0.02	0.00	36.20	0.14	100.06
S2317-135_R	small xx	0.05	0.30	31.03	19.04	0.46	12.33	0.00	0.01	0.00	35.90	0.15	99.27
S2317-135_R	small xx	0.04	0.31	31.53	18.75	0.44	12.43	0.00	0.01	0.00	35.57	0.16	99.25
S2317-135_R	small xx	0.04	0.26	30.12	19.96	0.44	12.39	0.00	0.00	0.00	36.53	0.16	99.91
S2317-135_R	small xx	0.04	0.31	28.10	20.22	0.48	11.68	0.00	0.00	0.00	38.40	0.14	99.37
S2317-135_R	small xx	0.04	0.35	30.62	19.75	0.42	12.31	0.00	0.01	0.00	36.37	0.13	99.99
S2317-135	rim	0.04	0.31	26.81	20.62	0.43	12.15	0.00	0.01	0.00	39.97	0.12	100.47
S2317-135	rim	0.04	0.32	24.85	20.89	0.39	11.83	0.00	0.01	0.00	42.28	0.10	100.71
S2317-135	rim	0.04	0.39	25.93	20.72	0.54	11.84	0.00	0.00	0.00	40.70	0.09	100.24
S2317-135	rim	0.05	0.37	28.24	22.04	0.43	11.72	0.00	0.00	0.00	37.09	0.11	100.06
S2317-135	rim	0.04	0.35	27.14	20.89	0.45	11.97	0.00	0.02	0.00	39.47	0.12	100.45
S2317-135	rim	0.02	0.41	27.39	20.63	0.39	12.22	0.00	0.03	0.00	39.14	0.13	100.36
S2317-135	rim	0.03	0.41	27.62	20.23	0.47	12.73	0.00	0.01	0.00	39.20	0.11	100.80
S2317-135	rim	0.06	0.37	25.50	21.31	0.48	11.57	0.01	0.01	0.00	40.76	0.09	100.15
S2317-135_R	rim	0.05	0.31	30.33	19.56	0.41	13.26	0.00	0.01	0.00	36.70	0.12	100.75
S2317-135_R	rim	0.12	0.34	31.24	19.19	0.39	13.18	0.00	0.01	0.00	35.66	0.15	100.29
S2317-135_R	rim	0.05	0.29	29.41	19.79	0.46	12.26	0.00	0.02	0.00	37.96	0.16	100.41
S2318-28E_R	core	0.05	0.19	33.74	17.59	0.42	14.38	0.00	0.00	0.00	33.04	0.14	99.55
S2318-28E_R	core	0.05	0.23	34.24	17.79	0.44	14.02	0.00	0.01	0.00	33.03	0.16	99.98
S2318-28E_R	core	0.06	0.18	36.46	16.40	0.34	15.11	0.00	0.02	0.00	30.43	0.19	99.20
S2318-28E_R	core	0.03	0.23	35.98	16.57	0.37	15.18	0.01	0.01	0.00	31.10	0.16	99.64
S2318-28E_R	core	0.05	0.22	36.48	16.25	0.34	15.54	0.00	0.00	0.00	30.66	0.18	99.74
S2318-28E_R	core	0.04	0.25	36.35	16.42	0.31	15.25	0.00	0.03	0.00	31.56	0.18	100.40
S2318-28E_R	core	0.03	0.22	34.26	16.86	0.36	14.72	0.00	0.00	0.00	33.05	0.20	99.71
S2318-28E_R	core	0.04	0.20	41.05	15.47	0.31	16.32	0.00	0.01	0.00	26.30	0.20	99.89
S2318-28E_R	core	0.01	0.20	35.41	17.19	0.40	14.63	0.00	0.00	0.00	31.58	0.17	99.60
S2318-28E_R	rim	0.03	0.24	34.50	17.03	0.41	15.13	0.00	0.01	0.00	31.80	0.17	99.33
S2318-28E_R	rim	0.03	0.20	35.75	16.73	0.38	15.35	0.00	0.00	0.00	30.74	0.19	99.36
S2318-28E_R	rim	0.05	0.24	35.38	16.83	0.39	14.93	0.00	0.00	0.00	32.08	0.17	100.07
S2318-28E_R	rim	0.05	0.19	35.34	16.94	0.39	14.72	0.00	0.01	0.00	32.31	0.16	100.12
S2318-28E_R	rim	0.03	0.20	36.16	17.02	0.32	15.03	0.01	0.00	0.00	31.16	0.14	100.08

S2318-28E_R	rim	0.04	0.23	36.35	17.45	0.34	14.73	0.00	0.01	0.00	31.16	0.14	100.44
S2318-28E_R	rim	0.03	0.24	34.13	17.60	0.38	14.54	0.00	0.00	0.00	33.49	0.18	100.59
S2318-31	core	0.03	0.86	24.47	23.70	0.49	11.19	0.00	0.00	0.00	38.56	0.17	99.47
S2318-31	core	0.01	0.84	25.33	22.92	0.49	11.46	0.00	0.01	0.00	38.21	0.13	99.41
S2318-31	core	0.03	0.78	25.23	23.45	0.50	11.49	0.00	0.02	0.00	38.48	0.16	100.12
S2318-31	core	0.03	0.84	25.43	23.15	0.52	11.34	0.00	0.03	0.01	38.18	0.16	99.69
S2318-31	core	0.03	0.79	25.47	23.42	0.52	11.36	0.01	0.02	0.00	37.91	0.14	99.67
S2318-31	core	0.01	0.86	25.56	23.47	0.46	11.39	0.00	0.05	0.00	37.92	0.11	99.84
S2318-31	core	0.02	0.84	25.19	22.89	0.47	11.46	0.00	0.01	0.00	38.57	0.17	99.63
S2318-31	core	0.05	0.82	25.17	23.35	0.46	11.59	0.00	0.01	0.00	38.32	0.15	99.93
S2318-31	core	0.04	0.82	24.81	23.28	0.49	11.25	0.00	0.00	0.00	38.91	0.13	99.72
S2318-31	rim	0.02	0.87	23.70	23.89	0.50	11.47	0.00	0.00	0.00	38.91	0.14	99.50
S2318-31	rim	0.04	0.91	24.37	23.66	0.44	11.31	0.00	0.03	0.00	38.74	0.16	99.67
S2318-31	rim	0.07	0.84	24.54	23.26	0.49	11.46	0.00	0.03	0.00	38.70	0.14	99.53
S2318-31	rim	0.04	0.84	24.53	23.69	0.46	11.47	0.00	0.01	0.00	38.76	0.15	99.97
S2318-31	rim	0.06	0.89	24.57	23.47	0.50	11.50	0.00	0.03	0.00	38.36	0.15	99.55
S2318-31	rim	0.03	0.85	24.46	23.96	0.52	11.19	0.01	0.00	0.00	38.81	0.18	100.01
S2318-31	rim	0.06	0.95	24.24	24.72	0.47	10.14	0.00	0.03	0.00	38.71	0.14	99.47
S2318-31	rim	0.04	0.76	24.20	24.11	0.48	10.79	0.00	0.02	0.00	38.59	0.13	99.12
S2318-31	rim	0.22	0.87	23.80	24.90	0.50	10.97	0.01	0.05	0.00	37.73	0.11	99.16
S2318-35	core	0.03	0.41	28.72	18.89	0.41	13.77	0.00	0.02	0.00	37.88	0.18	100.31
S2318-35	core	0.03	0.44	28.81	18.75	0.43	13.68	0.00	0.00	0.01	37.69	0.16	100.01
S2318-35	core	0.12	0.44	29.63	18.74	0.33	13.21	0.01	0.00	0.01	37.45	0.18	100.11
S2318-35	core	0.05	0.42	28.40	19.04	0.43	13.65	0.00	0.00	0.00	37.88	0.15	100.01
S2318-35	core	0.06	0.42	28.93	18.89	0.41	13.91	0.00	0.00	0.00	37.37	0.18	100.18
S2318-35	core	0.03	0.41	28.97	18.53	0.40	13.71	0.00	0.02	0.00	37.84	0.10	100.01
S2318-35	core	0.04	0.43	28.89	18.91	0.42	13.48	0.00	0.01	0.00	37.84	0.14	100.16
S2318-35	core	0.04	0.42	28.74	18.68	0.43	13.65	0.00	0.00	0.00	37.70	0.13	99.79
S2318-35	core	0.01	0.41	28.85	18.74	0.41	13.71	0.00	0.01	0.00	37.78	0.16	100.06
S2318-35	core	0.04	0.41	28.83	18.82	0.42	13.50	0.00	0.01	0.00	37.96	0.13	100.11
S2318-35	core	0.03	0.43	28.74	18.74	0.40	13.50	0.00	0.00	0.00	37.98	0.18	100.01
S2318-35	core	0.02	0.44	28.06	19.56	0.45	13.17	0.01	0.00	0.00	37.99	0.15	99.84
S2318-35	core	0.06	0.42	28.25	19.33	0.42	13.32	0.00	0.03	0.01	38.22	0.15	100.20
S2318-35	core	0.04	0.38	28.16	19.21	0.41	13.25	0.00	0.00	0.00	38.13	0.15	99.74
S2318-35	rim	0.04	0.39	27.85	19.20	0.42	13.20	0.00	0.00	0.00	38.87	0.16	100.14
S2318-35	rim	0.06	0.39	27.67	19.32	0.45	13.03	0.00	0.01	0.00	38.79	0.13	99.85
S2318-35	rim	0.05	0.47	27.66	20.32	0.42	12.73	0.00	0.01	0.00	38.73	0.10	100.50
S2318-35	rim	0.03	0.43	28.04	19.79	0.40	13.22	0.00	0.00	0.00	37.75	0.13	99.80
S2318-35	rim	0.03	0.41	27.27	20.29	0.44	13.05	0.00	0.00	0.00	38.59	0.15	100.23
S2318-35	rim	0.05	0.39	27.93	19.52	0.37	13.27	0.00	0.01	0.00	38.19	0.16	99.89
S2325-08_R	core	0.02	0.15	47.19	10.84	0.24	19.19	0.00	0.00	0.00	21.89	0.27	99.79
S2325-08_R	core	0.05	0.15	47.21	10.78	0.27	19.22	0.00	0.02	0.00	22.03	0.31	100.04
S2325-08_R	core	0.03	0.21	47.15	10.96	0.23	19.09	0.00	0.00	0.00	22.08	0.27	100.03

S2325-08_R	core	0.05	0.19	45.62	11.36	0.24	18.95	0.01	0.00	0.00	23.45	0.26	100.12
S2325-08_R	core	1.30	0.19	44.97	11.46	0.27	19.10	0.09	0.01	0.00	22.77	0.26	100.43
S2325-08_R	core	0.05	0.16	45.64	11.63	0.30	18.76	0.00	0.02	0.00	23.68	0.28	100.50
S2325-08_R	core	0.03	0.12	48.14	11.38	0.23	19.14	0.00	0.02	0.00	21.19	0.27	100.51
S2325-08_R	core	0.06	0.12	48.22	11.21	0.21	19.13	0.00	0.00	0.00	20.61	0.28	99.84
S2325-08_R	core	0.06	0.10	48.37	11.11	0.19	19.20	0.00	0.00	0.00	21.13	0.31	100.47
S2325-08_R	rim	0.02	0.08	49.57	10.97	0.24	19.48	0.00	0.01	0.00	19.60	0.27	100.25
S2325-08_R	rim	0.02	0.14	47.67	11.48	0.22	19.08	0.01	0.00	0.00	21.48	0.28	100.38
S2325-08_R	rim	0.02	0.15	44.91	11.63	0.24	18.57	0.01	0.00	0.01	23.92	0.28	99.75
S2325-08_R	rim	0.04	0.17	47.02	11.18	0.23	18.98	0.00	0.00	0.00	22.12	0.29	100.03
S2325-08_R	rim	0.02	0.12	46.56	11.18	0.23	18.77	0.00	0.00	0.00	22.83	0.28	99.98
S2325-08_R	rim	0.03	0.12	44.31	11.72	0.27	18.65	0.00	0.01	0.00	25.04	0.27	100.42
S2325-08_R	rim	0.04	0.15	44.96	11.44	0.25	18.52	0.00	0.02	0.00	23.95	0.28	99.61
S2325-08_R	rim	0.02	0.12	46.46	11.30	0.22	18.95	0.00	0.00	0.00	22.54	0.28	99.90
S2325-51_R	core	0.04	0.35	41.07	15.55	0.30	16.26	0.00	0.03	0.00	26.05	0.23	99.88
S2325-51_R	core	0.03	0.34	41.02	15.94	0.33	16.14	0.00	0.01	0.00	26.02	0.27	100.11
S2325-51_R	core	0.02	0.35	41.05	15.63	0.27	16.08	0.00	0.00	0.00	26.26	0.22	99.89
S2325-51_R	core	0.03	0.32	41.43	14.03	0.28	17.00	0.00	0.01	0.00	26.31	0.26	99.66
S2325-51_R	core	0.02	0.29	41.45	14.12	0.34	16.75	0.00	0.01	0.00	26.42	0.23	99.62
S2325-51_R	core	0.02	0.33	41.57	14.13	0.30	17.02	0.01	0.00	0.00	26.19	0.24	99.82
S2325-51_R	rim	0.03	0.25	40.84	16.68	0.28	15.57	0.00	0.03	0.00	26.04	0.22	99.94
S2325-51_R	rim	0.03	0.32	40.63	16.57	0.29	15.89	0.00	0.00	0.00	26.20	0.23	100.16
S2325-51_R	rim	0.04	0.32	39.25	14.40	0.32	16.23	0.00	0.00	0.00	29.19	0.22	99.97
S2325-51_R	rim	0.06	0.36	37.45	14.54	0.33	15.86	0.01	0.01	0.00	31.27	0.15	100.05
S2325-51_R	rim	0.04	0.39	36.54	15.37	0.35	15.48	0.03	0.01	0.01	31.43	0.16	99.79
S2325-55_R	core	0.05	0.32	39.75	15.56	0.31	16.68	0.00	0.01	0.01	27.42	0.21	100.32
S2325-55_R	core	0.02	0.33	39.76	15.82	0.29	16.54	0.01	0.02	0.00	27.88	0.23	100.89
S2325-55_R	core	0.01	0.36	39.51	15.81	0.36	16.61	0.00	0.01	0.00	27.91	0.22	100.81
S2325-55_R	core	0.02	0.37	36.75	16.24	0.34	15.81	0.01	0.01	0.00	30.34	0.19	100.08
S2325-55_R	core	0.04	0.43	36.68	16.43	0.33	15.71	0.00	0.00	0.00	30.72	0.17	100.51
S2325-55_R	core	0.04	0.42	37.22	17.11	0.36	15.46	0.00	0.03	0.00	29.50	0.20	100.35
S2325-55_R	core	0.04	0.43	36.56	17.14	0.30	15.47	0.01	0.04	0.00	29.99	0.19	100.17
S2325-55_R	core	0.02	0.48	34.75	17.75	0.33	15.00	0.00	0.05	0.01	32.21	0.20	100.79
S2325-55_R	rim	0.03	0.29	40.63	15.17	0.31	16.44	0.05	0.02	0.00	26.71	0.23	99.86
S2325-55_R	rim	0.01	0.32	39.01	15.53	0.31	16.22	0.00	0.02	0.00	27.77	0.22	99.43
S2325-55_R	rim	0.01	0.33	39.74	15.56	0.31	16.14	0.00	0.00	0.00	27.61	0.22	99.92
S2325-55_R	rim	0.04	0.38	34.59	17.56	0.34	14.60	0.01	0.00	0.00	31.89	0.15	99.56
S2325-55_R	rim	0.00	0.48	34.53	17.67	0.39	14.80	0.01	0.03	0.00	32.18	0.20	100.29

Appendix C

Trace element analysis

Trace element analysis of ABFZ clinopyroxenes

	Sr	Zr	Nb	La	Ce	Pr	Nd	Sm	Eu	Gd	Tb	Dy	Ho	Er	Tm	Yb	Lu
S2318-28Cpx1	3.69	7.32	0.22	0.23	0.88	0.00	1.08	0.77	0.29	1.53	0.33	2.27	0.00	1.57	0.00	1.47	0.19
S2318-28Cpx2	3.55	6.89	0.22	0.27	0.92	0.00	1.07	0.70	0.30	1.36	0.29	2.43	0.00	1.47	0.00	1.49	0.20
S2318-31CPXACORE3	2.96	9.95	0.07	0.16	0.81	0.26	1.97	1.35	0.50	2.91	0.60	4.18	0.87	2.64	0.36	2.21	0.30
S2318-31CPXARIM3	3.07	9.64	0.03	0.16	0.78	0.23	1.81	1.21	0.45	2.69	0.56	4.07	0.83	2.51	0.35	2.19	0.30
S2318-31CPXBCORE3	3.87	10.13	0.05	0.17	0.88	0.27	1.99	1.30	0.47	2.61	0.54	3.67	0.79	2.29	0.32	1.94	0.27
S2318-31CPXBRIM3	4.75	10.31	0.04	0.18	0.88	0.27	2.02	1.36	0.45	2.78	0.54	3.87	0.80	2.36	0.32	2.05	0.28
S2318-35CPXACORE4	2.89	11.31	0.08	0.27	1.13	0.30	1.91	1.02	0.39	1.94	0.39	2.63	0.56	1.61	0.23	1.38	0.19
S2318-35CPXARIM3	3.48	12.53	0.07	0.27	1.18	0.31	2.16	1.14	0.41	2.17	0.44	2.90	0.61	1.81	0.24	1.43	0.20
S2318-35CPXB1CORE3	2.41	12.55	0.06	0.26	1.18	0.31	2.07	1.15	0.43	2.12	0.42	2.94	0.59	1.74	0.24	1.45	0.19
S2318-35CPXB1RIM3	2.06	11.70	0.04	0.23	1.11	0.30	2.07	1.07	0.39	2.05	0.41	2.76	0.58	1.61	0.24	1.36	0.18
S2318-35CPXB2CORE3	2.67	11.03	0.05	0.24	1.02	0.27	1.79	1.01	0.37	1.92	0.38	2.62	0.54	1.55	0.21	1.29	0.17

S2318-35CPXB2RIM3	4.48	11.17	0.05	0.24	1.03	0.24	1.78	0.96	0.37	1.95	0.40	2.69	0.57	1.67	0.23	1.39	0.18
S2318-35Cpxcore1	2.26	10.58	0.17	0.24	1.08	0.00	1.78	1.00	0.38	1.89	0.37	2.61	0.00	1.59	0.00	1.33	0.18
S2318-35Cpxrim2	2.66	11.77	0.17	0.24	1.08	0.00	1.97	1.05	0.39	1.89	0.40	2.80	0.00	1.63	0.00	1.53	0.19
S2318-49CPXACORE2	9.65	27.05	0.49	0.79	2.87	0.70	4.47	1.82	0.63	2.62	0.50	3.42	0.74	2.32	0.33	2.10	0.29
S2318-49CPXARIM3	9.51	25.68	0.47	0.74	3.08	0.67	4.12	1.64	0.57	2.51	0.48	3.54	0.73	2.36	0.33	2.16	0.30
S2318-49CPXB1CORE3	8.88	23.53	0.38	0.80	3.04	0.70	3.92	1.64	0.58	2.55	0.46	3.28	0.69	2.07	0.30	1.87	0.26
S2318-49CPXB1RIM3	8.79	22.80	0.33	0.77	2.87	0.66	3.69	1.52	0.53	2.33	0.49	3.21	0.69	2.10	0.32	1.91	0.27
S2318-49CPXB2CORE3	8.32	18.41	0.34	0.68	2.60	0.59	3.50	1.40	0.51	2.20	0.40	2.90	0.61	1.92	0.27	1.69	0.24
S2324-04CPX1CORE3	54.39	40.86	0.05	0.81	5.14	1.22	6.69	2.22	0.86	3.02	0.46	2.38	0.36	0.85	0.11	0.59	0.08
S2324-04CPX1RIM3	46.13	48.86	0.04	0.83	4.46	1.06	5.81	2.05	0.79	3.00	0.48	2.47	0.38	0.95	0.12	0.66	0.09
S2324-04CPX3CORE3	42.86	36.37	0.03	0.79	4.24	1.07	5.96	1.95	0.75	2.68	0.43	2.19	0.35	0.82	0.10	0.59	0.08
S2324-04CPX3RIM3	46.00	42.31	0.04	0.80	4.35	1.02	5.69	1.91	0.75	2.77	0.45	2.30	0.37	0.92	0.11	0.66	0.09
S2324-04Cpxcore	47.95	36.28	0.20	0.92	5.21	0.00	6.71	2.21	0.82	3.01	0.43	2.38	0.00	0.87	0.00	0.62	0.08
S2324-04Cpxrim	44.23	38.00	0.22	0.94	4.90	0.00	5.75	1.92	0.77	2.76	0.40	2.31	0.00	0.92	0.00	0.72	0.09
S2325-01CCPX2CORE3	38.62	12.03	0.32	1.01	2.96	0.56	3.04	0.99	0.40	1.38	0.25	1.66	0.34	1.00	0.14	0.90	0.12
S2325-01CCPX2RIM3	36.68	12.05	0.27	0.92	2.75	0.54	2.89	0.98	0.38	1.34	0.24	1.62	0.34	0.99	0.14	0.90	0.13
S2325-01CCPX5CORE6	35.12	12.71	0.27	0.92	2.67	0.51	2.75	0.93	0.38	1.38	0.24	1.64	0.34	1.03	0.15	0.89	0.13
S2325-01CCPX5RIM3	40.20	12.94	0.26	0.80	2.47	0.49	2.78	0.92	0.33	1.40	0.25	1.61	0.35	1.03	0.14	0.94	0.13
S2325-01CCpxcore	31.97	10.16	0.43	0.90	2.48	0.00	2.72	0.89	0.35	1.31	0.21	1.39	0.00	0.89	0.00	0.81	0.12
S2325-01CCpxrim	32.60	10.61	0.40	0.88	2.55	0.00	2.69	0.91	0.36	1.28	0.23	1.52	0.00	0.95	0.00	0.81	0.12
S2325-03CPX2CORE_3	34.25	34.98	0.00	0.32	2.70	0.92	6.69	2.86	1.15	3.73	0.58	3.14	0.53	1.34	0.16	0.95	0.12
S2325-03cpx2core4	33.59	39.02	0.01	0.32	2.28	0.81	6.26	2.80	1.09	3.72	0.57	3.24	0.55	1.42	0.18	0.95	0.12
S2325-03CPX2RIM_2	31.93	35.35	0.00	0.28	2.20	0.72	5.20	2.55	0.97	3.32	0.52	2.85	0.50	1.29	0.17	0.98	0.12
S2325-03Cpxcore	28.70	31.33	0.16	0.26	2.06	0.00	5.13	2.25	0.95	3.16	0.50	2.87	0.00	1.39	0.00	1.02	0.14
S2325-03Cpxrim	29.86	32.76	0.13	0.24	1.99	0.00	4.77	2.27	0.87	3.11	0.50	2.83	0.00	1.28	0.00	0.96	0.15
S2325-05CPX2CORE3	56.98	32.23	0.02	0.54	2.68	0.67	4.16	1.62	0.69	2.66	0.49	3.30	0.68	1.93	0.24	1.44	0.19
S2325-05CPX2RIM2	59.76	35.18	0.05	0.56	2.71	0.67	4.01	1.60	0.72	2.65	0.52	3.33	0.71	1.94	0.26	1.59	0.20
S2325-05Cpxcore	42.83	26.90	0.16	0.49	2.39	0.00	4.15	1.69	0.66	2.73	0.50	3.43	0.00	1.96	0.00	1.58	0.22
S2325-05Cpxrim	34.97	32.65	0.25	0.68	2.16	0.00	3.20	1.35	0.46	2.17	0.42	2.89	0.00	1.70	0.00	1.36	0.21
S2325-08CPX1CORE3	36.84	26.99	0.21	0.63	2.84	0.75	5.00	2.19	0.86	3.11	0.53	3.30	0.65	1.77	0.24	1.41	0.19
S2325-08CPX1RIM3	37.97	31.96	0.23	0.67	3.05	0.81	5.34	2.32	0.95	3.41	0.59	3.74	0.73	2.00	0.27	1.51	0.20
S2325-51CPX1CORE3	2.71	23.56	0.01	0.37	2.13	0.58	3.94	1.75	0.70	3.10	0.64	4.37	0.93	2.82	0.39	2.47	0.33
S2325-51CPX1RIM3	2.56	25.35	0.01	0.33	1.98	0.59	3.88	1.91	0.66	3.32	0.68	4.64	0.97	2.90	0.40	2.39	0.32
S2325-51CPX2CORE3	3.93	15.89	0.01	0.29	1.72	0.49	3.08	1.38	0.57	2.41	0.47	3.40	0.72	2.23	0.32	2.00	0.27
S2325-51CPX2RIM3	3.35	15.65	0.01	0.21	1.31	0.39	2.58	1.26	0.45	2.34	0.45	3.10	0.64	1.93	0.26	1.53	0.21

S2325-51CPX3CORE3	2.82	20.03	0.01	0.33	1.94	0.55	3.64	1.71	0.62	2.84	0.57	3.83	0.82	2.35	0.33	2.06	0.27
S2325-51CPX3RIM3	2.25	26.62	0.01	0.28	1.83	0.58	4.10	2.11	0.62	3.53	0.67	4.61	0.96	2.78	0.38	2.27	0.29
S2325-51CPX4CORE3	2.96	24.70	0.01	0.36	1.97	0.58	3.97	1.88	0.65	3.48	0.66	4.57	0.98	2.90	0.40	2.42	0.32
S2325-51CPX4RIM3	2.45	33.01	0.01	0.30	1.87	0.60	4.41	2.35	0.67	4.18	0.80	5.47	1.14	3.26	0.44	2.49	0.34
S2325-55CPX1CORE3	12.49	21.89	0.00	0.32	2.17	0.65	4.33	1.98	0.77	3.29	0.62	4.29	0.89	2.67	0.37	2.25	0.32
S2325-55CPX1RIM3	5.26	23.01	0.00	0.26	1.95	0.61	4.23	2.03	0.72	3.51	0.65	4.35	0.90	2.61	0.37	2.21	0.29
S2325-55CPX2CORE3	3.03	23.31	0.00	0.27	2.12	0.68	4.66	2.15	0.75	3.68	0.68	4.51	0.91	2.59	0.35	2.19	0.28
S2325-55CPX2RIM4	2.62	27.62	0.00	0.28	2.12	0.73	5.24	2.39	0.81	3.92	0.74	4.92	1.01	2.95	0.40	2.42	0.32
S2325-55Cpxcore	2.93	20.80	0.10	0.28	2.19	0.00	4.46	2.03	0.80	3.15	0.58	3.95	0.00	2.36	0.00	2.06	0.26
S2325-55Cpxrim	2.46	21.64	0.10	0.23	1.95	0.00	4.36	1.99	0.69	3.14	0.61	4.12	0.00	2.40	0.00	2.03	0.28
S2326-01Dcpx1core5	20.01	27.77	0.00	0.33	2.29	0.66	4.33	2.04	0.84	3.36	0.65	4.53	0.95	2.89	0.41	2.58	0.35
S2326-01Dcpx1rim4	6.11	45.27	-0.01	0.31	2.28	0.78	5.60	2.71	0.86	4.78	0.92	6.45	1.32	3.87	0.52	3.05	0.41
S2326-01Dcpx2core4	25.07	30.23	0.00	0.40	2.17	0.63	4.28	2.04	0.83	3.48	0.68	4.83	1.03	3.06	0.43	2.68	0.38
S2326-01Dcpx2rim4	12.15	41.62	0.02	0.29	2.13	0.74	4.76	2.31	0.80	4.16	0.80	5.85	1.22	3.66	0.52	3.18	0.41
S2326-01Dcpx3core4	7.10	50.37	0.01	0.31	2.61	0.91	6.61	3.24	1.06	5.62	1.12	7.56	1.60	4.65	0.66	3.99	0.53
S2326-01Dcpx3rim4	15.06	60.76	0.01	0.32	2.58	0.89	6.71	3.48	1.00	6.38	1.16	8.57	1.72	5.10	0.69	3.97	0.53
S2326-02-cpx1	13.46	19.04	0.07	0.13	1.13	0.00	3.17	1.70	0.72	2.87	0.56	3.72	0.00	2.16	0.00	2.06	0.29
S2326-02-cpx2	12.53	19.45	0.06	0.12	1.20	0.00	3.26	1.77	0.76	2.95	0.56	3.91	0.00	2.37	0.00	2.27	0.30
S2326-02cpx2core4	14.99	20.33	0.01	0.13	1.18	0.43	3.38	1.71	0.75	3.18	0.60	4.16	0.87	2.61	0.37	2.29	0.31
S2326-02cpx2rim4	13.02	21.58	0.00	0.12	1.29	0.49	3.71	1.95	0.84	3.47	0.67	4.61	0.96	2.85	0.43	2.63	0.36
S2326-09-cpx1	3.76	21.24	0.08	0.12	1.35	0.00	3.69	1.79	0.69	2.89	0.57	3.96	0.00	2.29	0.00	2.02	0.28
S2326-09cpx1core4	7.62	29.13	0.01	0.15	1.54	0.60	4.82	2.36	0.90	4.16	0.75	5.07	1.05	3.11	0.43	2.57	0.35
S2326-09cpx1rim4	4.16	37.37	0.00	0.13	1.65	0.68	5.59	2.76	0.93	4.85	0.96	6.37	1.28	3.57	0.48	2.84	0.36
S2326-09-cpx2	2.15	32.28	0.01	0.13	1.44	0.00	4.70	2.51	0.88	4.43	0.89	5.87	0.00	2.79	0.00	2.52	0.33
S2326-09cpx2Acore4	17.54	23.53	0.00	0.16	1.43	0.52	3.70	1.91	0.80	3.30	0.62	4.19	0.87	2.66	0.36	2.21	0.31
S2326-09cpx2Arim4	14.43	29.82	0.01	0.16	1.44	0.58	4.32	2.17	0.87	4.29	0.82	5.39	1.02	3.27	0.40	2.52	0.36
S2326-09cpx2Bcore4	10.64	26.64	-0.01	0.15	1.47	0.57	4.31	2.14	0.87	3.65	0.68	4.65	0.95	2.87	0.40	2.47	0.34
S2326-09cpx2Brim3	8.87	32.16	0.00	0.18	1.63	0.67	5.30	2.56	1.06	4.38	0.86	5.64	1.22	3.32	0.48	3.00	0.38
S2326-15cpx1core4	42.52	31.78	0.03	0.72	3.19	0.94	5.70	2.03	0.80	2.86	0.51	3.19	0.59	1.65	0.21	1.37	0.18
S2326-15cpx1rim4	18.39	41.64	0.04	0.74	3.73	1.06	6.75	2.46	0.89	3.60	0.59	3.95	0.72	2.12	0.27	1.60	0.19
S2326-15cpx2core4	53.14	29.72	0.02	0.71	3.10	0.85	5.18	1.98	0.78	2.76	0.48	2.92	0.57	1.68	0.21	1.35	0.18
S2326-15cpx2rim4	48.97	33.26	0.02	0.70	3.07	0.84	5.25	1.93	0.76	3.05	0.52	3.23	0.64	1.81	0.25	1.60	0.21
S2326-16cpx1core4	28.04	31.37	0.04	0.32	2.18	0.71	4.75	1.99	0.85	2.96	0.50	3.30	0.64	1.88	0.25	1.59	0.20
S2326-16cpx1rim4	25.71	34.47	0.01	0.32	2.36	0.75	5.05	2.14	0.85	3.07	0.53	3.41	0.64	1.99	0.26	1.65	0.22

S2326-16cpx2core4	27.12	34.21	0.00	0.32	2.03	0.67	4.76	2.01	0.80	3.03	0.56	3.60	0.72	2.09	0.27	1.64	0.23
S2326-16cpx2rim4	27.61	34.32	0.01	0.36	2.02	0.63	4.47	1.80	0.79	3.00	0.55	3.63	0.74	2.09	0.28	1.78	0.24
S2326-16cpx3core4	29.21	32.74	0.02	0.31	2.10	0.67	4.75	2.01	0.82	3.13	0.56	3.47	0.69	2.07	0.29	1.75	0.22
S2326-16cpx3rim4	55.76	47.86	0.15	0.96	2.77	0.78	5.05	1.99	0.80	3.06	0.59	3.65	0.69	2.05	0.28	1.77	0.24
S2326-18-cpx1	3.54	4.52	0.07	0.06	0.24	0.00	1.19	0.81	0.36	1.52	0.30	2.18	0.00	1.29	0.00	1.12	0.15
S2326-18-cpx2	3.48	4.52	0.09	0.05	0.21	0.00	1.07	0.83	0.32	1.63	0.30	1.94	0.00	1.32	0.00	1.08	0.17
S2326-18cpx2core4	5.18	5.84	0.00	0.09	0.25	0.15	1.56	1.00	0.45	2.03	0.41	2.70	0.58	1.69	0.23	1.46	0.19
S2326-18cpx2rim4	5.69	5.75	0.00	0.06	0.19	0.12	1.19	0.82	0.36	1.55	0.33	2.47	0.48	1.49	0.21	1.37	0.17
S2326-18cpx3core4	4.71	6.06	0.01	0.04	0.24	0.15	1.43	0.99	0.43	2.02	0.40	2.79	0.57	1.72	0.23	1.38	0.19
S2326-18cpx3rim4	6.93	5.92	0.00	0.13	0.21	0.14	1.38	0.95	0.39	1.83	0.36	2.55	0.53	1.63	0.22	1.35	0.17
S2326-21-cpx1	13.60	13.45	0.07	0.10	1.04	0.00	2.59	1.30	0.59	2.20	0.41	2.98	0.00	1.72	0.00	1.52	0.21
S2326-21cpx1core4	13.10	18.86	0.00	0.13	1.12	0.43	3.41	1.77	0.71	3.00	0.57	3.87	0.79	2.37	0.32	1.99	0.29
S2326-21cpx1rim4	14.23	19.78	0.00	0.14	1.10	0.42	3.25	1.69	0.66	3.00	0.58	3.95	0.80	2.28	0.32	1.98	0.28
S2326-21-cpx2	12.80	16.76	0.07	0.13	1.21	0.00	3.09	1.72	0.67	2.65	0.49	3.35	0.00	2.07	0.00	1.78	0.22
S2326-21cpx3core4	14.52	17.24	0.00	0.13	1.14	0.43	3.35	1.70	0.72	2.87	0.56	3.68	0.77	2.27	0.32	1.88	0.26
S2326-21cpx3rim4	15.23	19.20	0.00	0.15	1.16	0.47	3.39	1.81	0.71	3.09	0.59	3.83	0.81	2.33	0.33	1.97	0.27
S2326-21cpx4core4	14.86	18.00	0.00	0.14	1.21	0.45	3.34	1.77	0.72	2.97	0.56	3.80	0.76	2.27	0.32	1.93	0.27
S2326-21cpx4rim4	15.65	19.13	0.00	0.14	1.25	0.46	3.31	1.83	0.71	3.07	0.55	3.97	0.81	2.45	0.35	2.05	0.27
S2326-24-cpx1	21.59	19.58	0.09	0.28	1.89	0.00	3.66	1.78	0.66	2.42	0.47	3.14	0.00	1.95	0.00	1.64	0.24
S2326-24cpx1core4	29.50	23.67	0.01	0.30	2.03	0.63	4.13	1.79	0.77	2.97	0.55	3.61	0.74	2.17	0.29	1.83	0.24
S2326-24cpx1rim4	28.60	23.26	0.00	0.31	2.03	0.60	3.96	1.75	0.73	2.73	0.52	3.47	0.72	2.12	0.29	1.76	0.24
S2326-24-cpx2	22.34	20.97	0.08	0.28	1.97	0.00	3.72	1.67	0.67	2.71	0.49	3.33	0.00	2.01	0.00	1.66	0.22
S2326-24cpx3core4	26.16	22.47	0.01	0.31	1.89	0.58	4.00	1.76	0.72	2.87	0.53	3.50	0.70	1.99	0.27	1.66	0.23
S2326-24cpx3rim4	27.62	26.71	0.11	0.46	2.11	0.63	4.17	1.76	0.73	3.02	0.55	3.58	0.71	2.20	0.29	1.81	0.25